An Approach to a Structure of the Virtual Photon using Dijet Events at HERA

Dissertation
zur Erlangung des Doktorgrades
des Fachbereichs Physik
der Universität Hamburg

vorgelegt von

Harald Labes
aus Kellinghusen

Hamburg
2003

Gutachter der Dissertation:	Prof. Dr. R. Klanner Prof. Dr. B. Naroska
Gutachter der Disputation:	Prof. Dr. B. Naroska Prof. Dr. V. Blobel
Datum der Disputation:	07.11.2003
Vorsitzender des Prüfungsausschusses:	Dr. H. D. Rüter
Vorsitzender des Promotionsausschusses:	Prof. Dr. R. Wiesendanger
Dekan des Fachbereichs Physik:	Prof. Dr. G. Huber

Abstract

The need of a partonic structure of the virtual photon to describe experimental data has been studied by comparing measurements of inclusive dijet cross sections of positron/proton interactions in the virtuality range $0.1 < Q^2 < 120$ GeV^2 to NLO QCD calculations. The measurements have been performed with the ZEUS experiment at the storage ring HERA using an integrated luminosity of 38.6 pb^{-1}. Jets were identified in the γ^*p center-of-mass frame of reference using the longitudinal invariant k_T cluster algorithm. The inclusive dijet cross sections were measured for jet transverse energies $E_{T1} > 7.5$ GeV and $E_{T2} > 6.5$ GeV in the pseudorapidity range $-3 < \eta_{1,2} < 0$, where the indices 1,2 refer to the jets with the highest and next highest transverse energy and the values refer to the γ^*p center-of-mass frame of reference. The results are presented as functions of Q^2, E_{T1}, η_{for} and x_γ^{obs}. Here, η_{for} is the pseudorapidity of the most forward jet and x_γ^{obs} is an estimation of the momentum fraction of the photon entering the hard part of the interaction.

Though the NLO QCD calculations including a parton density function for the virtual photon describe the experimental data better than those without, due to the large theoretical uncertainties no conclusions could be made that a partonic structure of the virtual photon is really necessary to describe the data.

Zusammenfassung

Die Notwendigkeit einer partonischen Struktur des virtuellen Photons zur Beschreibung experimenteller Daten ist untersucht worden durch einen Vergleich gemessener inklusiver Zwei-Jet Wirkungsquerschnitte von Positron/ Proton Wechselwirkungen im Virtualitätsintervall $0.1 < Q^2 < 120$ GeV^2 mit NLO QCD Rechnungen. Die Messungen wurden ausgeführt mit dem ZEUS Experiment am Speicherring HERA mit einer integrierten Luminosität von 38.6 pb^{-1}. Die Jets wurden im Massenmittelpunktsystem der Teilchen γ^* und p identifiziert unter Benutzung des longitudinal invarianten k_T Cluster Algorithmus. Die inklusiven Zwei-Jet Wirkungsquerschnitte wurden für transversale Jetenergien $E_{T1} > 7.5$ GeV und $E_{T2} > 6.5$ GeV im Pseudorapiditätsintervall $-3 < \eta_{1,2} < 0$ gemessen, wobei sich die Indices auf die Jets mit der höchsten bzw. nächthöchsten transversalen Energie beziehen und die Zahlenwerte für das γ^*p-Massenmittelpunktsystem gelten. Die Resultate sind dargestellt als Funktionen von Q^2, E_{T1}, η_{for} und x_γ^{obs}. Die Größe η_{for} bedeutet hier die Pseudorapidität des am stärksten in die Vorwärtsrichtung

verlaufenden Jets und x_γ^{obs} gibt eine Abschätzung des Impulsanteils des Photons, der in den harten Teil der Wechselwirkung einfließt.

Obwohl die NLO QCD Rechnungen, die eine Partondichteverteilung des virtuellen Photons enthalten, die gemessenen Daten besser beschreiben als solche, bei denen dies nicht der Fall ist, konnte wegen der großen theoretischen Unsicherheiten nicht auf eine wirkliche Notwendigkeit einer partonischen Struktur des virtuellen Photons zur Beschreibung der Daten geschlossen werden.

Contents

1 Photon Structure **19**

1.1 The Photon as the Quantum of the Electromagnetic Field . . 19
1.2 Quantum Mechanics and the Photon 22
1.3 The Photon in Quantum Field Theory 25
1.4 Hadronic Photon Structure 31
1.4.1 The VMD approach 32
1.4.2 The QCD approach 36

2 Theoretical Calculation of the ep–Scattering Cross Sections in NLO **42**

2.1 Photon Structure in ep–Interactions 42
2.2 Factorization and General expression for the Scattering Cross Section 44
2.3 Parton Density Functions 48
2.3.1 The Weizsäcker–Williams Approximation for $f_{\gamma/e}$ . . . 48
2.3.2 The PDFs of the Proton and the Photon 49
The DIS Scheme 49
The $\overline{MS}$ Scheme 49
The Factorization Scale μ_F 50
Determination of the PDFs 51
2.3.3 Examples of PDF's for the Photon 52
2.3.4 Evolution Equations 58
The DGLAP Equations 58
The BFKL equations 60
The CCFM equations 62
2.4 Regularization and Renormalization 64
2.5 The Hard Scattering Cross Section $d\sigma_{ij}$ in NLO 66
2.5.1 LO Contributions 67
2.5.2 NLO Corrections 71
2.5.3 Order of the Electron-Proton Cross Section 73
2.6 Fragmentation 75

2.6.1 The Independent Quark Model . . . 76
2.6.2 The String Fragmentation Model . . . 76
2.6.3 The Cluster Fragmentation Model . . . 78
2.7 Photon Structure in Next-to-Leading Order QCD and its Q^2 Dependence . . . 78

3 Experimental Setup 86
3.1 HERA . . . 86
3.2 The ZEUS Experiment . . . 88
3.2.1 The Central Tracking Detector . . . 90
3.2.2 The Uranium Calorimeter . . . 92
3.2.3 The Presampler . . . 93
3.2.4 The Small Angle Rear Tracking Detector . . . 94
3.2.5 The Hadron-Electron Separator . . . 96
3.2.6 The Beam Pipe Calorimeter . . . 97
3.2.7 The Luminosity Measurement (LUMI) . . . 100
3.2.8 The ZEUS Three-Level Trigger . . . 101

4 Kinematic Variables, their Reconstruction and the Measurement of the Cross Section 104
4.1 Introduction of the Kinematical Variables . . . 104
4.1.1 Virtuality, Inelasticity, the Bjorken–x and x_γ . . . 104
4.2 Transverse Energy and Pseudorapidity . . . 107
4.3 Reconstruction of the Kinematical Variables . . . 110
4.3.1 The Electron Method . . . 110
4.3.2 The Method of Jacquet and Blondel . . . 111
4.3.3 The Double–Angle Method . . . 113
4.3.4 Reconstruction Methods used for this Analysis . . . 114
4.3.5 The Estimator x_γ^{obs} . . . 115
4.4 Calculation of the Cross Section . . . 116

5 Jets and EFOs 119
5.1 The Cone Algorithm . . . 120
5.2 The Inclusive k_T Algorithm . . . 120
5.3 Snowmass Convention . . . 121
5.4 Energy Flow Objects . . . 122

6 Event Generators and JetViP 126
6.1 HERWIG . . . 126
6.2 PYTHIA . . . 127
6.3 LEPTO . . . 127

6.4 ARIADNE 128
6.5 The Program JetViP 129

7 Event Selection **133**

8 Unfolding Detector Effects and Determination of the Uncertainties **138**
8.1 Event Generation 139
8.2 Detector Simulation 139
8.3 x_γ^{obs} Reweighting Procedure 140
8.4 Bin-by-Bin Correction Method 148
8.5 Determination of the Uncertainties 167
8.5.1 Experimental Uncertainties 167
8.5.2 Theoretical Uncertainties 169

9 Results and Conclusions **172**
9.1 The Differential Dijet Cross Section $d\sigma/dQ^2$ 172
9.2 The Double Differential Dijet Cross Section $d^2\sigma/dQ^2 dE_{T1}$. 173
9.3 The Double Differential Dijet Cross Section $d^2\sigma/dQ^2 d\eta_{for}$. 174
9.4 The Double Differential Dijet Cross Section $d^2\sigma/dQ^2 dx_\gamma^{obs}$. 175
9.5 Influence of the Scale on the Dijet Cross Sections 176
9.6 Summary and Conclusions 176

List of Figures

1.1 Conversion of a photon into a e^+e^- pair in a nuclear electromagnetic field. 30
1.2 Shielding of the electrons charge by vacuum fluctuations of the photon. 30
1.3 Possible electromagnetic interaction of an electron with a nucleon in the view of the VMD-model. The photon transforms into a vector meson which than undergoes a strong interaction with the nucleon. 34
1.4 Development of the photons hadronic structure in the view of QCD. The left graph is usually referred to as the "point-like" contribution. 40

2.1 Examples of direct interactions (leading order in α_s) in of a photon with a parton of the proton: a) QCD–Compton effect, b) Boson–Gluon fusion. 43
2.2 Examples of resolved interactions (leading order in α_s) of a photon with a proton. Shown are interactions of a gluon and a quark from the photon with a quark and a gluon from the proton. 44
2.3 Measurements of the total photon-proton cross section at different center-of-mass energies. Full circles denotes results from H1, full triangles results from ZEUS and open squares from fixed target experiments. The full curve shows measurements of the total hadron-hadron cross section. 45
2.4 Factorization in an electromagnetic ep–interaction. The entire interaction is divided in "soft" and "hard" subinteractions which can be treated separately. The $f_{a/A}$ are "parton-density functions" giving the probability of finding a parton a in a particle A and $d\sigma_{ij}$ is the hard scattering cross section of a "parton" i from the electron off a parton j from the proton. . 46
2.5 Scattering of an electron from a quark with a gluon emission. 50

2.6 Splitting of a scattering process through the factorization scale μ_F separating subprocesses occurring with different time scales. 51
2.7 Ladder diagram showing the strong ordering in the transverse momenta of the interacting parton and the quanta it has emitted before it entered the interaction. This strong ordering is an assumption made in the derivation of the DGLAP equations. 59
2.8 Angular ordering of the emission of gluons from a parent gluon. Here, q_i denotes the momentum of the emitted gluon i. 63
2.9 Definition of the Lorentz invariant Mandelstam variables s, t and u. 66
2.10 Some leading order contributions to direct interactions. The first row shows "boson gluon fusion" while in the second row the diagrams contributing to the "QCD Compton scattering" are displayed. 68
2.11 Some leading order contributions to resolved interactions. . . . 69
2.12 Virtual corrections for a direct hard scattering process. The first row shows self-energy diagrams, the middle row propagator corrections and box diagrams and in the last row vertex corrections are displayed. 71
2.13 Virtual corrections for a resolved hard scattering process. The first row shows self-energy diagrams, the middle row propagator corrections and box diagrams and in the last row vertex corrections are displayed. 72
2.14 Generic diagrams for the real corrections in direct interactions. 73
2.15 Generic diagrams for the real corrections in resolved interactions. 74
2.16 Mechanism of the independent fragmentation model. A quark of flavor "a" produces a color field with its corresponding anti partner from which other quark/anti-quark pairs emerge. Quark "a" now combines with an anti-quark from such a pair ("$b\bar{b}$") to form a new meson (of rank 1). The remaining quark "b" then forms a meson of rank 2 from another quark/anti-quark etc. 81
2.17 Oscillatory mode of the Lund yoyo hadron. The quark/anti-quark starts to separate at x_0. At the time t_1 the constant attractive force stops a further separation and the particles turn around and move back. At time t_2 they reached an opposite configuration compared to t_1. The color force pulls them back again so that at t_3 the accomplished one cycle viewed from the configuration at t_1. 82

2.18 Starting from the initial configuration at t_0 a new $q\bar{q}$ pair is created at time t_1. The original string then decays into two strings at t_2. At t_3 these two new strings creates new $q\bar{q}$ pairs what leads to there decay at t_4, etc. This process proceeds until the energy of each string allows no further decay. 83
2.19 Schematic illustration of cluster fragmentation. The $q_a\bar{q}_a$ pair from the hard scattering process emits gluons which in turn decay into new $q\bar{q}$ pairs. The indices denote the spinor color. The pairs then combine to color neutral clusters which in turn decay into mesons. 84
2.20 Figure to illustrate the ambiguous notion of photon structure when next-to-leading order corrections are included. In a) a leading order direct (resolved) interaction is shown when the process in the dashed (dotted) rectangle denotes the hard part of the interaction. In b) the same diagram is shown but this time it corresponds to a next-to-leading order direct interaction when the process in the rectangle denotes the hard interaction. 85

3.1 Aerial view of DESY, showing the colliders PETRA and HERA. 87
3.2 The HERA accelerator complex. The left figure shows the layout of HERA, while the right figure displays the system of pre-accelerators. In the four experimental halls the following experiments are installed: ZEUS in the South hall, H1 in the North hall, HERA-B in the West hall and HERMES in the East hall. 88
3.3 The main components of the ZEUS detector along the beam pipe. See text for description of the components. 90
3.4 The main components of the ZEUS detector perpendicular to the beam direction. See text for description of the components (the vertex detector (VXD) was removed in 1995). 91
3.5 Layout of a CTD octant, each octant has nine superlayers. The even numbered layers are declined with respect to the beam axis ('Stereo angle'). The angles for each superlayers are also shown. 92
3.6 Layout of an FCAL module. The modules of the calorimeter are subdivided into EMC and HAC sections which in turn are divided into cells. A cell is read out on two opposite sides by one wavelength shifter each. 94
3.7 Front view of the RCAL. The shaded area is covered by the presampler. 95

3.8 Location of the SRTD inside the ZEUS-detector. The distances are not to scale. The range in polar angle covered by the SRTD is shown by the dotted lines. 96
3.9 Orientation and numbering scheme of the strips of the SRTD. The quadrants 2 and 4 are separated by 8 cm. 97
3.10 Drawing of the two BPC modules together with the wavelength shifters (WLS) and photomultiplier houses (PMT). . . 98
3.11 Location of the BPC modules with respect to the beam pipe and the interaction point. The funnel shaped beam pipe with the exit windows for the scattered electrons is also shown. . . 99
3.12 Location of the segments of the BPC North module. The shaded area indicates the fiducial area of this module. 100
3.13 Layout of the HERA magnet system and the ZEUS luminosity detector located in the HERA tunnel The gamma and electron detectors (LUMIG,LUMIE) are used for the luminosity measurement. 101
3.14 Schematic diagram of the ZEUS three level trigger. 102

4.1 Sketch showing a "resolved" electron–proton collision together with the relevant kinematic variables. k^μ (k'^μ) is the four-vector of the incident (outgoing) electron, a^μ (b^μ) the four-vector of the parton emerging from the photon (proton) and q^μ (P^μ) is the four-vector of the photon (proton) itself. 105
4.2 Energy–momentum relations in a photon–proton interaction in the HCM-frame of reference. $p_\parallel$ ($E_\parallel$) denotes the longitudinal p_T (E_T) the transverse momentum (energy) of the outgoing particle. 108
4.3 Distribution of x_γ^{obs} generated with HERWIG 5.9 for $Q^2 < 1$ GeV^2. The histogram shows the total distribution while the hatched one shows the direct part only. For $x_\gamma^{obs} < 0.75$ the resolved part dominates while for $x_\gamma^{obs} > 0.75$ the direct part yields the most contribution. The value $x_\gamma^{obs} = 0.75$ is indicated by a straight line. 117

5.1 This figure shows how EMC and HAC cells of the ZEUS calorimeter are combined with tracks to form EFOs. Four EMC cell islands (2,3,4,5) and one HAC cell island (1) are shown. The EMC cell islands 2 and 3 are combined with the HAC cell island 1 to form a cone island. In the next step the islands are matched to tracks. 123

6.1 The color dipole model in deep inelastic scattering. The struck quark forms a color dipole with the proton remnant. This dipole emits a gluon and two new dipoles from the quark and the remnant are formed. These dipoles in turn emit gluons which form further dipoles with the color charges, etc. 132

8.1 Effect of the geometrical filter for the event generator. The BPC surface represented by the grid and its fiducial area are shown in the ZEUS x–y plane. The filter accepts only those events lying within a azimuthal angle $\varphi = 2.2$ rad. These events are shown as points. 140
8.2 Comparison of data with events generated by HERWIG5.9 and simulated for DET-level for the distribution of x_γ^{obs} in the different Q^2-ranges. The dots show the data, the solid lines the generated events filled with normal weights and the hatched histogram the generated events after proper reweighting. For the proton the parton density function of MRSA was used, for the photon the parton density function GRV-LO. 144
8.3 Same as for Fig. 8.2 but for the distribution of Q^2. 145
8.4 Same as for Fig. 8.2 but for the distribution of E_{T1}. 146
8.5 Same as for Fig. 8.2 but for the distribution of η_{for}. 147
8.6 Visualization of the definition of the numbers N_1, N_2 and N_3 as given in the text. 149
8.7 Gaussian fits (solid line) to the difference $\Delta X = X_{HAD} - X_{DET}$ or $\Delta X / X_{HAD}$ of the quantities Q^2, E_{T1}, η_{for} and x_γ^{obs} obtained from HERWIG5.9 using MRSA as parton density function of the proton and GRV-LO as parton density function of the photon. The resolution, "Sigma", of the detector system can be read off from the plots. 153
8.8 Same as in Fig. 8.7 but for the quantities E_{T2}, η_1, y_{JB} and the positron energy (E_e) as measured by the CAL and by the BPC, respectively. 154
8.9 Purities for the distribution of Q^2 as obtained from events generated with HERWIG5.9 using MRSA as parton density function of the proton and GRV-LO as parton density function of the photon. 155
8.10 Same as in Fig. 8.9 but for the distribution of E_{T1}. 156
8.11 Same as in Fig. 8.9 but for the distribution of η_{for}. 157
8.12 Same as in Fig. 8.9 but for the distribution of x_γ^{obs}. 158

8.13 Efficiencies for the distribution of Q^2 as obtained from events generated with HERWIG5.9 using MRSA as parton density function of the proton and GRV-LO as parton density function of the photon. 159
8.14 Same as in Fig. 8.13 but for the distribution of E_{T1}. 160
8.15 Same as in Fig. 8.13 but for the distribution of η_{for}. 161
8.16 Same as in Fig. 8.13 but for the distribution of x_γ^{obs}. 162
8.17 Correction factors for the distribution of Q^2 as obtained from events generated with HERWIG5.9 using MRSA as parton density function of the proton and GRV-LO as parton density function of the photon. 163
8.18 Same as in Fig. 8.17 but for the distribution of E_{T1}. 164
8.19 Same as in Fig. 8.17 but for the distribution of η_{for}. 165
8.20 Same as in Fig. 8.17 but for the distribution of x_γ^{obs}. 166
8.21 Ratio of the ratios $r = E_{T,\mathrm{eff}}/p_{T,\mathrm{positron}}$ of data (r_{dat}) and simulated events (r_{sim}) plotted against the $E_{T,\mathrm{eff}}$ (see text) of the jets to obtain the jet energy scale uncertainty. The vertical lines denote the 1% limit. 169

9.1 The differential dijet cross section $d\sigma/dQ^2$ compared with next-to-leading order calculations of JetViP including hadronization corrections (see text for details). The parton density function CTEQ4M was used for the proton and the parton density function SaS1M was used for the photon. 178
9.2 The double differential dijet cross section $d\sigma/dQ^2dE_{T1}$ compared with next-to-leading order calculations of JetViP including hadronization corrections (see text for details). The parton density function CTEQ4M was used for the proton and the parton density function SaS1M was used for the photon. . 179
9.3 The double differential dijet cross section $d\sigma/dQ^2d\eta_{for}$ compared with next-to-leading order calculations of JetViP including hadronization corrections (see text for details). The parton density function CTEQ4M was used for the proton and the parton density function SaS1M was used for the photon. . 180
9.4 The forward bin $-0.8 < \eta_{for} < 0$ of the double differential dijet cross section $d\sigma/dQ^2d\eta_{for}$ compared with next-to-leading order calculations of JetViP including hadronization corrections (see text for details). The parton density function CTEQ4M was used for the proton and the parton density function SaS1M was used for the photon. 181

9.5 The double differential dijet cross section $d\sigma/dQ^2dx_\gamma^{obs}$ compared with next-to-leading order calculations of JetViP including hadronization corrections (see text for details). The parton density function CTEQ4M was used for the proton and the parton density function SaS1M was used for the photon. . 182

List of Tables

1.1 Terms contributing to the interaction of an electron spinor field with its electromagnetic photon field up to second order in QED. 41

2.1 Splitting functions in leading order QCD. 61
2.2 Squared matrix elements for the various Born terms of the direct hard scattering contributions. 68
2.3 Squared matrix elements for the various Born terms of the resolved hard scattering contributions. 70

3.1 HERA parameters and design values. In 1997 HERA operated with 174 colliding bunches, 15 positron-pilot bunches and 6 proton-pilot bunches. 89

7.1 Summary of the cuts defining the available phase space of the hadronic final state in the HCM-frame of reference and the technical cleaning cuts applied in the laboratory frame of reference. For details see text. 137

8.1 Resolution of the ZEUS detector system for the quantities used in this analysis. The resolutions refer to dimensionless quantities as explained in the text. 151

Introduction

The theoretical language which is nowadays commonly used to describe the interactions between subatomic particles is that of quantum field theory. In the spirit of quantum field theory, particles appear to be the quanta of certain "matter fields" while on the other hand classical fields like the electromagnetic field appear to be quantized and in this way assumes a "particle character".

In the classical picture an interaction between two particles is mediated by a "force field". In the picture of quantum field theory such an interaction proceeds by an exchange of the quanta of the force field between the interacting particles.

Photons are the "exchange quanta" of quantum electrodynamics, the field theoretical description of the interaction between electrically charged particles. In the language of quantum electrodynamics a charged particle interacts with another charged particle by the exchange of photons. The photon itself is considered to be a point like particle with spin 1 and electric charge 0. However, quantum electrodynamics also predicts that the photon is able to convert into a complicated state of particles (electrons, positrons, quarks, antiquarks,...) preserving the photons energy, momentum, spin and charge. Through these so called "quantum fluctuations" the photon acts as a source of particles and it is this phenomenon that lets the photon appear to have a "structure".

Depending on the value of the square of its four-momentum q^μ a photon is called "real" when $q_\mu q^\mu = 0$, what means that its rest mass is zero, and a photon is called "virtual" when $q_\mu q^\mu \neq 0$.[1] For this reason the quantity $Q^2 = -q_\mu q^\mu$ is called the "virtuality" of the photon.

For the real photon the concept of a structured particle is well established theoretically and experimentally while a highly virtual photon is considered to be predominantly point like. Considerable progress has been made recently to study the structure of the virtual photon theoretically [Chy00, Sas00,

[1] Actually this conditions are usually weakened to be $q_\mu q^\mu < 1\ \mathrm{GeV}^2$ for the real photon and $q_\mu q^\mu > 1\ \mathrm{GeV}^2$ for the virtual photon.

Kra00] and experimentally at LEP [Abb02, Acc98] and HERA [Adl00, Bre00]. However, the structure of the virtual photon expressed by a "parton density function" is still less well known than that of the real photon.

In this thesis the need for a structure of the virtual photon is studied by means of differential cross sections for events where at least two jets (a jet can be considered as a collimated "spray" of particles), appear in the final state. These so called inclusive dijet events were measured as functions of the virtuality of the photon (Q^2), the highest transverse jet energy in a particular event (E_{T1}), the pseudorapidity of the most forward jet (η_{for}) and the estimated fraction of the photon momentum entering the hard interaction (x_γ^{obs})[2]. These differential cross sections are measured with the ZEUS detector setup at HERA and compared to perturbative calculations of quantum chromodynamics (QCD)[3] in next-to-leading order in the strong coupling constant α_s.

This thesis is organized as follows: Chapter 1 introduces the concept of photon structure. A kind of a historical overview is given on how the photon appeared in physics, how a structure of the photon was discovered and how the photons structure is described by different theoretical pictures. Chapter 2 continues this theoretical introduction. It is shown how the concept of photon structure enters the calculation of the cross section of an actual electron (or positron)–proton interaction. The concept of factorization is introduced leading to a general formula for the cross section. The components of this formula are then explained in some detail considering also other theoretical concepts like the Weizsäcker-Williams approximation, factorization schemes, evolution equations etc. which are connected to them. The chapter ends with a discussion of photon structure in a next-to-leading order QCD calculation.

Chapter 3 gives a description of the experimental setup. The HERA storage ring and the ZEUS experiment are described, displaying their status in the run time period 1996/97 in which the data were taken, used in this analysis. Only those components of ZEUS are considered in some detail which were actually used by the analysis presented in this thesis.

Chapter 4 introduces the kinematical variables and explains in some detail the different methods used to reconstruct them from the various measured quantities.

Chapter 5 is devoted to the definition of the jets. The cone and the inclusive k_T algorithm are explained next to "energy flow objects", the objects which are actually combined to jets.

[2] All the quantities mentioned here are explained in some detail in chapter 4.

[3] Quantum chromodynamics is the quantum field theory describing the interactions of the strongly interacting particles, the quarks. The quanta of quantum chromodynamics are called gluons.

Chapter 6 deals with the programs used to perform theoretical calculations. The event (Monte Carlo) generators used for data and hadronization corrections are briefly described followed by a more detailed description of the program JetViP with which the next-to-leading order QCD calculations have been performed.

In chapter 7 the event selection criteria are given and in chapter 8 the unfolding of the detector effects is explained, introducing the x_γ^{obs} reweighting procedure and the bin-by-bin correction method. Chapter 8 closes with a discussion of the determined experimental and theoretical uncertainties.

In chapter 9 finally the results of the comparison of the measured differential inclusive dijet cross sections with the next-to-leading order QCD calculations are presented and discussed.

Chapter 1

Photon Structure

1.1 The Photon as the Quantum of the Electromagnetic Field

An arbitrary, time independent distribution of electric charge described by a charge density $\rho(\mathbf{r})$ located somewhere in space alters the properties of space. This means that to each point $\mathbf{r}$[1] in space an electric potential $\Phi(\mathbf{r})$ and an electric field $\mathbf{E}(\mathbf{r})$ is attributed which are connected by the relation $\mathbf{E}(\mathbf{r}) = -\nabla\Phi(\mathbf{r})$. A test charge q at point $\mathbf{r}$ experiences this new feature of space through the Coulomb-force $\mathbf{F}(\mathbf{r}) = q\mathbf{E}(\mathbf{r})$, acting on it. In this way, the test charge interacts with the charge distribution $\rho(\mathbf{r})$ via the field it produces. A similar situation shows up when one considers a time independent current of charge characterized by a current density $\mathbf{j}(\mathbf{r})$. This current produces a vector potential $\mathbf{A}(\mathbf{r})$ and a magnetic flux density $\mathbf{B}(\mathbf{r})$ which are connected by the relation $\mathbf{B}(\mathbf{r}) = \nabla \times \mathbf{A}(\mathbf{r})$. A test charge q moving with constant velocity $\mathbf{v}$ is influenced by this "new feature" of space through the Lorentz force $\mathbf{F}(\mathbf{r}) = q\mathbf{v} \times \mathbf{B}(\mathbf{r})$ it experiences. These two types of fields, the electric and the magnetic field, producing these two types of forces, the Coulomb and the Lorentz force, seem to be independent of each other but actually they are not. M. Faraday and J.C. Maxwell revealed a deep connection between both types of interaction and showed that electric and magnetic fields which are varying with time are actually inducing each other. This was the first time, that two apparently distinct interactions, here the electric and the magnetic interactions, were unified into one, to the so called *electromagnetic interaction*. Furthermore Maxwell was able to show that the electromagnetic field is completely described by a set of four equations, nowadays known

[1] Bold face letters are denoting 3-vector quantities.

as *Maxwell's equations*. These are most elegantly expressed in terms of the four-potential $\mathrm{A}^\mu = (\Phi, \mathbf{A})$ and the four-current $\mathrm{j}^\mu = (\rho, \mathbf{j})$[2]. From A^μ one further defines the electromagnetic field tensor and its dual by

$$\mathrm{F}^{\mu\nu} = \partial^\mu \mathrm{A}^\nu - \partial^\nu \mathrm{A}^\mu \qquad \text{and} \qquad \tilde{\mathrm{F}}^{\mu\nu} = \frac{1}{2}\epsilon^{\mu\nu\rho\sigma}\mathrm{F}_{\rho\sigma}, \tag{1.1}$$

where ∂^μ is the usual shorthand form of the derivative with respect to $x_\mu = g_{\mu\nu}x^\nu$[3] that means $\partial^\mu = \frac{\partial}{\partial x_\mu}$. The tensor $\mathrm{F}^{\mu\nu}$ can be considered as the four dimensional generalization of the three dimensional curl and $\epsilon^{\mu\nu\rho\sigma}$ is the totally antisymmetric Levi-Civita tensor:

$$\epsilon^{\mu\nu\rho\sigma} = \begin{cases} +1 \text{ if } (\mu\nu\rho\sigma) \text{ is an even permutation of } (0123) \\ \text{-1 if } (\mu\nu\rho\sigma) \text{ is an odd permutation of } (0123) \\ \ 0 \text{ otherwise.} \end{cases} \tag{1.2}$$

In terms of these quantities, Maxwell's equations simply reads:

$$\partial_\mu \mathrm{F}^{\mu\nu} = \mathrm{j}^\nu \qquad \text{and} \qquad \partial_\mu \tilde{\mathrm{F}}^{\mu\nu} = 0. \tag{1.3}$$

Fully written these equations gives of course the familiar four relations:

$$\nabla \cdot \mathbf{E} = \nabla \cdot \left(-\frac{\partial \mathbf{A}}{\partial\, \mathrm{t}} - \nabla\Phi \right) = \rho \quad ; \quad \nabla \times \mathbf{B} - \frac{\partial \mathbf{E}}{\partial\, \mathrm{t}} = \nabla \times \nabla \times \mathbf{A} + \frac{\partial}{\partial \mathrm{t}} \nabla\Phi = \mathbf{j}$$

$$\nabla \cdot \mathbf{B} = \nabla \cdot \nabla \times \mathbf{A} = 0 \quad ; \quad \nabla \times \mathbf{E} + \frac{\partial \mathbf{B}}{\partial\, \mathrm{t}} = \nabla \times \left(-\nabla\Phi + \frac{\partial \mathbf{A}}{\partial\, \mathrm{t}} \right) = 0$$

In this form, Maxwell's equations show clearly the intimate connection between the electric field and the magnetic flux-density and the electric potential and the magnetic vector potential, respectively, when the fields vary with time.

Maxwell's equations form the framework of what is called *Classical Electrodynamics*. It works very well in explaining daily life phenomena like incandescent light, electric motors acting in the diverse electric machines, transmitting and receiving of electromagnetic waves etc., and even the propagation of light in matter is described very well in this framework as long as the macroscopic aspects of the phenomena are concerned. However, in describing the mutual electromagnetic interactions of subatomic particles or their interaction with the electromagnetic field in general, the continuous

[2]Throughout this thesis Heaviside-Lorentz rationalized units are used, so that $e^2/4\pi hc = \alpha = 1/137$, where e is the electric charge of the electron ($e = 1.626 \cdot 10^{-19}$ As) and h is Planck's constant ($h = 6.6256 \cdot 10^{-34}$ Js).

[3]In this thesis the Minkowsky metric $g_{\mu\nu}$ with $\mathrm{Tr}\, g_{\mu\nu} = -2$ is used.

space-time description provided by Maxwell's equations turned out to be of rather limited validity.

One of the first instances where the continuous electromagnetic field theory failed was the emission spectrum of so called "blackbody" radiation[4]. It was M. Planck (around 1900) who successfully solved this problem by assuming that the atoms making up the radiator behave like harmonic oscillators, and that each atom oscillates with a given frequency ν. He further assumed that each oscillator can absorb or emit radiation energy (E) only in an amount proportional to this frequency, that is $E = h\nu$. The variable h is the proportionality constant which nowadays is known as *Planck's constant*. The crucial point here is, that in this way Planck performed a quantization of the electromagnetic energy, because the energy of an oscillator can now only attain certain values, which are $h\nu, 2h\nu, 3h\nu$, etc., so that in general the possible energy values of an oscillator with frequency ν are $E_n = nh\nu$. This is in contradiction to Maxwell's equations, which permits a continuous emission or absorption of energy. This quantization of the electromagnetic energy in fact gave birth of *quantum mechanics*.

Further experimental evidence for the quantization of the electromagnetic field came from the *Photoelectric-* and the *Compton- Effect*. In 1887, while investigating the electric discharge between two electrodes H. Hertz observed that the intensity of the discharge increased when the electrodes were illuminated with ultraviolet light. And one year later W. Hallwachs found that certain metals such as zinc, potassium or sodium gave rise to an electronic emission when illuminating their surfaces. Obviously there occurs an interaction between the incident electromagnetic radiation and the electrons in the metal which are moving quasi freely through the metals crystal lattice. By this interaction the electrons are released from the metal surface and this is called Photoelectric Effect and the released electrons "photoelectrons". It was observed that for each substance there is a threshold frequency ν_0 of electromagnetic radiation such that, no matter how intense the radiation may be, no photoelectrons are produced for radiation of frequency less than ν_0.

In 1905 A. Einstein gave an explanation for this frequency dependence of photoelectron production in agreement with experiment. He assumed light is not just an electromagnetic wave but consist of a stream of massless "corpuscles" each carrying energy equal to $E = h\nu$, as suggested by Planck. In this way he found for the threshold frequency $\nu_0 = \phi_0/h$, where ϕ_0 is the so called *work function* of the metal giving the minimum energy needed to remove an electron from its surface. Another phenomenon revealing the

[4]A blackbody is a hypothetical entity which absorbs all energy, reflects none and emits energy with perfect efficiency.

corpuscular nature of electromagnetic radiation is the Compton effect. In the early 1920's A.H. Compton first observed and analyzed the effect that when electromagnetic radiation passed through a region in which free electrons are present, in addition to the incident radiation, another radiation of smaller frequency appears. Also this effect was easily explained by assuming that the electromagnetic wave (the light) is made up of particles with zero rest mass, energy $E = h\nu$ and momentum $p = E/c$ which are scattered off the free electrons. Exploiting energy and momentum conservation yields:

$$\frac{1}{\nu'} - \frac{1}{\nu} = \frac{\lambda_C}{c}(1 - \cos\theta) \tag{1.4}$$

Here ν is the frequency of the incident wave, ν' the frequency of the scattered wave, θ the angle between the incident and the scattered wave and $\lambda_C = h/m_e c$ the so called "Compton wavelength" with m_e the mass of the electron. So all these experimental evidences indicate that the electromagnetic field is of a double nature. On the one hand side it behaves like a continuous field as proposed by Maxwell's equations what explains all macroscopic phenomena but on the other hand when certain microscopic phenomena are concerned the electromagnetic field shows up a discontinuous behavior as being composed of individual particles or quanta. In 1926 the chemist G.N. Lewis [Lew26] called these quanta of the electromagnetic field *photons* and this name holds up to this day.

1.2 Quantum Mechanics and the Photon

In the last section examples were given, where a continuous field had to be interpreted in terms of particles or quanta to explain certain microscopic phenomena. In turn, in the first quarter of the last century it was observed, that microscopic particles like electrons, next to their properties identifying them as particles under certain circumstances behave like wave fields, e.g. electrons scattered off a crystal lattice give rise to specific diffraction pattern on a fluorescence screen, what is typical for waves. So on the microscopic scale, particles and wave fields are intimately connected. This observation and others like the quantization of the energy and angular momentum of electrons bound to atoms, the stability of atoms or the formation of chemical bonds and the inability of classical mechanics and electrodynamics to explain all these phenomena led to the development of *quantum mechanics*.

In quantum mechanics every particle or more generally "quantum state" of a particle or system of particles is represented by a so called "wave function" containing all the physical information about this state. This wave

function is obtained from an appropriate equation of motion. As long as the system under consideration has a classical analog, this equation of motion can be obtained from its classical Hamiltonian by means of the so called *correspondence principle*. This principle states, that all dynamical quantities (Coordinate vector, momentum, energy, etc.) have to be replaced by corresponding operators. The replacements which have to be made are:

$$\mathbf{p} \to -i\hbar\nabla; \quad E \to i\hbar\frac{\partial}{\partial t}; \quad \mathbf{q} \to \mathbf{q} \tag{1.5}$$

The coordinate operator $\mathbf{q}$ simply means "multiplication by the corresponding coordinate". For a classical quantity composed of several of the dynamical quantities (e.g. the Hamiltonian, the angular momentum, etc.) this replacement has to be done in such a way that the resulting quantum mechanical operator is hermitian. This requirement is necessary because the eigenvalues of the operator (the eigenvectors are the already cited wave functions) are the measurable values of the corresponding classical quantity and these are real and only hermitian operators have an exclusively real spectrum of eigenvalues.

For a non-relativistic particle of mass m moving under the influence of a time independent potential $\mathrm{V}(\mathbf{r})$ the classical Hamiltonian reads:

$$H = \frac{\mathbf{p}^2}{2m} + V(\mathbf{r}) \tag{1.6}$$

and from the correspondence principle the Hamiltonian operator is given by:

$$-\frac{\hbar^2}{2m}\nabla^2\psi(\mathbf{r},t) + V(\mathbf{r})\psi(\mathbf{r},t) = i\hbar\frac{\partial\psi(\mathbf{r},t)}{\partial\, t} \tag{1.7}$$

This last equation (1.7) is called *Schrödinger equation* [Sch26] and the function $\psi(\mathbf{r},t)$ is the wave function containing the characteristics of the particles state. The application of this equation was and still is very successful. By means of Schrödinger's equation it was possible to give a satisfactory explanation of the nature of the chemical bond that constrains atoms to form a molecule and the bond angles in molecules like that of methane or water. From this equation it was also possible to explain quantitatively a variety of features of the light emission spectra of hydrogen. However, Schrödinger's equation has its limitation since it is derived from a non-relativistic equation and thus is itself not manifestly covariant. Also, it does not account for the electrons spin what has to be introduced by hand to explain some fine structure of atomic light-emission spectra.

A relativistic equation of motion for the wave function was obtained by W. Gordon [Gor26] and O. Klein [Kle27]. Starting point is the Hamiltonian

of a relativistic, free moving particle of mass m given by:

$$H = \sqrt{p^2c^2 + m^2c^4}, \tag{1.8}$$

which yields the *Klein-Gordon equation* by means of the correspondence principle:

$$-\hbar^2 \frac{\partial^2 \psi(q,t)}{\partial\, t^2} = -\hbar^2 c^2 \nabla^2 \psi(q,t) + m^2c^4 \psi(q,t) \tag{1.9}$$

This equation is clearly covariant but it allows for a free particle to have negative energies. This comes from the fact that in the Klein-Gordon equation a derivative of second order with respect to time appears and this in turn originates from squaring (1.8) to obtain (1.9), introducing an additional square root with negative sign for the energy. A work around to this problem was tried by P. Dirac who was looking for a covariant equation containing only a first order derivative with respect to time [Dir28]. The resulting *Dirac equation* for a relativistic spin 1/2 particle moving under the action of an electromagnetic interaction represented by the four-potential A^μ reads:

$$\left(i\hbar\gamma^\mu \frac{\partial}{\partial\, x^\mu} - \frac{e\gamma^\mu A_\mu}{c} - mc \right) \Psi(x) = 0 \quad \text{or} \tag{1.10}$$

$$\left(i\hbar \not{\nabla} - \frac{e \not{A}}{c} - mc \right) \Psi(x) = 0 \tag{1.11}$$

In the last of the two equations the Feynman-dagger was introduced which is defined through $\not{a} = \gamma^\mu g_{\mu\nu} a^\nu$ with a^ν an arbitrary four-vector. The γ^μ's are the 4×4 Dirac-matrices so that Ψ(x) cannot be an ordinary wave function like in the solutions of the Schrödinger- or Klein-Gordon equations. Instead, Ψ(x) is a four component vector, called a *spinor*.

The first two components describe a particle with positive energy in two different spin states. The first component refers to a particle state with "spin up" and the second component to a state with "spin down". The third and fourth components however refers to the two different spin states of a particle with negative energy even in the case where $A^\mu = 0$ where the particle moves freely. So, also Dirac's equation cannot circumvent the appearance of negative energy states for free particles. However, Dirac turned this apparent disadvantage into a success by redefining the vacuum as having all the negative energy states filled, forming the so called "Dirac sea", and then predicting anti-particles. After Dirac, an anti-particle appears when a particle with negative energy is exited into a state with positive energy and so leaving a "hole" in the Fermi sea. This hole is then interpreted as the anti-particle. Shortly after this prediction the anti-particle of the electron, the

positron, was found. Beside the prediction of anti-matter the Dirac equation gives also the correct magnetic momentum of the electron and explains quite well the fine structure of the hydrogen spectrum.

Than in 1947 W. Lamb and R. Retherford measured very precisely the fine structure of the hydrogen spectrum and confirmed an early assumption about a shift of the $2S_{1/2}$ level upwards compared to the $2P_{1/2}$ level [Lam51, Lam57]. This so called *Lamb shift* could not be explained by simply solving the Dirac equation. More sophisticated methods had to be applied here. This shift originates from the coupling of the electron to the quantum fluctuations of the electromagnetic field of the nucleus through which it moves. It is again the quantized character of the electromagnetic field that means the photon that must be taken into account here. But from (1.7) and (1.10) it is clear, that in the quantum mechanics outlined so far in this section, the electromagnetic field appears only through its classical potential A^μ. Again, the photon led to a new development in physics. Indeed, the proper treatment of the Lamb shift inspired enormously the development of quantum electrodynamics (QED) and quantum field theory in general.

1.3 The Photon in Quantum Field Theory

In quantum mechanics sketched so far in the last section, a particle is described by a wave function which in turn is the solution of an appropriate equation of motion. This kind of description is commonly referred to as *first quantization*. It was also outlined in the previous sections how the electromagnetic field had to be given a particle interpretation to explain a variety of experimental observations. So, associated with the electromagnetic field are particles, the photons. But one can also take the opposite point of view and say that associated with the photons is a field, the electromagnetic field. Quantum field theory now generalizes this point of view. Every particle is associated with a corresponding field which in turn will be appropriately quantized. The particles now appear as the quanta of their associated fields and interactions between particles are now described by interactions of the corresponding fields. This procedure is referred to as *second quantization*.

Starting point is the Lagrange formalism of classical mechanics. A system of N point particles with generalized coordinates q_i and corresponding generalized velocities $\dot{q}_i$ is described by a Lagrangian $L(q_1, ..., q_N, \dot{q}_1, ..., \dot{q}_N, t)$. From Hamilton's principle, that means from a variation of the action

$$S = \int L(q_1, ..., q_N, \dot{q}_1, ..., \dot{q}_N, t)\, dt \tag{1.12}$$

with respect to the q_i's (with $i \in \{1, 2, ..., N\}$ the Euler-Lagrange equations

$$\frac{d}{dt}\frac{\partial L}{\partial \dot{q}_i} - \frac{\partial L}{\partial q_i} = 0 \tag{1.13}$$

are obtained which yield directly the equations of motion for the q_i's. A field on the other hand is described by a Lagrange density (also called Lagrangian for short) $\mathcal{L}(\phi(x^\mu), \partial_\mu \phi(x^\mu), t)$ which is connected to the Lagrange function by $L = \int \mathcal{L}\, d^3x$. The field amplitudes ϕ here play the role of the coordinates, while the x^μ take over the part of the index i. So, because the x^μ have an infinite range, the field is considered to be an infinite dimensional system. The corresponding action now reads

$$S = \int \mathcal{L}(\phi(x^\mu), \partial_\mu \phi(x^\mu), t)\, d^4x \tag{1.14}$$

and Hamilton's principle yields the Euler-Lagrange equation for the field:

$$\frac{\partial}{\partial x^\mu}\frac{\partial \mathcal{L}}{\partial(\partial\phi/\partial x^\mu)} - \frac{\partial \mathcal{L}}{\partial \phi} = 0, \tag{1.15}$$

from which the equation of motion for the field directly follows. The generalization to a system of N fields is straight forward. In this case, the Lagrangian is simply a function of the N field amplitudes and possibly their corresponding derivatives resulting in N Euler-Lagrange equations from which the equations of motion for each field follows. Once the fields are obtained, they have to be quantized. There are two ways to do this. The first method is called *canonical quantization*. Here the field is turned into an operator by expanding the field in a complete set of wave functions of the corresponding first quantized theory and then require that the field and its canonical momentum defined by $\pi = \partial\mathcal{L}/\partial\dot{\phi}$ obey certain commutation or anti-commutation rules, respectively. The operator obtained in this way acts on the quantum states of the field, that is on its associated particle states. These states are making up a certain Hilbert space, called *Fock space*. Through the action of the operator, quantum states are annihilated while its adjoint ($\phi^\dagger$) creates field quanta, assuming that there exists a certain ground state of the field, called the vacuum $|0\rangle$. It should be noted here, that though the vacuum plays a crucial role in quantum field theory, up to this day there is no experimental proof for its existence! The physical relevant transition amplitudes in an interaction between fields are then obtained by means of vacuum expection values of time ordered products of certain field operators, yielding the so called Propagators or Green's functions, respectively. Quite different from this approach of field quantization is the second one called *path integral quantization* [Dir33, Fey48]. This is in fact the most contemporary approach nowadays because of its many advantages:

- It provides the simplest, most direct way to obtain Feynman rules for any field theory.
- It provides a method for obtaining exact, numerical solutions of strongly interacting field theories (where the perturbation expansion does not work). These methods are referred to as *lattice gauge calculations.*
- It provides a connection between field theory and statistical mechanics.
- It provides a general theoretical framework of a systematic study of advanced topics in field theory like renormalization and the appearance of anomalies.

But the biggest advantage lies in the fact that the fields are treated as c-numbers[5] obeying certain algebras instead of being turned into operators. The quantization is here performed by defining a generating functional Z[J] of some arbitrary source function J that for a scalar field reads:

$$Z[J] = \frac{\int \mathcal{D}\phi \, \exp\left(i \int \mathcal{L} + J\phi \, d^4x\right)}{\int \mathcal{D}\phi \, \exp\left(i \int \mathcal{L} \, d^4x\right)} \tag{1.16}$$

$\mathcal{D}\phi$ here denotes the integration over *all* infinite many functions ϕ turning the integrals into *functional integrals.* Though this measure is divergent it is believed, however, that the functional integrals are convergent. The Green's functions are then obtained from certain functional derivatives of Z[J] with respect to J at J = 0.

Let's turn now to QED. The Lagrangian for electrons and their anti-particles the positrons interacting through their electromagnetic field is given by[6] [Bjo65]:

$$\mathcal{L}(x) = \bar{\Psi}(x)\left(i \not{\nabla} - e_0 \not{A}(x) - m_0\right)\Psi(x) - \frac{1}{4} F_{\mu\nu}(x) F^{\mu\nu}(x), \tag{1.17}$$

where $\bar{\Psi}(x) = \Psi^\dagger \gamma^0$. If there is in addition an external potential present, this is easily included by replacing $\not{A}(x)$ by $\not{A}(x) + \not{A}^{ext}(x)$. In the operator formalism the spinor field Ψ destroys (creates) electron (positron) states while its adjoint $\bar{\Psi}$ creates (destroys) electrons (positrons) from the vacuum. The photon as the quantum of the electromagnetic field emerges here by the quantization of the four-potential A^μ. From this quantization process one gets the following properties of the photon [Gro93]:

- The photon is a pointlike object.

[5] c-numbers are just ordinary numbers opposed to q-numbers meaning operators.

[6] From now on units are used in which $\hbar = c = 1$.

- As emerging from the quantization of a vector field $\mathbf{A}$ it should also have vector properties. In fact, from investigations of the field under rotations one finds that the photon has spin one.

- The photon is massless and transversely polarized. This follows from defining A^0 by the Coulomb potential what in turn requires the Coulomb gauge condition $\nabla \cdot \mathbf{A} = 0$ to hold by current conservation. Hence, only two components of $\mathbf{A}$ can be chosen freely, while the third component is then fixed by $\nabla \cdot \mathbf{A} = 0$. If one attributes the photon with a mass μ the Lagrangian has to be modified by adding a term $\frac{1}{2}\mu^2 A_\nu A^\nu$. By current conservation the gauge is now fixed by the Lorentz condition $\partial_\nu A^\nu = 0$ which now allows three independent polarization states, the transverse states and in addition a longitudinal state. So virtual photons for which $\mu \neq 0$ can have a longitudinal polarization.

To reveal more properties of the photon and its influence on interactions between particles let's consider QED with only one spinor field, the electron, interacting with the electromagnetic field, up to second order in a perturbative treatment. The transition amplitude for a system in an initial state (i) to end up by an interaction in a final state (f) is given by the corresponding S-matrix element:

$$S_{fi} = \langle f | \, U_I(-\infty, +\infty) \, | i \rangle \,, \tag{1.18}$$

where $U_I(-\infty, +\infty)$ is the time translation operator transforming an initial state $|i\rangle$ that is assumed to be free at $t = -\infty$ through the interaction into a state that will be free at $t = +\infty$. So U_I contains the whole physics of the interaction. It is defined by:

$$U_I = T \exp\left[-i \int d^4x \, \mathcal{H}_I\right]. \tag{1.19}$$

Here, $\mathcal{H}_I$ denotes the interaction Hamiltonian which is the part of the full Hamiltonian involving products of Ψ and A. The Hamiltonian itself is given by a Legendre transformation of the Lagrangian: $\mathcal{H} = \pi\phi - \mathcal{L}$. The exponential function is only meant as a shorthand for its series representation and T is the time ordering operator meaning that the fields appearing in $\mathcal{H}_I$ have to be ordered in such a way the one at the later time stands always to the left of the other. Up to second order this reads:

$$U_I = \mathbf{1} - i \int d^4x \, \mathcal{H}_I(x) - \frac{1}{2} \int\int d^4x_1 \, d^4x_2 \, T\left[\mathcal{H}_I(x_1)\mathcal{H}_I(x_2)\right] \tag{1.20}$$

Using (1.17), combining the first and second order one gets (formally):

$$U_I \;\; = \;\; \mathbf{1} - \frac{e^2}{2} \int d^4x_1 \, d^4x_2 \, \{(\text{disconnected term} = 0)$$

$$
\begin{aligned}
&+ \quad \text{(annihilation and exchange terms)} \\
&+ \quad \text{(Compton scattering terms)} \\
&+ \quad \text{(electron self-energy term)} \\
&+ \quad \text{(vacuum polarization term)} \\
&+ \quad \text{(vacuum bubble term)}\} \, . \qquad (1.21)
\end{aligned}
$$

In the last equation the time ordered product was expanded in a sum of "normal ordered" products by means of *Wick's theorem* [Dys49, Wic50]. A normal ordered product of field operators is defined by writing all annihilation operators to the right of all creation operators and is denoted by enclosing the product by colons. The individual terms, their mathematical representation and the corresponding Feynman graphs are shown in Tab. 1.1.

The "contracted" terms denoted by an overline are the usual two point Green's functions defined by $\overline{\phi(x)\phi^\dagger(y)} = \langle 0| \, T\left(\phi(x)\phi^\dagger(y)\right) |0\rangle$. From the diagrams in the table one sees clearly that opposed to ordinary quantum mechanics, the photon plays a crucial role in QED. Here, it appears as the gauge boson mediating the electromagnetic interaction between charged particles.

In Tab. 1.1 another interesting feature of the photon is shown. The graph for the annihilation interaction shows how an electron-positron pair first annihilates to a (virtual) photon which after some time allowed by Heisenbergs uncertainty principle decays again into an electron-positron pair. So it seems so, as if there was an intimate connection between these two fermions and the boson. In particular, the decay process of the photon could be interpreted in the sense, that the photon is being composed of electrons and positrons and that through the decay this "electromagnetic structure" of the photon suddenly shows up.

Indeed, such an interaction was the first instance where the photon reveals a kind of structure [Bau78]. In the early 1930's Tarrant [Tar32] and Chao [Cha30] first demonstrated an anomalously high absorption of X-rays in matter with energy above about 1 MeV. The experiment of Anderson and Neddermeyer [And33] followed which demonstrated that this was attributable to the conversion of the X-rays into electron-positron pairs. Subsequently Oppenheimer and Plesset [Opp33] showed that these results were consistent with a process in which the X-ray photon decays into e^+e^- by coupling to the electromagnetic field of the atoms in the absorber (see Fig. 1.1). This coupling to an external electromagnetic field is crucial to conserve momentum because the X-ray photon is real in this case. Furnished with a first formulation of QED, Bethe and Heitler [Bet34] were able to perform the first precision calculation of the cross section for this process.

Another example where the photon shows up a structure are "vacuum

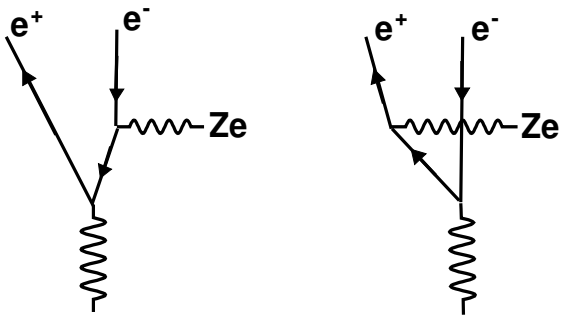

Figure 1.1: Conversion of a photon into a e^+e^- pair in a nuclear electromagnetic field.

fluctuations" (see Tab. 1.1). Here the photon emitted by the electron fluctuates into a e^+e^- pair which after some time allowed by Heisenbergs uncertainty principle annihilates again into a photon. This "fluctuation driven" structure of the photon is responsible for many phenomena concerning electromagnetic interactions. The actual energy dependence of the electromagnetic coupling $\alpha_{em} = e^2/4\pi$ is caused by these vacuum fluctuations (see Fig. 1.2). An electron traversing space time continously emits photons an

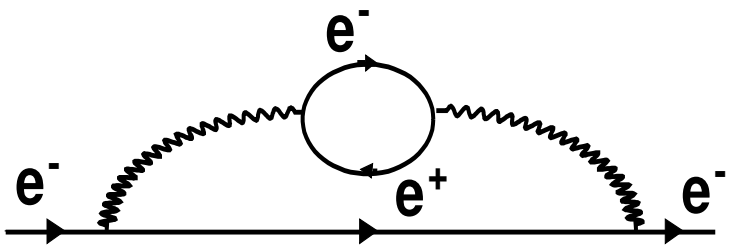

Figure 1.2: Shielding of the electrons charge by vacuum fluctuations of the photon.

reabsorb them again. In this way it interacts with its own electromagnetic field ("self-energy-term", see Tab. 1.1). If this photon fluctuates into a e^+e^- pair before it is reabsorbed by the electron, a test charge located in some distance to the electron does not see its real (the "naked") charge but instead the charge of the electron *plus* the charge of the "fluctuation cloud"

developed from the photon that is the e^+e^- pair. So in this way, the charge of the electron is shielded by the vacuum fluctuations of the photon. The interaction of the test charge with the electron is of course again mediated via photons. The shielding can then be understood in the way that the charge of the electron is smeared out by the presence of the fluctuating particles and the mediating photon can interact with the electron as well as with the fluctuation particles. But the higher the momentum transfer (and so the momentum carried by the photon) in such an interaction is, the more deeply the photon can penetrate through the fluctuation cloud, and so it becomes more likely that the photon will hit the electron itself. Thus, with increasing momentum transfer the more of the electrons naked charge contribute to the interaction and the stronger the interaction will be, meaning an increase of the coupling constant α_{em}.

Another example where the vacuum fluctuations contribute is the Lamb shift (see above). Its contribution is about -27 MHz (note the minus sign!) to the overall shift of about 1058 MHz. Since the Lamb shift can be measured with an accuracy of about 0.01 MHz, this effect makes a small but important contribution to the total, and the overall agreement between theory and experiment proofs the impact of the vacuum fluctuations.

So, to summarize, QED shows that electromagnetic interactions are mediated by photons which are in general massless, pointlike, transversely polarized quantum states with spin 1. But QED also shows that these photons can exhibit a fluctuation driven electromagnetic structure and how this structure contributes to an actual interaction. So it seems reasonable to write the photons physical state vector as:

$$|\gamma\rangle_{phys} = |\gamma\rangle_{bare} + a\left|e^+e^-\right\rangle. \tag{1.22}$$

Here $|\gamma\rangle_{bare}$ represents the pointlike part of the photon and the factor a is the probability of the photon to split up into an e^+e^- pair.

However, as the accessible energies of the experiments became higher and higher it became clear that this picture of a photon is still too simple.

1.4 Hadronic Photon Structure

When the first experiments on photoproduction (meaning processes where the exchanged photon is quasi real) of pions and electron scattering from nucleons were carried out, it became clear that the view of a photon as being attributed with an electromagnetic structure appears as a rather incomplete picture. In reality the photon should have an internal structure very similar to that of hadrons except that it occurs with a relative probability only of

order $\alpha_{em} = \frac{1}{137}$. At lower energies this hadronic structure is not visible since the photon has not enough energy to materialize into those states during an interaction. In the following subsections it is outlined how the hadronic structure of the photon appeared experimentally and how it was explained by theory. For a more detailed treatment see [Bau78].

1.4.1 The VMD approach

A first hint of a hadronic photon structure came from electron scattering experiments by Hofstadter et al. [Hof56] which had revealed that the proton has an extended charge distribution. This was accounted for by a positive pion cloud in the proton. However, electron–neutron scattering experiments [Hug53, Mel56] as well as electron–deuteron scattering experiments [McI56] had revealed that the neutron has no such charge structure, whereas by charge symmetry it should have a negative pion cloud. In 1957, Nambu [Nam57] suggested a way out of this puzzle. If the electron would be able to exchange vector mesons rather than a photon with the nucleon the effect of the negative pion cloud in the neutron would be canceled while at the same time the charge of the positive pion cloud in the proton would be enhanced. Another puzzle was noted by Drell [Dre58]. He pointed out that in the dispersion theory[7] approach to the electromagnetic form factors there is a difficulty of simultaneously accounting for the magnitude and the radius of the magnetic moment of the nucleon. Subsequently, Frazer and Fulco [Fra59] were able to explain the observed form factors in terms of a $\pi\pi$ resonance in the $I = 1$, $J = 1$ state (thus a vector meson) with a total energy of approximately 550 MeV.

During the same period Sakurai [Sak60] developed a theoretical framework taking these new observations into account by taking advantage of a general gauge theory developed by Yang and Mills [Yan54]. Because the Yang-Mills theory forms the bases not only for the unified electroweak theory of Weinberg, Glashow and Salam but also plays an important role in quantum chromodynamics, to give here some more details it is worth to give it a closer look. Quantum electrodynamics as described above forms a U(1) gauge theory. That means that the physics and thus the form of the Lagrangian is invariant under a local gauge transformation. This gauge

[7] Dispersion theory was used to determine cross sections etc. before the advent of QCD by investigating analyticity properties of the scattering amplitude using Cauchy's integral formula. Nowadays it is still used to model phenomena which cannot be treated yet by perturbative QCD ("Regge-phenomenology").

transformation is performed by the replacements:

$$A_\mu \longrightarrow A_\mu + \frac{1}{e}\partial_\mu \Lambda \tag{1.23}$$

$$\phi \longrightarrow e^{-i\Lambda}\phi. \tag{1.24}$$

Here Λ is considered to be a function of spacetime. The last replacement means a phase transformation of the wave function ϕ of a charged particle coupled to the electromagnetic field by simply multiplying it by a complex number, making the whole gauge transformation to form a U(1) group. Yang and Mills now generalized these results to the case where the Lagrangian has a higher symmetry than U(1) to formulate a theoretical framework for the hypothesis that isospin symmetry is a local symmetry. The simplest generalization is that to the SU(2) group. The Lagrangian Yang and Mills obtained reads:

$$\mathcal{L}_{YM} = \frac{1}{2}\left(D_\mu \phi\right) \cdot \left(D^\mu \phi\right) - \frac{m^2}{2}\phi \cdot \phi - \frac{1}{4}\mathbf{W}_{\mu\nu} \cdot \mathbf{W}^{\mu\nu}. \tag{1.25}$$

In this Lagrangian the field ϕ is a three component vector. The field $\mathbf{W}_{\mu\nu}$ is defined by:

$$\mathbf{W}_{\mu\nu} = \partial_\mu \mathbf{W}_\nu - \partial_\nu \mathbf{W}_\mu + g\mathbf{W}_\mu \times \mathbf{W}_\nu, \tag{1.26}$$

where g is some coupling constant. It takes over the role of $F_{\mu\nu}$ of the electromagnetic theory and $\mathbf{W}_\mu$ correspondingly the role of A_μ. But contrary to the case of QED these gauge fields here appear as vectors. This is so because the SU(2) group is made up by rotations in some three-dimensional space while the U(1) group is the group of rotations in the complex plane. So the gauge transformation are in this model associated with rotations in a three-dimensional space (e.g. "isospin space"). The "covariant derivative" D_μ is defined by:

$$D_\mu \phi = \partial_\mu \phi + g\mathbf{W}_\mu \times \phi. \tag{1.27}$$

A local gauge transformation in this model is performed by the replacements:

$$\phi \longrightarrow \phi - \mathbf{\Lambda} \times \phi \tag{1.28}$$

$$\mathbf{W}_\mu \longrightarrow \mathbf{W}_\mu - \mathbf{\Lambda} \times \mathbf{W}_\mu + \frac{1}{g}\partial_\mu \mathbf{\Lambda}. \tag{1.29}$$

The three-vector $\mathbf{\Lambda}$ is here again a function of spacetime and is the angle by which the vector ϕ is rotated in the corresponding three-dimensional space. It should be mentioned that because of the appearance of the cross-product in the Yang-Mills-Lagrangian as well as in the definition of the "field-strength" $\mathbf{W}_{\mu\nu}$ and the covariant derivative D_μ this theory forms a *Non-Abelian* gauge theory.

Now, after *Noether's theorem*, every symmetry of the Lagrangian is connected to a conserved quantity. In this way the gauge symmetry in QED is connected to charge conservation. In the case of the Yang-Mills theory the conserved quantity should be the vector quantity "isospin". This idea now was taken up by Sakurai who believed that the ρ meson was the isospin gauge field like the photon is the gauge field in QED. He further assumed that the ω or ϕ mesons or some combination of both was the gauge field for baryon number conservation, and that the K(890) meson was the gauge field coupled to strangeness. This coupling should be "universally" meaning that there is just one coupling constant for each type of vector mesons. This theory was further discussed and extended by others (see e.g. [Bau78]) and these ideas confluented into a model called **V**ector-**M**eson-**D**ominance (VMD)[8] with the additional assumption (for simplicity and definiteness) that vector-meson poles at $Q^2 = -m_V^2$ [9] dominate the Q^2 dependence of the matrix element under consideration, hence the name of the model. In the view of this model, in an electromagnetic interaction the mediating photon couples to a vector meson (it must be a vector meson by angular momentum and quantum number conservation because the photon itself is a vector particle) and furthermore it can transform into such a vector meson which then enters the interaction in place of the photon, see Fig. 1.3. However, one nowadays

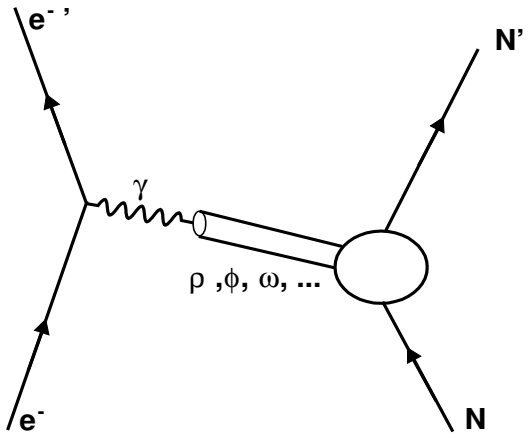

Figure 1.3: Possible electromagnetic interaction of an electron with a nucleon in the view of the VMD-model. The photon transforms into a vector meson which than undergoes a strong interaction with the nucleon.

[8] Sometimes also called Vector-Dominance-Model (VDM).

[9] Q^2 is the negative of the exchanged photons mass squared.

believes that there is no gauge theory for isospin. The ρ meson cannot be the isospin gauge field because it is massive and that destroys gauge invariance. But it should be mentioned here, that Weinberg, Glashow and Salam were able to overcome this problem in their electroweak theory which is also founded on the Yang-Mills theory. They achieved this by introducing the concept of "spontaneous symmetry breakdown", a process which is believed to explain the fact that the gauge bosons of the electroweak theory (W,Z^0) are massive. However, the VMD-model received a fair amount of experimental support.

In this model, the probability amplitude A for a particular vector meson V emerging from the photon is proportional to a factor $\frac{m_V^2}{m_V^2+Q^2}$. This factor is obtained from a first order perturbative calculation where the photon is considered to split electromagnetically into vector mesons. So for the cross section as being proportional to A^2 one gets:

$$\sigma \sim A^2 \propto \left(\frac{m_V^2}{m_V^2+Q^2}\right)^2 = \frac{1}{Q^4}\left(\frac{m_V^2}{1+\frac{m_V^2}{Q^2}}\right)^2 . \tag{1.30}$$

If $Q^2 \gg m_V^2$, then expanding the term $1/(1+\frac{m_V^2}{Q^2})^2$ yields:

$$\sigma \sim \frac{m_V^4}{Q^4} - 2\frac{m_V^6}{Q^6} + 3\frac{m_V^8}{Q^8} - ... \tag{1.31}$$

So for high virtualities of the photon the leading Q^2 dependence of the cross section is $\sigma \sim \frac{1}{Q^4}$. This indicates that the VMD contribution to the cross section decreases very fast with increasing Q^2.

The first time VMD failed to describe the experimental data happened with the SLAC-MIT measurements of inelastic electron scattering [Blo69, Bre69]. It was found that the inelastic electron scattering cross section was much higher than predicted by VMD. At the same time colliding e^+e^- experiments revealed that the photon's hadronic structure must be considerably richer than a simple superposition of ρ, ω and ϕ. Many attempts have been made to generalize VMD and to account for the observed discrepancies. However, almost at the same time a field theoretical approach to explain strong interactions was developed called *quantum chromodynamics* (QCD) which nowadays is considered to be the fundamental theory of strong interactions. So QCD should be able to account fully for the photon's hadronic structure (actually it is only used for the perturbatively treatable part of the photon structure, see below).

1.4.2 The QCD approach

In 1967 Bjorken [Bjo67] predicted for high electron-nucleon scattering involving a high virtual, high energetic photon a scaling behavior of the cross section meaning that there is no scale of mass or length present and the variation of the cross section is predictable solely from the variation of the dimensionless ratio $x = \frac{Q^2}{2P_\mu q^\mu}$, where P^μ is the nucleons four-momentum and q^μ the four-momentum of the exchanged photon. Feynman [Fey69] found an explanation for this behavior by assuming that the nucleon is made up of pointlike, non-interacting particles which he called *partons*. A similar consideration was made by Gell-Mann and Zweig [Gel64, Zwe64] to explain the classification of observed hadrons.

They called the particles forming hadrons *quarks*. It was found that the quarks and the partons should essentially be the same, so it is nowadays usually referred to as the quark/parton model (QPM). But the experiments cited in the last subsection not only brought up the breakdown of VMD but showed also that when the virtuality Q^2 of the exchanged photon becomes very high than the cross sections starts again to depend on Q^2, a phenomenon referred to as "scaling violation"[10].

A photon with increasing energy and virtuality probes increasingly smaller distances in the nucleon. So scaling violation could be explained when beside quarks the nucleon exhibits an additional substructure that appears on a very small length scale. QCD now gives an explanation of this additional substructure by assuming that the quarks actually interact with each other and that they do this in a similar way as electric charged particles do, by the exchange of some gauge bosons mediating the strong interaction. The additional structure thus arises from quantum fluctuations of this gauge boson like in the electromagnetic case.

There are six types ("flavors") of quarks and their corresponding antiquarks: up(u), down(d), strange(s), charm(c), bottom(b) and top(t). They are the quanta of their associated fermion-spinor fields, having spin 1/2 and fractional electric charge: (u,c,t) carry $+\frac{2}{3}|e|$ and (d,s,b) carry $-\frac{1}{3}|e|$, where $|e|$ is the value of the electron's charge. But these particles interact predominately via the strong interaction which is about 100 times larger than the electromagnetic interaction. So quarks carry also a "strong charge" called color of which there are three types usually denoted by "red" (r), "blue" (b) and "green" (g). The strong interaction is mediated by a bosonic gauge field which quanta are referred to as *gluons*. The crucial point here is that gluons, contrary to their electromagnetic counterpart the photons, carry color that

[10] Actually, scaling violation also depends on the value of x. For $0.1 < x < 0.2$ there is *no* scaling violation observable for all values of Q^2.

is they are charged. Therefore gluons can interact with each other. This makes calculations in QCD much more complicated compared to QED and special calculational tools like "lattice field theory", etc. have to be invoked. Actually a gluon carries color and anti-color giving rise to a total of nine possible gluon states; a color SU(3) octet: (r$\bar{g}$,r$\bar{b}$,g$\bar{r}$, g$\bar{b}$,b$\bar{r}$,b$\bar{g}$,$\frac{1}{\sqrt{2}}(r\bar{r}-g\bar{g})$, $\frac{1}{\sqrt{6}}(r\bar{r}+g\bar{g}-2b\bar{b})$) and an SU(3) singlet: $\frac{1}{\sqrt{3}}(r\bar{r}+g\bar{g}+b\bar{b})$. The singlet gluon couples equally to all quarks, and is independent of the octet. It is usually ignored because it would lead to unphysical phenomena like an infinite range of the nuclear forces.

One consequence of the fact that the gluons carry color is "anti-shielding". Analogous to the electromagnetic case vacuum fluctuations of the gluon shield the color charge of a quark (see Fig. 1.2 but with electron, photon and e^+e^- pair replaced by quark, gluon and $q\bar{q}$ pair). But here, the situation is somewhat different. When the energy and momentum of a gluon emitted by some test quark increases and thus also its "resolving power" increases, the gluon is more likely to see the "bare" color charge of the quark. But now the quark can radiate its color away be emitting itself a gluon. So the charge distribution spreads out and the test gluon sees a diffuse color cloud leading to a decrease of the interaction strength and so to a decrease of the strong coupling α_s. Because this happens at high momentum transfer, by the uncertainty principle the length scale is small. But when the length scale becomes large (low momentum transfer), the interaction strength between the quarks becomes quite strong. This is the reason for "confinement"[11], meaning that quarks are always bound together and never appear as free particles. So if one tries to pull two quarks apart from each other the energy of this system increases by the interaction of the exchanged gluons so that at some point it becomes more favorable for the system to decay into two new quark-anti-quark pairs. Because of this strong interaction, their matrix elements are usually hardly calculable. However, at high momentum transfers α_s is small so that the quarks can be treated as quasi-free ("asymptotic freedom") and perturbative calculations should become possible.

QCD is a field theory and as such all relevant physical entities are contained in its Lagrangian which is investigated in some detail now, following [Ste95]. The QCD-Lagrangian can be decomposed into three parts:

$$\mathcal{L}_{eff}^{QCD}\left[\psi_f(x),\bar{\psi}_f,A(x),c(x),\bar{c}(x);g,m_f\right]=\mathcal{L}_{invar}+\mathcal{L}_{gauge}+\mathcal{L}_{ghost}. \quad (1.32)$$

It is a function of the quark fields (ψ_f), the gluon field (A(x)), the ghost field (c(x), see below) and the parameters g and m_f. The distinct quark flavors

[11] also called "infrared-slavery" because it happens at low momentum transfers and so large wavelengths

are labeled by f. $\mathcal{L}_{invar}$ makes up the main part of $\mathcal{L}_{eff}$ and is invariant under a local SU(N_c) gauge transformation. N_c is the number of available charges (colors) and so for QCD $N_c = 3$. The functional form of $\mathcal{L}_{invar}$ is derived from the Yang-Mills theory (see eq. 1.25) and is given by:

$$\mathcal{L}_{invar} = \sum_f \bar{\psi}_f \left(i \not{D}[A] - m_f \right) \psi_f - \frac{1}{4} F^2[A]. \tag{1.33}$$

Here,

$$D_{\mu,ij} = \delta_{ij}\partial_\mu + igA_{\mu a} \left(T_a^{(F)} \right)_{ij} \tag{1.34}$$

and

$$F_{\mu\nu,a}[A] = \partial_\mu A_{\nu a} - \partial_\nu A_{\mu a} - gC_{abc}A_{\mu b}A_{\nu c}. \tag{1.35}$$

$F_{\mu\nu,a}$ is the nonabelian field strength tensor. It is defined in terms of the gluon vector field A_b^μ with $N_c^2 - 1$ components b. g is the strong QCD coupling related to α_s by $\alpha_s = \frac{g^2}{4\pi}$. The C_{abc}, $a, b, c = 1...N_c^2 - 1$ are real numbers and called the structure constants of SU(N_c) which define its Lie algebra. This is defined by the commutation relations of the $N_c \times N_c$ matrices $\left(T_a^{(F)} \right)_{ij}$ of which there are $N_c^2 - 1$:

$$\left[T_a^{(F)}, T_a^{(F)} \right] = iC_{abc}T_c^{(F)}. \tag{1.36}$$

If the $T_a^{(F)}$ are taken to be hermitian, QCD looks much like QED. D_{ij}^μ is the covariant derivative in SU(N_c). It acts on the spinor quark fields, with color indices $i, j = 1...N_c$. In QCD the distinct flavors are only distinguished by their masses m_f. A local gauge transformation is performed by the transformation matrix:

$$U_{ji}(x) = \left[\exp \left\{ i \sum_{a=1}^{N_c^2-1} \beta_a(x) T_a^{(F)} \right\} \right]_{ji}, \tag{1.37}$$

with $\beta_a(x)$ a real function. The spinor and gluon fields then transforms as:

$$\psi_{f,\alpha,j}(x) \rightarrow U_{ji}(x)\psi_{f,\alpha,i}(x) \tag{1.38}$$

$$A_\mu(x) \rightarrow U(x)A_\mu(x)U^{-1}(x) + \frac{i}{g} \left[\partial_\mu U(x) \right] U^{-1}(x). \tag{1.39}$$

With this transformation rules, $\mathcal{L}_{invar}$ is gauge invariant. However, this gauge invariance makes $\mathcal{L}_{invar}$ somewhat difficult to quantize. The work around is

to add a gauge-fixing Lagrangian and ghost Lagrangians. The gauge-fixing terms can be chosen almost freely. Two common choices are:

$$\mathcal{L}_{gauge} = -\frac{\lambda}{2}\sum_{a=1}^{N_c^2-1}\left(\partial_\mu A_a^\mu\right)^2 \qquad 1 < \lambda < \infty \tag{1.40}$$

$$\mathcal{L}_{gauge} = -\frac{\lambda}{2}\sum_{a=1}^{N_c^2-1}\left(n \cdot A_a\right)^2 \qquad \lambda \to \infty. \tag{1.41}$$

Here n^μ is a fixed vector. The first one is called "covariant" gauge and in the case $\lambda = 1$ it is the Feynman gauge. The second equation defines the "axial" or "physical" gauges. In this case there is no need for additional ghost fields (see below). Choosing $n^2 = 0$ defines the so called "light-cone" gauge. The physical gauge is also called the "$n \cdot A = 0$" gauge because in the case $\lambda \to \infty$ a nonzero value of this term would yield an infinite action. For the use of the covariant gauge one also has to add a ghost Lagrangian:

$$\mathcal{L}_{ghost} = (\partial_\mu \bar{c}_a)(\delta_{ad}\partial^\mu - gC_{abd}A_b^\mu)c_d. \tag{1.42}$$

$c_a(x)$ and $\bar{c}_a(x)$ are scalar ghost and anti-ghost fields. They ensure that in an SU(N_c) theory the gauge fixing does not destroy the unitarity of the S-matrix that governs the interaction of quarks and gluons.

Now, let's return to the question on how the hadronic structure of the photon is described in the QCD picture. In this picture, a photon once carrying enough energy can split up into a quark-anti-quark pair. These in turn can interact with each other strongly by exchanging gluons. If the transverse momentum of this $q\bar{q}$-pair is low, this will lead to a bound state, actually a vector meson. This is a process which cannot be treated perturbatively in QCD and so other methods must be used to give a satisfactory description. Those processes are usually modeled by the VMD model, described above.

But if on the other hand the transverse momentum of the $q\bar{q}$-pair is large, these particles can emit energetic gluons which in turn convert into $q\bar{q}$-pairs and so a complicated hadronic structure may come up and this kind of process can be treated by perturbative QCD, see Fig. 1.4. So in QCD the state vector of the photon reads:

$$|\gamma\rangle = |\gamma\rangle_{bare} + \sum_{\rho,\omega,\phi}\frac{e}{f_V}|V\rangle + \sqrt{P_{q\overline{q}}}\,|q\overline{q}\rangle \tag{1.43}$$

$|\gamma\rangle_{bare}$ represents the bare structureless, pointlike part of the photon. The next two terms are due to the hadronic structure. The first of these terms represents the part which cannot be treated perturbatively and is usually described by VMD. Here the ratio e/f_V is the transition amplitude for $\gamma \to V$

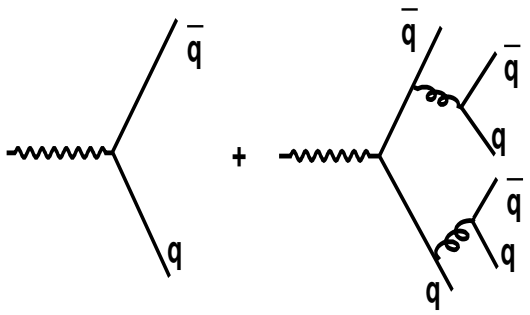

Figure 1.4: Development of the photons hadronic structure in the view of QCD. The left graph is usually referred to as the "point-like" contribution.

and $|V\rangle$ represents a vector meson state. The second part is the perturbatively treatable one. It emerges from the hard process $\gamma \to q\bar{q}$ and $P_{q\bar{q}}$ is the probability for this process to occur. Also this contribution is Q^2 dependent and it decreases with increasing Q^2 like $\sim \ln \frac{\mu^2}{Q^2}$, where μ^2 is some "scale factor" (see below). It should be mentioned that the picture of the hadronic part of the photon as suggested by (1.43) should not be treated too seriously. Actually it is not easy to separate perturbative and non-perturbative parts consistently and in reality there is a smooth transition from one to the other.

Disconnected term (= 0)

$$: \bar{\Psi}(x_1)\gamma^i\Psi(x_1)A^i(x_1)\bar{\Psi}(x_2)\gamma^j\Psi(x_2)A^j(x_2) :$$

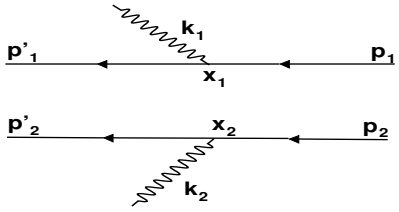

Annihilation and exchange terms

$$\overline{A_\mu(x_1)A_\nu(x_2)} : \bar{\Psi}(x_1)\gamma^\mu\Psi(x_1)\bar{\Psi}(x_2)\gamma^\nu\Psi(x_2) :$$

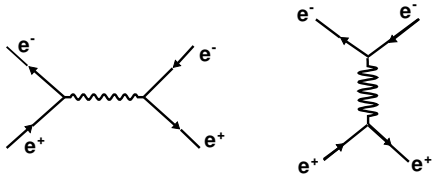

Compton scattering terms

$$2 : \bar{\Psi}(x_1)\gamma^i A^i(x_1)\overline{\Psi(x_1)\bar{\Psi}(x_2)}\gamma^j A^j(x_2)\Psi(x_2) :$$

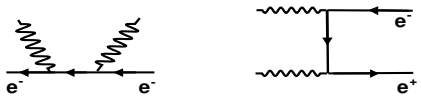

Electron self-energy term

$$2\overline{A_\mu(x_1)A_\nu(x_2)} : \bar{\Psi}(x_1)\gamma^\mu\overline{\Psi(x_1)\bar{\Psi}(x_2)}\gamma^\nu\Psi(x_2) :$$

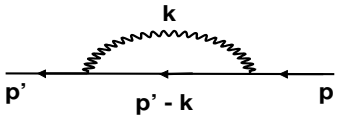

Vacuum polarization term

$$-\gamma^j_{\beta\prime\alpha\prime}\overline{\Psi_{\alpha\prime}(x_1)\bar{\Psi}_\alpha(x_2)}\gamma^i_{\alpha\beta}\overline{\Psi_\beta(x_2)\bar{\Psi}_{\beta\prime}(x_1)} : A^j(x_1)A^i(x_2) :$$

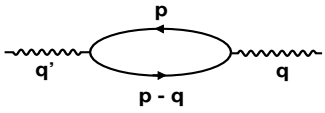

Vacuum bubble term

$$-\gamma^\mu_{\beta\prime\alpha\prime}\overline{\Psi_{\alpha\prime}(x_1)\bar{\Psi}_\alpha(x_2)}\gamma^\nu_{\alpha\beta}\overline{\Psi_\beta(x_2)\bar{\Psi}_{\beta\prime}(x_1)}\ \overline{A_\mu(x_1)A_\nu(x_2)}$$

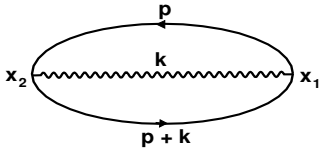

Table 1.1: Terms contributing to the interaction of an electron spinor field with its electromagnetic photon field up to second order in QED.

Chapter 2

Theoretical Calculation of the ep–Scattering Cross Sections in NLO

2.1 Photon Structure in ep–Interactions

In the quantum mechanical picture the interaction between electrons (positrons) and protons take place by the exchange of a gauge boson. At the high energies provided by HERA (for a description of HERA see below) it could be either a photon or a Z^0-boson (so called "neutral current" event) or one of the $W^{\pm}$-bosons (so called "charged current" event) depending on whether the interaction is of an electromagnetic or weak type. This thesis is about photon structure, and so only neutral current events with photon exchange will be discussed here.

In the previous chapter it was outlined how a photon acquires a hadronic structure. Generally one discriminates between two different types of interactions. In a *direct* interaction the photon enters the hard scattering with the partons of the proton "as such" that is as a point-like, structureless object and all the energy it has received from the electron is available for this process. Examples of such interactions (up to "leading order" in the strong coupling constant α_s) are shown in Fig. 2.1. Diagram 2.1 a) shows the "strong" analog to the electromagnetic Compton-effect (see Tab. 1.1). The incident photon is absorbed by a quark of the proton in an electromagnetic interaction. Contrary to QED the quark then remits a gluon in a strong interaction. Diagram 2.1 b) shows an example of a boson–gluon fusion. A gluon of the proton splits into a quark–anti-quark pair via a strong interaction and then the photon interacts electromagnetically with one of these new

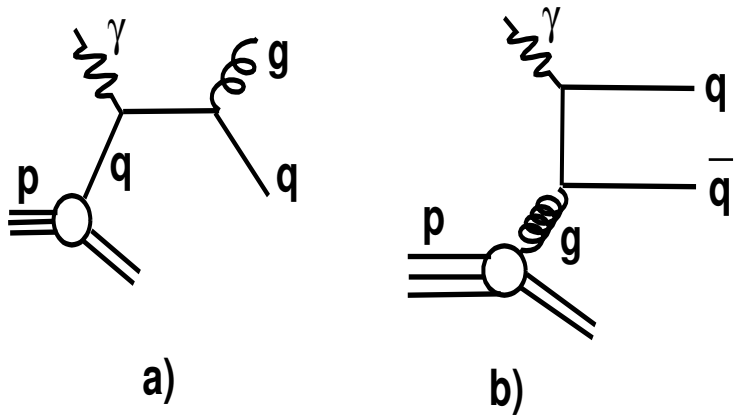

Figure 2.1: Examples of direct interactions (leading order in α_s) in of a photon with a parton of the proton: a) QCD–Compton effect, b) Boson–Gluon fusion.

created pairs.

The other type of interactions are called *resolved* interactions. Here the photon acts as a source of partons. Due to vacuum fluctuations it develops a hadronic structure. If the interaction is soft, the VMD contribution dominates, where the partons emerging from the photon are assumed to form vector mesons. An example of such an interaction was already shown in Fig. 1.3 in the last chapter. If on the other hand the interaction is hard, a quasi free parton of the fluctuation cloud enters the interaction with a parton of the proton. Possible examples of such interactions are shown in Fig. 2.2. Because the energy and momentum of the photon is now distributed over the particles making up its structure, only part of it enters the scattering process.

In this way, a soft resolved interaction is analogous to a hadron-hadron interaction while a hard resolved interaction is analogous to a parton-parton interaction. Measurements of the total photon–proton cross section at different center-of-mass energies $\sqrt{s_{\gamma p}}$ as shown in Fig. 2.3 are confirming this fact at least for soft interactions. In this figure full circles denotes measurements of the H1-collaboration [Aid95], full triangles the measurements of the ZEUS-collaboration [De94a] and open squares the measurements of fixed target experiments [Bal88]. The full line shows a parameterization based on

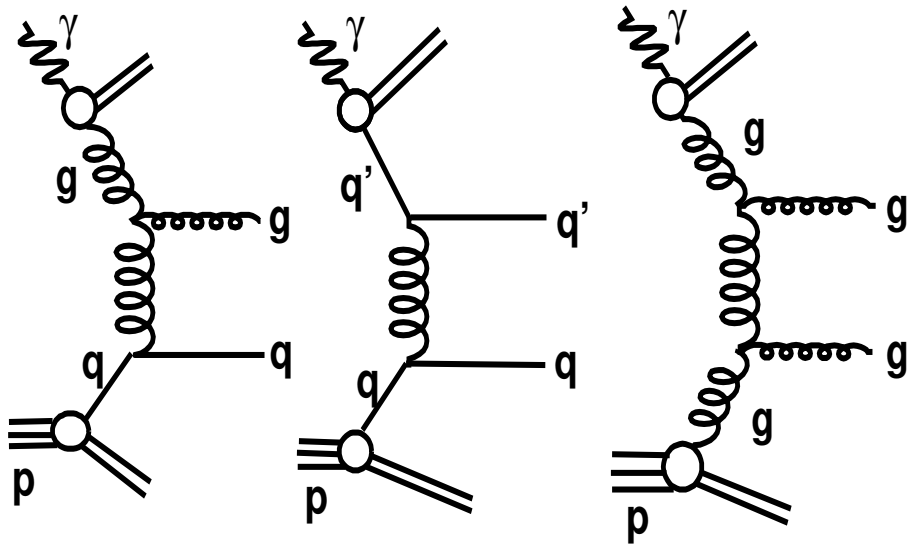

Figure 2.2: Examples of resolved interactions (leading order in α_s) of a photon with a proton. Shown are interactions of a gluon and a quark from the photon with a quark and a gluon from the proton.

fixed target data of hadron-hadron interactions (from [Don92]) using "Regge phenomenology". The comparison of these measurements clearly indicates that the photon-proton total cross section shows the same energy dependence as the hadron-hadron total cross section. So at least for soft collisions, HERA behaves more like a hadron-hadron collider rather than an electron-proton collider.

2.2 Factorization and General expression for the Scattering Cross Section

An electron interacts with a proton via exchange of a photon. Actually many processes are involved in such an interaction. The electron emits a photon in a purely electromagnetic interaction. Then the photon splits electromagnetically into a quark and an anti-quark, these in turn by strong interactions emit gluons which convert again into quark–anti-quark pairs etc. As was explained in the last chapter, this development of a hadronic photon structure can only in part be treated perturbatively since it contains also non-perturbative contributions described by means of the VMD. In a hard interaction a parton from the hadronic photon structure or the photon itself then interacts with a

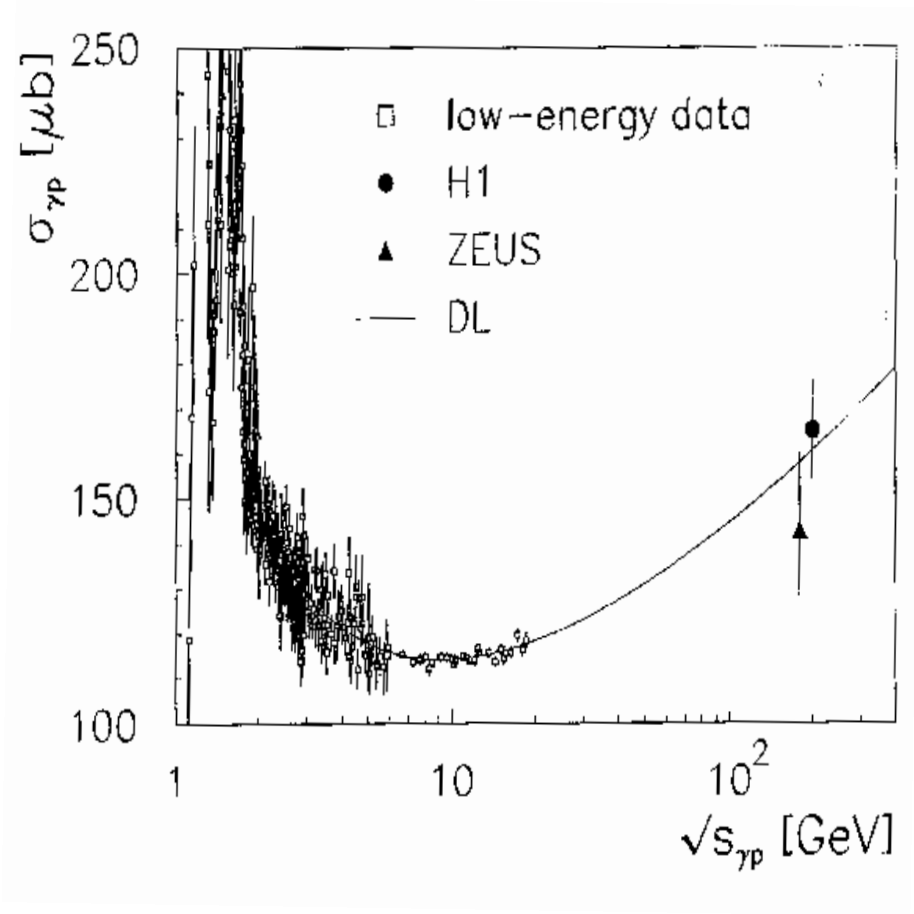

Figure 2.3: Measurements of the total photon-proton cross section at different center-of-mass energies. Full circles denotes results from H1, full triangles results from ZEUS and open squares from fixed target experiments. The full curve shows measurements of the total hadron-hadron cross section.

parton from the proton which can be treated completely perturbatively. The parton of the proton on the other hand may also emerge from a process with non-perturbative contributions. The outgoing partons now cannot exist as free particles due to confinement and so they "fragment" into hadrons which in turn form a collimated spray of particles called "jet". This transition of quarks or gluons to observable jets is also a non-perturbative process. So the cross section for such an interaction can generally not be treated completely by the application of perturbation theory since it contains both, contributions from perturbative and contributions from non-perturbative processes. This is sketched in Fig. 2.4. Since non-perturbative calculations in QCD are hardly feasible, the full cross section for an ep-interaction cannot be fully cal-

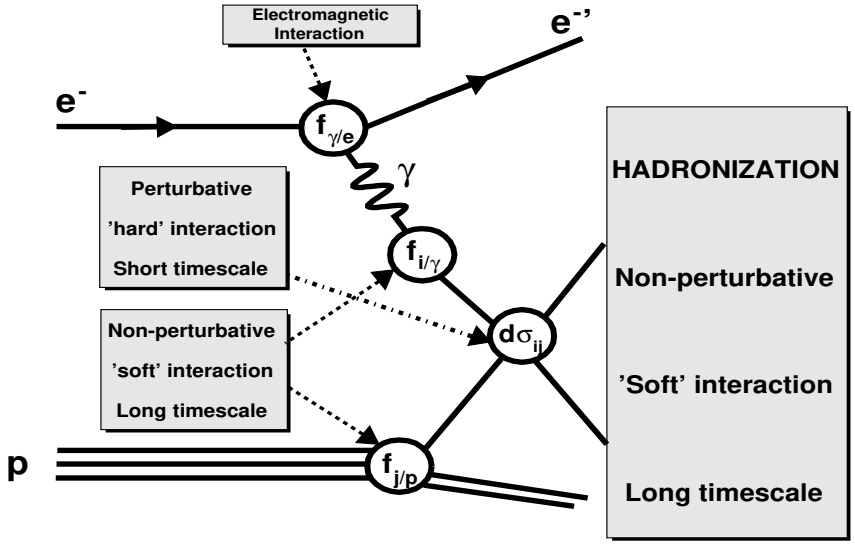

Figure 2.4: Factorization in an electromagnetic ep–interaction. The entire interaction is divided in "soft" and "hard" subinteractions which can be treated separately. The $f_{a/A}$ are "parton-density functions" giving the probability of finding a parton a in a particle A and $d\sigma_{ij}$ is the hard scattering cross section of a "parton" i from the electron off a parton j from the proton.

culated. Indeed there are only a few exceptions like e^+e^- annihilation into hadrons and other interactions with no hadrons in the initial state which can be treated throughout perturbatively, at least for some inclusive observables. A way out of this dilemma is provided by *factorization*, meaning that perturbative and non-perturbative contributions to the cross section can be separated in a systematic way. Factorization theorems can be considered as field theoretic realizations of the parton model and e.g. in ep-scattering factorization finds a quite simple intuitive explanation (see [Col89]). When viewed from the center-of-mass frame of the ep-system, two things happen to the proton assuming that the interaction takes place via virtual, direct photon exchange at high energy and momentum transfer. The proton appears as Lorentz contracted in the direction of the collision, and its internal interactions of the partons are time dilated. From this it follows that as the center-of-mass energy increases, by the uncertainty principle the lifetime of any partonic state of the proton gets larger, while the time the electron needs to traverse the proton is shortened. So when the fluctuation time of the partons inside the proton is much shorter than the passing time of the electron, the proton will be in a single partonic state meaning that the number of par-

tons does not change during the time the electron needs to cross it. So the proton appears as "frozen" during this time for the partons do not interact. Each parton carries a definite fraction x of the protons momentum in the center-of-mass frame. So it is reasonable to think of the electron interacting with the individual partons from the proton rather than with the proton as a whole. And when the momentum transfer is very high, the virtual photon cannot travel far so when in addition the parton density of the proton is not too high, it is likely that the electron interacts with only one single parton.

The resulting final state partons interact with each other to form hadrons ("hadronization" or "fragmentation") and also in the initial state there occur interactions between partons for the case of a resolved interaction. These initial and final state interactions are also assumed to occur on time scales that are longer than the one of the hard scattering so these interactions will again not interfere with the hard scattering process. To summerize: The mutual interactions of the partons in the proton as well as the initial and final state interaction between the partons occur time-dilated as seen from the center-of-mass frame of the ep-system and so they do not interfere with the hard interactions of a parton with the photon. For this reason the cross section for this process may thus be computed by combining probabilities, rather than amplitudes, treating the different interactions taking place on different time scales as independent of each other. So, the cross section can be written in the factorized form as:

$$\begin{aligned} d\sigma_{ep}(Q^2) &= \sum_{i,j} \int_0^1 d\xi_\gamma f_{\gamma/e}(\xi_\gamma, Q^2) \int_0^1 d\xi_i f_{i/\gamma}(\xi_i, \mu_F^2) \cdot \\ &\quad \int_0^1 d\xi_j f_{j/p}(\xi_j, \mu_F^2)\, d\sigma_{ij}(\xi_i, \xi_j, Q^2, \mu_F, \alpha_s). \end{aligned} \tag{2.1}$$

In this equation $f_{a/A}(\xi, \mu_F^2)\, d\xi$ is the probability of finding a parton a inside the particle A carrying a fraction ξ of A's momentum in the interval $[\xi, \xi + d\xi]$ at the scale μ_F^2. This function is called *parton density function* (PDF) of the particle A. The indices i and j denote partons from the photon and the proton, respectively. In the case of a direct interaction the parton i is simply the photon itself. The perturbatively calculable cross section between the partons is given by $d\sigma_{ij}$. The sum runs over all partons of the photon and the proton. The parameter μ_F is the so called "factorization scale", explained below. It should be noted here that the cross section as given by (2.1) is a purely "partonic" cross section since in the final state only free parton jets appear. The formation of hadrons from these partons is not included in (2.1). How the hadronization process is taken into account is described in some detail in section 2.6.

2.3 Parton Density Functions

In this section the part of the content of (2.1) is examined in some detail that is the "photon density" of the electron and the parton density functions of the photon and the proton. The hard parton-parton scattering cross section is treated in the next section. However, the techniques of handling divergencies which inevitably occur in computing these cross sections ("regularization" and "renormalization") are closely connected to factorization and the concept of parton density functions and are thus also discussed in this section.

2.3.1 The Weizsäcker–Williams Approximation for $f_{\gamma/e}$

In 1934 C.F. Weizsäcker and E.J. Williams [Wei34, Wil34] developed independently a method to handle processes involving electromagnetic interactions of relativistic particles, called the *method of virtual quanta* or **W**eizsäcker-**W**illiams-**A**pproximation (WWA). It rests on the observation that the electromagnetic field of a rapidly moving charged particle is similar to that of a pulse of radiation. So, in an actual interaction between a relativistic charged particle and some other system it should be reliable to take on the view of an interaction of radiation (the *virtual quanta*) with the same system. This is also called *the equivalent photon approximation.* By use of a Fourier analysis they were also able to show that the transverse photons dominate the longitudinal photons in the process of electromagnetic radiation from a relativistic particle. It should be noted that E. Fermi has already used essentially the same method ten years before to calculate the energy loss by ionization via the absorption of X-ray by atoms [Fer24]. Weizsäcker and Williams obtained in this way a photon emission spectrum for the electron but for real and therefore transverse polarized photons only. It was later extended to virtual photons (see [Bud75]) and reads:

$$f^T_{\gamma/e}(y,Q^2) = \frac{\alpha_{em}}{2\pi}\left(\frac{1+(1-y)^2}{y}\frac{1}{Q^2} - \frac{2m_e^2 y}{Q^4}\right), \tag{2.2}$$

for transverse photons and

$$f^L_{\gamma/e}(y,Q^2) = \frac{\alpha_{em}}{2\pi}\frac{2(1-y)}{y}\frac{1}{Q^2} \tag{2.3}$$

for longitudinal photons. Here α_{em} is the electromagnetic fine structure constant, y is the energy fraction of the electron carried by the photon and m_e is the electron mass. For $Q^2 \gg m_e^2$ the second term in brackets in (2.2) can be neglected with respect to the first term. At HERA the accuracy of the WWA was studied for the case of photoproduction, and corrections to the WWA were found to be at a few percent level, see [Baw89, Kla95].

2.3.2 The PDFs of the Proton and the Photon

While there is only one possibility to define a function giving the "photon content" of the electron this is not the case for the parton density functions of the proton or the photon. The reason is that beyond lowest order in perturbation theory there is much ambiguity in separating the hard scattering process from the parton distribution functions. In higher orders those parts of the calculation giving not rise to singularities can be arbitrarily distributed between the PDF's and the hard parton–parton scattering cross section. So one has to introduce a prescription, a unique scheme how to perform the factorization to remove this ambiguity. Such a scheme is called *factorization scheme*. While it is a mere matter of taste or convenience which scheme one chooses, it is absolutely crucial to use schemes consistently, and to know in which scheme a calculation, or comparison of theory and data was carried out. The two most commonly used factorization schemes are the DIS and the $\overline{MS}$ schemes.

The DIS Scheme

The **D**eep **I**nelastic **S**cattering (DIS) scheme is sometimes preferred because of its close correspondence to experiment [Alt79]. In this scheme one demands that in a perturbative calculation order by order the corrections to the hard scattering cross section be absorbed into the distribution functions of the quarks and the anti-quarks so that at $\mu_F = Q$ the hard scattering cross section is exactly equal to its value resulting from the parton-model. However, this definition does not fix the gluon distribution.

The $\overline{MS}$ Scheme

The modified **M**inimal **S**ubtraction scheme ($\overline{MS}$) is the factorization scheme most often used because of its theoretical elegance and calculational simplicity [Bar78]. In this scheme the parton density functions are considered to be matrix elements of some operators counting the number of partons in an particular quantum state of the hadron. So the density function of a parton i with longitudinal momentum xp and transverse momentum $\mathbf{k}_T$ in an hadron h with momentum p is given by [Cur80, Col82]:

$$f_{i/h}(x, \mu_F^2) = \int \frac{d^2\mathbf{k}_T}{(2\pi)^2} \left\langle h(p) \left| b_i^\dagger(xp, \mathbf{k}_T) b_i(xp, \mathbf{k}_T) \right| h(p) \right\rangle . \tag{2.4}$$

The rightmost operator b_i annihilates the parton i from the hadron and the left operator $b_i^\dagger$ creates it again. So this expression of the parton density

function can be thought of as the expection value of the "number operator" $b_i^\dagger b_i$ in the hadronic state.

The Factorization Scale μ_F

The essence of factorization is to attribute long time processes to parton density functions and short time processes to the hard scattering cross section. As an example Fig. 2.5 shows the direct interaction of an electron with a quark from the proton which has emitted a gluon with transverse momentum $\mathbf{k}_T$ before it entered the interaction with the mediating photon. Associated with the time scale of a process is an energy scale due to the

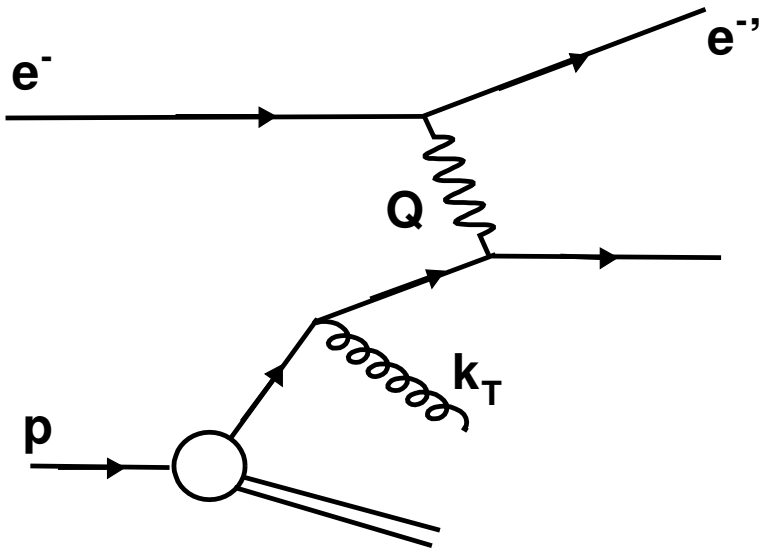

Figure 2.5: Scattering of an electron from a quark with a gluon emission.

uncertainty principle. When one actually computes the Feynman diagram one finds that the transverse momentum of the emitted gluon can range from order m (the mass of the hadron where the parton emitting the gluon belongs to) to order Q. Thus factorization in this case has the consequence that a gluon emission with $\mathbf{k}_T^2 \sim m^2$ (long time scale) is part of the parton distribution function while a gluon emission with $\mathbf{k}_T^2 \sim Q^2$ (short time scale) is considered as part of the hard scattering cross section. This split up of the cross section into factors associated with long and short time scales requires the introduction of an additional mass scale, the *factorization scale* μ_F. So in an actual calculation of the diagram in Fig. 2.5 one has to integrate over

$\mathbf{k}_T$. This is generally done in the way that the contributions from $\mathbf{k}_T^2 < \mu_F^2$ are counted to belong to the parton density functions which are then convoluted with the lowest order hard cross section. On the other hand those contributions from $\mathbf{k}_T^2 > \mu_F^2$ are attributed to the higher order parts of the hard cross section which is then convoluted with the lowest order parts of the parton density functions. This splitting of the process into contributions to different subprocesses via μ_F is illustrated in Fig. 2.6. In a real calculation

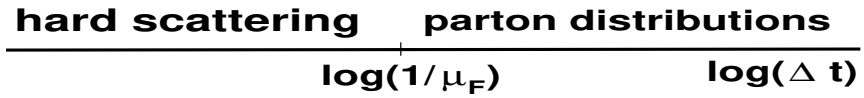

Figure 2.6: Splitting of a scattering process through the factorization scale μ_F separating subprocesses occurring with different time scales.

this splitting is accomplished with the aid of "dimensional regularization". A further consequence is that in (2.1) both the parton density functions $f_{i/\gamma}$, $f_{j/p}$ and the hard parton–parton cross section $d\sigma_{ij}$ depend on μ_F while the electron–hadron cross section should not depend on μ_F. However, in a fixed order perturbative calculation there is still a small dependence on μ_F that becomes less the more higher order terms are included in the calculation.

Determination of the PDFs

With the $\overline{MS}$ definition there exists a theoretical framework from which the PDFs should in principle be calculable, e.g. by means of lattice QCD, see [Sop96]. Currently, however, they are determined from experiment. Factorization states that the entire interaction can be split up in *independent* subinteractions. So a parton density function describing such a subinteraction should not depend on the actual total interaction. In this sense the parton density functions are universal and a parton density function obtained from one process should be the same in a completely different process.

To obtain the PDFs, so called "global fits" to data from experiment of several different types are performed. To do this, one chooses a parameterization of the x-dependence of the parton distributions at some standard factorization scale μ_0. Having obtained some set of values for the parameters describing e.g. $f_{j/p}(x, \mu_0)$, one can than determine $f_{j/p}(x, \mu)$ for all higher values of μ by means of "evolution equations" to be described below. The

parameters in $f_{j/p}(x, \mu_0)$ are systematically varied to obtain the best fit to all of the available data from the various experiments.

In the case of the proton there are essentially two groups doing the most comprehensive analyses, The **C**oordinated **T**heoretical–**E**xperimental Project on **Q**CD or CTEQ for short [Pum02] and the group of **M**artin, **R**oberts, **S**terling and **T**horne (MRST) [Mar02].

The available photon distribution functions can be grouped into three classes depending on the theoretical concepts used. To the first class belongs the parton distribution functions of DG [Dre85], LAC [Abr91] and WHIT [Hag95][1]. These distribution functions are purely phenomenological fits to the data. Their starting point is an x-dependent ansatz for the distribution functions. In the second class falls the parameterizations of GRV [Glu92], GRSc [Glu99], AFG [Aur94] and GS [Gor92, Gor97]. They obtain their input functions from the measured pion structure function, using VMD arguments and the additive quark model or VMD and quark parton model results in the case of GS. The last class consists of the parameterization of SaS [Sch93, Sch95]. They use the ideas of the two other classes and in addition relate their distribution functions to the measured total photon–proton cross sections.

2.3.3 Examples of PDF's for the Photon

In this subsection the properties of some popular PDF's for the photon are briefly discussed. For a more detailed information see the references to the original publications. The compilation given here follows [Nis00]. The data used to fit the unknown parameters were taken from e^+e^- collider experiments like PLUTO, TASSO, CELLO, JADE, TOPAZ, OPAL, ALEPH, L3 and DELPHI. Here especially the results from $\gamma\gamma$ scattering were considered. Concerning the virtualities of the photons, Q^2 denotes the virtuality of the "probe" photon while P^2 is usually used to denote the virtuality of the target photon.

First some parton distribution functions for the real photon:

1. **DG** [Dre85]: This group was the first which determined parton distribution functions for the photon. They used evolution equations in leading order perturbation theory (see below) and an x-dependent ansatz with 13 free parameters at a scale $\mu_0^2 = Q_0^2 = 1$ GeV^2. The parameters were fitted to the preliminary data of the PLUTO collaboration [Ber83] at $Q^2 = 5.3$ GeV^2 which were the only available data at this time. Further assumptions had to be made due to the small amount of

[1] The letters are referring to the first letter of the names of the corresponding authors, see the References.

available data. The parton distribution functions for quarks with the same charge were set equal ($f_{u/\gamma} = f_{c/\gamma}$, $f_{d/\gamma} = f_{s/\gamma}$) and the input distribution for the gluon was set to zero and then generated dynamically. Three independent sets of parameterizations were obtained corresponding to three different numbers of active quark flavors($n_f = 3, 4, 5$). Because they are independent, they are not smooth at the threshold where a heavier quark flavor becomes active. The heavy quarks charm and bottom (included for $Q^2 > 20$ GeV^2 (charm) and $Q^2 > 200$ GeV^2 (bottom)) were treated as massless and enter the evolution equations only via the number of flavors.

2. **LAC** [Abr91]: This group used essentially the same procedure like DG. An x-dependent ansatz containing 12 free parameters was used. Because they had a much richer pool of data available (for the many sources see the original publication) no additional assumptions about the input distributions had to be made. Evolution equations in leading order perturbation theory for four quark flavors were used. The charm quark contributes only for $W > 2m_c$ where W is the invariant mass of the hadronic final state of an interaction and m_c the charm quark mass. Otherwise the charm quark is treated as massless. There is no distribution function for bottom quarks available. Three sets of parton distribution functions were constructed (LAC1–3). The sets LAC1 and LAC2 starts from $\mu_0^2 = Q_0^2 = 4$ GeV^2 whereas LAC3 starts from $\mu_0^2 = Q_0^2 = 1$ GeV^2. In the set LAC1 the gluon distribution was parameterized as $x f_{g/\gamma}(x) \sim x^b(1-x)^c$, where b and c were determined from fits to the data. In LAC2 b is fixed to zero. In LAC3 the gluon is treated quite differently, see [Abr91].

3. **WHIT** [Hag95]: Six sets of parameterizations were constructed by this group (WHIT1–6). Like the afore mentioned groups they use evolution equations in leading order at an input scale $\mu_0^2 = Q_0^2 = 4$ GeV^2 for the three light quark flavors. The charm quark was introduced ($m_c = 1.5$ GeV) in the region ($4 < Q^2 < 100$ GeV^2) using the Bethe-Heitler formula. For $Q^2 > 100$ GeV^2 the "massive" evolution equation from [Glu82] was used. A parton distribution function including the bottom quark is not available. For light quarks the distribution functions are separated into those that stems from the process $\gamma \to q\bar{q}$, here called "valence"quarks and those that stems from the process $\gamma g \to q\bar{q}$, here called "sea" quarks. The valence quark distributions are parameterized as functions of x and Q_0 while the sea quark distributions are approximated by using the Bethe-Heitler formula at $Q^2 = Q_0^2$ and

a value of 0.5 GeV^2 for the mass of the light quarks. For the gluon distribution the ansatz $xf_{g/\gamma}(x) = a(c+1)(1-x)^c$ was chosen. The six parameterizations are given through the six different combinations resulting from the fixed values $a = 0.5, 1$ and $c = 3, 9, 15$. The group WHIT1–3 is using $a = 0.5$ and the group WHIT4–6 the parameter value $a = 1$ making this group of parameterizations to start rising earlier for decreasing values of x. The parameterizations for the quark distributions are then obtained by fit to the data (for the many sources of the data used see the original publication) with the additional requirement $x_min > Q^2/(Q^2 + W^2_{max})$ to remove that part of the data that was taken at the upper acceptance boundary for W^2.

4. **GRV** [Glu92]: This group constructed parton density functions in leading as well as next-to-leading order perturbation theory. To model the VMD part of the photon structure the parton distribution functions for the pion (exploiting the similarity of the π and the ρ mesons) from [Rey92] were used. The starting distributions have the functional form $f_{q/\gamma} = f_{\bar{q}/\gamma} = f_{g/\gamma} = \kappa\frac{4\pi\alpha_{em}}{f_\rho^2} f_\pi^2(x, Q^2)$ with $xf_\pi^2(x, Q_0^2) \sim x^b(1-x)^c$, where $b > 0$ is required. The proportionality factor κ was introduced to take into account higher mass mesons and the parameter value $\frac{1}{f_\rho^2} = 2.2$ was taken from [Ber87]. The only free parameter which was fitted to the data (for the various sources see the original publication) is κ. The fits were performed in the region $0.71 < Q^2 < 100$ GeV^2 with the additional requirement $W > 2$ GeV to avoid resonance production. The evolution is done using the full evolution equations with start values $\mu_0^2 = Q_0^2 = 0.25$ GeV^2 for the leading order distributions and $\mu_0^2 = Q_0^2 = 0.3$ GeV^2 for the next-to-leading order distributions. The part of the photons parton density function that can be treated perturbatively was generated dynamically using the evolution equations and required to vanish at $Q^2 = Q_0^2$. The evolution equations were used in the DIS_γ factorization scheme for massless quarks. Charm and bottom quarks were included via the Bethe-Heitler formula using $m_c = 1.5$ GeV and $m_b = 4.5$ GeV. At high values of W they were treated as being massless.

5. **AFG** [Aur94]: This group has used a similar strategy like the GRV group. The starting scale for the evolution was set to $\mu_0^2 = Q_0^2 = 0.5$ GeV^2 obtained from the requirement that the perturbatively treatable part of the parton density functions should vanish at $Q^2 = Q_0^2$. So the input was completely taken from the VMD part of the density functions. For this part a coherent sum of the low mass vector

mesons ρ, ω and ϕ was used. A difference to the GRV group is the usage of the $\overline{MS}$ factorization scheme with an additional technical input obtained from studies of the factorization scheme dependence and the momentum integration of the box diagram. In this way the parton distribution functions became process independent and therefore universal in contrast to the GRV ansatz using the DIS_γ factorization scheme which introduces a process dependence (see [Aur94]). An additional factor K was included to adjust the VMD contribution. This value was set to one in a standard setting or obtained from fits to data (see the original publication). The evolution was performed with three massless quark flavors for $Q^2 < 2m_c^2 = 2$ GeV^2 and for four flavors for $Q^2 > 2m_c^2$. There is no parton distribution function for the bottom quark available.

6. **GS** [Gor92, Gor97]: Parton density functions from this group are also available in leading as well as next-to-leading order perturbation theory. In a first ansatz a starting scale $\mu_0^2 = Q_0^2 = 5.3$ GeV^2 has been used [Gor92] and later when more data have been included the starting scale was set to $\mu_0^2 = Q_0^2 = 3.0$ GeV^2 [Gor97] . To constrain the gluon distribution data from jet production have been included which are sensitive to the gluon distribution via the resolved photon processes in jet production (see the original publications). The data, however, turned out to be not precise enough for this purpose.

   For the parameterization a VMD ansatz was chosen supplemented with contributions from the perturbatively treatable part of the hadronic photon structure based on the lowest order Bethe-Heitler formula for three low mass quark flavors. These contributions were necessary due to the high input scales. The quark masses were constrained to the ranges $0.25 < m_u = m_d < 0.4$ GeV and $0.35 < m_s < 0.55$ GeV. The mass values obtained by fit to the data are $m_u = m_d = 0.29$ GeV and $m_s = 0.41$ GeV (see [Gor92]). The contributions from charm quarks were also included using the Bethe-Heitler formula with $m_c = 1.5$ GeV up to $Q^2 = 50$ GeV^2. For $Q^2 > 50$ GeV^2 a four flavor massless approach was chosen which overestimates the charm contribution. As in the case of the AFG distribution functions the $\overline{MS}$ factorization scheme with an additional technical input was chosen. The leading and next-to-leading order parton density functions were connected by the requirements that they are identical at Q_0^2 and share the same gluon distribution function.

7. **GRSc** [Glu99]: This group used the same strategy as that of GRV. The differences are the use of a new pion input [Rey99] and some conceptual

changes. As in the case of the AFG parameterizations a coherent sum of vector mesons was used and as a consequence no free parameter had to be obtained by fits to data. The value of α_s was changed from the approximate next-to-leading order formula to the exact solution of the renormalization equations for α_s in next-to-leading order. The contribution from charm quarks was included via a leading order Bethe-Heitler formula with $m_c = 1.4$ GeV compared to 1.5 GeV in the case of GRV.

8. **SaS** [Sch93, Sch95]: Two different sets of parameterization in leading order perturbation theory were obtained by this group. Both sets are using a massless evolution for the light quarks and include the charm and bottom quarks via the Bethe-Heitler formula with $m_c = 1.3$ GeV and $m_c = 4.6$ GeV. The motivation for constructing two sets came from an investigation of the correlation between the size of the non-perturbative part of the parton density functions (usually modeled by VMD) and the starting scale Q_0^2. So two sets were constructed using different input scales; SaS1 with $\mu_0^2 = Q_0^2 = 0.36$ GeV^2 and SaS2 with $\mu_0^2 = Q_0^2 = 4$ GeV^2. Clearly, SaS2 contains the larger VMD contribution to fit the data. For the SaS1 set the normalization and the starting scale were obtained by an analysis of γp scattering data. The shape of the VMD contribution is fitted to the data. The SaS2 distribution is changed in its functional form and includes an additional proportionality factor K in the VMD part whats value is obtained from fits to the data and found to be $K = 2.422$. This factor was introduced to include higher mass mesons and to compensate for the fact that no perturbatively treatable contribution is allowed to evolve in the region $0.36 < Q^2 < 4$ GeV^2. The subdivision of the parton density functions in perturbatively and non-perturbatively parts was made explicit in these parameterizations. This allows an independent treatment of both parts, e.g. in simulating the hadronic final state in an interaction, one can examine the effects of the perturbative and the non-perturbative parts of the photon structure. The perturbatively treatable part is further divided into a part that gives the probability for the process $\gamma \to q\bar{q}$ and a so called "state" distribution describing the parton distribution functions within this $q\bar{q}$ state. This was made to ease the use of the parton density functions in Monte Carlo programs using the parton shower concept (see below). The parton density functions were obtained in the $\overline{MS}$ factorization scheme (SaS1M, SaS2M) and in the DIS_γ scheme (SaS1D, SaS2D). For the sources of the data used for the fits see the original publication.

There are also several parton density functions available for transverse virtual photons. Different approaches were performed because there is no unique prescription how to extend the parton density functions for the real photon to the case of virtual photons. They are generally constructed in a way that they reproduce the correct limits for large and small virtualities. There is one approach, namely that of the DG group which does not depend on a specific choice of a parton density function for the real photon. In addition to this the groups GRS, GRSc and SaS have extended there parameterizations for the real photon to that of a transverse virtual photon. These are in the following briefly discussed. For more detailed information see the original publications.

1. **DG** [Dre94]: The approach of this group is quite simple. Some parton density function for the real photon is simply multiplied by a P^2 dependent factor which suppresses the gluon density function more than those for the quarks:

$$\begin{aligned} f_{q_i/\gamma}(x,Q^2,P^2) &= f_{q_i/\gamma}(x,Q^2)\cdot\left[\frac{\ln\frac{Q^2+P^2}{P^2+P_c^2}}{\ln\frac{Q^2+P_c^2}{P_c^2}}\right] = q_i^\gamma(x,Q^2)\cdot L \\ f_{g/\gamma}(x,Q^2,P^2) &= f_{g/\gamma}(x,Q^2)\cdot L^2. \end{aligned}$$

   Here, P_c^2 is chosen to be a "typical" hadronic scale ($P_c^2 \leq 1$ GeV^2). With choice the parton density functions are globally suppressed what means that the x-dependence of the parton density functions for the real photon are not altered.

2. **GRS** [Glu95]: This group used a boundary condition at $Q^2 = \max(P^2, Q_0^2)$ similar to the one they used for real photons. It allows a smooth interpolation between large P^2 and $P^2 = 0$. A constant non-perturbative input for $0 < P^2 < Q_0^2$ is used for the evolution equations. The evolution equations were chosen to be the same as for the real photons and Q_0^2 is used as starting scale. The parton density functions are obtained by solving these inhomogeneous evolution equations in leading or next-to-leading order perturbation theory (see below). Heavy quarks were included via a Bethe-Heitler equation modified to cover the case $P^2 > 0$.

3. **GRSc** [Rey99]: This group just extended their parameterization for the real photon to virtual photons by the assumption that the photon virtuality is entirely accounted for by flux factors what is valid for $Q^2 \gg P^2$. Consequently all partonic subprocesses are calculated as if

$P^2 = 0$. Also the charm contribution for the case $P^2 > 0$ is calculated from a Bethe-Heitler formula for $P^2 = 0$.

4. **SaS** [Sch95, Sch96]: This group used a dispersion integral in the mass of the $q\bar{q}$ pair as a representation of the parton density functions of the virtual photon, discussed in [Bjo89]. The $q\bar{q}$ fluctuations are treated as a discrete sum of vector meson states and a high mass continuous spectrum which can be calculated perturbatively. Both of the terms are suppressed by different P^2-dependent terms. Different sets of boundary conditions and evolution equations were proposed for the virtual photons parton density functions which differ in the order of P^2/Q^2. They are accessible in the parameterizations via the parameter IP2. The heavy quarks were treated in the same way as the group GRS did.

2.3.4 Evolution Equations

The parton distribution functions are determined from experimental data at a fixed factorization scale μ_0. To obtain their values for arbitrary scales μ one uses so called "evolution equations" which extrapolate the distribution functions by means of perturbation calculations. To be able to apply perturbation theory, μ must be large so that $\alpha_s(\mu^2)$ is small enough. Furthermore, to carry out such perturbative calculations, additional assumptions have to be made restricting the phase space for which the obtained results hold. The evolution is then thought of to happen in a way that a quark emits gluons and a gluon emits other gluons or converts into a quark-anti-quark pair before it enters the interaction. The most important evolution equations are the ones of DGLAP, BFKL and CCFM which will be discussed in some detail below.

The DGLAP Equations

The approach of **D**okshitzer, **G**ribov, **L**ipatov, **A**ltarelli and **P**arisi (DGLAP) [Dok77] starts with the assumption that the transverse momenta of the parton after each emission step are "strongly ordered" in the sense that $Q_0^2 \ll k_{T1}^2 \ll ... \ll k_{Ti}^2 \ll ... \ll Q^2$. Here Q_0^2 is the virtuality of the parton at the start of the emission cascade and Q^2 the virtuality of the exchanged photon, see also Fig. 2.7. This condition also implies a strong ordering in the transverse momenta of the emitted quanta, that is $p_{Ti} \ll p_{T(i+1)}$. To evaluate a ladder diagram of the type shown in Fig. 2.7 with n rungs in a perturbative treatment one has to perform integrations of the form

$$\alpha_s \int \frac{dk_{Ti}^2}{k_{Ti}^2} \cdots \int \frac{dx_i}{x_i}. \tag{2.5}$$

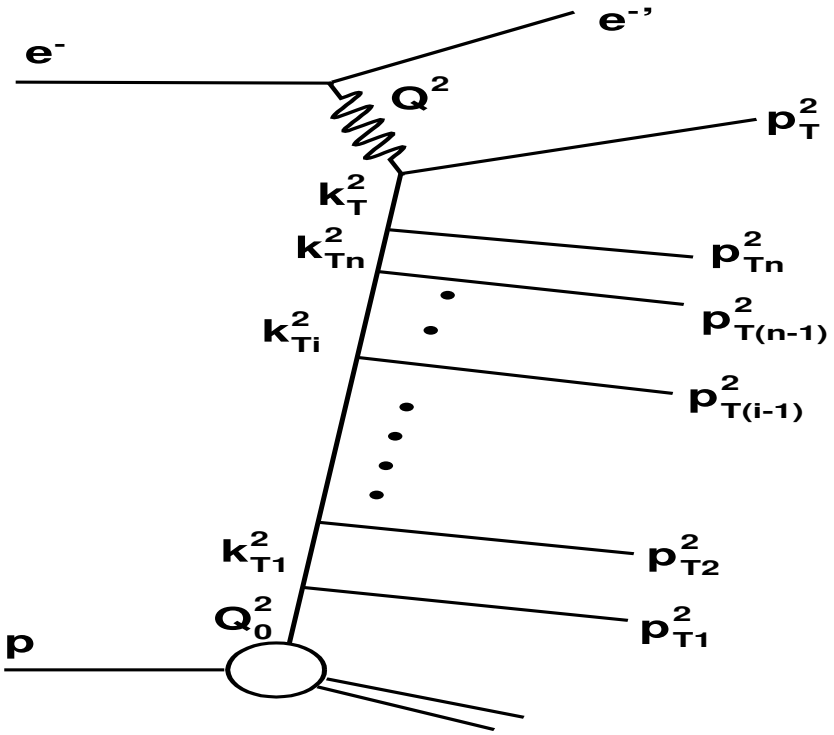

Figure 2.7: Ladder diagram showing the strong ordering in the transverse momenta of the interacting parton and the quanta it has emitted before it entered the interaction. This strong ordering is an assumption made in the derivation of the DGLAP equations.

The dots in this equation denotes propagators and currents of the involved quantum states and i the rung of the ladder. With the assumption of strong ordering these integrations can be carried out for all n rungs of the ladder resulting in expressions $\propto (\alpha_s \ln \frac{Q^2}{Q_0^2})^n$. When the k_T's are strongly ordered large logarithms are obtained which compensate the smallness of α_s. This forbids a truncation of the sum over the rungs. Instead one has to sum all diagrams up to $n = \infty$. This is done by a so called "resummation" where the perturbative series is rearranged in such a way that the largest terms come first. This yields the so called **L**eading **L**og (LL) approximation because each power in α_s is accompanied by the same power of $\ln \frac{Q^2}{Q_0^2}$. In this way one gets the DGLAP evolution equations which are typically written in the form of integro-differential-equations. For the proton they read:

$$\frac{df_{q_i/p}(x,\mu^2)}{d\,\ln \mu^2} = \frac{\alpha_s}{2\pi}[P_{qq}(x) \otimes f_{q_i/p}(x,\mu^2) + P_{qg}(x) \otimes f_{g/p}(x,\mu^2)], \quad (2.6)$$

$$\frac{df_{g/p}(x,\mu^2)}{d\ \ln\mu^2} = \frac{\alpha_s}{2\pi}[\sum_i P_{gq}(x)\otimes f_{q_i/p}(x,\mu^2) + P_{gg}(x)\otimes f_{g/p}(x,\mu^2)] \quad (2.7)$$

For the photon one obtains the equations:

$$\begin{aligned}\frac{df_{q_i/\gamma}(x_\gamma,\mu^2)}{d\ \ln\mu^2} &= \frac{\alpha_{em}}{2\pi}e_q^2 P_{q\gamma}(x_\gamma) + \frac{\alpha_s}{2\pi}[P_{qq}(x_\gamma)\otimes f_{q_i/\gamma}(x_\gamma,\mu^2) \\ &\quad + P_{qg}(x_\gamma)\otimes f_{g/\gamma}(x_\gamma,\mu^2)], \quad (2.8)\\ \frac{df_{g/\gamma}(x_\gamma,\mu^2)}{d\ \ln\mu^2} &= \frac{\alpha_s}{2\pi}[\sum_i 2P_{gq}(x_\gamma)\otimes f_{q_i/\gamma}(x_\gamma,\mu^2) \\ &\quad + P_{gg}(x_\gamma)\otimes f_{g/\gamma}(x_\gamma,\mu^2)]. \quad (2.9)\end{aligned}$$

Here, x (x_γ) is the momentum fraction of the proton (photon) carried by the parton, e_q is the fractional charge of the quark q in units of the electron charge and P_{aA} denotes the so called *splitting functions* giving the probability that a particle A splits off a particle a. Here the symbol $\otimes$ is used to denote the "Mellin convolution" defined by[2]:

$$(f\otimes g)(x) = \int_x^1 f(\frac{x}{y})g(y)\frac{dy}{y}. \quad (2.10)$$

One should note that the evolution equation for the quark-density of the photon contains an inhomogeneous term $\frac{\alpha_{em}}{2\pi}e_q^2 P_{q\gamma}(x_\gamma)$ which stems from the "point-like" part of the photon structure due to the process $\gamma\to q\bar{q}$, see Fig. 1.4. The expressions $\frac{\alpha_s}{2\pi}P_{aA}(z)$ gives the probability per unit $\ln\frac{\mu^2}{\mu_0^2}$ for parton splittings of the form $A\to a+b$, where the resulting parton a carries a momentum fraction z of the original parton A and b denotes an additional parton. The splitting functions can be calculated perturbatively. Table 2.1 contains their mathematical expressions in leading order perturbation theory. For the special case that next to the strong ordering of each parton emission step in k_T it is also a strong ordering in the corresponding x required, that is $x\ll ...\ll x_{i+1}\ll x_i\ll x_0$, the DGLAP equations can be solved analytically yielding the so called **D**ouble **L**eading **L**og (DLL) solutions, see [Rob90]. The name of these solutions stem from the fact that the integrations in (2.5) give large logarithmic terms of the form $\propto(\alpha_s(\mu^2)\ln\frac{\mu^2}{\mu_0^2}\ln\frac{1}{x})^n$.

The BFKL equations

The DGLAP approximations are not valid any longer when x is small but μ^2 not large enough to reach the region where one can obtain a DLL so-

[2]Its connection to the original convolution $(f*g)(x)=\int f(x-y)g(y)dy$ is revealed by making the substitutions $x=\ln t$ and $y=\ln\tau$, yielding $(f*g)(t)=\int f(t/\tau)g(\tau)\frac{d\tau}{\tau}$ with a slight redefinition of f and g.

$P_{qq}^{(1)}(z) = \frac{4}{3}\frac{1+z^2}{1-z}$	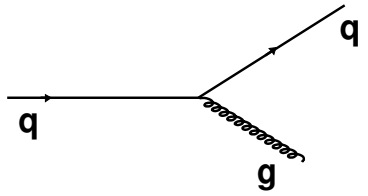
$P_{gq}^{(1)}(z) = \frac{4}{3}\frac{1+(1-z)^2}{z}$	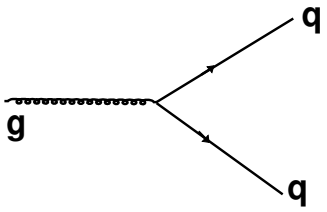
$P_{qg}^{(1)}(z) = \frac{1}{2}(z^2+(1-z)^2)$	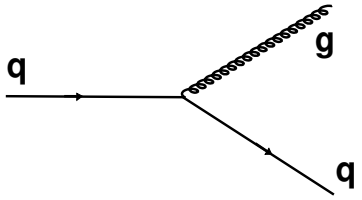
$P_{gg}^{(1)}(z) = 6\left(\frac{z}{1-z}+\frac{1-z}{z}+z(1-z)\right)$	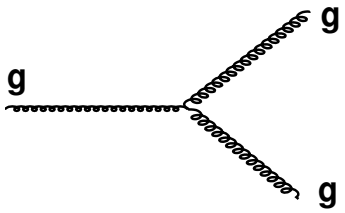

Table 2.1: Splitting functions in leading order QCD.

lution. For the case that $1/x$ is large and μ^2 is finite and fixed the approach of **B**alitsky, **F**adin, **K**uarev and **L**ipatov (BFKL) gives a reliable evolution equation. Usually only gluons are discussed because they are assumed to dominate at small values of x [Kur72, Bal78]. In this approach those diagrams are summed up in which x_i is strongly ordered according to $x \ll ... \ll x_{i+1} \ll x_i \ll x_0$ while no ordering in k_T is imposed. The resulting evolution equation is given by:

$$\frac{\partial f_{g/p}(x,k_T^2)}{\partial \ln(1/x)} = \frac{3\alpha_s}{\pi} k_T^2 \int_0^\infty \frac{dk'^2_T}{k'^2_T}\left[\frac{f_{g/p}(x,k'^2_T) - f_{g/p}(x,k_T^2)}{|k'^2_T - k_T^2|} + \frac{f_{g/p}(x,k_T^2)}{\sqrt{4k'^4_T + k_T^4}}\right]. \tag{2.11}$$

It should be noted here that the BFKL-equation gives an evolution of $f_{g/p}(x, k_T^2)$ with respect to small x. It can be solved for $f_{g/p}(x, k_T^2)$ for any small x and all k_T^2 once $f_{g/p}(x, k_T^2)$ is known for some x_0.The scale μ^2 is fixed here. If α_s is fixed, the equation can be solved analytically. The result in leading order perturbative QCD is:

$$\begin{aligned} \frac{f_{g/p}(x, k_T^2)}{\sqrt{k_T^2}} &\propto \frac{(x/x_0)^{-\lambda}}{\sqrt{2\pi\lambda'' \ln(x_0/x)}} \exp\left[\frac{-\ln^2(k_T^2/\bar{k_T}^2)}{2\lambda'' \ln(x_0/x)}\right] \\ &\propto \left(\frac{x}{x_0}\right)^{-\lambda}. \end{aligned} \tag{2.12}$$

Here, $\lambda = \frac{N_c \alpha_s}{\pi} \cdot 4 \ln 2$ and $\lambda'' = \frac{N_c \alpha_s}{\pi} \cdot 28\zeta(3)$ where N_c is the number of active colors. The value $\bar{k_T}^2$ specifies the starting point of the evolution and $\zeta(x)$ is the Riemann ζ-function where $\zeta(3) = 1.202$. From this solution the gluon density is expected to rise like a power of $1/x$ as x decreases. Another phenomenon that is predicted by the BFKL-equation is "k_T diffusion" in contrast to the k_T ordering in the DGLAP approach. From (2.12) one sees that $f_{g/p}(x, k_T^2)/\sqrt{k_T^2}$ considered as distribution function of k_T is of the Gaussian form in $\ln k_T^2$ and has a width that increases with the "BFKL evolution length" $\sqrt{\ln(x_0/x)}$. For this reason, an individual evolution path will follow a kind of random walk in k_T^2 and an ensemble of evolution paths will show up a diffusion pattern according to the Gaussian distribution in $\ln k_T^2$.

The CCFM equations

The approach of **C**atani, **C**iafaloni, **F**iorani and **M**archesini (CCFM) unifies the approaches of DGLAP and BFKL [Cia87, Cat90]. In addition so called "color coherence effects" which are interferences between gluon states are taken into account. This is achieved by summing up those diagrams in which the emitted partons are ordered by the emission angle in the way that $\theta_{i+1} > \theta_i$, see Fig. 2.8. For simplicity the emission of gluons from a parent gluon is shown. Considering again only on gluons the CCFM evolution equation is given by:

$$\bar{q}^2 \frac{d}{d\bar{q}^2} \frac{x\mathcal{A}(x, k_T, \bar{q})}{\Delta_s(\bar{q}, \mu_0)} = \int dz \frac{d\phi}{2\pi} \frac{\tilde{P}(z, \bar{q}/z, k_T)}{\Delta_s(\bar{q}, \mu_0)} x\mathcal{A}(x, k_T, \bar{q}/z). \tag{2.13}$$

In this equation $\bar{q}$ denotes the momentum of the last emitted gluon in the emission chain, k_T the initial transverse momentum of the parent gluon ϕ the azimuth angle around the parent gluon and $\mathcal{A}$ the so called *unintegrated gluon*

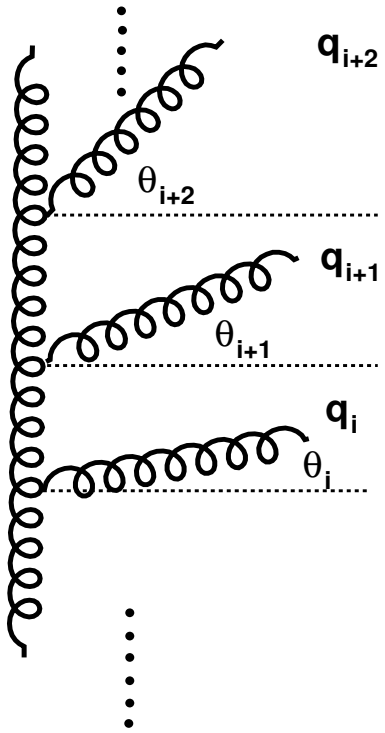

Figure 2.8: Angular ordering of the emission of gluons from a parent gluon. Here, q_i denotes the momentum of the emitted gluon i.

density. The function Δ_s is the *Sudakov form factor* of the gluon [Sud56] and $\tilde{P}$ the splitting function given by:

$$\tilde{P}(z,q,k_T) = \frac{\bar{\alpha}_s(q(1-z))}{1-z} + \frac{\bar{\alpha}_s(k_T)}{z}\Delta_{ns}(z,q,k_T). \tag{2.14}$$

Here, Δ_{ns} is the non-Sudakov form factor and $\bar{\alpha}_s = \frac{C_A \alpha_s}{\pi}$, where C_A denotes the number of colors[3] The actual gluon density is finally obtained from the unintegrated gluon density via

$$xG(x,\bar{q}) \simeq \int_0^{\bar{q}^2} dk_T^2 \, x\mathcal{A}(x,k_T^2,\bar{q}). \tag{2.15}$$

For high μ^2 and high x the CCFM approach resembles the DGLAP results while for finite μ^2 and high $1/x$ it resembles the BFKL results but here it leads to a reduction of the exponent λ and a reduction of the k_T diffusion phenomenon.

[3]Actually C_A denotes an invariant quantity under the change of the representation of SU(n). And here it is just the dimension n of the representation.

2.4 Regularization and Renormalization

Intimately connected to factorization are *regularization* and *renormalization*. To compute the total ep-cross section one has to integrate (2.1) over the available region in phase space. This is a non-trivial task because the next-to-leading order corrections to $d\sigma_{ij}$ are singular in some points in phase space making the integral divergent. There are different types of divergencies. Divergencies appearing as an unlimited rise of the integral in the high energy region are called UV-divergencies because high energy means small wavelengths. On the other hand, divergencies encountered at low energy are correspondingly called IR-divergencies. Both types of divergencies appear in the so called *virtual* as well as in the *real* next-to-leading order correction terms (virtual and real corrections are discussed in some detail in the next section). In the virtual corrections the singularities show up through internal loops in the corresponding Feynman diagrams while in the real corrections they appear from the emission of a parton with low or almost zero momentum ("soft" singularities) and from partons emitted collinear to an incident parton ("collinear" singularities). The IR-divergencies of the virtual corrections and the soft singularities of the real corrections are not critical because they cancel each other what was shown by Kinoshita, Lee and Nauenberg [Kin62]. Actually they were able to show that the cancellation of these particular type of divergencies holds generally true to all orders in perturbation theory. However, all other singularities need a special treatment. Any method to isolate the singularities and to make the phase space integral finite is called a regularization method. As was shown by Bohr and Rosenfeld [Boh55], operators in a field theory (and so also in QCD) are intrinsically singular, so altering the singular behavior necessarily destroys some physical feature of the theory. For instance, Pauli–Villars regularization which introduces a fictious mass field to make the phase space integration finite destroys hermiticity and gauge invariance in non-abelian theories like QCD and lattice regularization destroys Poincaré invariance. Very common is the so called *dimensional regularization* [Hoo72] that destroys scale invariance but restores gauge invariance what is essential to QCD. In dimensional regularization all quantities are extended to a dimension larger than four, e.g to $d = 4 + 2\epsilon$ with ϵ being an arbitrary positive number. This of course enlarges also the phase space over which the integration has to be performed. The physical result is then obtained from the limit $\epsilon \to 0$. In this enlarged dimensions the phase space integrals turn out to be finite and can be evaluated. However, by dimensional regularization the problem of singular expressions is not removed but only shifted. To obtain a physical meaningful result one has to go back to four dimensions in other words one has to consider the limit of

vanishing ϵ. And here the divergencies are encountered again by poles in $1/\epsilon$. To make the expressions finite one has to perform a renormalization. It turns out that the divergencies appear in terms attributed to the mass of the interacting particles and the coupling constant. One way to renormalize the singular expressions is to redefine the mass and the coupling constant by replacing the singular expressions by appropriate finite physical expressions (the measured mass[4] for example). It should be noted here that in this way the "renormalized" coupling constant gains an explicit dependence on an arbitrary mass scale (μ_R) which had to be introduced in dimensional regularization to keep the coupling constant dimensionless. In this way it becomes the "running" coupling constant already mentioned in chapter 1. Another way of performing renormalization is the method of counterparts. Here one adds terms (the "counterparts) to the Lagrangian describing the interaction which leave the form of the Lagrangian (and therefore the physics it contains) unaltered but lead to the same singularities compared to the unrenormalized theory but with *opposite* sign. So in an actual calculation the singularities of the unrenormalized theory will cancel against the singularities from the counterparts. It turns out however that this method is completely equivalent to the method of redefining mass an coupling constant. For more detailed information and explicit calculations concerning regularization and renormalization see [Ryd96].

Factorization provides a further way to handle the divergencies. The singularities can be factored out and then are attributed to the parton density function the parton causing the singularity is due to. The parton density function which became singular through this process is then replaced by the finite one obtained from measurements in the way described in the sections above. However, the absorption of singularities into the parton density functions is scheme dependent. For instance in the $\overline{MS}$ scheme as little as possible is absorbed into the parton density functions (to one loop actually only the collinear divergent term, the other divergencies are handled by renormalizing the coupling constant) while in the DIS scheme all corrections are absorbed into the parton density functions [Ste95].

[4]In perturbative QCD the partons are actually treated as massless so here only renormalization of the coupling constant applies.

2.5 The Hard Scattering Cross Section $d\sigma_{ij}$ in NLO

In this section the calculation of the hard differential cross section $d\sigma_{ij}$ is outlined. As it describes the hard scattering process the strong coupling constant α_s should be small enough so that perturbation theory can be applied. This means that the matrix elements can be evaluated in a power series of α_s. For the analysis presented in this thesis terms of **L**eading **O**rder (LO) and **N**ext-to-**L**eading **O**rder (NLO) in α_s are taken into account. The general differential cross section element for the production of n particles in the final state from two initial partons i, j in given by [Kla98]:

$$d\sigma_{ij}^{(n)}(ij \to jets) = \frac{1}{2s}\overline{|\mathcal{M}|^2} d\Omega^{(n)}. \tag{2.16}$$

Here $\frac{1}{2s}$ is the flux factor depending on the Mandelstam variable s. For the definition of the Mandelstam variables (s, t, u) for a two particle final state see Fig. 2.9. The n particle phase space element $d\Omega^{(n)}$ in d dimensions is

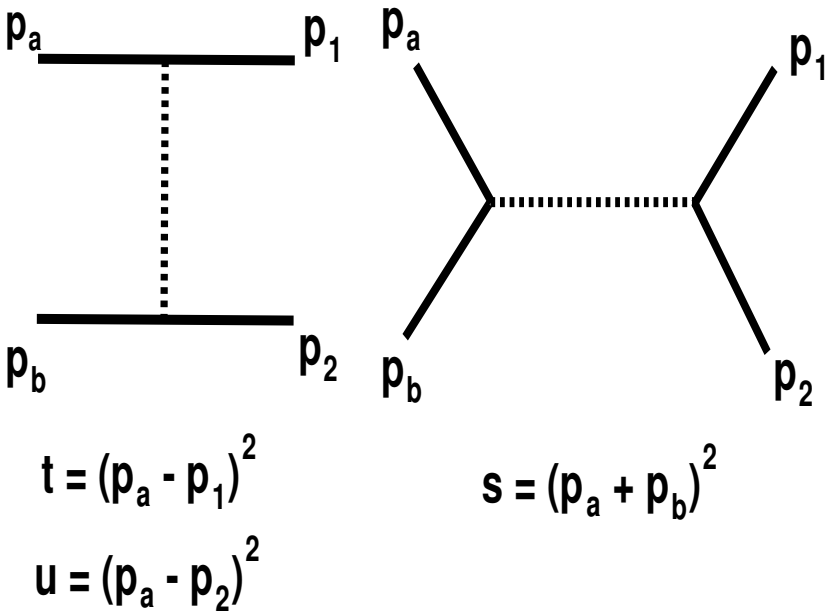

Figure 2.9: Definition of the Lorentz invariant Mandelstam variables s, t and u.

defined by:

$$d\Omega^{(n)} = \int (2\pi)^d \prod_{a=1}^{n} \delta^d \left(p_i + p_j - \sum_{b=1}^{n} p_b \right) \frac{\delta(p_a^2)}{(2\pi)^{d-1}} d^d p_a . \tag{2.17}$$

The delta functions in this expression assure energy-momentum conservation. To single out the singularities dimensional regularization is applied, so all expressions are evaluated in $d = 4 + 2\epsilon$ dimensions. The squared matrix element $\overline{|\mathcal{M}|^2}$ contains the actual scattering process in leading and next-to-leading order. It is averaged over initial and summed over final spin and color states. In calculating $\mathcal{M}$ the two possibilities for a photon to interact, direct and resolved interactions, respectively, have to be taken into account.

2.5.1 LO Contributions

The leading order contributions are given by the Born terms of the perturbative expansion for the matrix element. The matrix element of the leading order direct hard scattering process is of $\mathcal{O}(\alpha_{em}\alpha_s)$ and that of the leading order resolved hard scattering process is of $\mathcal{O}(\alpha_s^2)$. Only two particles will appear in the final state so that one needs only the two particle phase space element:

$$d\Omega^{(2)} = \int (2\pi)^d \prod_{a=1}^{2} \delta^d \left(p_i + p_j - \sum_{b=1}^{2} p_b \right) \frac{\delta(p_a^2)}{(2\pi)^{d-1}} d^d p_a . \tag{2.18}$$

Some diagrams contributing to the leading order direct interaction are shown in Fig. 2.10. The matrix element squared for the QCD Compton scattering is given by, see also [Kla98, Fie89]:

$$|\mathcal{M}|^2_{\gamma q \to g q} = e^2 e_q^2 g^2 \mu_R^{4\epsilon} T_{\gamma q \to g q}(s,t,u), \tag{2.19}$$

with

$$T_{\gamma q \to g q}(s,t,u) = 8 n_c c_f (1-\epsilon) \left[(1-\epsilon) \left(-\frac{u}{s} - \frac{s}{u} - \frac{2Q^2(s+u+Q^2)}{su} \right) + 2\epsilon \right]. \tag{2.20}$$

In these equations, e and e_q are the charges of the electron and the quark, respectively, $g^2 = 4\pi\alpha_{em}$ and μ_R is the renormalization scale, discussed in the last section. The factor c_f is the so called color factor taking into account the contributions of the different possible color charges of the quarks. The matrix element for boson gluon fusion is obtained from (2.19) by simply crossing the initial quark with the final gluon, that is $(s \leftrightarrow t)$ and multiplying by (-1) for crossing a fermion line. In the same way one obtains the contributions

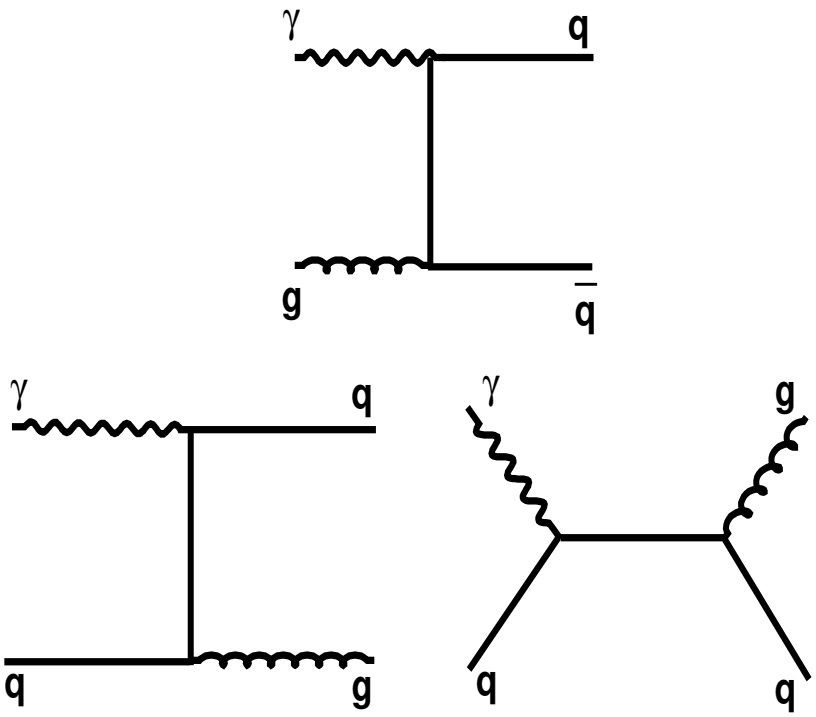

Figure 2.10: Some leading order contributions to direct interactions. The first row shows "boson gluon fusion" while in the second row the diagrams contributing to the "QCD Compton scattering" are displayed.

for incoming anti-quarks ($\gamma\bar{q} \to g\bar{q}$) by crossing ($s \leftrightarrow u$). These leading order direct matrix elements have been known since quite some time, see [Aur87, Bae89, Boe93]. They are summarized in Tab. 2.2. Some diagrams

Direct Process	Squared Matrix Element
$\gamma q \to gq$	$\lvert\mathcal{M}\rvert^2_{\gamma q\to gq}(s,t,u)/4n_c$
$\gamma\bar{q} \to g\bar{q}$	$\lvert\mathcal{M}\rvert^2_{\gamma q\to gq}(u,t,s)/4n_c$
$\gamma g \to q\bar{q}$	$-\lvert\mathcal{M}\rvert^2_{\gamma q\to gq}(t,s,u)/(8(1-\epsilon)n_c c_f)$

Table 2.2: Squared matrix elements for the various Born terms of the direct hard scattering contributions.

of the leading order resolved contributions are displayed in Fig. 2.11. The

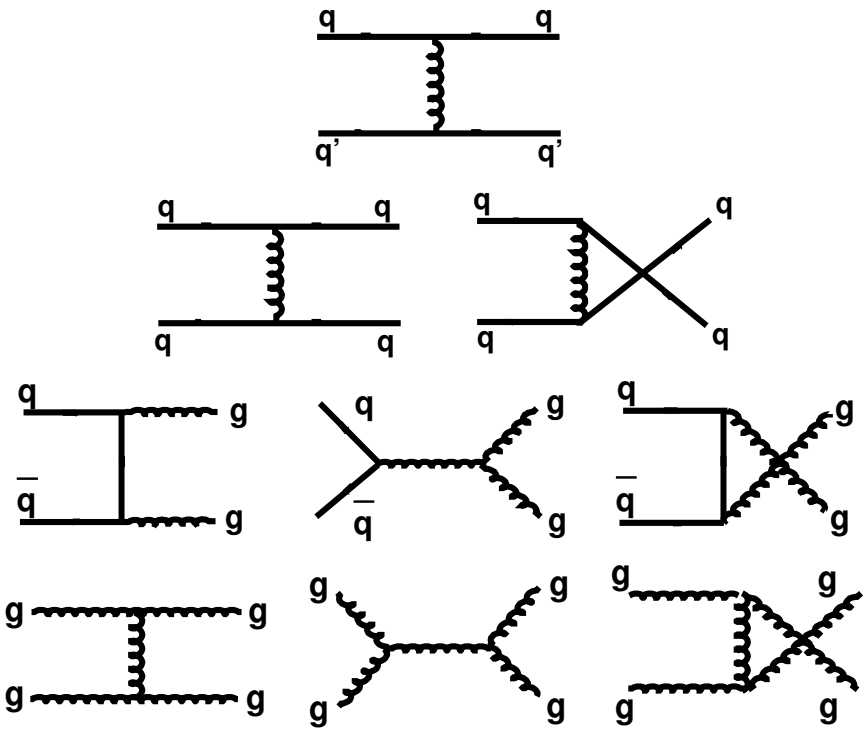

Figure 2.11: Some leading order contributions to resolved interactions.

first row shows the only contributing diagram of two interacting quarks with different flavor. The corresponding matrix element squared is:

$$|\mathcal{M}|^2_{qq'\to qq'}(s,t,u) = g^4 \mu_R^{4\epsilon} T_{qq'\to qq'}(s,t,u), \tag{2.21}$$

with

$$T_{qq'\to qq'}(s,t,u) = 4n_c c_f \left(\frac{s^2+u^2}{t^2} - \epsilon\right). \tag{2.22}$$

The second row of Fig. 2.11 shows the scattering process of two quarks with the same flavor. Because they are indistinguishable there are two contributing diagrams which have to be added. For this process one obtains:

$$T_{qq\to qq}(s,t,u) = -8c_f(1-\epsilon)\left(\frac{s^2}{ut} + \epsilon\right). \tag{2.23}$$

The third row of Fig. 2.11 displays various quark–anti-quark interactions what yields:

$$T_{q\bar{q}\to gg}(s,t,u) = 4c_f(1-\epsilon)\left(\frac{2n_c n_f}{ut} - \frac{2n_c^2}{s^2}\right)(t^2+u^2+\epsilon s^2). \tag{2.24}$$

Finally, in the last row of Fig. 2.11 the gluon-gluon interactions are shown. The gluons are indistinguishable and interact in a non-abelian way, i.e. they interact among themselves. This leads to:

$$T_{gg\to gg}(s,t,u) = 32 n_c^3 c_f (1-\epsilon)^2 \left(3 - \frac{ut}{s^2} - \frac{us}{t^2} - \frac{st}{u^2}\right). \tag{2.25}$$

All other possible diagrams can be obtained from the above ones by use of crossing relations. The complete result can be found in [Ell86]. The squared matrix elements are summarized in Tab. 2.3.

Resolved Process	Squared Matrix Element
$qq' \to qq'$	$\lvert\mathcal{M}\rvert^2_{qq'\to qq'}(s,t,u)/4n_c^2$
$q\bar{q}' \to q\bar{q}'$	$\lvert\mathcal{M}\rvert^2_{qq'\to qq'}(u,t,s)/4n_c^2$
$q\bar{q} \to \bar{q}'q'$	$\lvert\mathcal{M}\rvert^2_{qq'\to qq'}(t,s,u)/4n_c^2$
$qq \to qq$	$(\lvert\mathcal{M}\rvert^2_{qq'\to qq'}(s,t,u) + \lvert\mathcal{M}\rvert^2_{qq'\to qq'}(s,u,t) + \lvert\mathcal{M}\rvert^2_{qq\to qq}(s,t,u))/8n_c^2$
$q\bar{q} \to q\bar{q}$	$(\lvert\mathcal{M}\rvert^2_{qq'\to qq'}(u,t,s) + \lvert\mathcal{M}\rvert^2_{qq'\to qq'}(u,s,t) + \lvert\mathcal{M}\rvert^2_{qq\to qq}(u,t,s))/4n_c^2$
$q\bar{q} \to gg$	$\lvert\mathcal{M}\rvert^2_{q\bar{q}\to gg}(s,t,u)/8n_c^2$
$qg \to qg$	$-\lvert\mathcal{M}\rvert^2_{q\bar{q}\to gg}(t,s,u)/8(1-\epsilon)n_c^2 c_f$
$\bar{q}g \to \bar{q}g$	$-\lvert\mathcal{M}\rvert^2_{q\bar{q}\to gg}(t,u,s)/8(1-\epsilon)n_c^2 c_f$
$gg \to q\bar{q}$	$\lvert\mathcal{M}\rvert^2_{q\bar{q}\to gg}(s,t,u)/16(1-\epsilon)^2 n_c^2 c_f^2$
$gg \to gg$	$\lvert\mathcal{M}\rvert^2_{gg\to gg}(s,t,u)/2!16(1-\epsilon)^2 n_c^2 c_f^2$

Table 2.3: Squared matrix elements for the various Born terms of the resolved hard scattering contributions.

2.5.2 NLO Corrections

The next-to-leading order terms in the perturbative series of the matrix element are characterized by an additional order in α_s compared to the leading order terms. There are two different types of corrections. One additional order of α_s is obtained by simply introducing another gluon line into the leading order diagrams. This type of correction is called "virtual correction". Another process that adds an additional order is the emission of an additional parton in the final state. This type of correction is called "real correction". Examples of direct, virtual corrections are shown in Fig. 2.12. One can distinguish three types of corrections. Self-energy corrections are

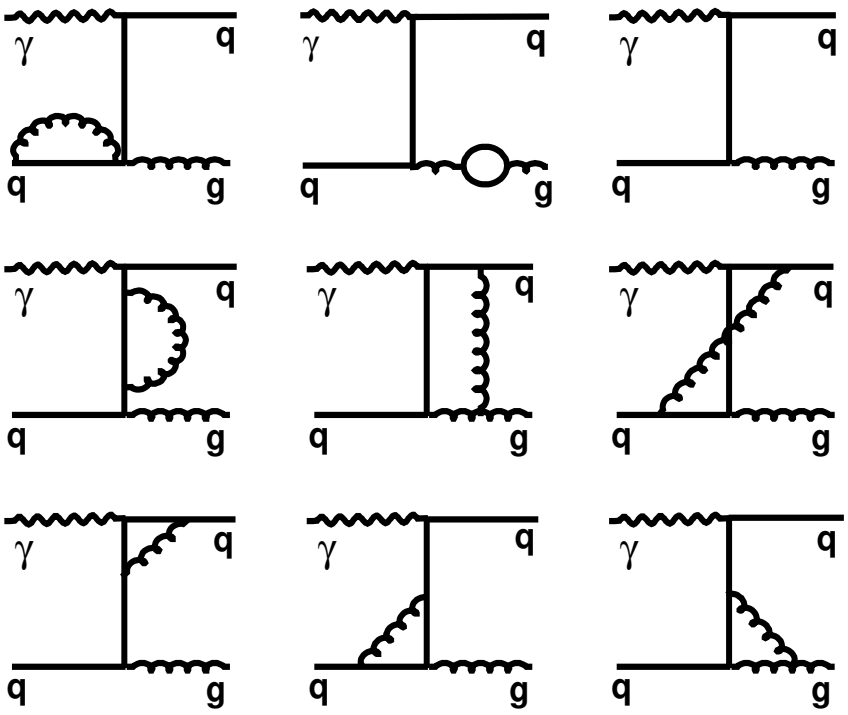

Figure 2.12: Virtual corrections for a direct hard scattering process. The first row shows self-energy diagrams, the middle row propagator corrections and box diagrams and in the last row vertex corrections are displayed.

shown in the first row of Fig. 2.12. The loop correction in the middle diagram denotes a quark, gluon or ghost loop (see chapter 1). The middle row displays propagator corrections and box diagrams. In the last row various vertex corrections are shown. The diagrams for the process $\gamma g \to q\bar{q}$ are obtained as in the leading order case by crossing the incoming quark line with

the outgoing gluon line, that is by $(s \leftrightarrow t)$ and multiplying by (-1) for crossing of a fermion line. The order of these processes can be read off directly from the diagrams to be $\mathcal{O}(\alpha_{em}\alpha_s^3)$. These contributions are well known from higher order calculations of the interaction $e^+e^- \to q\bar{q}g$ [Ell81, Fab82]. The formulae are not displayed here because of their length. They can be found in [Kla98] or the references just cited.

Examples of the virtual corrections for the resolved interactions are shown in Fig. 2.13. As in the case of direct interactions, the first row shows self-

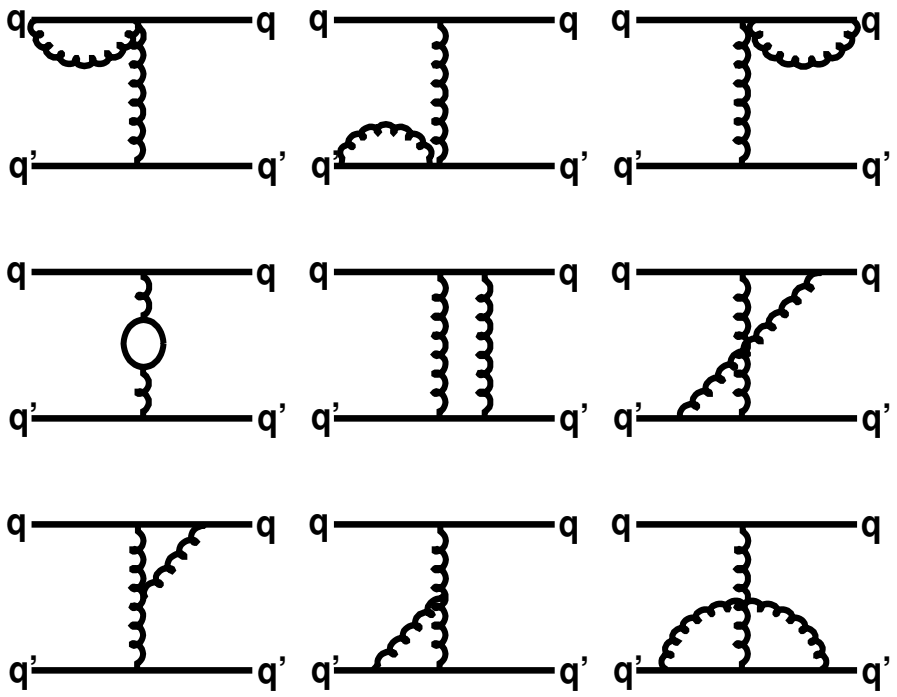

Figure 2.13: Virtual corrections for a resolved hard scattering process. The first row shows self-energy diagrams, the middle row propagator corrections and box diagrams and in the last row vertex corrections are displayed.

energy term, the middle row vertex corrections and box diagrams while the vertex corrections are displayed in the last row. The circle in the first diagram of the middle row has the same meaning as in the direct case. The complete set of diagrams as well as the lengthy formula expressions of the matrix elements can be found in [Ell86]. The order of these diagrams is $\mathcal{O}(\alpha_s^4)$.

For the real corrections one has to take into account that the final state now contains three particles and the phase space element $d\Omega$ has to be mod-

ified accordingly. From (2.17) one gets:

$$d\Omega^{(3)} = \int (2\pi)^d \prod_{a=1}^{3} \delta^d \left(p_i + p_j - \sum_{b=1}^{3} p_b \right) \frac{\delta(p_a^2)}{(2\pi)^{d-1}} d^d p_a. \tag{2.26}$$

The generic diagrams for the direct, real corrections are shown in Fig. 2.14. There are two different mechanisms for the real corrections of the QCD

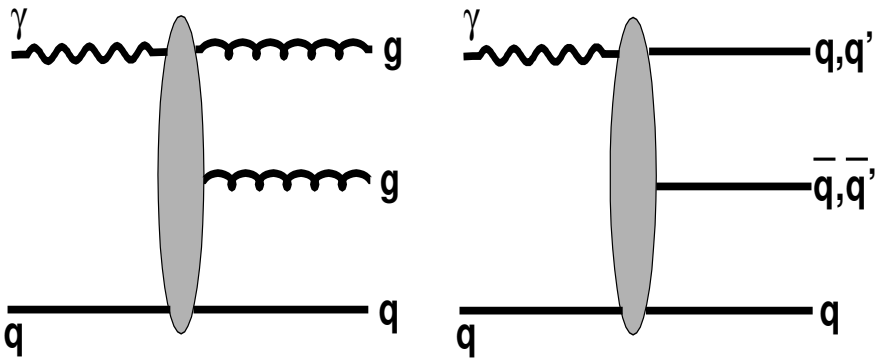

Figure 2.14: Generic diagrams for the real corrections in direct interactions.

Compton effect. Either, a gluon is radiated from the quark or the gluon leading to the left diagram of Fig. 2.14 or a quark-anti-quark pair is emitted by a gluon as depicted in the right diagram. Diagrams for incoming gluons or anti-quarks can be obtained as usual by crossing a final quark or gluon line with the incoming quark line. The matrix elements can be found in [Kla98]. The order of these matrix elements (squared) is again $\mathcal{O}(\alpha_{em}\alpha_s^3)$.

The generic diagrams of the real corrections for the resolved processes are shown in Fig. 2.15. The gluon initiated processes with quarks in the final state are obtained by crossing one or two gluon lines into the initial state. Processes with incoming anti-quarks are obtained by crossing an incoming and an outgoing quark line. The resulting matrix elements can be found in [Kla98, Ell86]. The order of the squared matrix elements is $\mathcal{O}(\alpha_s^4)$.

2.5.3 Order of the Electron-Proton Cross Section

To summerize: leading order direct contributions are of $\mathcal{O}(\alpha_{em}\alpha_s)$ while the leading order resolved contributions are of $\mathcal{O}(\alpha_s^2)$. The next-to-leading order virtual corrections of the direct contributions are of $\mathcal{O}(\alpha_{em}\alpha_s^3)$ while for the resolved contributions one gets an $\mathcal{O}(\alpha_s^4)$ and the same holds true for the

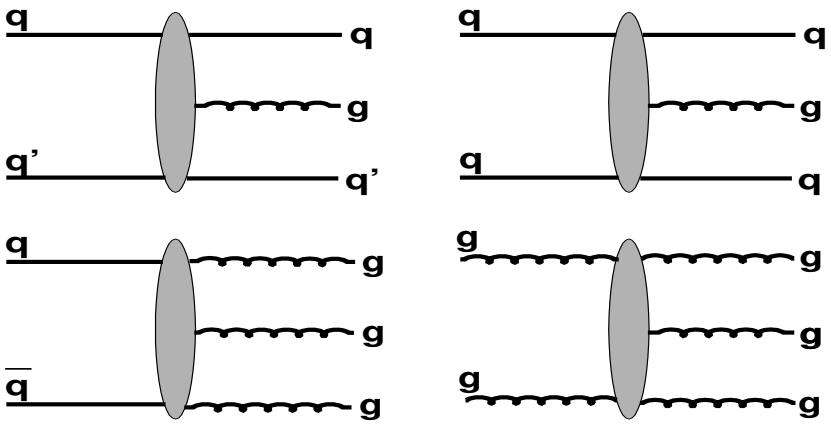

Figure 2.15: Generic diagrams for the real corrections in resolved interactions.

real corrections. But what are now the leading and next-to-leading orders of the "total" electron-hadron cross section? First it must be noted that the resolved contributions now have to be multiplied by the photon-PDF what introduces an additional order $\mathcal{O}(\alpha_{em}/\alpha_s)$. For this reason the resolved contributions are of the same order as the corresponding direct contributions: leading order direct and resolved contributions are of $\mathcal{O}(\alpha_{em}\alpha_s)$ and in next-to-leading order for both virtual and real corrections they are of $\mathcal{O}(\alpha_{em}\alpha_s^3)$. To get the electron-hadron cross section, one has to add all contributions and square them. This yields:

$$\begin{aligned} \mathcal{O}(d\sigma_{ep}) &= |\sqrt{\alpha_{em}\alpha_s} + \sqrt{\alpha_{em}\alpha_s^3}|^2 \\ \mathcal{O}(d\sigma_{ep}) &= \alpha_{em}\alpha_s + 2\alpha_{em}\alpha_s^2 + \mathcal{O}(\alpha_{em}\alpha_s^3). \end{aligned} \tag{2.27}$$

So the leading order contributions to $d\sigma_{ep}$ are of $\mathcal{O}(\alpha_{em}/\alpha_s)$ stemming directly from the leading order terms of the hard scattering cross section $d\sigma_{ij}$ while the next-to-leading order contributions are of $\mathcal{O}(\alpha_{em}\alpha_s^2)$ due to the interference of the leading and next-to-leading order contribution of $d\sigma_{ij}$.

Finally one word about the involved scales. An actual calculation contains two scales, the factorization scale μ_F and the renormalization scale μ_R. To specify the actual values one usually sets $\mu_F^2 = \mu_R^2 = \mu^2$ and e.g. $\mu^2 = p_T^2$, where p_T^2 is the highest transverse momentum that appears in the hard interaction.

2.6 Fragmentation

The calculations of a scattering cross section outlined so far are not really complete. It was, at least in principle, shown how a differential cross section is calculated where a photon or a parton from the fluctuating photon interacts with a parton from the proton yielding again partons in the final state. However, free quarks or anti-quarks have yet not been observed in nature. Theoretically, the mechanism of confinement (see the previous chapter) forbids the existence of free quarks at large distances. So as the quark and anti-quark are moving away from each other due to confinement something must happen to them that leads to the variety of hadrons which are actually detected and measured in an experiment. This process where hadrons are formed from one initializing quark is called *fragmentation*.

In an actual calculation the fragmentation, is handled via so called "fragmentation functions". If $z = \frac{E_h}{E_q}$ is the fraction of energy a created hadron of type h carries with respect to the initial parton energy (E_q) then the fragmentation function $D_q^h(z, Q^2)$ is the number of hadrons of type h created from parton q per energy fraction range dz. Energy conservation requires the normalization:

$$\sum_{allh} \int_0^1 z D_q^h(z, Q^2) dz = 1. \tag{2.28}$$

The cross section with hadrons in the final state is then obtained from the cross section with partons in the final state by multiplying the latter one with an appropriate sum of fragmentation functions. This may be illustrated for the case of electron–positron annihilation [Fie89]:

For the partonic differential cross section with respect to z one has:

$$d\sigma(e^+e^- \to q\bar{q}) = 3\frac{4\pi}{3}\frac{\alpha_{em}^2}{Q^2} e_q^2 \, dz, \tag{2.29}$$

where e_q^2 is the electric charge of quark q. For the hadronic differential cross section with a hadron h in the final state one gets from (2.29):

$$d\sigma(e^+e^- \to h + X) = 3\frac{4\pi}{3}\frac{\alpha_{em}^2}{Q^2} \sum_{i=1}^{n_f} e_{q_i}^2 \left(D_{q_i}^h(z, Q^2) + D_{\bar{q}_i}^h(z, Q^2) \right) dz. \tag{2.30}$$

Clearly, n_f is again the number of available flavors and X is some hadronic remnant because an inclusive cross section is concerned here. The problem now consists of finding expressions for the fragmentation functions. One difficulty lies in the fact that fragmentation is a long distance process and can therefore not be treated by perturbation theory; it is a non-perturbative process. Another point is that up to now it is not finally understood how

fragmentation really proceeds in nature so that there are several different models currently in use to explain fragmentation and to obtain expressions for the fragmentation functions. Three of these models shall now be considered more closely: the independent quark model, the string fragmentation model and the cluster model.

2.6.1 The Independent Quark Model

The independent quark model (also called FF[5] parameterization) assumes that fragmentation and therefore also quark jets can be analyzed on the basis of a recursive principle, see [Fie78, Fie89]. The idea behind this ansatz is that an initial quark of some flavor "a" produces a color field when it moves away from the corresponding anti-quark (see also Fig. 2.16). In this color field new quark/anti-quark pairs are produced. The quark "a" then combines with an anti-quark of such a new produced pair, say "$b\bar{b}$", to form a new meson "$a\bar{b}$". The remaining quark "b" then combines with an anti-quark of another pair etc. In this way a hierarchy of mesons is formed. The meson "$a\bar{b}$" is of rank 1 the meson "$b\bar{c}$" of rank 2 etc. Each new meson formation starts with the residual energy of the preceding meson formation so the whole chain of meson production stops when the energy becomes too low for further particle production.

In this model it is assumed that the resulting fragmentation functions scale, that means they depend only on the dimensionless energy fraction z and not on Q^2 ($D_q^h(z, Q^2) \rightarrow D_q^h(z)$). Another assumption of this model is that all partons emerging in an event fragment independently (hence the name of the model). This leads to inconsistencies like violation of energy and momentum conservation which have to be cured by hand.

2.6.2 The String Fragmentation Model

The string fragmentation model [And86, And98, Art74, Bow81] is similar to the independent quark model. It bases on the so called "Lund model". In the view of this model a color field is established between the quark and the anti-quark giving rise to a *constant, attractive* force that binds them together and clearly leads to a potential energy of the system linear in the particles separation. The color field is of course made up of gluons which mediates the interaction between the quark and its anti partner. But, as outlined in chapter 1, QCD is a non-abelian field theory what shows up in the fact that the gluons not only interact with the quarks and anti-quarks but also

[5] FF stands for the authors Field and Feynman.

among each other. A resultant effect is that the color field between the quark and the anti-quark is restricted to a narrow string like region between these two particles so that at the endpoints (the two particles) there is no color field present anymore. The whole string is not a static object. Because of the attractive force acting on the particles it rather exhibits an oscillatory motion. May for instance at the beginning the particles move outwards, say the quark to the left and the anti-quark to the right. Then by the action of the attractive force the particles are decelerated and their kinetic energy is transferred to the color field. At some point the motion stops and then the force pulls the particles back, against each other, so the quark is now moving to the right while the anti-quark is moving to the left, see Fig.2.17. Due to the action of the force the particles are accelerated gaining kinetic energy from the color field. They then pass moving outwards again until their motion is stopped and turned around by the color force another time, etc. Because of this oscillatory motion in the language of the Lund model such a hadron or hadron state is called a "yoyo hadron" or "yoyo state", respectively. It was also shown that the energy of the string on the average over one period of oscillation is distributed between quarks and color field in a way that half of the energy is carried by the color field.

A quark/anti-quark pair created in a hard scattering process will in general contain such an amount of energy that the resultant string does not correspond to a stable hadron state. Such an unstable string will decay. Inside the color field a new quark/anti-quark pair is created where this process used up all the color fields energy in the vicinity of these particles to produce them. So between these newly created particles there is no color field present and in this way these particles form the endpoints of two new strings that is, the original string decays into two new ones, see Fig.2.18. In this way confinement enters the model. The decay mechanism yields only new strings but no free quarks or anti-quarks. These new strings can of course themself contain too much energy to form a stable hadron and decay in further strings. This process then continues until all created hadrons are stable. The fragmentation functions obtained from the string model show the same scaling behavior as those from independent quark fragmentation, that is, these functions depend on z only. Furthermore the string fragmentation can be formulated in a covariant way so it does not suffer from the shortcomings mentioned in connection with the independent quark fragmentation. In a more refined consideration as the one outlined above also quantum mechanical interference effects in gluon radiation are taken into account. As pointed out above, color charges are only appearing as endpoints of a string. So a gluon as it carries two color charges must be the endpoint of two strings showing up as a kink in the color string connecting the quark and the anti-quark.

Due to destructive gluon interference the radiation of a gluon and therefore hadron production in the region opposite to the gluon is suppressed. This occurs naturally because in the framework of the Lund model there can not be an additional direct string connection between the endpoint quarks in a $qg\bar{q}$ configuration.

2.6.3 The Cluster Fragmentation Model

In the cluster fragmentation model [Fie83, Web84] the hadronization process starts with a parton shower cascade. The quark and anti-quark emerging from the hard process radiate gluons which decays into further quark/anti-quark pairs which again emit gluons etc. It is now assumed that at the point where the energy of the gluons is so low that the process could not be treated perturbatively anymore, all gluons are converted into quark/anti-quark pairs. A further assumption is that the created quarks develop color strings with a corresponding anti-partner to form color neutral objects called clusters (see Fig.2.19) which can be thought to be exited meson states (resonances). From this "preconfinement phase" [Ama79, Bas79, Mar80] hadrons are created by decay of these clusters. If the cluster mass is small only a few number of parameters is needed to describe the decay. However, in the case of large mass clusters, quantum interference must be taken into account to forbid the formation of not allowed hadrons. Large mass clusters split longitudinally similar to the Lund string model before they decay into final hadrons.

2.7 Photon Structure in Next-to-Leading Order QCD and its Q^2 Dependence

Considering higher orders in perturbative QCD, the notation of photon structure ceases to be a well defined concept. Actually only in leading order perturbative QCD the term photon structure is unambiguously defined. In higher orders and so already in next-to-leading order this concept becomes arbitrary. This is illustrated in Fig. 2.20. A diagram is shown as it contributes to the matrix element when next-to-leading order corrections are taken into account (see also Figs. 2.14, 2.15). However, whether to speak of a direct or a resolved interaction depends on what one considers to be the hard part of the interaction. If in Fig. 2.20 a) the part included in the dashed rectangle is the hard interaction then it is clearly a leading order direct process and the quark q' is considered to belong to the proton structure. But if on the other hand the part included in the dotted rectangle denotes the hard interaction then it is a leading order resolved process and the anti-quark $\bar{q}$

belongs to the photon structure. In Fig. 2.20 b) all outgoing partons are considered to be involved in the hard interaction so the diagram is due to a next-to-leading order direct process. So already in a theoretical description up to next-to-leading order corrections, a clear distinction between direct and resolved processes cannot be done anymore. A next-to-leading order direct process can equally well be considered as a leading order resolved process. So the question arises whether a hadronic photon structure provided by an additional parton density function for the photon is still necessary when next-to-leading order corrections are included.

Another question arises from the fact that the hadronic structure of the photon dies out with increasing virtuality. As was shown at the end of the last chapter the perturbatively treatable part of the photon structure decreases like $\sim \ln \frac{\mu^2}{Q^2}$ while the part which cannot be treated in perturbation theory decreases like $\sim \frac{1}{Q^4}$. So one can ask for the virtuality from which on photon structure is not necessary anymore. Of course, due to the ambiguity just cited above, including the next-to-leading order contributions one always has some photon structure present, so the question here is more precisely up to which virtuality an additional photon structure provided by a parton density function for the photon is needed.

To study these questions inclusive dijet differential cross sections measured with the ZEUS experiment at the electron-proton collider HERA[6] in different ranges of the photon virtuality Q^2 have been investigated. To allow a simple interpretation of the data, only simple differential cross sections have been used, namely: $d\sigma/dQ^2$, $d^2\sigma/dQ^2dE_{T1}$, $d^2\sigma/dQ^2d\eta_{for}$ and $d^2\sigma/dQ^2dx_\gamma^{obs}$. Here E_{T1} is the transverse energy of the most energetic jet and $\eta_{for} = \max(\eta_1, \eta_2)$ where 1 and 2 denotes the two jets with the highest energy[7]. To remove the kinematics from the scattering of the electron, the cross sections have been measured in the **H**adronic **C**enter of **M**ass (HCM) frame of reference what is actually the center-of-mass frame of the photon-proton system. In this way most of the momentum and energy flow transverse to the line connecting the incoming photon and proton is due to the QCD processes and is not obscured by an additional transverse momentum/energy flow compensating that from the scattered electron. The results of the measurements are then compared to theoretical calculations in next-to-leading order QCD as provided by the program JetViP described in a later chapter. Up to the time of this writing it is the only program available that includes a hadronic photon structure via a parton density function for the photon. The

[6]See next chapter for a detailed description of the experimental setup.

[7]The quantities E_T and η and the notion "jet" are explained in detail in chapters 4 and 5.

result of the comparison is presented in the last chapter.

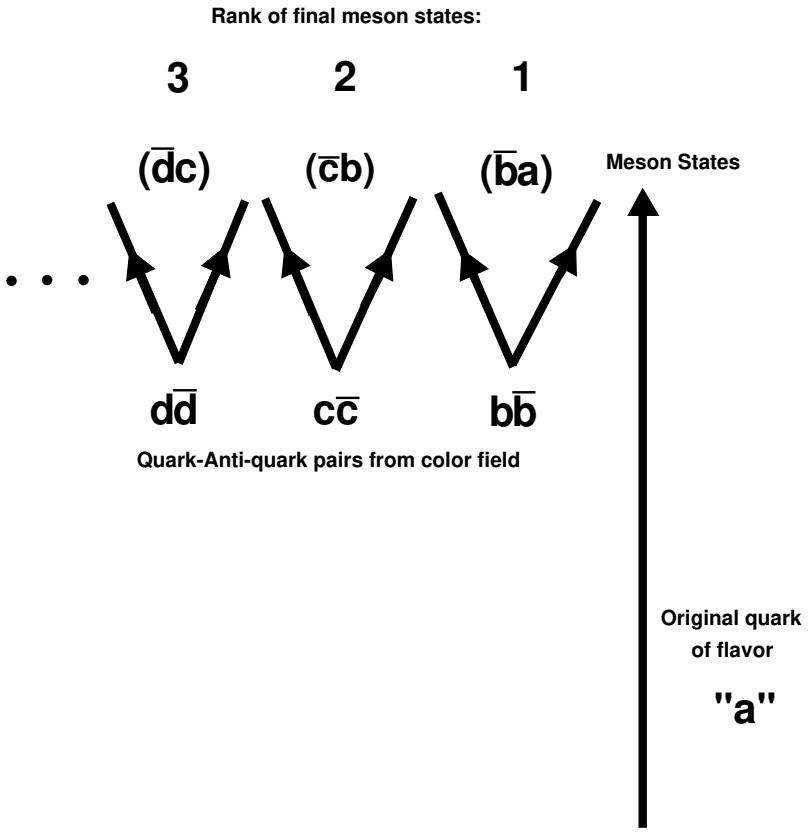

Figure 2.16: Mechanism of the independent fragmentation model. A quark of flavor "a" produces a color field with its corresponding anti partner from which other quark/anti-quark pairs emerge. Quark "a" now combines with an anti-quark from such a pair ("$b\bar{b}$") to form a new meson (of rank 1). The remaining quark "b" then forms a meson of rank 2 from another quark/anti-quark etc.

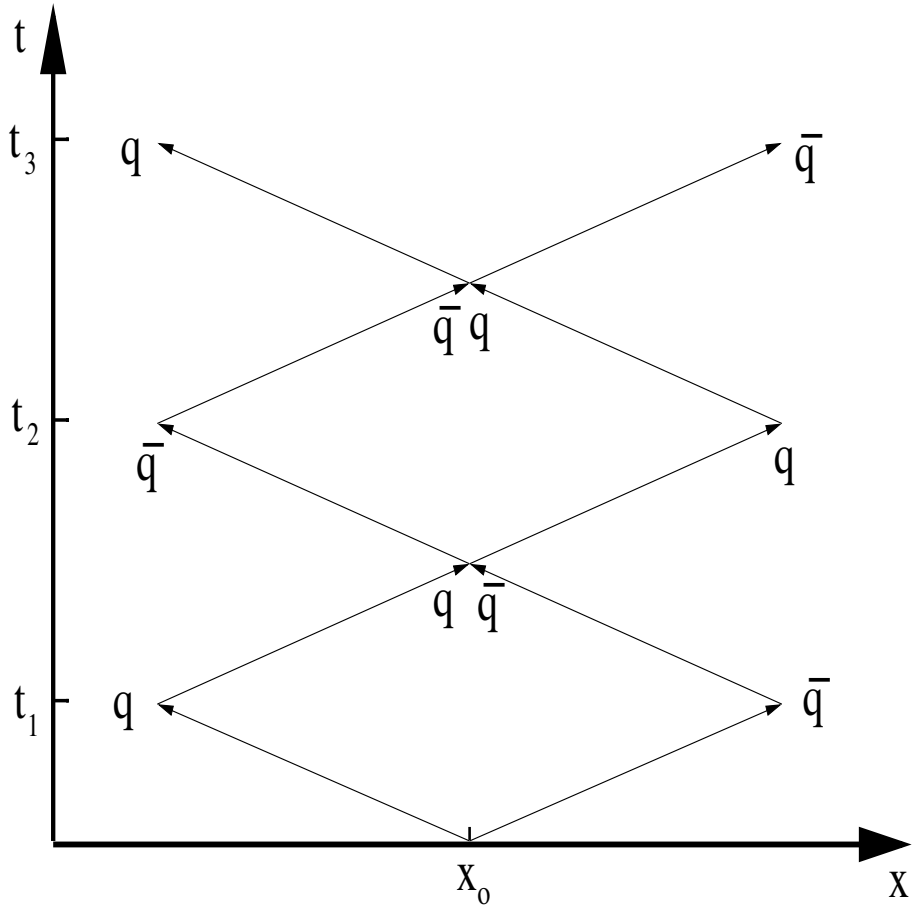

Figure 2.17: Oscillatory mode of the Lund yoyo hadron. The quark/anti-quark starts to separate at x_0. At the time t_1 the constant attractive force stops a further separation and the particles turn around and move back. At time t_2 they reached an opposite configuration compared to t_1. The color force pulls them back again so that at t_3 the accomplished one cycle viewed from the configuration at t_1.

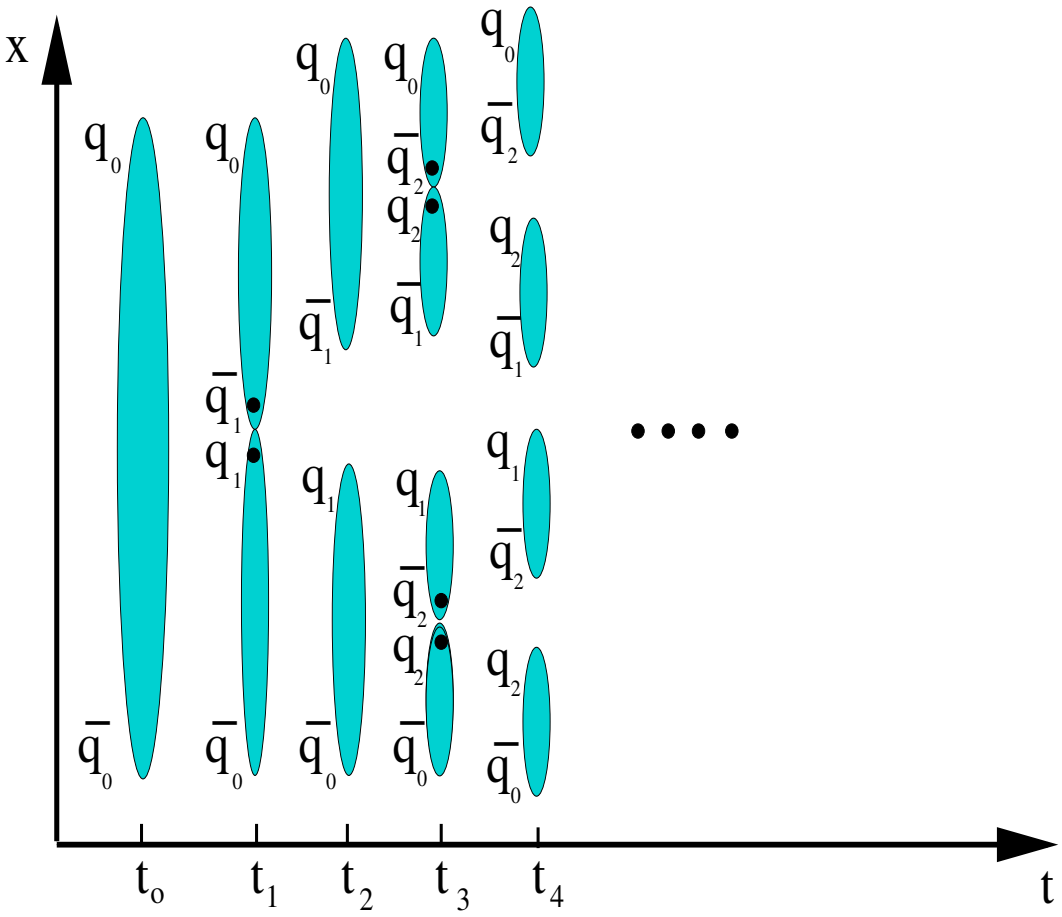

Figure 2.18: Starting from the initial configuration at t_0 a new $q\bar{q}$ pair is created at time t_1. The original string then decays into two strings at t_2. At t_3 these two new strings creates new $q\bar{q}$ pairs what leads to there decay at t_4, etc. This process proceeds until the energy of each string allows no further decay.

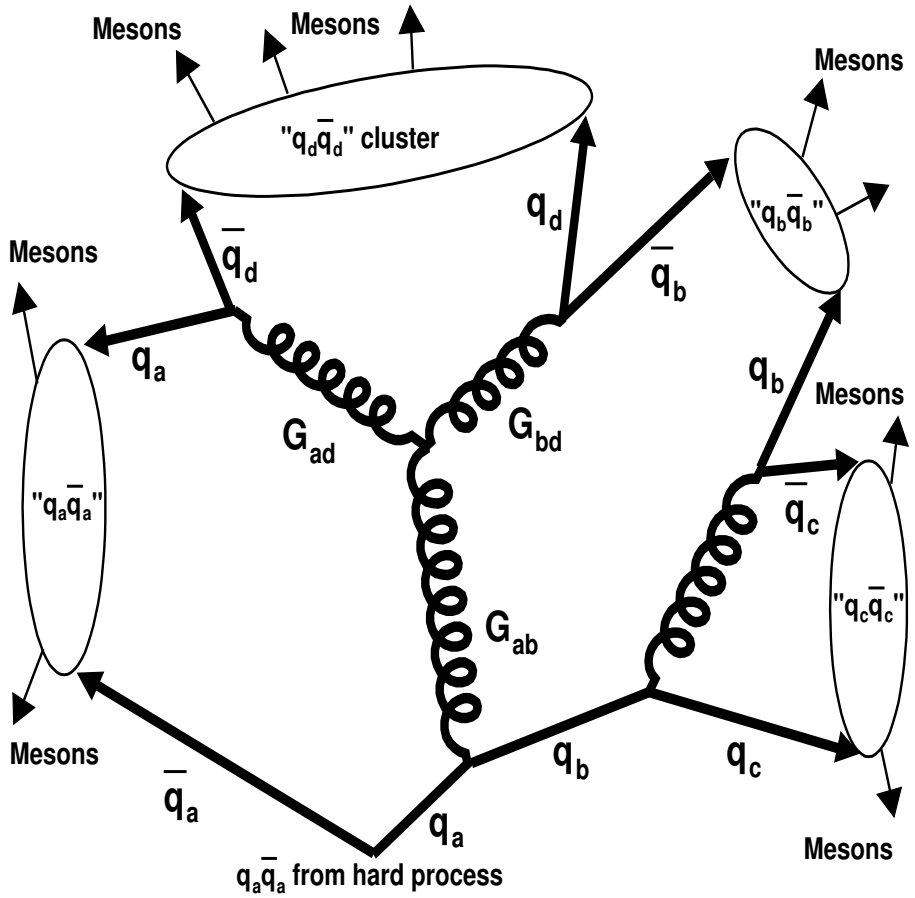

Figure 2.19: Schematic illustration of cluster fragmentation. The $q_a\bar{q}_a$ pair from the hard scattering process emits gluons which in turn decay into new $q\bar{q}$ pairs. The indices denote the spinor color. The pairs then combine to color neutral clusters which in turn decay into mesons.

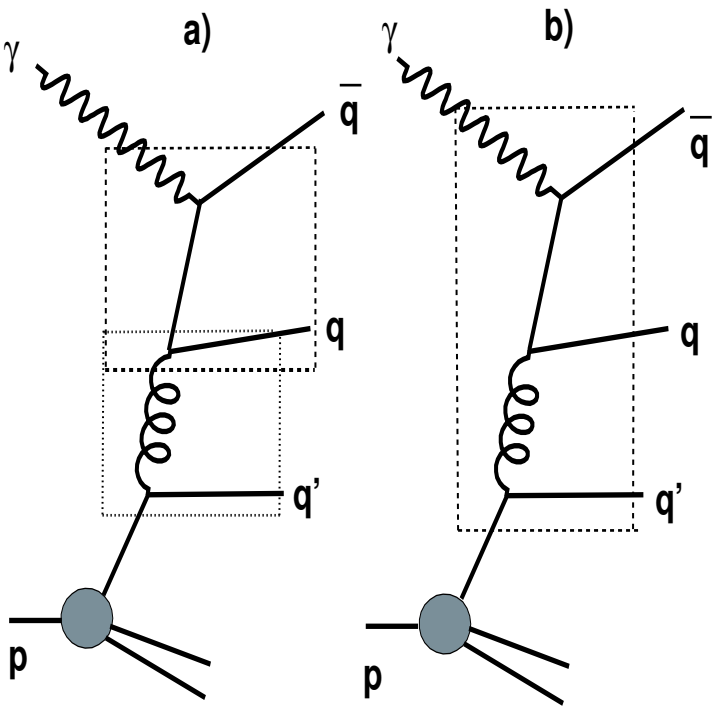

Figure 2.20: Figure to illustrate the ambiguous notion of photon structure when next-to-leading order corrections are included. In a) a leading order direct (resolved) interaction is shown when the process in the dashed (dotted) rectangle denotes the hard part of the interaction. In b) the same diagram is shown but this time it corresponds to a next-to-leading order direct interaction when the process in the rectangle denotes the hard interaction.

Chapter 3

Experimental Setup

3.1 HERA

HERA, (shorthand form for **H**adronen-**E**lektronen- **R**ing-**A**nlage) was designed to investigate the structure of the proton by means of electron-proton (ep) collisions. Up today, it is the only facility of this kind in the world. HERA was approved in 1984 and first collisions were observed in 1991. Fig. 3.1 shows an aerial view of the DESY area in Hamburg/Bahrenfeld. The two largest accelerator facilities PETRA and HERA are shown as dashed circles. Also the four halls taking up the experiments are indicated.

HERA actually consists of two storage rings. One for electrons and one for protons. The design energy for the electrons is 30 GeV and for the protons 820 GeV. Each of these storage rings consists of four 90° arcs connected by 360 m long straight sections. The HERA tunnel is located 10 m – 25 m below ground. To focus the protons and keep them on the circular path, high magnetic field strengths are necessary due to the high mass of the protons. Therefore superconducting magnets are used for the proton storage ring. The four experimental halls are situated in the middle of the straight sections. There are two collider experiments, H1 and ZEUS, which are located in the northern and southern halls respectively. For these experiments the electron and the proton beam are brought to collision in such a way that in the interaction regions of the respective experiments electrons and protons collide head-on at zero crossing angle. Two further experiments have been installed at HERA. Both are fixed-target experiments making use of only the electron beam or the proton beam respectively. HERMES [HER93] is located in the eastern hall and investigates the spin structure of the proton by scattering polarized electrons off a hydrogen target. The aim of HERA-B [HEB94] on the other hand was to study the $\mathcal{CP}$-violation in the $B^\circ\bar{B}^\circ$- system. This

Figure 3.1: Aerial view of DESY, showing the colliders PETRA and HERA.

experiment is located in the western hall and uses the halo region of the proton beam where the protons interact with a wire target to produce the desired B-mesons. Fig.3.2 shows an overview of the HERA collider layout (left figure). The right figure shows the system of pre-accelerators at DESY.

In a first step the electrons and protons are accelerated using linear accelerators. In Fig. 3.2 they are denoted by 'Elektronen-Linac', 'Positronen-Linac' and 'H^--Linac', respectively. The pre-accelerated electrons (positrons) are accumulated in a small storage ring PIA (**P**ositron-**I**ntesity-**A**ccumulator) until sufficient intensity is reached. In a next step, the electrons (positrons) are injected into DESY II, while the protons are injected into DESY III, where they are further accelerated. The pre-acceleration process is accomplished by injecting the electrons (positrons) and protons into PETRA for further acceleration. In the last step the particles are injected into HERA and are accelerated to their final energies.

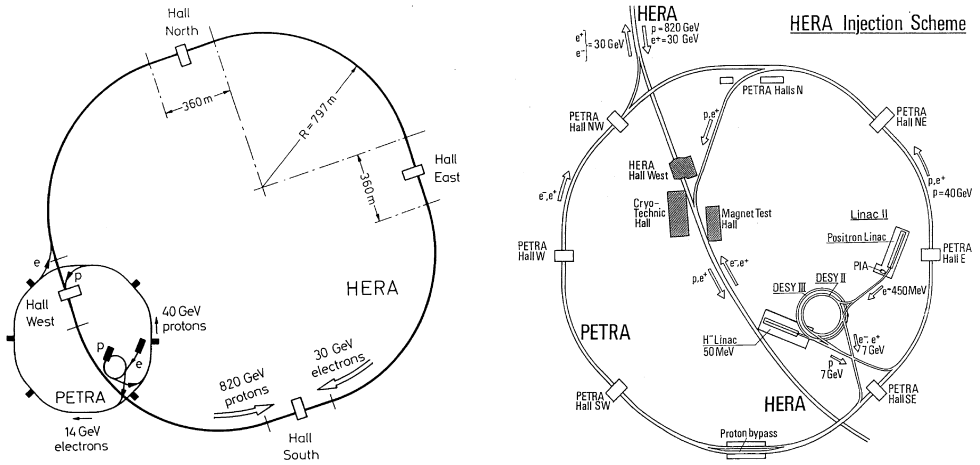

Figure 3.2: The HERA accelerator complex. The left figure shows the layout of HERA, while the right figure displays the system of pre-accelerators. In the four experimental halls the following experiments are installed: ZEUS in the South hall, H1 in the North hall, HERA-B in the West hall and HERMES in the East hall.

From 1995 to 1997 positrons were used instead of electrons. The reason were severe lifetime problems of the electron beam. These are most likely due to capturing of positively charged dust which originates from ion getter pumps from the HERA electron vacuum system by the electron beam [DES94]. With the installation of new pumps during the winter shutdown 1997/1998 the problem has significantly reduced and HERA was able to switch back to electrons in 1998. A compilation of several HERA parameters and the corresponding design values (status 1996/97 where the data used in this analysis were taken) can be found in Tab. 3.1.

3.2 The ZEUS Experiment

The ZEUS detector is a hybrid, general purpose detector whose components are designed to study the various aspects of hadrons and leptons emerging from ep-interactions. It went into operation in 1992. The energy, direction and type of the produced particles are measured with high precision. The coordinate system of the ZEUS detector is a right-handed Cartesian system with its axis defined by the central tracking detector (see below). The origin of this system is located at the nominal interaction point. The Z-axis points in the direction of the proton beam, the X-axis horizontally towards the center of HERA and the Y-axis points upwards perpendicular to the XZ-plane. The

HERA parameters	Design Values		Values of 1997	
	$e^{\pm}$	p	e^{+}	p
Circumference (m)	6336			
Energy (GeV)	30	820	27.6	821.2
Center-of-mass energy (GeV)	314		301	
Injection energy (GeV)	14	40	12	40
Energy loss per turn (MeV)	127	$1.4 \cdot 10^{-10}$	127	$1.4 \cdot 10^{-10}$
Current (mA)	58	160	36	78
Magnetic field (T)	0.165	4.65	0.165	4.65
Number of bunches	210	210	174+15	174+6
Bunch crossing time (ns)	96			
Horizontal beam size (mm)	0.301	0.276	0.2	0.2
Vertical beam size (mm)	0.067	0.087	0.054	0.054
Longitudinal beam size (mm)	0.8	11	0.8	11
Specific luminosity ($cm^{-2}s^{-1}mA^{-2}$)	$3.6 \cdot 10^{29}$		$5.0 \cdot 10^{29}$	
Instantaneous luminosity ($cm^{-2}s^{-1}$)	$1.6 \cdot 10^{31}$		$1.45 \cdot 10^{31}$	
Integrated luminosity per year (pb^{-1}/a)	35		36.5	

Table 3.1: HERA parameters and design values. In 1997 HERA operated with 174 colliding bunches, 15 positron-pilot bunches and 6 proton-pilot bunches.

polar angle (θ) is determined relative to the Z-axis, while the azimuth angle (ϕ) is determined relative to the X-axis. With this definition of the polar angle it follows for the incoming electron beam that $\theta = 180°$ while for the incoming proton beam $\theta = 0°$. The +Z-direction is defined as the *forward*, the –Z-direction as the *backward* direction. ZEUS can be divided into main detectors, located around the nominal interaction point and several small detectors located along the beam pipe in forward as well as in backward direction. Fig. 3.3 shows the main parts along the beam pipe while Fig. 3.4 depicts a view perpendicular to the beam direction. The center-of-mass of the incoming *ep* system is moving in the forward direction relative to the laboratory-frame. This is due to the energy difference of the electron (27.5 GeV) and the proton (820 GeV). The design of ZEUS is therefore asymmetric with respect to the Z-axis because of the resulting large forward-backward asymmetry of the *ep* final state system.

In the following only those components are described in some detail which are used in this analysis. For further details and a description of the remaining components see [Hol93] and the references cited below.

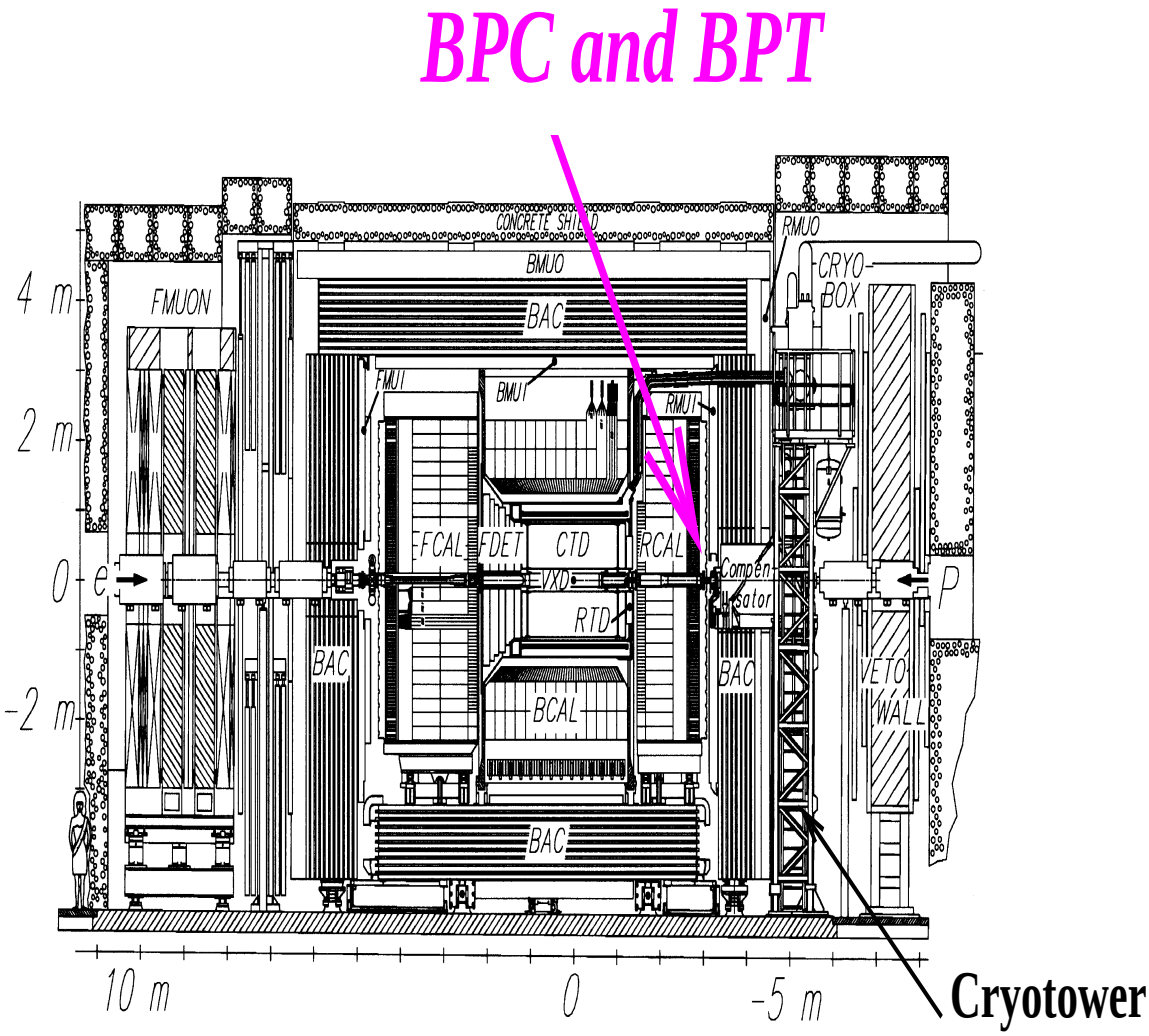

Figure 3.3: The main components of the ZEUS detector along the beam pipe. See text for description of the components.

3.2.1 The Central Tracking Detector

The **C**entral-**T**racking **D**etector (CTD) is a cylindrical drift chamber [Fos93]. It is enclosed by a superconducting solenoid which produces an axial magnetic field of 1.43 T, see Fig. 3.3. It provides a high precision measurement of the location and the direction of the paths of charged particles as well as the determination of the primary event vertex, that is the actual interaction point, with high precision. The CTD covers a polar angle of $15° < \theta < 164°$

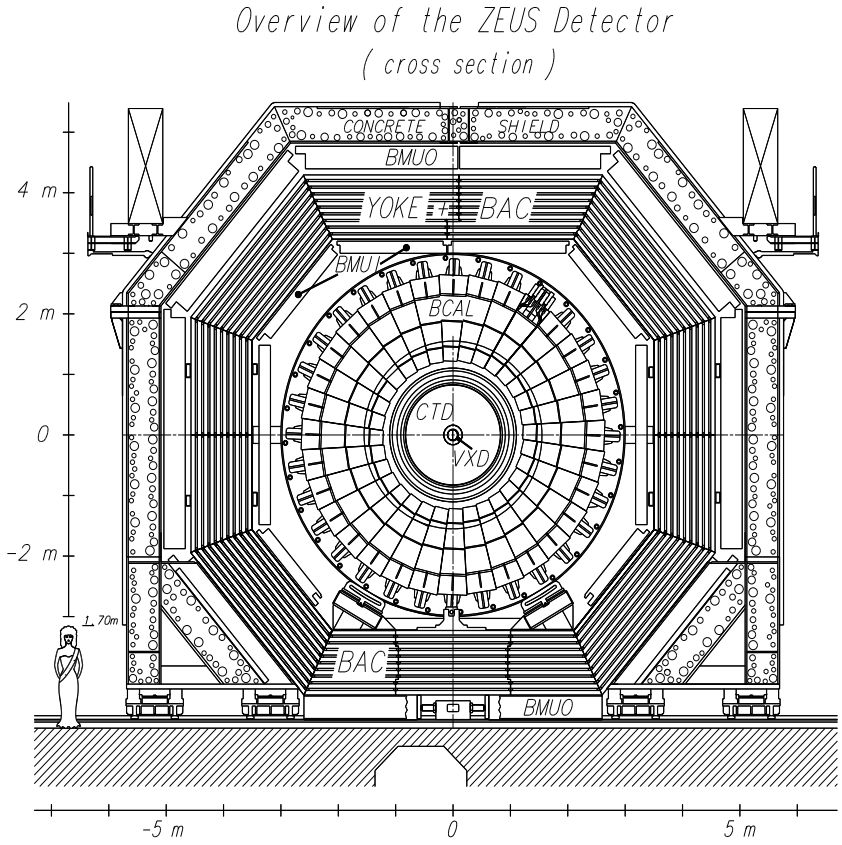

Figure 3.4: The main components of the ZEUS detector perpendicular to the beam direction. See text for description of the components (the vertex detector (VXD) was removed in 1995).

corresponding to a range in pseudorapidity (for a definition of this quantity see chapter 4) of $2.04 < \eta < -1.96$ and the full range in the azimuthal angle ϕ. Its active volume has a length of 205 cm, an inner radius of 18.2 cm and an outer radius of 79.4 cm. It operates with a gas mixture consisting of 83% Ar, 5% CO_2 and 12% C_2O_6. The CTD is designed as multi-cell superlayer chamber and is subdivided into eight sections and nine superlayers. Fig. 3.5 shows one of its octants. The CTD consists of 576 cells. Each cell is equipped with eight sense wires. A total of 24192 field wires are installed. The number of cells increases from 32 in the innermost layer up to 96 cells for the outermost layer. Of the nine superlayers the five odd-numbered axial layers have their sense wires parallel to the beam axis while the remaining four have sense wires declined by $\sim 5^\circ$ with respect to the beam axis (see also Fig. 3.5). The position resolution of the CTD in the r–ϕ plane is about 230

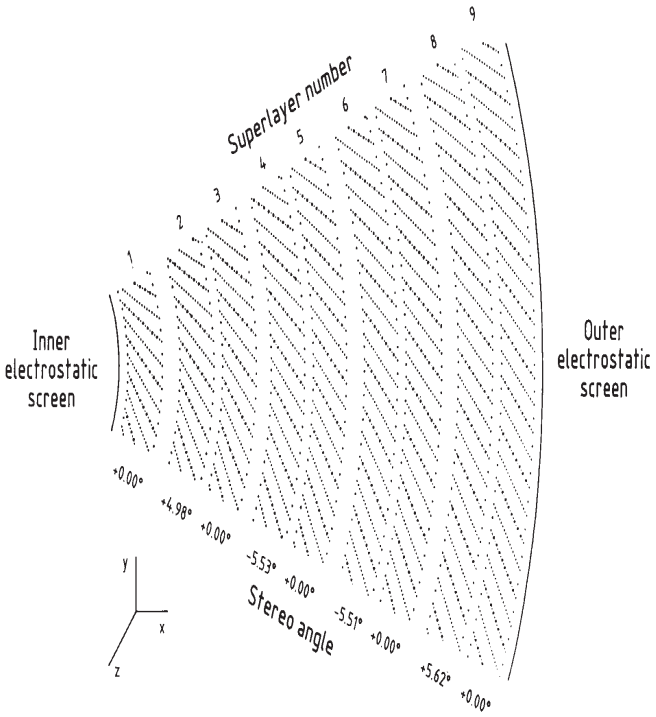

Figure 3.5: Layout of a CTD octant, each octant has nine superlayers. The even numbered layers are declined with respect to the beam axis ('Stereo angle'). The angles for each superlayers are also shown.

μm and the transverse momentum resolution is $\frac{\Delta p_t}{p_t} = 0.005 \cdot p_p/\mathrm{GeV} \oplus 0.0016$. The position of the interaction point in X and Y is measured with a resolution of 0.1 cm and in Z with a resolution of 0.4 cm. To provide additional means of track reconstruction in the forward as well as in the backward direction, the CTD was supplemented by the FTD and RTD, respectively. The **F**orward-**T**racking-**D**etector (FTD) consists of three sets of planar drift chambers with a **T**ransition-**R**adiation- **D**etector (TRD) in between. The **R**ear-**T**racking-**D**etector (RTD) is one planar drift chamber with three layers.

3.2.2 The Uranium Calorimeter

The ZEUS **U**ranium **CAL**orimeter (UCAL) is a high resolution compensating sampling calorimeter. Its response to electrons and hadrons of equal energy is the same ($E_{elec}/E_{had} = 1.00 \pm 0.02$). It is divided into three parts to cover the widest possible range in the polar angle [And91, Der91, Ber93].

The forward calorimeter (FCAL) covers $2.2° < \theta < 39.9°$, the barrel calorimeter (BCAL) $36.7° < \theta < 128.1°$ and the rear calorimeter (RCAL) covers $128.1° < \theta < 176.5°$ (see Fig.3.3). In this way the UCAL covers $\sim$99.6% of the solid angle around the interaction point. All parts are built of alternating layers of 3.3 mm thick depleted uranium (^{238}U) and 2.6 mm thick plastic scintillator plates (SCSN38). Uranium was used as absorber medium to compensate energy losses due to breakup of nuclei, nuclear excitation and evaporating neutrons (and protons). These processes cannot be observed in a conventional calorimeter. The extra energy realesed by fast neutron and proton fission of ^{238}U makes up for these "invisible" energy losses (what also depends on the appropriate choice of the relation between absorber and "active" scintillator material). Furthermore, the natural radioactivity of ^{238}U is used as reference to calibrate the readout channels to a precision of $< 0.2\%$. Each of the three calorimeter parts is subdivided into single modules. The modules themselfs are transversally separated into towers and the towers in turn longitudinally into electromagnetic (EMC) and hadronic (HAC) sections. The layout of an FCAL module is shown in Fig. 3.6. The FCAL and RCAL modules are planar and perpendicular to the beam axis (see Fig. 3.3) while the BCAL modules are wedge shaped and projective in the polar angle (see Fig. 3.4). The design of the three parts take the asymmetry of the electron and proton energies into account resulting from different particle densities and energies. The calorimeter modules are further segmented into cells. Each EMC section is divided transversally into four cells (two in the RCAL) while the HAC sections are not. Instead they are longitudinally subdivided into two (one in the RCAL) hadronic cells (HAC1, HAC2). Each cell is read out on opposite sides by two wavelength shifters. Each of these wavelength shifters in turn is connected to one photomultiplier tube. This information is used to provide a limited reconstruction of the position of the measured particle, to determine its total energy and to check the uniformity of the readout. In testbeam experiments the energy resolution for hadrons was found to be $\sigma_{\mathrm{h}}(\mathrm{E})/\mathrm{E} = 0.35/\sqrt{\mathrm{E/GeV}}$ that for the electrons $\sigma_{\mathrm{e}}(\mathrm{E})/\mathrm{E} = 0.18/\sqrt{\mathrm{E/GeV}}$ (see the references above).

3.2.3 The Presampler

Due to preshowering processes in dead material, particles reaching the calorimeter lose part of their energy. Predominantly electrons and positrons are affected by these processes. The presampler [Bam96] measures on an event by event basis this energy loss. The presampler consists of scintillator tiles which are mounted in front of the calorimeter modules and are read out

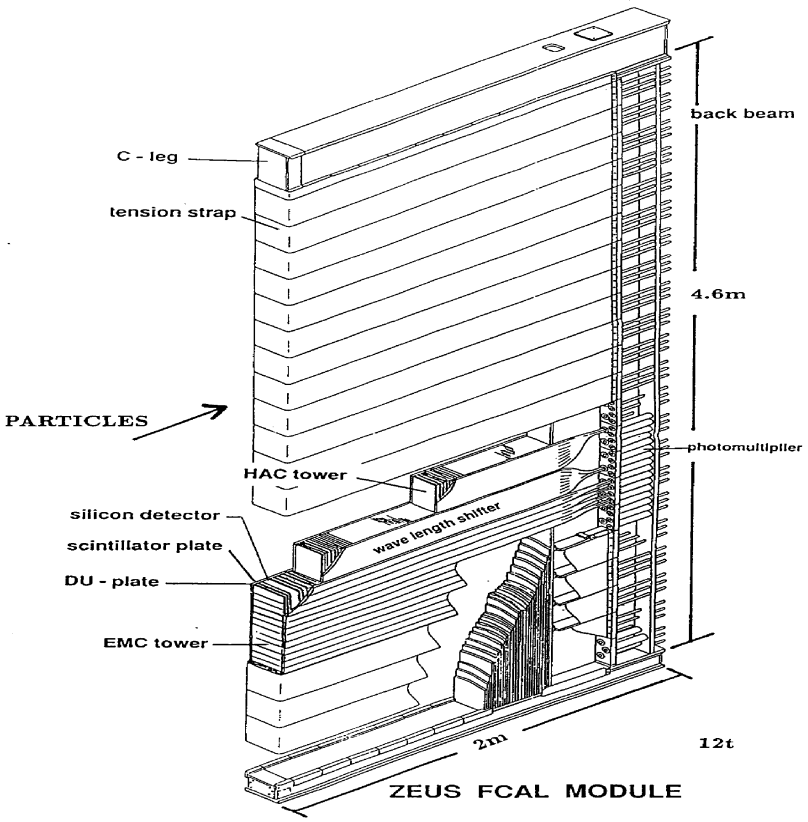

Figure 3.6: Layout of an FCAL module. The modules of the calorimeter are subdivided into EMC and HAC sections which in turn are divided into cells. A cell is read out on two opposite sides by one wavelength shifter each.

by wavelength shifters. 1995 the FCAL and the RCAL were equipped with those scintillator tiles. They cover a large fraction of the RCAL surface and have a size to match the HAC segmentation of 20 cm $\times$ 20 cm. Fig. 3.7 shows a front view of the RCAL. The shaded area shows the region covered by the presampler.

3.2.4 The Small Angle Rear Tracking Detector

The *S*mall angle **R**ear **T**racking **D**etector was built to provide additional measurements concerning different aspects of an event. Its main goals are [Bam95, Bam97]:

- Improve the measurement of the position and angle of elecrons and positrons, respectively, which have low Q^2 and are therefore scattered

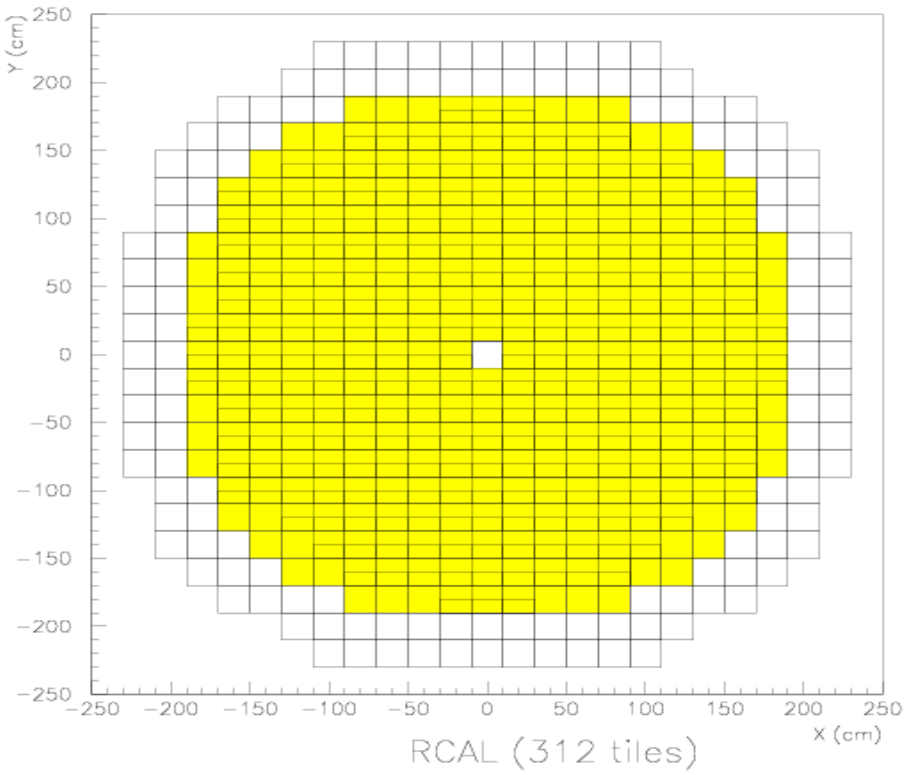

Figure 3.7: Front view of the RCAL. The shaded area is covered by the presampler.

under a small angle.

- Recognition of preshowering electrons (positrons) to provide the possibility to correct for energy loss in inactive material.
- Yielding timing information to allow rejection of upstream events from proton beam-gas interactions.

The SRTD is installed directly in front of the RCAL at a position Z = -147.95 cm (see Fig. 3.8). It consists of polystyrene scintillator strips (5 mm × 9.8 mm × 240/440 mm) arranged in two planes of four 24 cm × 44 cm quadrants

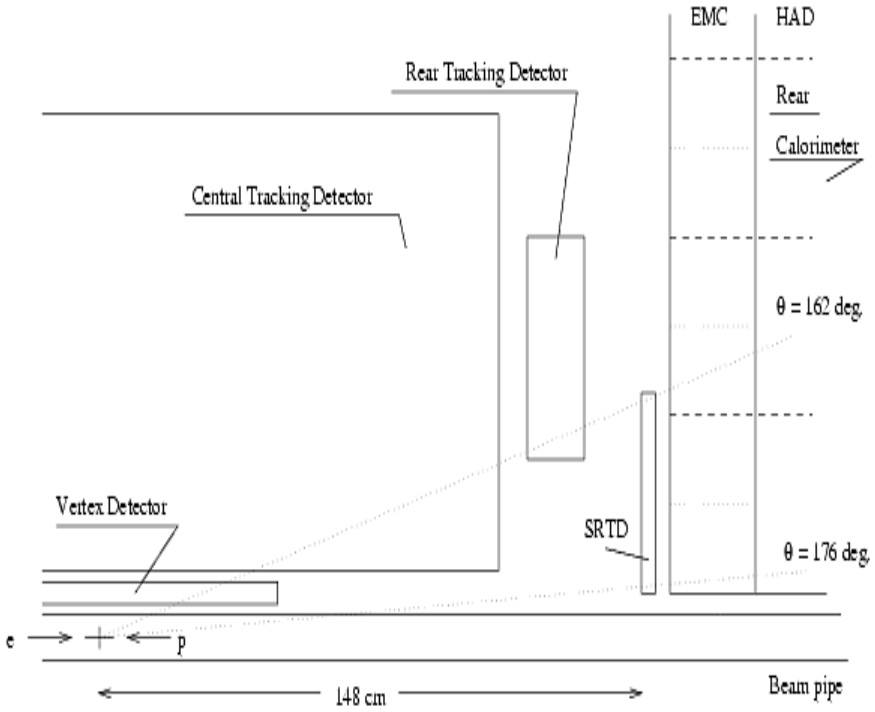

Figure 3.8: Location of the SRTD inside the ZEUS-detector. The distances are not to scale. The range in polar angle covered by the SRTD is shown by the dotted lines.

each as shown in Fig. 3.9. The strips are read out by photomultiplier tubes. The range in polar angle covered by the SRTD is $162° < \theta < 178°$. The 9.8 $\pm$ 0.05 mm wide strips allow for a position resolution of $\sim$3 mm. The timing resolution of the SRTD is 0.6 ns. There is a 10% uncertainty in the absolute energy scale of the SRTD which yields a total 1% uncertainty of the electron (positron) energy (see references above).

3.2.5 The Hadron-Electron Separator

As another means to improve the measurement of electrons and positrons, a **H**adron-**E**lectron **S**eparator (HES) was installed inside the RCAL and FCAL [HES91]. Isolated electrons can be identified cleanly by the electromagnetic and hadronic sections of the calorimeter. The aim of HES is to improve the identification particularly of electrons with high transverse momentum inside a jet. The HES consists of 28.9 $\times$ 30.5 mm^2 silicon diodes placed at a

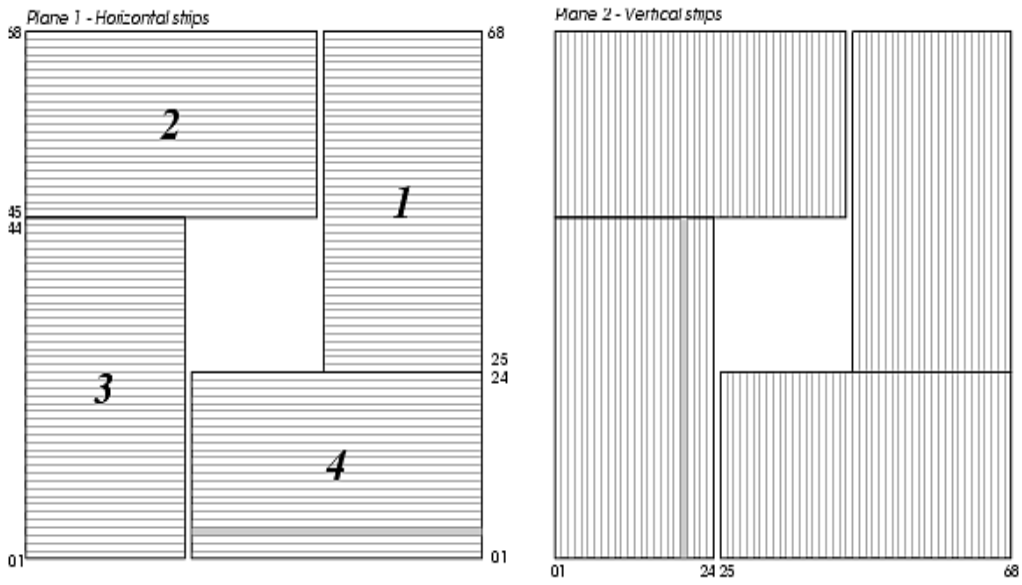

Figure 3.9: Orientation and numbering scheme of the strips of the SRTD. The quadrants 2 and 4 are separated by 8 cm.

longitudinal depth of 3.3 radiation lengths corresponding to the approximate maximum of the electromagnetic shower position. The separation between hadrons and electrons is based on the fact that hadrons have an interaction length which is ∼20 times larger than that of the electrons. So hadrons produce in average a smaller HES signal than the electrons. Because of the fine segmentation of HES it can also be used to improve the position resolution for electrons in the calorimeter. HES provides a spatial resolution of about 9 mm for a single diode hit. If more than one adjacent diodes are hit, they are clustered to at most 3 × 3 diodes around the most energetic diode what yields a further improved resolution of 5 mm.

3.2.6 The Beam Pipe Calorimeter

The purpose of the **B**eam **P**ipe **C**alorimeter (BPC) [Bre97] is to detect electrons (positrons) which are scattered under an angle less than 40 mrad with respect to the initial beam direction. These electrons emerge from *ep* interactions at low Q^2 ($Q^2 < 1$ GeV^2 and very low x ($x < 10^{-3}$). So this component plays a crucial role in the analysis presented in this thesis. The BPC was installed in the ZEUS detector in 1995. It is located close to the beam pipe at approximately Z = -2.5 m to Z = -3.2 m between the RCAL and the

compensator magnet, see Fig. 3.3. In 1997 the BPC was furnished with the **B**eam **P**ipe **T**racker (BPT), a lead tungstate ($PbWO_4$) tracker. Because this component is not used in this analysis, it is not further described here.

The BPC consists of two modules, located at Z = -293.7 cm on the right (BPC-South) and on the left side (BPC-North) of the beam pipe. Both modules are designed as segmented tungsten-scintillator modules. The design of the modules is shown in Fig. 3.10. The beam pipe was modified to include

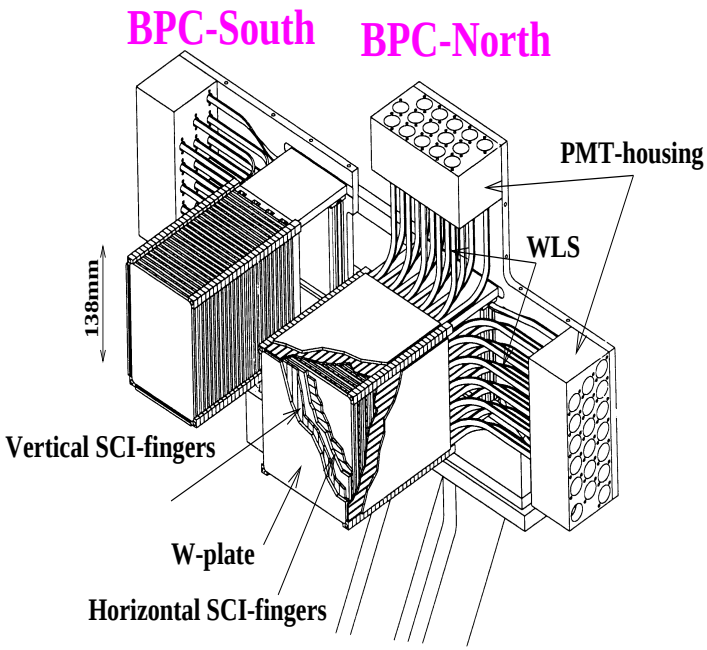

Figure 3.10: Drawing of the two BPC modules together with the wavelength shifters (WLS) and photomultiplier houses (PMT).

two exit windows at Z = -249.8 cm. The exit windows are made of 1.5 mm thick aluminum corresponding to 0.016 X_0[1] to allow the electrons to exit the beam pipe with minimal interference. The two modules and the modified beam pipe are shown in Fig. 3.11. The dimensions of the two BPC modules and the exit window are restricted by the surrounding RCAL

[1] X_0 denotes the "radiation length". It is actually the depth radiation can penetrate a medium up to which the intensity of the incident radiation (I_0) is decreased to I_0/e, where $e = 2.1728...$ is the Euler number.

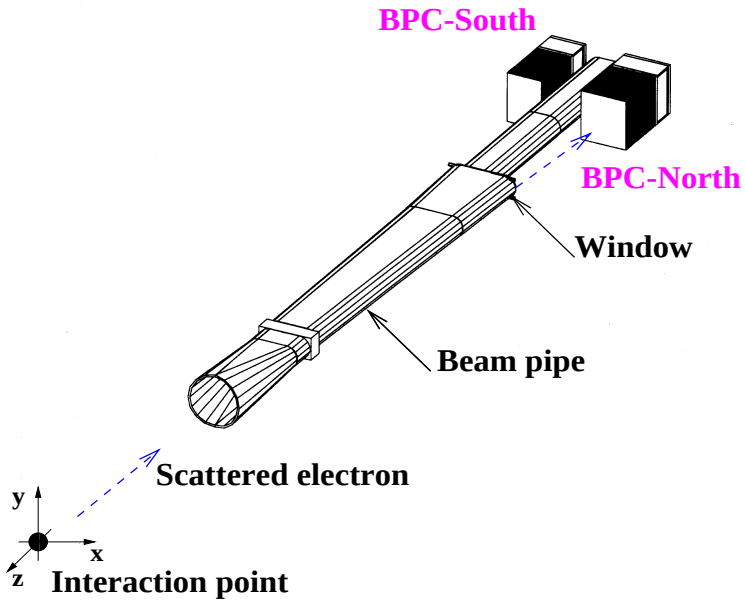

Figure 3.11: Location of the BPC modules with respect to the beam pipe and the interaction point. The funnel shaped beam pipe with the exit windows for the scattered electrons is also shown.

modules. Therefore both modules have the same dimensions in Y (13.0 cm) and Z (16.0 cm), but have different dimensions in X (BPC South 9.8 cm, BPC North 13.8 cm).

The area of a BPC module front face which can be used for a high precision measurement is restricted by the dimensions of the beam pipe exit windows. This "fiducial area" is to first approximation given by the projection of the beam pipe exit window onto the module front face. For the BPC North module the fiducial area is constrained by $5.37 < \mathrm{X} < 9.57$ cm, $-2.62 < \mathrm{Y} < 2.98$ cm and in addition by the requirements $Y + X < 11.35$ cm and $Y - X < -10.99$ cm taking into account the actual location of the module with respect to the ZEUS coordinate frame. In Fig. 3.12 the segments of the BPC North module are depicted in the ZEUS XY-plane. The shaded area covers the segments inside the fiducial area. The dimensions of the fiducial area of the BPC South module are not given here because in this analysis only the North module is used. The energy resolution of the BPC

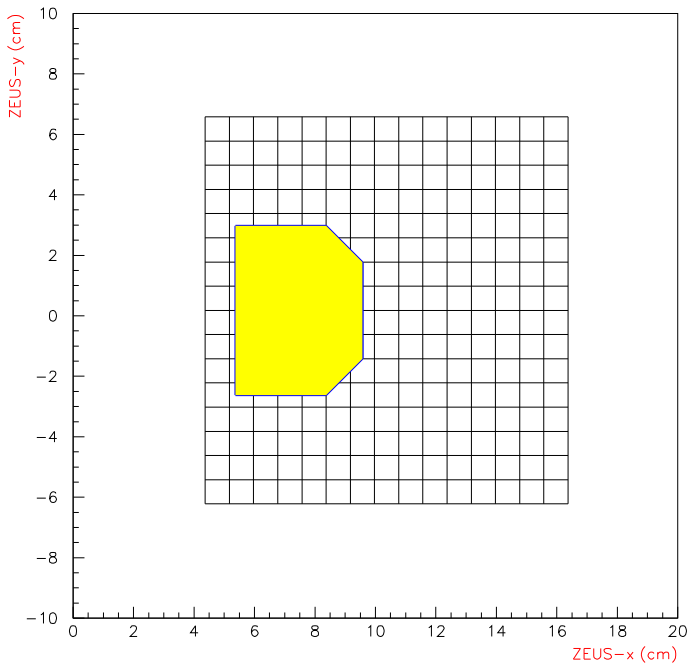

Figure 3.12: Location of the segments of the BPC North module. The shaded area indicates the fiducial area of this module.

was determined from test beam measurements to be $0.17/\sqrt{E(\mathrm{GeV})}$. The spatial resolution of the BPC in the fiducial area was found to be better than 1 mm. For further details of the BPC and the BPT see [Fri99] and references herein.

3.2.7 The Luminosity Measurement (LUMI)

The ZEUS luminosity detectors are installed in the backward (-Z)-direction, inside the HERA tunnel. Bremsstrahlung emerging from the Bethe-Heitler-process ($ep \rightarrow e\gamma p$) [Bet34] is used to measure the luminosity of the ep-beams. The cross section to a precision of 0.5%, so a precise measurement of the photon rate yields a high precision value for the luminosity. The layout of the HERA magnet system and the ZEUS luminosity detector is shown in Fig. 3.13. The ZEUS experiment uses two lead/scintillator electromagnetic calorimeters to measure the photon (LUMIG) and the scattered electron (LUMIE), respectively. They are installed at Z = -34 m (LUMIE)

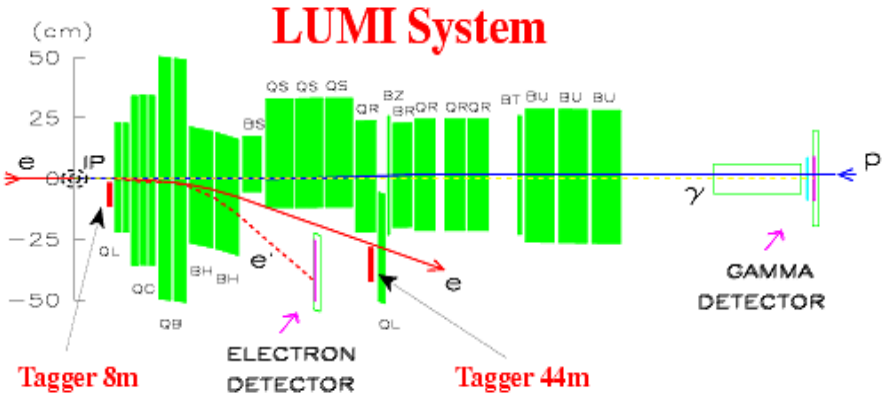

Figure 3.13: Layout of the HERA magnet system and the ZEUS luminosity detector located in the HERA tunnel The gamma and electron detectors (LUMIG,LUMIE) are used for the luminosity measurement.

and Z = -107 m (LUMIG). At Z = -92 m a Be-Cu window was installed in the beam pipe to reduce the influence of inactive material. Photons from the Bethe-Heitler process with $\theta_\gamma < 0.5$ mrad are detected by the LUMIG [And92, Pio93] calorimeter. The energy resolution of this calorimeter investigated in test beam experiments was found to be $0.18/\sqrt{\mathrm{E(GeV)}}$, but the carbon/lead filter which was placed in front of the calorimeter to shield it against synchrotron radiation reduces the resolution to an actual value of $0.23/\sqrt{\mathrm{E(GeV)}}$. At a depth of $7X_0$ 1 cm wide scintillator strips are installed inside the LUMIG calorimeter what allows for an impact position determination with a resolution of 0.2 cm in X and Y.

The LUMIE [And92, Pio93] calorimeter is used to measure the scattered electron from the Bethe-Heitler process. It is not further described here because it is not used in the analysis presented in this thesis. Originally it was intended to determine the luminosity by a simultaneous measurement of the photon and the electron. But it turned out that the measurement of the photons alone is enough to have a precise determination of the luminosity.

3.2.8 The ZEUS Three-Level Trigger

The ZEUS experiment is furnished with a three-level trigger system. This trigger system serves to separate on-line background from *ep*-events and to reduce the total event rate to a reasonable level. The background events are

dominated by interactions between the proton beam and residual gas in the beam pipe at a rate of the order of 10–100 kHz. Other background events originate from beam halo interactions, electron interactions with the beam gas and cosmic ray events. The layout of the ZEUS trigger system is shown in Fig. 3.14. Each ZEUS component has its own first (FLT) and second level

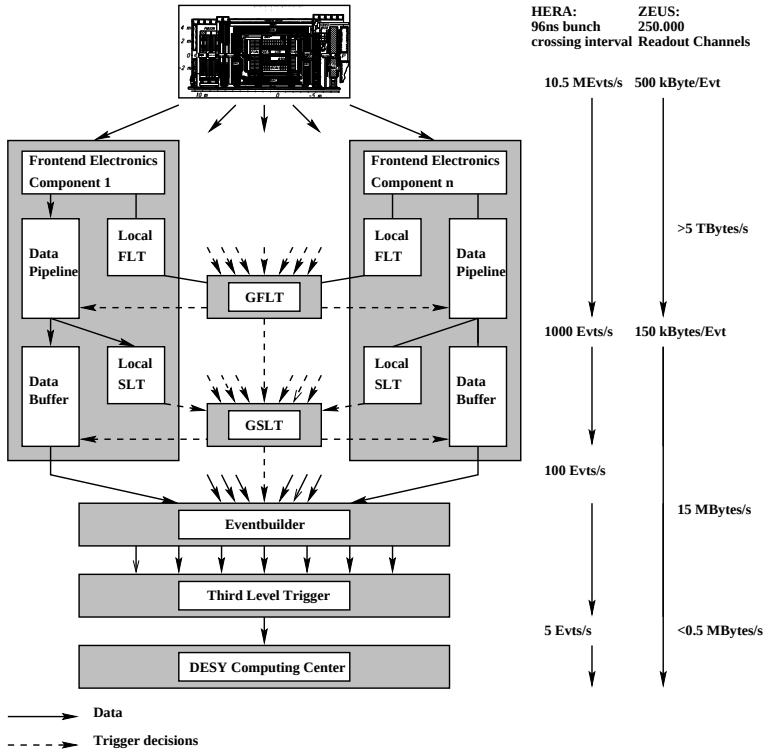

Figure 3.14: Schematic diagram of the ZEUS three level trigger.

trigger (SLT). On the first level, the particular event is analyzed within 25 clock cycles (one HERA clock cycle corresponds to the bunch spacing time of 96 ns). From the result of this analysis, the FLT decides whether to accept the event or to reject it. To avoid dead time, the component readout and FLT systems are pipelined using 10.4 MHz pipelines. The trigger decision is transferred to the **G**lobal-**F**irst- **L**evel-**T**rigger (GFLT). Here, the information of all component FLTs is assembled and logical combinations of this global information is used to determine the GFLT decision. This takes about 20 bunch crossings. After the FLT decision, the event rate is reduced below 1 kHz. If an event is accepted by the GFLT, the data stored in the pipeline are transferred to the components SLT, where they are stored in memory buffers. The component SLTs are based on a network of programmable

transputers. On the second level background events are identified and rejected. This is achieved by using more sophisticated algorithms than those used by the FLT. The result of the SLT decision is then transferred to the **G**lobal-**S**econd- **L**evel-**T**rigger (GSLT) [Uij92] where the results of all local SLTs are combined to come to a final decision. After the SLT, the event rate is already reduced down to about 100 Hz. If the event is also accepted by the GSLT, the information of all components is transferred to the "Event-builder", which combines all the data and consists of a PC farm of 40 CPUs. The data is formatted in the ADAMO format [Gre89] which is used at the **T**hird-**L**evel-**T**rigger (TLT) and in the offline reconstruction and analysis. After the TLT decision, the event rate is reduced to a few Hz. The data volume finally stored on tape is less than 0.5 MBytes/s. The user has access to the data as well as to the Monte Carlo simulations of the detector components via the analysis environment EAZE, what stands for **E**ffortless **A**nalysis of **Z**EUS **E**vents. By inserting his own code into this environment, the user can reconstruct the relevant quantities and can perform refined selection cuts on the data corresponding to the particular analysis he has planed.

Chapter 4

Kinematic Variables, their Reconstruction and the Measurement of the Cross Section

4.1 Introduction of the Kinematical Variables

The most important variables describing the kinematics of an event produced in an electron–proton collision are shown in Fig. 4.1. The figure displays an example of such an interaction where the photon acts as a source of partons and one of these partons initiates the hard subprocess (a so called "resolved" process).

4.1.1 Virtuality, Inelasticity, the Bjorken–x and x_γ

One important variable is the so called "virtuality". The square of the momentum four-vector of a particle (p^μ) in Minkowski space is equal to the square of its invariant mass:

$$p_\mu p^\mu = E^2 - \mathbf{p}^2 = m^2. \tag{4.1}$$

Here E and $\mathbf{p}$ are the energy and three-momentum of the particle. The four-momentum of the photon q^μ is given by the difference of the four-momenta of the incident (k^μ) and outgoing electron (k'^μ), see Fig. 4.1. So for its squared invariant mass one gets:

$$Q^2 = -q_\mu q^\mu = -(k^\mu - k'^\mu)^2. \tag{4.2}$$

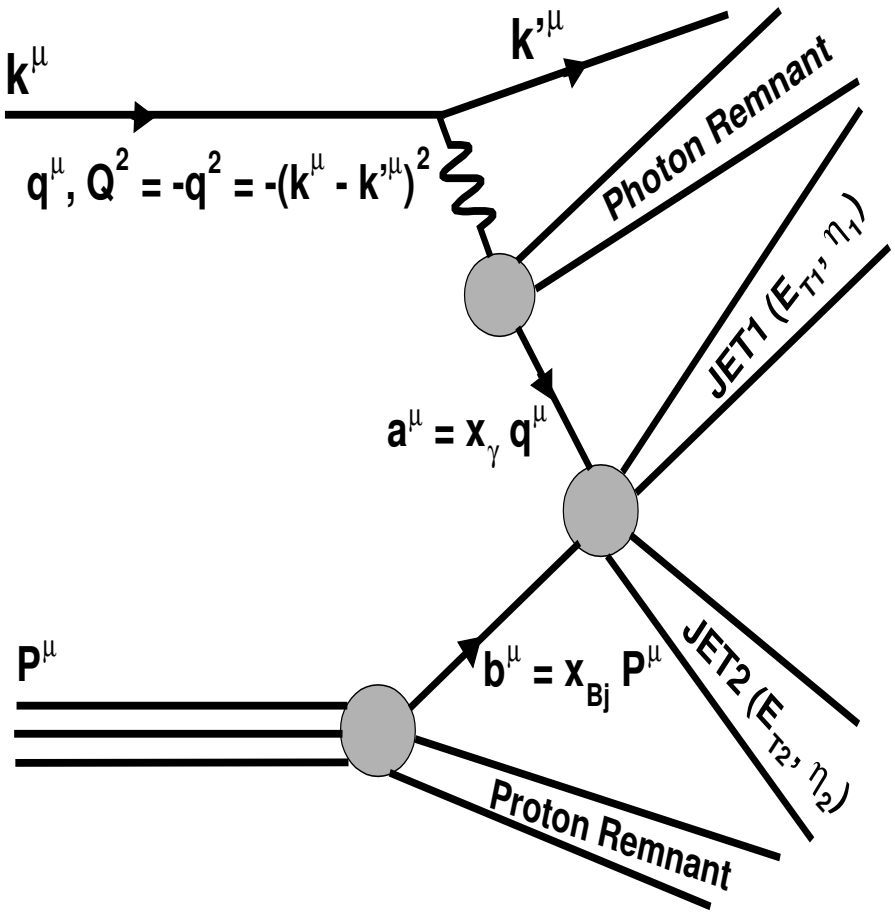

Figure 4.1: Sketch showing a "resolved" electron–proton collision together with the relevant kinematic variables. k^μ (k'^μ) is the four-vector of the incident (outgoing) electron, a^μ (b^μ) the four-vector of the parton emerging from the photon (proton) and q^μ (P^μ) is the four-vector of the photon (proton) itself.

A real photon is massless, so $Q^2 = 0$ in this case. However, a virtual photon has acquired mass and in this case $Q^2 \neq 0$. So Q^2 can be considered as a measure of the virtuality of the photon, hence its name "virtuality". From the definition it is clear that $-Q^2$ is equivalent to the Mandelstam t variable (see chapter 2). Another important variable (not displayed in Fig. 4.1) is the "inelasticity" y. It is defined by:

$$y = \frac{q_\mu P^\mu}{k_\mu P^\mu} = \frac{E_\gamma E_p - \mathbf{p}_\gamma \cdot \mathbf{p}_p}{E_e E_p - \mathbf{p}_e \cdot \mathbf{p}_p}, \tag{4.3}$$

where P^μ is the four-vector of the proton, see Fig. 4.1. E_γ ($\mathbf{p}_\gamma$), E_e ($\mathbf{p}_e$) and E_p ($\mathbf{p}_p$) are the energies (momenta) of the photon, electron and proton, respectively. From the last equality of (4.3) one sees that in the rest frame of the proton where $\mathbf{p}_p = 0$ one simply has $y = \frac{E_\gamma}{E_e}$. The same holds true for the case of photoproduction for in this case the photon is emitted (almost) in the direction of the electron. So from (4.3) one gets

$$y = \frac{E_\gamma E_p - \mathbf{p}_\gamma \cdot \mathbf{p}_p}{E_e E_p - \mathbf{p}_e \cdot \mathbf{p}_p} = \frac{E_\gamma E_p (1 - \cos\theta_\gamma)}{E_e E_p (1 - \cos\theta_e)} = \frac{E_\gamma}{E_e} \tag{4.4}$$

for photoproduction where θ_γ (θ_e) are the scattering angles of the photon (electron) and the fact $\theta_\gamma = \theta_e$ has been used. So here y is just the fraction of the electrons energy carried by the photon. In this way y can be interpreted as a measure of the electrons energy fraction entering the interaction. From this interpretation and from (4.3) it follows that $y \in (0, 1)$, since E_γ cannot be negative or larger than E_e.

Another quantity is the Bjorken–x (x_{Bj}). It represents the energy–momentum fraction of the incident proton carried by the parton from the proton that is struck in the interaction. One can obtain an analytical expression for x_{Bj} by considering a direct interaction between a photon and a parton from the proton in the so called "infinite–momentum frame". In this frame of reference the proton is assumed to have a very large three-momentum so that all partons in the proton move essentially in the direction of the proton and any internal transverse momenta can be neglected. Then, from energy–momentum conservation one gets:

$$(x_{Bj} P^\mu + q^\mu)^2 = m^2 \approx 0 \tag{4.5}$$

and therefore:

$$x_{Bj}^2 P_\mu P^\mu + 2 x_{Bj} P_\mu q^\mu + q_\mu q^\mu \approx 0. \tag{4.6}$$

The mass m denotes the mass of the struck quark. In the case of deep inelastic scattering the relation $|x_{Bj}^2 P_\mu P^\mu| \ll q_\mu q^\mu$ holds, i.e. the squared proton mass weighted by x_{Bj}^2 is much smaller than the photons virtuality, and so one finally obtains:

$$x_{Bj} = \frac{-q_\mu q^\mu}{2 P_\mu q^\mu} = \frac{Q^2}{2 P_\mu q^\mu}. \tag{4.7}$$

This variable was originally introduced by Bjorken in his scaling hypothesis stating that lepton–nucleon cross sections do not depend on Q^2 but on x_{Bj}, a dimensionless quantity in the limit $Q^2 \to \infty$ (see also chapter 1). Later, Feynman gave it the interpretation as the energy-momentum fraction of the

proton carried by a struck parton in the framework of his just developed parton model [Fey72]. From its definition it is also clear that $x_{Bj} \in (0,1)$.

As outlined in chapters 1 and 2 the photon can act as a source of partons and in this way develop a partonic structure. So one can define for this photon structure a quantity similar to x_{Bj}. This quantity is x_γ and it is defined as the energy–momentum fraction of the photon carried by a parton emerging from the photons quantum fluctuations. If a^μ is the four–momentum of that parton, then, in the photons rest frame, x_γ is defined by $a^\mu = x_\gamma p^\mu$ or $x_\gamma = E_a/E_\gamma$. Again, $x_\gamma \in (0,1]$ where $x_\gamma = 1$ means that no splitting of the photon has happened and the photon acts as a pointlike particle.

4.2 Transverse Energy and Pseudorapidity

As already mentioned in chapter 2, a parton emerging from the hard interaction forms hadrons which then appear as a collimated bunch of particles called a "jet". Two characteristic variables describing a particle inside a jet are the *transverse energy* (E_T) and the *pseudorapidity* (η).

The energy (E) of a free particle is given by (1.6) with $c = 1$:

$$H = E = \sqrt{m^2 + \mathbf{p}^2}, \tag{4.8}$$

where m denotes the mass and $\mathbf{p}$ the three–momentum of the particle. In the high relativistic regime one can usually neglect the mass of the particle because here the relation $m^2 \ll |\mathbf{p}^2|$ holds. So one has the simple energy–momentum relationship $E = |\mathbf{p}|$. The momentum is usually splitted into two parts (see Fig. 4.2): One part parallel to the line connecting the interacting proton and electron (or photon and proton in the HCM-frame) called longitudinal momentum ($p_\parallel$) and another part perpendicular to the interaction line called transverse momentum (p_T). In the same way the total energy is related to the total momentum of the particle, one defines a "longitudinal energy" and a "transverse energy" by the relations $E_\parallel = p_\parallel$ and $E_T = p_T$, respectively. One should note that because $E = |\mathbf{p}| = \sqrt{p_\parallel^2 + p_T^2}$ these energy components add up like vector components and *not* like scalars as one would expect. So one has $E = \sqrt{E_\parallel^2 + E_T^2}$.

One can rewrite (1.6) to give:

$$E^2 - \mathbf{p}^2 = m^2. \tag{4.9}$$

This means that in E–p-space a free particle "lives" on a hyperbolic surface determined by its mass m. So one can introduce an angle w and express E

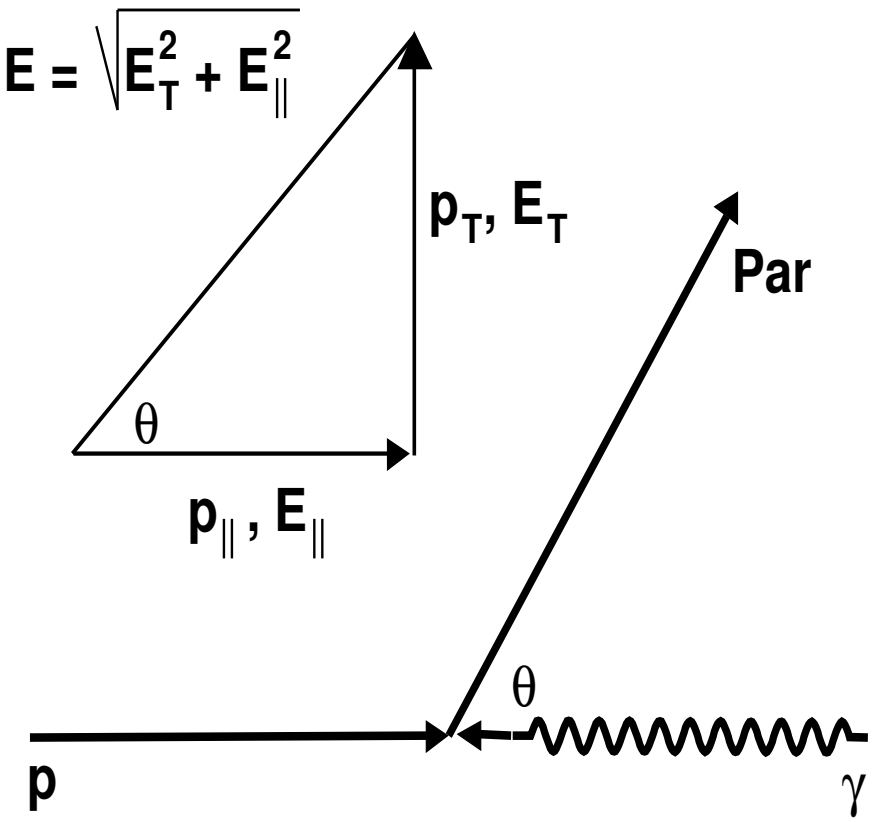

Figure 4.2: Energy–momentum relations in a photon–proton interaction in the HCM-frame of reference. $p_{\|}$ ($E_{\|}$) denotes the longitudinal p_T (E_T) the transverse momentum (energy) of the outgoing particle.

and the modulus of the momentum $\mathbf{p}$ by means of the hyperbolic functions:

$$p = m \sinh w \tag{4.10}$$

$$E = m \cosh w. \tag{4.11}$$

These relations clearly fulfill (4.9). From the classical Hamiltonian (1.6) and the canonical equations of motion one obtains for the velocity of the particle:

$$v = \frac{\partial H}{\partial p} = \frac{p}{E} = \tanh w. \tag{4.12}$$

For the last equal sign the relations (4.10) were used. For small values of w one yields from (4.12) by expanding the hyperbolic tangens the simple

relation $v \approx w$ so the velocity becomes equal to the angle w. For this reason w is called the *rapidity* [1] of the particle. To obtain an explicit expression for w one reverses (4.12) and by use of $v = p/E$ one gets:

$$w = \frac{1}{2} \ln \frac{1+v}{1-v} = \frac{1}{2} \ln \frac{E+p}{E-p}. \tag{4.13}$$

The rapidity has a very nice property under Lorentz boosts. If a particle moves with w_A in a frame A its rapidity in a frame B moving with velocity v in the direction of the momentum of the particle with axis parallel to that of A, is simply given by $w_B = w_A + w$ where w is given through $v = \tanh w$. That is, the rapidity variable is additive (see also [And98]). Furthermore one can define the rapidity for a special direction which may be important for the dynamical situation just considered. If this direction is denoted by the vector $\mathbf{r}$, then the rapidity with respect to $\mathbf{r}$ is defined by:

$$w_r = \frac{1}{2} \ln \frac{E+p_r}{E-p_r}, \tag{4.14}$$

where p_r is the component of $\mathbf{p}$ along the direction of $\mathbf{r}$. Let θ be the angle between $\mathbf{p}$ and $\mathbf{r}$. Then using $p_r = p \cos\theta$ one can cast the expression for w_r into the form:

$$w_r = \frac{1}{2} \ln \frac{E+p\cos\theta}{E-p\cos\theta}. \tag{4.15}$$

For a massless particle like a real photon one has $E = p$ so for this case one gets:

$$w_r = \frac{1}{2} \ln \frac{1+\cos\theta}{1-\cos\theta} = \ln \cot\left(\frac{\theta}{2}\right) = -\ln \tan\left(\frac{\theta}{2}\right). \tag{4.16}$$

In this way the angle under which the particle appears with respect to some given axis is directly related to its rapidity. To obtain a corresponding expression for massive particles where the relation $E = p$ is at least approximatively valid in the high relativistic regime and to retain the already mentioned transformation properties, one defines a similar quantity called *pseudorapidity*:

$$\eta = -\ln \tan\left(\frac{\theta}{2}\right). \tag{4.17}$$

At ZEUS the direction of the incident proton is taken to be the reference direction. As said in the previous chapter it defines the positive Z-direction of the ZEUS frame of reference. So here θ denotes the angle under which a particle emerges from the electron–proton interaction (see also Fig. 4.1) and is directly related to the pseudorapidity of the particle via (4.17).

[1] Actually the letter y is usually used for the rapidity but because this letter is already used to denote the inelasticity, the letter w was chosen.

4.3 Reconstruction of the Kinematical Variables

The kinematical variables introduced in the last section must be "reconstructed" from the available detector information. The E_T and η of the particles are directly calculated from the measured four-vectors. However, the variables y, x_{Bj} and Q^2 can be determined from different sources depending on what information from the detector components is available. In the following three commonly used reconstruction methods are described in some detail: The electron method, the method of Jacquet and Blondel and the double-angle method.

4.3.1 The Electron Method

The electron method uses the available information of the incident and scattered electron to reconstruct the kinematical variables. For the four-momenta in the ZEUS–laboratory frame of reference one has (see also Fig. 4.1):

$$k^\mu = (E_e, 0, 0, -E_e) \tag{4.18}$$
$$k'^\mu = (E'_e, p_{ex}, p_{ey}, p_{ez}) \tag{4.19}$$
$$P^\mu = (E_p, 0, 0, E_p). \tag{4.20}$$

By direct inserting of these four-vectors into the definitions of the variables ((4.2) for Q^2, (4.3) for y and (4.7) for x_{Bj}) one gets:

$$y_{elec} = 1 - \frac{E'_e}{2E_e}(1 - \cos\theta_e) \tag{4.21}$$
$$Q^2_{elec} = 2E_e E'_e(1 + \cos\theta_e) \tag{4.22}$$
$$x_{elec} = \frac{E'_e(1 + \cos\theta_e)}{2y_{elec}E_p}. \tag{4.23}$$

One should note that the scattering angle of the electron θ_e is measured from the positive z-direction that is from the direction of the incoming proton.

The resolution of the electron method can be estimated from simple Taylor series expansion of the variables:

$$\frac{\delta y_{elec}}{y_{elec}} = -\frac{1}{2E_e y_{elec}}\left[2\sin^2\frac{\theta_e}{2}\cdot\delta E'_e + (E'_e\sin\theta_e)\cdot\delta\theta_e\right] \tag{4.24}$$
$$\frac{\delta Q^2_{elec}}{Q^2_{elec}} = \frac{1}{E'_e}\cdot\delta E'_e - \tan\frac{\theta_e}{2}\cdot\delta\theta_e \tag{4.25}$$
$$\frac{\delta x_{elec}}{x_{elec}} = \left(\frac{1}{E'_e} + \frac{\sin^2\frac{\theta_e}{2}}{E_e y_{elec}}\right)\cdot\delta E'_e + \left(\frac{E'_e\sin\theta_e}{2E_e y_{elec}} - \tan\frac{\theta_e}{2}\right)\cdot\delta\theta_e. \tag{4.26}$$

The resolution for Q^2 is quite good except at high scattering angles of the electron because the tan diverges in the limit $\theta_e \to \infty$. The expressions for the resolutions of x and y are divergent in the limit $y \to 0$. So in these limiting cases a precise measurement of the electrons energy and scattering angle is necessary to obtain reliable results by use of the electron method.

4.3.2 The Method of Jacquet and Blondel

The electron method can be used as long as the electron can be measured with reliable precision by the detector. But in the case of photoproduction the electron is not or only slightly scattered so that it vanishes through the beam pipe and is not detected by any of the detectors components. In such a case the kinematical quantities must be determined from a measurement of the hadronic final state. Such a method was developed by F. Jacquet and A. Blondel [Jac79]. From energy-momentum conservation one has (see again Fig. 4.1):

$$k^\mu + xP^\mu = k'^\mu + h^\mu. \tag{4.27}$$

Here x denotes the Bjorken-x and h^μ is the four-vector of the hadronic final state defined by:

$$h^\mu = (E_h, p_{hx}, p_{hy}, p_{hz}) = (\sum_i E_i, \sum_i p_{xi}, \sum_i p_{yi}, \sum_i p_{zi}), \tag{4.28}$$

where the sum runs over all particles in the hadronic final state. Splitten up in components (4.27) reads:

$$\begin{aligned} E_e + xE_p &= E'_e + E_h & (4.29)\\ -E_e + xE_p &= E'_e \cos\theta_e + E_h \cos\gamma \,(\text{longitudinal momentum}) & (4.30)\\ 0 &= E'_e \sin\theta_e - E_h \sin\gamma \,(\text{transversal momentum}). & (4.31) \end{aligned}$$

Here γ is the polar angle of the hadronic final state which will in turn be defined by the kinematic variables (see below). From (4.3) together with (4.27) one obtains for y:

$$\begin{aligned} y_{JB} &= \frac{(k_\mu - k'_\mu)P^\mu}{k_\mu P^\mu} = \frac{(h_\mu - xP_\mu)P^\mu}{k_\mu P^\mu} & (4.32)\\ &= \frac{h_\mu P^\mu}{k_\mu P^\mu} = \frac{E_p(E_h - E_h\cos\gamma)}{2E_eE_p} & (4.33)\\ &= \frac{E_h(1-\cos\gamma)}{2E_e} = \frac{\sum_i (E_i - p_{zi})}{2E_e}. & (4.34) \end{aligned}$$

In the calculations above it was assumed that all particles are massless so that products like $P_\mu P^\mu$ vanish. Further $k_\mu P^\mu = 2E_e E_p$ was used what is immediately obtained by inserting the respective four-vectors.

To obtain a respective expression for x one adds (4.29) to (4.30) and gets:

$$2xE_p = E'_e(1 + \cos\theta_e) + E_h(1 + \cos\gamma). \tag{4.35}$$

Using the definition of x_{Bj}, (4.7) with $q_\mu P^\mu = yk_\mu P^\mu = 2E_e E_p y$ and Q^2_{elec} (see above) to eliminate the term containing θ_e one finds:

$$\frac{Q^2}{2E_e y} = \frac{Q^2}{2E_e} + E_h(1 + \cos\gamma). \tag{4.36}$$

Solving this equation for Q^2 yields:

$$Q^2_{JB} = \frac{2E_e y_{JB} E_h(1 + \cos\gamma)}{1 - y_{JB}}, \tag{4.37}$$

and using the expression for y_{JB} one finally obtains:

$$Q^2_{JB} = \frac{E_h^2 - p_{hz}^2}{1 - y_{JB}} = \frac{\left(\sum_i p_{xi}\right)^2 + \left(\sum_i p_{yi}\right)^2}{1 - y_{JB}} = \frac{E_h^2 \sin^2\gamma}{1 - y_{JB}}. \tag{4.38}$$

The Bjorken-x is now easily obtained from y_{JB} and Q^2_{JB}:

$$x_{JB} = \frac{Q^2_{JB}}{4E_e E_p y_{JB}}. \tag{4.39}$$

The scattering angle of the hadronic system γ is now defined as follows: From the expressions of y_{JB} and Q^2_{JB} it is clear that these variables can be obtained without a knowledge of γ. So these quantities can in turn be used to define γ. To do this one just has to eliminate E_h^2 in the expression of Q^2_{JB} by use of the y_{JB}. This yields:

$$\cos\gamma = \frac{Q^2_{JB}(1 - y_{JB}) - 4E_e^2 y_{JB}^2}{Q^2_{JB}(1 - y_{JB}) + 4E_e^2 y_{JB}^2}. \tag{4.40}$$

One can show (see [Ben91]) that under certain assumptions this definition is equal to the energy weighted average of the cosines of the particles in the hadronic final state:

$$(\cos\gamma)_{JB} = \frac{\sum_i E_i \cos\gamma_i}{\sum_i E_i}. \tag{4.41}$$

An estimation for the resolution of this method can again be obtained from a Taylor series expansion:

$$\frac{\delta y_{JB}}{y_{JB}} = \frac{\delta E_h}{E_h} + \cot\left(\frac{\gamma}{2}\right) \cdot \delta\gamma, \tag{4.42}$$

$$\frac{\delta Q^2_{JB}}{Q^2_{JB}} = \frac{2 - y_{JB}}{1 - y_{JB}} \cdot \frac{\delta E_h}{E_h} + \left(2\cot\gamma + \frac{y_{JB}}{1 - y_{JB}} \cdot \cot\left(\frac{\gamma}{2}\right)\right) \cdot \delta\gamma, \tag{4.43}$$

$$\frac{\delta x_{JB}}{x_{JB}} = \frac{1}{1 - y_{JB}} \cdot \frac{\delta E_h}{E_h} + \left(2\cot\gamma + \frac{2y_{JB} - 1}{1 - y_{JB}} \cdot \cot\left(\frac{\gamma}{2}\right)\right) \cdot \delta\gamma. \tag{4.44}$$

To use the Jacquet–Blondel method one needs a precise measurement of the energy and angle of the hadronic final state four-momentum. Furthermore one sees that contrary to the electron method the resolution is good for low values of y_{JB} but becomes bad when $y_{JB} \to 1$.

4.3.3 The Double–Angle Method

The electron–method and the Jacquet–Blondel method both require a precise measurement of the energy either of the scattered electron or the hadronic final state. A method that avoids these energy dependencies is the double–angle method. Here, the kinematic variables are reconstructed by a measurement of the scattering angles of the electron θ_e and the hadronic final state γ. The corresponding formulas can be obtained directly from those of the Jacquet–Blondel method.

By subtracting (4.30) from (4.29) and eliminating E'_e by means of (4.31) one obtains:

$$2E_e = E_h \frac{\sin\gamma + \sin\theta_e - \sin(\theta_e + \gamma)}{\sin\theta_e}. \tag{4.45}$$

Inserting this into the expression for y_{JB} that contains $\cos\theta_e$ immediately yields:

$$y_{DA} = \frac{\sin\theta_e(1 - \cos\gamma)}{\sin\gamma + \sin\theta_e - \sin(\theta_e + \gamma)}. \tag{4.46}$$

Inserting this result into Q^2_{JB} and eliminating E_h by means of (4.45) gives:

$$Q^2_{DA} = 4E_e^2 \frac{\sin\gamma(1 + \cos\theta_e)}{\sin\gamma + \sin\theta_e - \sin(\theta_e + \gamma)}. \tag{4.47}$$

Finally, from inserting both expressions in x_{JB} one obtains:

$$x_{DA} = \frac{E_e}{E_p} \frac{\sin\gamma(1 + \cos\theta_e)}{\sin\theta_e(1 - \cos\gamma)} = \frac{E_e}{E_p} \frac{\sin\gamma + \sin\theta_e + \sin(\theta_e + \gamma)}{\sin\gamma + \sin\theta_e - \sin(\theta_e + \gamma)}. \tag{4.48}$$

The last equation is obtained by multiplying nominator and denominator of the first expression by $\sin\gamma + \sin\theta_e - \sin(\theta_e + \gamma)$. Taylor series expansion gives for the resolution of the double–angle method:

$$\frac{\delta y_{DA}}{y_{DA}} = -\frac{1 - y_{DA}}{\sin\gamma} \cdot \delta\gamma - \frac{1 - y_{DA}}{\sin\theta_e} \cdot \delta\theta_e, \tag{4.49}$$

$$\frac{\delta Q^2_{DA}}{Q^2_{DA}} = -\frac{y_{DA}}{\sin\gamma} \cdot \delta\gamma + \left(\frac{y_{DA}}{2\cos^2\left(\frac{\theta_e}{2}\right)\tan\left(\frac{\gamma}{2}\right)} - \frac{1}{\sin\theta_e} \right) \cdot \delta\theta_e, \tag{4.50}$$

$$\frac{\delta x_{DA}}{x_{DA}} = -\frac{1}{\sin\gamma} \cdot \delta\gamma + \left(\frac{y_{DA}}{2\cos^2\left(\frac{\theta_e}{2}\right)\tan\left(\frac{\gamma}{2}\right)} - \frac{y_{DA}}{\sin\theta_e} \right) \cdot \delta\theta_e. \tag{4.51}$$

The resolution of the double–angle method is quite good for all variables. Only for very large and very low angles θ_e and γ the resolution becomes worse.

4.3.4 Reconstruction Methods used for this Analysis

To reconstruct Q^2, y and the energy of the scattered electron (actually positron) as precise as possible a combination of all three methods is used. The energy of the scattered positron can be obtained from its scattering angle and the scattering angle of the hadronic system (so to say by the double–angle method) by combining (4.47) with (4.22) what yields:

$$E_e^{'DA} = \frac{2E_e \sin\gamma}{\sin\gamma + \sin\theta_e - \sin(\theta_e + \gamma)} \tag{4.52}$$

For the data set used in this analysis (ZEUS run period 1996/97) it was shown in [Cha01] that when the positron lies inside the CTD acceptance and the hadronic scattering angle is less than $\sim 90°$ the double–angle method leads to a better energy resolution than the corrected calorimeter resolution for the energy of the scattered positron. This region also corresponds to high Q^2 where this quantity is also well reconstructed by the double–angle method. So the double–angle method was used to reconstruct the positrons energy and Q^2 when the positron lies inside the CTD acceptance and the hadronic scattering angle is less than $\sim 90°$. Outside this region, for the positron energy the corrected energy of the calorimeter was taken and Q^2 was reconstructed by the electron method since this method has a good resolution for Q^2 over the whole considered kinematic region (see above) so also at low scattering angles of the positron when it lies outside the CTD acceptance but is still detected by the calorimeter or the BPC.

As explained in a later chapter, in this analysis events are selected for which $y \in (0.2, 0.55)$ that is y is quite small. Therefore the method of Jacquet and Blondel is chosen to reconstruct y since this method yields the better resolution for small values of y as was shown above.

4.3.5 The Estimator x_γ^{obs}

The value of the variable x_γ is not so easily reconstructed from the experimental data. To get at least an estimation of this variable a similar variable denoted by x_γ^{obs} was defined (see also [Der94]): Considering a parton from the photon with four-momentum $x_\gamma^{obs} q^\mu$ interacting with a parton from the proton with four-momentum $x_P P^\mu$, energy-momentum conservation yields:

$$x_\gamma^{obs} q^\mu + x_{Bj} P^\mu = J_1^\mu + J_2^\mu, \tag{4.53}$$

where J_1^μ and J_2^μ are the four-vectors of the two jets with the highest transversal energy (see also Fig. 4.1). From this equation it is clear that x_γ^{obs} is a pure "leading order variable" in the sense that the relation $x_\gamma^{obs} = x_\gamma$ is only strictly valid for two-body processes correctly described by perturbative QCD in leading order. But for events with more than two jets this variable is at best an estimation of the real x_γ. For this reason it is denoted differently from x_γ and the superscript *obs* stands for "observed". To obtain an analytical expression for x_γ^{obs} one multiplies (4.53) by P_μ what yields:

$$x_\gamma^{obs} P_\mu q^\mu = P_\mu J_1^\mu + P_\mu J_2^\mu, \tag{4.54}$$

and so one obtains:

$$x_\gamma^{obs} = \frac{P_\mu J_1^\mu + P_\mu J_2^\mu}{P_\mu q^\mu}. \tag{4.55}$$

Again all particles are assumed to be massless. Consisting only of four-vector products x_γ^{obs} is clearly a Lorentz invariant quantity. This equation can be rewritten in several ways. From the derivation of y_{JB} one sees directly that $P_\mu q^\mu = E_p \sum_i (E_i - p_{zi})$. The numerator can be expressed in various ways:

$$\begin{aligned}
P_\mu J_1^\mu + P_\mu J_2^\mu &= E_p E_{J1} - \mathbf{p}_p \cdot \mathbf{p}_{J1} + E_p E_{J2} - \mathbf{p}_p \cdot \mathbf{p}_{J2} \\
&= E_p \sum_{i=1,2} (E_{Ji} - p_{Jzi}) && (4.56) \\
&= E_p \sum_{i=1,2} E_{Ji}(1 - \cos\theta_{Ji}) && (4.57) \\
&= E_p \sum_{i=1,2} E_{Ji}(1 - \tanh\eta_{Ji}) && (4.58) \\
&= E_p \sum_{i=1,2} E_{Ti} \cdot e^{-\eta_{Ji}}. && (4.59)
\end{aligned}$$

Here θ_{Ji} denotes the polar angle of the ith jet in the ZEUS frame of reference. The last equation is obtained from the definition of η, see (4.17), and the relation $E_T = E \sin\theta$. From the definition of η one also gets $\cos\theta_{Ji} = \tanh\eta_{Ji}$. It should be noted that these relations also hold in the HCM frame[2] because the transformation is done in such a way that after the boost is performed the new four-vectors are rotated so that the incident proton momentum points again in the positive z-direction. So for x_γ^{obs} one gets:

$$x_\gamma^{obs} = \frac{\sum_{i=1,2}(E_{Ji} - p_{Jzi})}{\sum_i (E_i - p_{zi})} \tag{4.60}$$

$$= \frac{\sum_{i=1,2} E_{Ji}(1 - \tanh\eta_{Ji})}{y_{JB}(E_e - p_{ez})}. \tag{4.61}$$

In this analysis the expression (4.61) was used. It is obtained from (4.58) and the derivation of y_{JB} (4.32)–(4.34) taking into account that generally $k_\mu P^\mu = E_p(E_e - p_{ez})$. This holds also in the HCM frame where the angle between the incident electron and the proton is not necessarily equal to π. A commonly used expression in the LAB frame is:

$$x_\gamma^{obs} = \frac{\sum_{i=1,2} E_{Ti} \cdot e^{-\eta_{Ji}}}{2E_e y_{JB}}. \tag{4.62}$$

The advantage of the variable x_γ^{obs} is that it allows a topological discrimination between direct and resolved contributions. This is shown in Fig. 4.3 where the distribution of x_γ^{obs} is shown as obtained from a simulation using the event generator HERWIG5.9. These events are created for the case of photoproduction, i.e. $Q^2 < 1$ GeV^2, where the photon is known to have a hadronic structure. The histogram shows the total distribution that includes both direct and resolved events. The hatched histogram on the contrary shows only the direct contribution. The direct contribution dominates for values of x_γ^{obs} larger than 0.75. The value $x_\gamma^{obs} = 0.75$ is indicated by a straight line. For values less than 0.75 the direct contributions becomes less and less important and in this region the resolved events dominate. Since direct and resolved contributions are topologically well distinguished, the variable x_γ^{obs} is used for the reweighting procedure to be described below.

4.4 Calculation of the Cross Section

Now that the data distribution of some variable (in the following denoted by Y) is properly corrected one can obtain the desired cross section or differential

[2]For the HCM frame the LAB quantities are of course to be exchanged with the corresponding ones in the HCM frame.

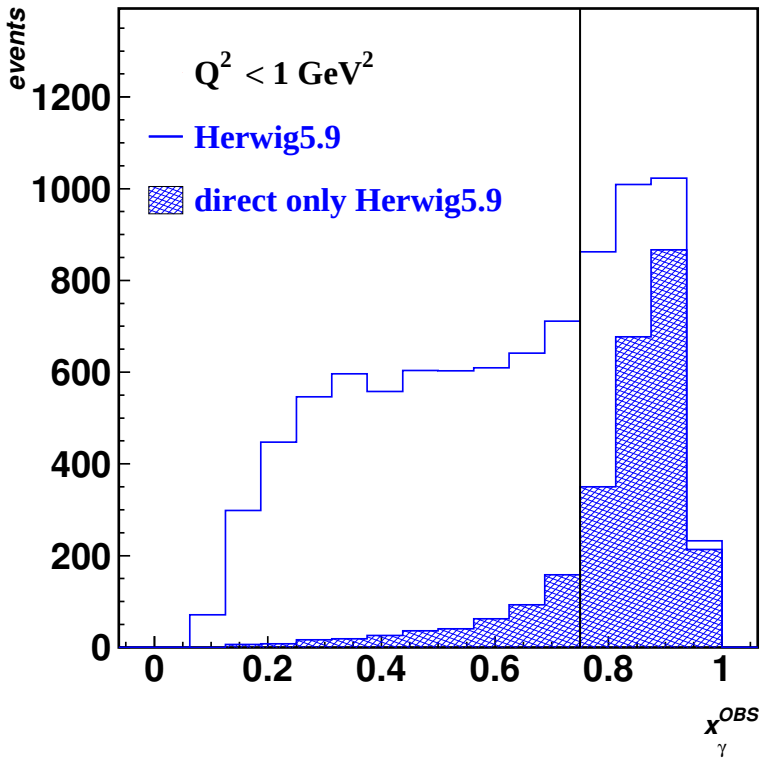

Figure 4.3: Distribution of x_γ^{obs} generated with HERWIG 5.9 for $Q^2 < 1$ GeV^2. The histogram shows the total distribution while the hatched one shows the direct part only. For $x_\gamma^{obs} < 0.75$ the resolved part dominates while for $x_\gamma^{obs} > 0.75$ the direct part yields the most contribution. The value $x_\gamma^{obs} = 0.75$ is indicated by a straight line.

cross section in the following way: The interaction rate in some interval of Y is connected to the cross section via:

$$\dot{N}_i = \sigma_i \cdot \mathrm{L}. \tag{4.63}$$

Here, a subscript i is added to the cross section and the interaction rate to refer to the bin of the histogram corresponding to the range of Y. The quantity L is the so called *luminosity* giving the particle flux provided by the storage ring. In this way the luminosity is a measure for the probability that a particle of one bunch undergoes a collision with a particle of the bunch that comes to meet. It is given by:

$$\mathrm{L} = \frac{b}{4\pi} \frac{N_1 N_2}{\sigma_x^* \sigma_y^*} f \tag{4.64}$$

or

$$\mathrm{L} = \frac{1}{4\pi e^2 f b}\frac{I_1 I_2}{\sigma_x^* \sigma_y^*}. \tag{4.65}$$

The variable b gives the number of bunches inside the storage ring assuming they are equally spaced while N_1 and N_2 are the number of particles of types 1 and 2 inside each bunch. f is the turning frequency of the bunches. The σ's are denoting the cross sections of the bunches in x and y direction where it is assumed that these cross sections are equal for both types of particle bunches. The asterisk on both symbols indicates the corresponding values at the interaction point. Equation (4.65) is obtained from the former by introducing the particle currents $I_i = N_i e f b$ where e of course is the elementary charge. To get the number of events which is actually filled into the histogram one has to integrate (4.63) over the time the data were accumulated:

$$N_i = \sigma_i \cdot \int_{obstime} \mathrm{L}\, dt = \sigma_i \cdot \mathcal{L}. \tag{4.66}$$

The quantity $\mathcal{L}$ is called *integrated luminosity*. So for the cross section one simply gets:

$$\sigma_i = \frac{N_i}{\mathcal{L}}, \tag{4.67}$$

and for the differential cross section one just has to divide by the range of the quantity Y corresponding to bin i:

$$\left(\frac{d\sigma_i}{dY}\right)_i = \frac{N_i}{\mathcal{L}(\Delta Y)_i}. \tag{4.68}$$

Chapter 5

Jets and EFOs

The definition of a jet as being a collimated spray of particles is quite loose since it is just a qualitative statement. To give a precise quantitative physical definition of a jet one has to set up rules after which a given distribution of particles is divided into jets. Such a set of rules or algorithm specifying how to break up a given particle distribution into jets must meet the following conditions:

1. It must yield infrared safe observables. An observable is said to be infrared safe if, for any n-parton configuration, adding an infinitely soft parton does not affect the observable at all.

2. It must yield collinear safe observables. An observable is collinear safe if, for any n-parton configuration, replacing any massless parton by an exactly collinear pair of massless partons does not affect the observable at all.

3. The corrections which have to be applied to parton jets to take subsequently hadronization into account should be small.

4. The items above should also hold up to higher orders in perturbation theory.

There are two algorithms frequently used in hadron–hadron interactions: The *cone algorithm* and the *inclusive k_T algorithm*. They should now be described in some detail. Both algorithms use the definition of an opening angle between two particles i and j given by:

$$R_{ij} = \sqrt{(\eta_i - \eta_j)^2 + (\phi_i - \phi_j)^2}, \tag{5.1}$$

which is invariant under longitudinal Lorentz boosts.

5.1 The Cone Algorithm

The basic principle of a cone algorithm [Ste77] is to find some start particle, the "seed" and construct a cone with a given opening angel R around it. Typical values for this opening angles are $R = 0.7$ and $R = 1$. Then, every particle with $R_{i,seed} = \sqrt{(\eta_i - \eta_{seed})^2 + (\phi_i - \phi_{seed})^2} < R$ meaning every particle, that lies inside the cone, is assigned to a jet. This procedure is repeated with different seeds until all particles are merged into jets. The selection of a seed is generally not fixed and different approaches are possible. The EUCELL algorithm [Ell92] for instance uses the particle with the highest E_T as seed. After one jet is found its associated particles are removed from the initial particle distribution and the procedure is repeated until all jets are found. However, this algorithm is not infrared safe and therefore obsolete!

The advantage of the cone algorithm is that it is conceptually easy and easy to implement. However, a lot of problems have been encountered with these intuitive algorithms and more modern versions are quite complicated. There are some disadvantages of the cone algorithm. The number of found jets depends in most cone algorithms on the presence of soft particles so they are not infrared safe and they are also not collinear safe, see [Sey98]. The only infrared and collinear safe algorithm is the CDFCONE algorithm [Abe92]. Further, to handle the possible overlap of two jets one needs to introduce an additional parameter R_{sep} specifying the maximally allowed distance between two partons inside a jet. In this way it provides the distance where the calculation switches from one to two jets. The variable R_{sep} is not known a priori, but depends on the details of the jet algorithm [Ell92]. However, it exists an algorithm that avoids all the problems of the cone algorithm completely, namely the inclusive k_T algorithm [Sey98] and for this reason there is no necessity anymore to use the cone algorithm at all.

5.2 The Inclusive k_T Algorithm

The inclusive k_T algorithm [Ell93] is a cluster algorithm which is conceptually similar to the cone algorithm but avoids ambiguities like the choice of seeds and overlapping cones. It is also infrared and collinear safe. Introducing a free parameter R specifying the opening angle of the jets, the particles are clustered according to the following steps:

1. For every pair of particles one defines a "closeness":

$$d_{ij} = \min(E_{Ti}^2, E_{Tj}^2) R_{ij}^2 \approx \min(E_{Ti}^2, E_{Tj}^2) R_{ij}^2 \theta_{ij} \approx k_T^2. \tag{5.2}$$

The last two approximations hold when the polar angle θ_{ij} between the two particles i and j is small. The quantity k_T is the difference of the transverse momenta of both particles.

2. For every particle one defines a closeness to the beam particles:

$$d_{ib} = E_{Ti}^2 R^2. \tag{5.3}$$

3. If $\min d_{ij} < \min d_{ib}$ (see (5.3) particle i and j are merged to a jet denoted by i. (Other merging schemes are also possible, see [Cat93].) For small angles between the particles $d_{ij} \approx k_{Tij}$ (see above) so that the merging condition reads $\min d_{Tij} < \min k_{Tib}$, hence the name "$k_T$ algorithm".

4. If $\min d_{ib} < \min d_{ij}$, the jet i is complete.

These steps are repeated until all jets are complete. Then, all opening angles within each jet are $< R$ and all opening angles between the jets are $> R$.

For the analysis presented here, the KTCLUS version of the k_T algorithm of [Ell93] was used for jet finding which corresponds exactly to the procedure explained above, except that it needs also an E_T cut to separate hard processes from soft ones.

5.3 Snowmass Convention

Up to this point the quantities E_T and η are only defined for single particles. The corresponding quantities for jets are defined from the E_T's and η's of the particles constituting a jet according to the "Snowmass Convention" [Abe92]:

$$E_T^{jet} = \sum_i E_T^i \tag{5.4}$$

$$\eta^{jet} = \frac{1}{E_T^{jet}} \sum_i E_T^i \eta^i \tag{5.5}$$

$$\phi^{jet} = \frac{1}{E_T^{jet}} \sum_i E_T^i \phi^i. \tag{5.6}$$

Here ϕ^{jet} (ϕ^i) denotes the azimuth angle of the jet (particle) in the given frame of reference. The sum runs over all particles ascribed to a jet. The E_T of the jet (E_T^{jet}) is the sum of the E_T's of the particles. The η^{jet} and ϕ^{jet} are given by the sum over the corresponding particle quantities weighted by the particles fraction of E_T with respect to E_T^{jet}.

5.4 Energy Flow Objects

What one observes in a detector system are not really the particles themselves. What one actually sees instead are energy deposits in the calorimeter cells or tracks in the tracking system resulting from gas ionization and both effects are caused by the particles. The information of the calorimeter and the tracking system can be combined in a certain way to form a so called **E**nergy **F**low **O**bject (EFO)[1].

The energy deposits in the calorimeter have two origins. They stem from charged as well as from neutral particles. While the neutral particles can only be detected in the calorimeter, the charged particles are also detected by the tracking system. The tracking system often yields a better accuracy for the measured energy of the particles than the calorimeter. This is especially true at low energy and in situations when the particle has to traverse dead material beyond the tracking system before it reaches the calorimeter, e.g. the solenoid coil of the CTD. It was found that the combined information of the calorimeter and the tracking system can significantly improve the reconstruction of the hadronic final state [Bri98].

The EFOs are formed in the following way: Adjacent cells in the EMC and HAC sections of the calorimeter are combined into "cell islands" . Adjacent EMC cell islands and HAC cell islands are then combined to "cone islands", see Fig. 5.1. The position of the cone islands is determined by the logarithmic center of gravity of the shower. In the next step the tracks of the particles must be matched to the calorimeter islands. Only "good" tracks are used which are defined to be those which traversed at least four superlayers of the CTD, have a transverse momentum in the range $0.1 < p_T < 20$ GeV and are fitted to the primary vertex, see [Tun01]. For tracks that passed more than seven superlayers, the maximum p_T is increased to 25 GeV. A track matches an island if the distance of closest approach between the island and the extrapolated track is less than 20 cm, or if the distance of closest approach is less than the maximum radius of the island projected on a plane perpendicular to a line drawn from the vertex to the island. The result of this procedure are groups of associated tracks and islands. It should be noted that more than one track can be associated to an island. In a next step one has to decide what energy information to use, the information from the tracks or that from the calorimeter. There are three cases where the situation is clear.

- A track matching the above requirements for a "good" track but is not

[1] ZEUS internally they are also called ZUFOs what stands for **Z**EUS **U**nidentified **F**low **O**bjects.

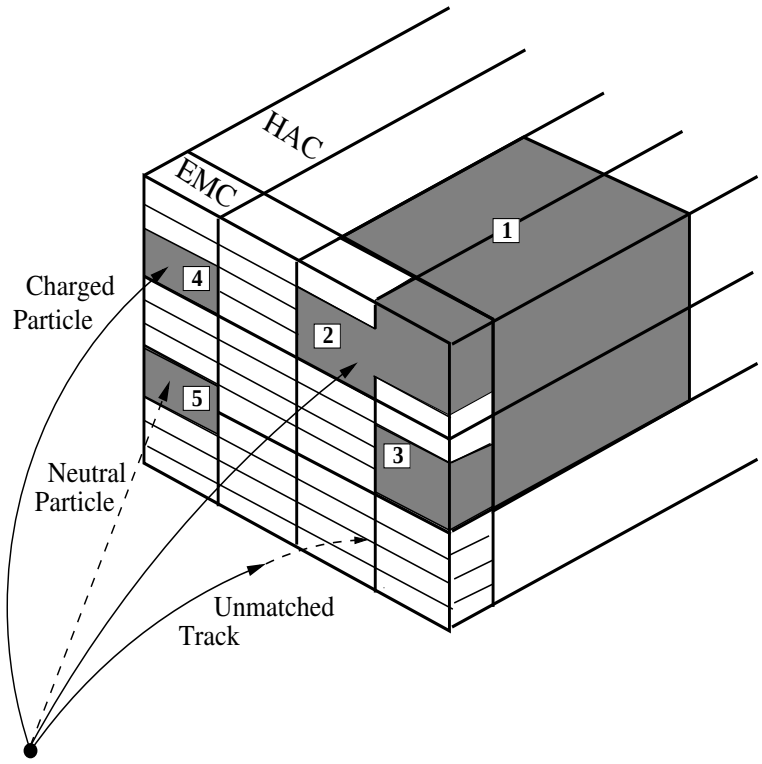

Figure 5.1: This figure shows how EMC and HAC cells of the ZEUS calorimeter are combined with tracks to form EFOs. Four EMC cell islands (2,3,4,5) and one HAC cell island (1) are shown. The EMC cell islands 2 and 3 are combined with the HAC cell island 1 to form a cone island. In the next step the islands are matched to tracks.

associated with any calorimeter island is counted as "charged energy". The energy is then determined from assuming the particle to be a pion.

- A calorimeter island not associated with any track is counted as "neutral energy" and its value is determined from the calorimeter information.

- For a calorimeter island associated with more than three tracks the energy is determined from the calorimeter information.

In the case of a calorimeter island matching exactly one track, the track information is favored if the following two requirements are encountered:

- The track momentum exceeds the energy measured by the calorimeter within the resolution of the measured ratio E_{CAL}/p, i.e. if the condition

$\frac{E_{CAL}}{p} < 1.0 + 1.2 \cdot \sigma\left(\frac{E_{CAL}}{p}\right)$ is fulfilled. The uncertainty on the ratio is increased by an additional 20% to account for the underestimation of the resolution of the track momentum which was obtained from testbeam data.

- The relative uncertainty on the measurement of the track momentum is smaller than the relative uncertainty on the calorimeter measurement, that is $\frac{\sigma(p)}{p} < \frac{\sigma(E_{CAL})}{E_{CAL}}$.

Calorimeter islands and tracks with the properties of muons are treated separately. In these cases the tracking information is favored over the calorimeter information if:

- $E_{CAL} < 5$ GeV
- $\frac{E_{CAL}}{p} < 0.25$
- $p_T < 30$ GeV.

The more complicated cases of track–island matches (1-to-2, 1-to-3, 2-to-1 and 2-to-2) are treated in a similar way as the 1-to-1 match. One uses the same decision rules but with the single track/island quantities replaced by:

- $E_{CAL} \to \sum_i E_{i,CAL}$ (the sum runs over all calorimeter islands)
- $p \to \sum_i p_i$ (the sum runs over all matched tracks)
- $\sigma(E_{CAL}) \to \sqrt{\sum_i (\sigma(E_{i,CAL}))^2}$
- $\sigma(p) \to \sqrt{\sum_i (\sigma(p_i))^2}$.

Small energy deposits in the detector at large polar angles often do not originate from the hard interaction. Such background events are generally known as "backsplash" and can be caused by several mechanisms [Gro98]:

- A high energy shower occurs in the CAL, low energy neutral particles (e.g. photons and neutrons) can escape from the front of the CAL and traverse the detector, leaving a small energy deposit far away from the original shower;
- Scattering or showering in the front material of the CAL (e.g. beam pipe, CTD wall, etc.);
- Noisy calorimeter cells;

- Overlay events.

Such background events can strongly bias the measurement of $\sum_i (E_i - p_{i,z})$ and therefore the associated calorimeter islands (there are usually no tracks present) are removed from the EFOs[2].

[2]For polar angles larger than 90°, $p_{i,z} < 0$ and consequently adds to E_i.

Chapter 6

Event Generators and JetViP

To correct the data for detector effects one needs two types of information. First one needs events with precisely known properties and second, one needs a knowledge about how the detector will modify them. The first kind of information is provided by so called event- or **M**onte **C**arlo (MC) generators the second kind of information by a detector simulation program. In this section the event generators used for this analysis are briefly described. At the end of this chapter the program JetViP is described what was used to perform the theoretical QCD calculations in next-to-leading order.

6.1 HERWIG

The event generator HERWIG, **H**adron **E**mission **R**eactions **W**ith **I**nterfering **G**luons, is a general-purpose event generator for the simulation of hard lepton-lepton, lepton-hadron and hadron-hadron scattering and for soft hadron-hadron collisions [Mar92]. HERWIG uses leading order matrix elements and in addition parton showers to account for higher orders. The emission of partons initiated by partons entering or leaving the hard interaction is simulated by parton showers similar to the DGLAP (leading $\ln Q^2$, see chapter 2) approach. The shower is terminated when the partons virtuality Q^2 becomes so low and hence α_s so large that a perturbatively treatment is not justified anymore. The initial state shower corresponds to the evolution of a parton shower from the parton that enters the hard interaction. The particles produced in this shower are ordered in $E \cdot \theta$, where E is the energy and θ the angle of the radiated parton with respect to the initial partons path. The partons from the final state shower initiated by the partons leaving the hard interaction are assumed to be ordered in the angle with respect to the initial parton. To simulate hard processes as accurately as possible QCD matrix

elements in leading order are implemented. The results from the parton showers and from the calculation using matrix elements are then matched appropriately. In this way HERWIG uses a so called (**M**atrix **E**lements + **P**arton **S**howers) model or MEPS for short. The hadronization is simulated by a simple cluster model (see again chapter 2). Also clusters from the proton/photon remnants in ep scattering are taken into account. They account for so called "underlying soft events" where a parton from the hard process interacts with a parton from the remnant. The flux of photons from the electron (positron) is determined from the Weizsäcker-Williams approximation. Direct as well as resolved processes can be simulated separately.

6.2 PYTHIA

The emphasis of PYTHIA, the name was adopted from the historical Pythia the priestess of the oracle of Delphi, is on multiparticle production in collisions as ep, pp and e^+e^- [Sjo01]. As in the case of HERWIG, PYTHIA uses parton showers to simulate parton production. Hard processes are simulated by the use of QCD matrix elements in leading order which are matched to the shower results (MEPS model, see above). Contrary to HERWIG the emitted partons are not ordered with respect to their emission angle but instead with respect to their virtuality. For the hadronization process the string fragmentation model (see chapter 2) is used. This model is implemented in JETSET, a subpackage of PYTHIA [Sjo94]. The flux of photons from the electron (positron) is calculated from the Weizsäcker-Williams approximation. As in the case of HERWIG, direct and resolved processes can be simulated separately.

6.3 LEPTO

The LEPTO event generator [Ing91, Ing97] is very similar to HERWIG. The emission of partons entering or leaving the hard interaction is simulated with a combination of leading log DGLAP parton showers and leading order QCD matrix elements to correct for hard scattering processes. An angular ordering of the produced partons is imposed to model color coherence (interference of gluon emissions). The hadronization is modeled by the string fragmentation approach. A special feature of LEPTO is the implication of soft color interactions [Edi97] in the hadronization leading to a rearrangement of the strings. This feature enables LEPTO to describe qualitatively events with large "rapidity gaps" as they occur in so called diffractive events and was

switched off for this analysis.

6.4 ARIADNE

In ARIADNE [Lon92] the multi-parton production is also modeled by parton showers but in contrary to the event generators discussed so far the shower is not produced by a DGLAP type evolution but instead by the so called **C**olor **D**ipole **M**odel (CDM) [Gus86, Gus88, And89]. The CDM model is closely related to the Lund string model, see the discussion of string fragmentation in chapter 2. In this model a quark of a hadron struck in a hard interaction leaves this hadron but due to confinement it cannot exists isolated and is therefore still connected to the hadrons remnant via a color string. This system forms a color dipole. One color pole is clearly constituted by the struck quark. The other color pole is made up by the hadrons remnant.

The formerly color neutral hadron is now one quark missing and so the remnant carries the anti-color corresponding to that of the struck quark. As an electric dipole can emit photons a color dipole can emit gluons. Such a gluon will form two new dipoles with the original quark and the remnant, each such dipole then emits a gluon, these gluons span new dipoles between the other charges, etc. (see Fig. 6.1). It is assumed that these dipoles radiate independently. This model uses the leading order cross section for the emission of gluons in the soft gluon approximation for the transverse momentum and the rapidity. It reads:

$$d\sigma = \frac{n_c \alpha_s}{2\pi} \frac{dp_T^2}{p_T^2} dw, \tag{6.1}$$

where n_c is the number of active colors. The cross section is clearly uniform in rapidity and in $\ln p_T^2$. In contrast to a parton shower of the DGLAP type it is not possible in the CDM to distinguish between initial and final parton showers. The phase space for a subsequent emission of a gluon is bound by the transverse momentum k_T of the previous emission. However, the final gluon configuration is not ordered in k_T when ordered according to increasing rapidity because of the mentioned uniformity of the emission probability. Another point is that the emission of gluons at high transverse momentum is suppressed due to the extendedness of the remnant. This is taken into account by a special phenomenological parameter of order 1 fm. In a newer version of the CDM also the color charge of the struck quark is assumed to be spread out, depending on the size of the quark that can be resolved by the incident photon.

In ARIADNE the shower as modeled by the CDM very well accounts for contributions from the QCD Compton effect and actually it makes sense only for this type of interaction. In fact, to take into account the matrix element, the first emitted gluon is made harder according to a particular process from the QCD Compton matrix element. Contributions from boson gluon fusion are introduced by hand by adding the corresponding leading order matrix element. The hadronization is performed like in PYTHIA and LEPTO with the string fragmentation model using the JETSET routine.

6.5 The Program JetViP

The theoretical calculations in next-to-leading order perturbative QCD as outlined in chapter 2 are performed by using the program "**Jet**s with **Vi**rtual **P**hotons" or JetViP for short, [Pot99, Pot00]. This program is presently the only program that provides next-to-leading order calculations also for the resolved interactions involving a parton density function for the photon. Equation (2.1) for the differential ep-cross section is implemented in the form:

$$d\sigma_{ep} = dQ^2\, dy \sum_{i,j} \int d\xi_i d\xi_j f_{j/p}(\xi_j, Q^2) d\sigma_{i,j} \cdot$$
$$\frac{\alpha_{em}}{2\pi Q^2}\left[\frac{1+(1-y)^2}{y} f^T_{i/\gamma}(\xi_i, Q^2) + \frac{2(1-y)}{y} f^L_{i/\gamma}(\xi_i, Q^2)\right] \tag{6.2}$$

The parton density functions $f^U_{i/\gamma}$ ($f^L_{i/\gamma}$) are the transverse polarized (longitudinal polarized) parts of these functions. In the case of direct interactions one has simply $f^{T,L}_{i/\gamma} d\sigma_{i,j} = \delta(1-\xi_i) d\sigma_{\gamma,j}$. In JetViP actually only the $f^T_{i/\gamma}$ part is implemented while $f^L_{i/\gamma}$ is only accounted for in direct interactions via the delta function because no longitudinal virtual photon parton density function has been constructed so far. The factors multiplying $f^T_{i/\gamma}$ and $f^L_{i/\gamma}$ are clearly the "equivalent photon approximation" formulae (2.2) and (2.3) where in the first formula the term proportional m_e^2 has been neglected. As outlined in chapter 2, the cross section can be decomposed into three parts:

$$d\sigma = d\sigma^B + d\sigma^V + d\sigma^R. \tag{6.3}$$

Clearly $d\sigma^B$ denotes the leading order Born contribution and $d\sigma^V$ ($d\sigma^R$) are the next-to-leading order virtual (real) corrections. The next-to-leading order contributions show up singularities which are differently handled by JetViP.

The virtual contributions show infrared as well as ultraviolet singularities due to phase space integrations over internal loops. They are regularized using dimensional regularization ($d = 4 - 2\epsilon$ space time dimensions). The

ultraviolet singularities are subtracted in the $\overline{\text{MS}}$ scheme. The infrared singularities appear in ϵ^{-n} terms (in the limit $\epsilon \to 0$) due to the regularization process. They are canceled against poles from the real corrections. The singularities in the real corrections stem from collinear and soft outgoing partons. In JetViP they are handled by the "phase-space slicing method", see [Kla96, Kla98] for more details than presented here. The method consists in splitting the integration over the phase-space in two parts, one that contains all the singularities and one that is free of singularities and the integration can be carried out directly. This is illustrated in the integration over the phase-space of the third particle:

$$d\sigma^R = \int_0^1 |\mathcal{M}_{2\to 3}|^2 \, d\Omega^{(3)} = \int_0^{y_s} |\mathcal{M}_{2\to 3}|^2 \, d\Omega^{(3)} + \int_{y_s}^1 |\mathcal{M}_{2\to 3}|^2 \, d\Omega^{(3)}. \quad (6.4)$$

To separate the different regions of phase-space, a technical parameter y_s (the "slicing parameter") was introduced. The first integral on the right hand side ($d\sigma_1(y_s)$) contains all the singularities while the second one ($d\sigma_2(y_s)$) is now finite due to the cut-off at the lower integration boundary. The integration of this integral is carried out in JetViP by using Monte Carlo techniques. To integrate the first integral the three-body phase space is split into a two-body phase space and a singular phase-space $d\Omega^{(s)}$ due to the third particle producing the singularity:

$$d\sigma_1(y_s) = d\Omega^{(2)} \int_0^{y_s} |\mathcal{M}_{2\to 3}|^2 \, d\Omega^{(s)}. \quad (6.5)$$

The integration is again performed by using dimensional regularization as already used in the case of the virtual corrections. The remaining integral over the two-body phase space can be further split into a part containing initial state singularities and a part containing final state singularities ($d\sigma_1 = d\sigma^I + d\sigma^F$). The infrared poles are canceled by the poles from the virtual corrections. Other terms containing simple poles in ϵ are absorbed into the parton density function of the hadronic state where the initial parton producing the singularity was emitted from.

When in adding $d\sigma_1(y_s)$ and $d\sigma_2(y_s)$ gives $d\sigma^R$, the dependence on y_s should cancel ($d\sigma^R = d\sigma_1(y_s) + d\sigma_2(y_s)$). However, in the evaluation of $d\sigma_1(y_s)$ terms of $\mathcal{O}(y_s \ln^n y_s)$ are neglected so that the matching of the two integrals in not complete and y_s must be chosen sufficiently small in the numerical treatment of $d\sigma_2(y_s)$ to yield a reliable result. For the analysis presented here, a value $y_s = 0.001$ was chosen [Pot01].

JetViP allows to calculate cross sections with an additional parton density function for the photon separately from those without one. For a complete calculation including also contributions from the photons parton density function one has to run JetViP three times. In a first run one performs

the calculations without the photons parton density function and in a second run one performs these calculations with a parton density function included. In JetViP the results of the calculations are usually filled directly into histograms. To obtain the final result one principally just has to add the contents of the corresponding histograms of both calculations. However, singularities from the splitting $\gamma \to q\bar{q}$ resulting from collinear or soft particles in the calculations without parton density function are also contained in those including one. Here the singularities are absorbed into the parton density function of the photon[1]. So to avoid double counting the singularities, one contribution must be subtracted from the calculations. This is done by running the program a third time calculating exactly this splitting term. So taking into account that the splitting result is filled into the histogram with negative sign the final result is obtained by just adding up all three histograms from the three runs (without photon pdf + with photon pdf + splitting).

In this analysis JetViP was run with CTEQ4M as parton density function for the proton and SaS1M as parton density function for the photon. The value of α_s was taken from the PDFLIB using a second order expression of α_s where the influence of a varying number of quark flavors are taken into account, i.e. it is the α_s used by the chosen parton density function for the proton. For the factorization and renormalization scales JetViP uses a common value:

$$\mu^2 = \mu_F^2 = \mu_R^2 = a \cdot p_T^2 + b \cdot Q^2. \tag{6.6}$$

The real parameters a and b are to be adjusted be the user. For p_T JetViP takes the highest value of the transverse momentum from the generated outgoing partons.

[1] See the treatment of "renormalization" in chapter 2.

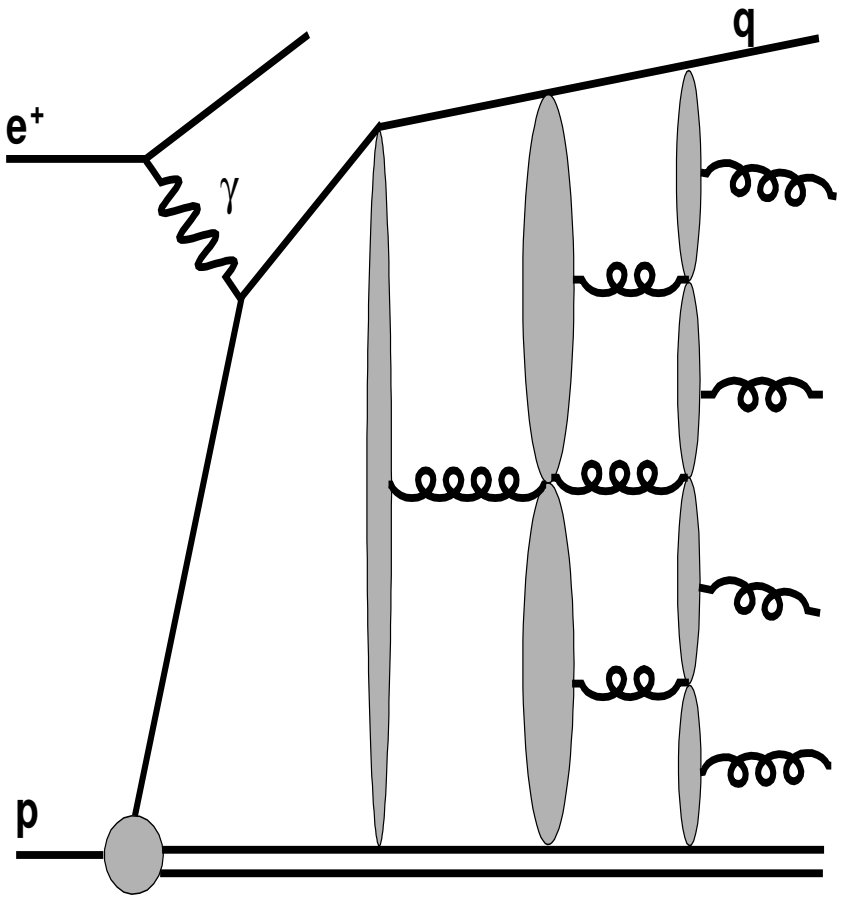

Figure 6.1: The color dipole model in deep inelastic scattering. The struck quark forms a color dipole with the proton remnant. This dipole emits a gluon and two new dipoles from the quark and the remnant are formed. These dipoles in turn emit gluons which form further dipoles with the color charges, etc.

Chapter 7

Event Selection

In the analysis presented in this thesis inclusive di-jet events (that means events with two or more jets) are investigated in the hadronic center-of-mass (HCM) frame of reference. The jets are defined through the longitudinal invariant k_T-algorithm. To define the considered phase space and to refine the removal of background events, several cuts on the kinematical variables are performed. The data entering this part of the analysis are already corrected for several effect:

Some calorimeter cells have "noisy" photomultipliers. An algorithm described in [Sav98] is used to decide whether to correct or to reject this event.

Another effect stems from inaccuracies in the absolute energy scale of the calorimeter and the simulation. These inaccuracies are also corrected. For details see [Rep96, Cal98].

For the reconstruction of the kinematical variables a combination of the electron-method, the double–angle method and the method of Jacquet-Blodel was used as explained in chapter 4. To study the dependence of the cross sections on the virtuality Q^2 of the photon the cross sections were measured in different ranges of Q^2. The width of these ranges were chosen in accordance with the detector resolution (see next chapter). These are in detail:

* $0.1 < Q^2 < 0.55$ GeV^2
* $1.5 < Q^2 < 4.5$ GeV^2
* $4.5 < Q^2 < 10.5$ GeV^2
* $10.5 < Q^2 < 49.0$ GeV^2
* $49.0 < Q^2 < 120.0$ GeV^2

For the first bin lying in the photoproduction region ($Q^2 < 1\text{GeV}^2$) the scattered electron was measured be means of the BPC (for details see the former chapter). In the DIS case (all other bins) the electron could be measured by means of the main calorimeter.

For the other variables the following cuts were applied:

- Cut on eta and E_T (all in HCM-frame):
  - $-3.0 < \eta_{1,2} < 0.$
  - $E_{T1} > 7.5$ GeV
  - $E_{T2} > 6.5$ GeV

  Jet 1 is the one with the highest transverse energy, jet 2 the one with the second highest transverse energy. The cut on eta and therefore on the polar angle under which the jets appear is applied to select only those events with jets inside the region of the calorimeter which is best understood. In the laboratory frame of reference this corresponds to a range $-1.125 < \eta_{1,2}^{LAB} < 1.875$ in η or to $17^\circ < \theta < 144^\circ$ in the polar angle. For high values of the pseudorapidity the resolution of the calorimeter becomes quite poor. The use of different cuts in the highest and in the second highest transverse jet energies is motivated by a more stable behavior of the perturbative QCD calculations in next-to-leading order. In these calculations difficulties arise when $E_{T1} \approx E_{T2}$. In this region of phase space large negative contributions to the matrix element from soft virtual terms (loop contributions) appear which at next-to-leading order of the perturbative expansion cannot be fully canceled by large positive terms from the emission of soft real gluons since real gluon emission is kinematically suppressed. This leads to poor predictions of the cross sections in this region (for a detailed discussion of this problem, see [Frx97]). So to measure cross sections for which the theoretical predictions are reliable, an asymmetric cut on the E_T's was chosen.

- Cut on the inelasticity:
  - $0.2 < y_{JB} < 0.55$

  The lower cut removes background from beam-gas events. These events move predominantly in the forward direction thus appearing at low y. The quite low upper cut was chosen because of the low acceptance of the BPC measuring events in the lowest Q^2 bin. For consistency reasons this cut was not changed for the other ranges in Q^2 measured by the main calorimeter.

Further cuts are imposed on the electron finding procedure. The scattered electron was searched by means of the SINISTRA95 electron finder, see [Abr95]. This algorithm analyses calorimeter islands of energy depositions in the calorimeter and uses additional information like the ratio of the energy deposited in the electromagnetic part of the calorimeter to the total deposited energy, the shower profile and tracking information. The evaluation of the data was performed by means of a neural network. SINISTRA was used in a run mode[1] where electron candidates are found with the highest possible probability and where additionally a search for a charged track pointing towards the vertex is performed when possible. This track search is performed to avoid confusing the electron with a photon which has a similar signature but gives no track in the CTD. The cuts applied to the SINISTRA output are:

* $\mathcal{P} > 0.9$
* $E_{elec} > 10$ GeV

$\mathcal{P}$ is the probability that an electron candidate has been found. Electrons misidentified by SINISTRA generally show up with a low energy. Events with such fake electrons are removed by the cut on E_{elec}.

To further improve the rejection of background events and to ensure that the particles are detected by the component detectors in regions where these components are well understood, additional geometrical cuts are applied:

* $|z_{vertex}| < 40$ cm

This cut removes some fraction of beam gas interactions and ensures that the event occurs in that part of the CTD which is well understood.

- Box cut for DIS events.
  * $|x_e| > 14$ cm
  * $|y_e| > 9$ cm

  Here x_e and y_e are the vertex corrected[2] positions of the identified scattered electron in the calorimeter. This cut ensures that the scattered electron was found well inside the calorimeter and that there is no energy leak of the electromagnetic shower through which the electron is identified at the edges of the calorimeter.

[1] This mode is accessible via "user option 5".

[2] The actual position of the interaction point, the vertex, is subtracted from measured positions of the particles to obtain their coordinates in the ZEUS frame of reference for which the nominal interaction point constitutes the origin.

- Box and energy cuts for the BPC for photoproduction events

  * $5.37 < x_{e,BPC} < 9.57$ cm
  * $-2.62 < y_{e,BPC} < 2.98$ cm
  * $x_{e,BPC} + y_{e,BPC} < 11.35$ cm
  * $x_{e,BPC} - y_{e,BPC} < 10.99$ cm

  Again, $x_{e,BPC}$ and $y_{e,BPC}$ are the positions of the identified electron but this time on the surface of the BPC. The cut ensures that the electron lies within the fiducial volume of the BPC module, see Fig. 3.12.

  * $\Delta x_{shower}, \Delta y_{shower} < 0.7$ cm

  Here, Δx_{shower} and Δy_{shower} denote the width of the electromagnetic shower developed in the BPC from the scattered electron in x and y direction, respectively. This cut is applied to discriminate electromagnetic showers from background events.

  * $E_e > 12.5$ GeV

  This cut on the electrons energy reconstructed by the BPC is applied to further reduce contaminations from background events. Those background arises e.g. from scattered electrons which have emitted a photon before they were detected by the BPC, from electrons which already started an electromagnetic shower by traversing dead material in front of the BPC (so called preshowered electrons), or from showers initiated by hadrons produced in interactions with rest-gas in the beam pipe. The contribution from such events decreases as the electron energy increases.

All cuts are summarized in Tab. 7.1.

Phase space defining cuts in the HCM-frame	
Jets transverse energy	$E_{T1} > 7.5$ GeV, $E_{T2} > 6.5$ GeV
Jets pseudorapidity	$-3.0 < \eta_{1,2} < 0$
Technical cleaning cuts in the laboratory frame	
Inelasticity	$0.2 < y_{JB} < 0.55$
Cuts on electron finder	$\mathcal{P} > 0.9$, $E_{elec} > 10$ GeV
Vertex cut	$\lvert z_{vertex}\rvert < 40$ cm
Box cut (DIS events)	$\lvert x_e\rvert > 14$ cm, $\lvert y_e\rvert > 9$ cm
Box cut (BPC events)	$5.37 < x_{e,BPC} < 9.57$ cm $-2.62 < y_{e,BPC} < 2.98$ cm $x_{e,BPC} + y_{e,BPC} < 11.35$ cm $x_{e,BPC} - y_{e,BPC} < 10.99$ cm
BPC shower widths	$\Delta x_{shower}, \Delta y_{shower} < 0.7$ cm
BPC energy cut	$E_e > 12.5$ GeV

Table 7.1: Summary of the cuts defining the available phase space of the hadronic final state in the HCM-frame of reference and the technical cleaning cuts applied in the laboratory frame of reference. For details see text.

Chapter 8

Unfolding Detector Effects and Determination of the Uncertainties

Since a detector system like ZEUS does not measure the physics events perfectly, the data have to be corrected for these detector effects. A data correction is generally done in five steps:

1. Events with well known properties must be generated using a simulation program.

2. The generated events are passed through a detector simulation to obtain an information about the detector effects.

3. The created events (generated and simulated events) are processed by the reconstruction chain (electron finding, jet finding, etc.) followed by the application of the various cuts as applied to the data (see the last chapter).

4. It must be assured that the simulated events really describe the measured data before they can be used for the correction procedure. This is often not the case because of inappropriate approximations made in the event generators and imperfections in the detector simulation. Therefore a reweighting procedure is applied to the simulated events to get an agreement with the measured data.

5. The reweighted events are used to correct the measured data.

The items listed above (except item 2 which is treated in the previous chapter) are covered by the following sections. The last section summerizes the systematic uncertainties of this analysis.

8.1 Event Generation

Events must be generated whose properties are well known. This is done by event generators. For the analysis presented here, the event generator HERWIG5.9 has been used together with the proton parton density function of MRSA and the photon parton density function of GRV-LO, where LO indicates that the leading order version of this parameterization was used. The parton density functions are provided via the PDFLIB [Plo95]. To avoid the generation of events which would never pass the above discussed cuts, two filters were applied, a "jet filter" and in the case of the lowest Q^2 bin in addition a "geometrical filter". The jet filter requires that at least two jets were found (using a k_T jet-finder) with a transverse jet energy $E_T > 3$ GeV and $\eta < 3$ in the laboratory frame of reference. Both cuts were chosen loose enough so that they cannot bias the final measurement. The geometrical filter serves to select only those events with electrons measured in the vicinity of the BPC-north module. Only those events can pass this filter where the scattered electrons lie within an azimuth angle φ enclosed by two lines in the ZEUS x–y plane, starting from the origin and passing through the points (3.4 cm, -6.7 cm) and (3.4 cm, 6.8 cm), respectively. This yields $\varphi = 2.2$ rad. Fig.8.1 shows the effect of the geometrical filter. It shows the BPC surface (represented by the grid) together with the BPCs fiducial volume in the ZEUS x–y plane. The generated events from the event generator are shown as scatter plot and are extrapolated to the BPCs surface at $z = -293.8$ cm. The lack of events near the origin comes from the requirement that the events should always have $Q^2 > 0.005$ GeV^2. Assuming that the interactions are azimuthally symmetric, the geometrical reduction factor of the filter is given by $2\pi/\varphi = 2.8$. That means that only one out of three generated events is accepted by the geometrical filter. In the actual analysis the real number of events passing all cuts applied to the events detected by the BPC is extrapolated by multiplying the actual detected number by this geometrical factor to account for the BPCs low geometrical acceptance.

8.2 Detector Simulation

The generated events must be passed through the detector simulation. In the case of ZEUS the detector simulation is performed by the program "**MO**nte Carlo for **Z**EUS **A**nalysis, **R**econstruction and **T**rigger" or MOZART for short. This program simulates the full ZEUS detectors using the GEANT package [Bru87]. MOZART simulates for every particle its interaction with the detector material, possible decays, the signals produced by every detector

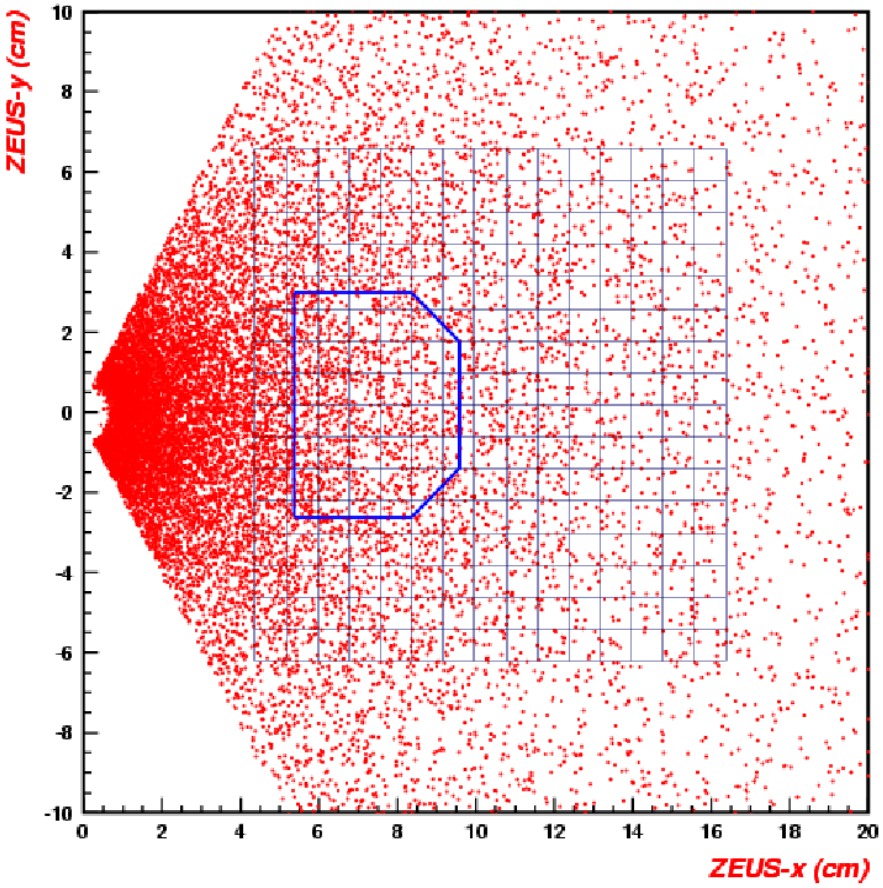

Figure 8.1: Effect of the geometrical filter for the event generator. The BPC surface represented by the grid and its fiducial area are shown in the ZEUS x–y plane. The filter accepts only those events lying within a azimuthal angle $\varphi = 2.2$ rad. These events are shown as points.

component including the various sources of noise and the digitization of the signals. After the simulation one has two event samples at hand. One contains the original events from the event generator and are called the hadron level (HAD-level) events and another that contains the same events, but after the detector simulation. These are called detector level (DET-level) events.

8.3 x_γ^{obs} Reweighting Procedure

The distribution of a physical quantity in a data sample is typically represented by a histogram. Each bin of a histogram generally contains a mixture

of events emerging from direct and resolved interactions. However, event generators are most often not capable to produce the correct mixture, since they contain approximations which are not able to describe the data. The mixing of the two types of events has to be done by hand. In the analysis presented here this mixing was performed as follows:

The event generators give for each generated event sample some additional information. Among others these are the total cross section of the generated events and the "reduction" factor which is defined by the ratio of the total number of actually generated events and the number of events accepted by the applied filter ($f^{red} = N^{gen}/N^{acc}$). These quantities are obtained separately for direct and resolved event samples. From the total cross section and the *measured* luminosity ($\mathcal{L}$) one obtains the expected number of direct (resolved) events in the data sample by $N^{exp}_{dir(res)} = \sigma_{dir(res)} \cdot \mathcal{L}$. This corresponds to a certain number of generated direct (resolved) events given by $N^{gen}_{dir(res)} = f^{red}_{dir(res)} \cdot N^{acc}_{dir(res)}$. Then, for an arbitrary physical quantity one obtains the expected number of direct (resolved) events in a bin i of a histogram ($N^{exp}_{i,dir(res)}$) from the actual number determined in the analysis procedure ($N^{act}_{i,dir(res)}$) by a simple relational ansatz:

$$\frac{N^{exp}_{i,dir(res)}}{N^{act}_{i,dir(res)}} = \frac{\sigma_{dir(res)} \cdot \mathcal{L}}{f^{red}_{dir(res)} \cdot N^{acc}_{dir(res)}}, \tag{8.1}$$

yielding

$$N^{exp}_{i,dir} = \frac{\sigma_{dir} \cdot \mathcal{L}}{f^{red}_{dir} \cdot N^{acc}_{dir}} \cdot N^{act}_{i,dir} = f^{wgt}_{dir} \cdot N^{act}_{i,dir} \tag{8.2}$$

$$N^{exp}_{i,res} = \frac{\sigma_{res} \cdot \mathcal{L}}{f^{red}_{res} \cdot N^{acc}_{res}} \cdot N^{act}_{i,res} = f^{wgt}_{res} \cdot N^{act}_{i,res}. \tag{8.3}$$

So one gets two weight factors; one for direct and one for resolved events:

$$f^{wgt}_{dir} = \frac{\sigma_{dir} \cdot \mathcal{L}}{f^{red}_{dir} \cdot N^{acc}_{dir}} \tag{8.4}$$

$$f^{wgt}_{res} = \frac{\sigma_{res} \cdot \mathcal{L}}{f^{red}_{res} \cdot N^{acc}_{res}}. \tag{8.5}$$

The mixing of the events is now simply performed by filling the histograms with the weight factor of the corresponding type of event (direct or resolved). It should be noted that these weight factors do neither depend on the actual physical quantity nor do they depend on the bin of the histogram. The weight factors are not only supplied to the DET-level events but also to those of the HAD-level.

However, as mentioned above, the agreement between DET-level events and measured data must be enforced by a reweighting procedure. This procedure starts from the distribution of x_γ^{obs} and introduces two new parameter a and b via the ansatz:

$$N_i^{x_\gamma^{obs}} = a \cdot N_{i,dir}^{x_\gamma^{obs}} + b \cdot N_{i,res}^{x_\gamma^{obs}} \tag{8.6}$$

Here i again denotes the bin of the corresponding histogram and $N_{i,dir(res)}^{x_\gamma^{obs}}$ are the numbers of direct (resolved) events in that bin weighted by (8.4) or (8.5), respectively. The parameters a and b have to be determined in such a way that the resulting distribution for x_γ^{obs} fits the corresponding distribution of the measured data. There are no further constraints made on a and b to allow a fit of the shape *and* the normalization of the x_γ^{obs} distribution. The reason why the distribution of x_γ^{obs} is used is simply the fact that here the direct and resolved contributions are well distinguished (see chapter 4). As a result a and b can be varied almost independently. Other distributions show very similar shapes of the distributions of the direct and resolved contributions. This could result into physically meaningless values for the parameters a or b suggesting unphysical contributions from direct or resolved interactions.

The actual determination of the parameters a and b is performed by means of the *least square method* using the ansatz:

$$S(a,b) = \sum_i \frac{\left(N_{i,dat}^{x_\gamma^{obs}} - a \cdot N_{i,dir}^{x_\gamma^{obs}} - b \cdot N_{i,res}^{x_\gamma^{obs}}\right)^2}{\sigma_i^2}. \tag{8.7}$$

Here the sum runs over all bins of the histogram, $N_{i,dat}^{x_\gamma^{obs}}$ is the content of the ith bin of the actual data distribution and σ_i^2 is the sum of the squares of the statistical errors $\sigma_i^2 = \sigma_{i,dat}^2 + \sigma_{i,dir}^2 + \sigma_{i,res}^2$. The parameters a and b are then determined by the requirement that their actual values minimize S. Thus, they are obtained by the conditions

$$\frac{\partial S}{\partial a} = 0 \quad \text{and} \quad \frac{\partial S}{\partial b} = 0, \tag{8.8}$$

leading to the set of two equations:

$$a \cdot \sum_i \frac{(N_{i,dir}^{x_\gamma^{obs}})^2}{\sigma_i^2} + b \cdot \sum_i \frac{N_{i,dir}^{x_\gamma^{obs}} N_{i,res}^{x_\gamma^{obs}}}{\sigma_i^2} = \sum_i \frac{N_{i,dat}^{x_\gamma^{obs}} N_{i,dir}^{x_\gamma^{obs}}}{\sigma_i^2} \tag{8.9}$$

$$a \cdot \sum_i \frac{N_{i,dir}^{x_\gamma^{obs}} N_{i,res}^{x_\gamma^{obs}}}{\sigma_i^2} + b \cdot \frac{(N_{i,res}^{x_\gamma^{obs}})^2}{\sigma_i^2} = \sum_i \frac{N_{i,dat}^{x_\gamma^{obs}} N_{i,res}^{x_\gamma^{obs}}}{\sigma_i^2}. \tag{8.10}$$

The solution of these equations for a and b are simplest obtained from Cramer's rule yielding:

$$a = \frac{\frac{(N_{i,res}^{x_\gamma^{obs}})^2}{\sigma_i^2}\sum_i \frac{N_{i,dat}^{x_\gamma^{obs}} N_{i,dir}^{x_\gamma^{obs}}}{\sigma_i^2} - \sum_i \frac{N_{i,dir}^{x_\gamma^{obs}} N_{i,res}^{x_\gamma^{obs}}}{\sigma_i^2}\sum_i \frac{N_{i,dat}^{x_\gamma^{obs}} N_{i,res}^{x_\gamma^{obs}}}{\sigma_i^2}}{\sum_i \frac{(N_{i,dir}^{x_\gamma^{obs}})^2}{\sigma_i^2}\frac{(N_{i,res}^{x_\gamma^{obs}})^2}{\sigma_i^2} - (\sum_i \frac{N_{i,dir}^{x_\gamma^{obs}} N_{i,res}^{x_\gamma^{obs}}}{\sigma_i^2})^2} \tag{8.11}$$

$$b = \frac{\sum_i \frac{(N_{i,dir}^{x_\gamma^{obs}})^2}{\sigma_i^2}\sum_i \frac{N_{i,dat}^{x_\gamma^{obs}} N_{i,res}^{x_\gamma^{obs}}}{\sigma_i^2} - \sum_i \frac{N_{i,dir}^{x_\gamma^{obs}} N_{i,res}^{x_\gamma^{obs}}}{\sigma_i^2}\sum_i \frac{N_{i,dat}^{x_\gamma^{obs}} N_{i,dir}^{x_\gamma^{obs}}}{\sigma_i^2}}{\sum_i \frac{(N_{i,dir}^{x_\gamma^{obs}})^2}{\sigma_i^2}\frac{(N_{i,res}^{x_\gamma^{obs}})^2}{\sigma_i^2} - (\sum_i \frac{N_{i,dir}^{x_\gamma^{obs}} N_{i,res}^{x_\gamma^{obs}}}{\sigma_i^2})^2} \tag{8.12}$$

From (8.6) and the (8.2–8.5) one can now define new weight factors by:

$$f_{dir}^{rewgt} = \frac{\sigma_{dir}\cdot\mathcal{L}\cdot a}{f_{dir}^{red}\cdot N_{dir}^{acc}} \tag{8.13}$$

$$f_{res}^{rewgt} = \frac{\sigma_{res}\cdot\mathcal{L}\cdot b}{f_{res}^{red}\cdot N_{res}^{acc}}. \tag{8.14}$$

In a new analysis run these weight factors are then applied to fill the events into the histograms to obtain the "reweighted" distributions of the events for the event generator and for the detector simulation. The new weight factors are of course applied to all relevant distributions of physical quantities and not only to those of x_γ^{obs}. The method is successful if after the reweighting procedure all distributions, and not only the one for which the weights have been worked out, are well described.

For each Q^2-region an independent pair (a, b) of reweighting parameters has been calculated. The result of the reweighting procedure on the x_γ^{obs} distribution is shown in Fig. 8.2. The data are shown as dots, the events from HERWIG5.9 on DET-level are shown as histograms. The solid lines show the distribution of the generated events before the reweighting procedure was applied. They clearly overestimate the data in all Q^2-ranges for almost all bins in x_γ^{obs}. The hatched histograms show the same distributions but after the reweighting procedure has been applied. For all Q^2-ranges the data are generally well described. For the other relevant physical quantities (Q^2, E_{T1} and η_{for}) the corresponding comparisons of data to generated events are shown in Figs. 8.3, 8.4 and 8.5In all cases the unreweighted generator events overestimate the data. The reweighted events on the other hand give a good description. It should be mentioned here, that an event generator using leading order matrix elements is generally not able to predict the correct cross section normalization. The fit of the parameters a and b takes the normalization from the measured data and in addition adjusts the ratio of data and simulated events.

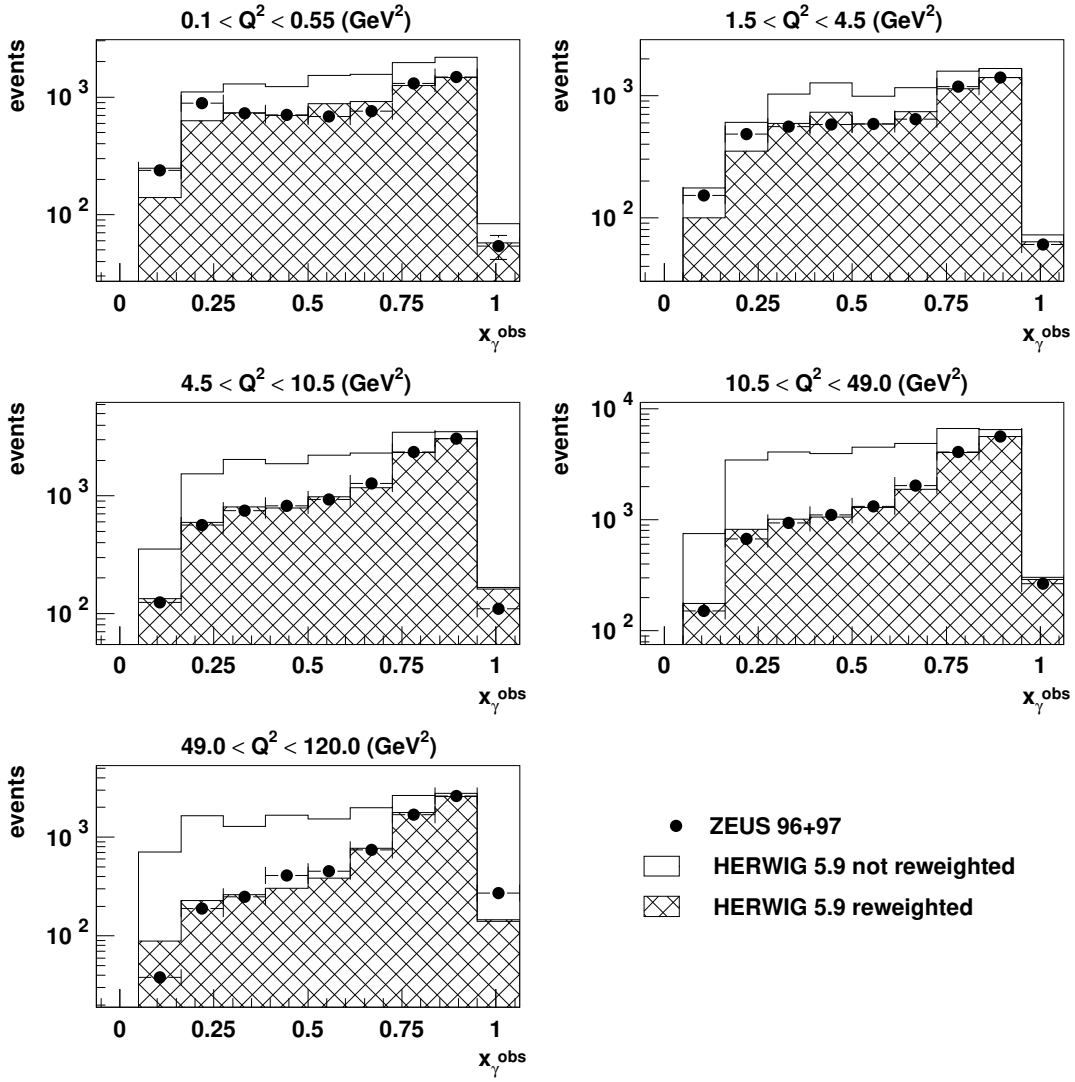

Figure 8.2: Comparison of data with events generated by HERWIG5.9 and simulated for DET-level for the distribution of x_γ^{obs} in the different Q^2-ranges. The dots show the data, the solid lines the generated events filled with normal weights and the hatched histogram the generated events after proper reweighting. For the proton the parton density function of MRSA was used, for the photon the parton density function GRV-LO.

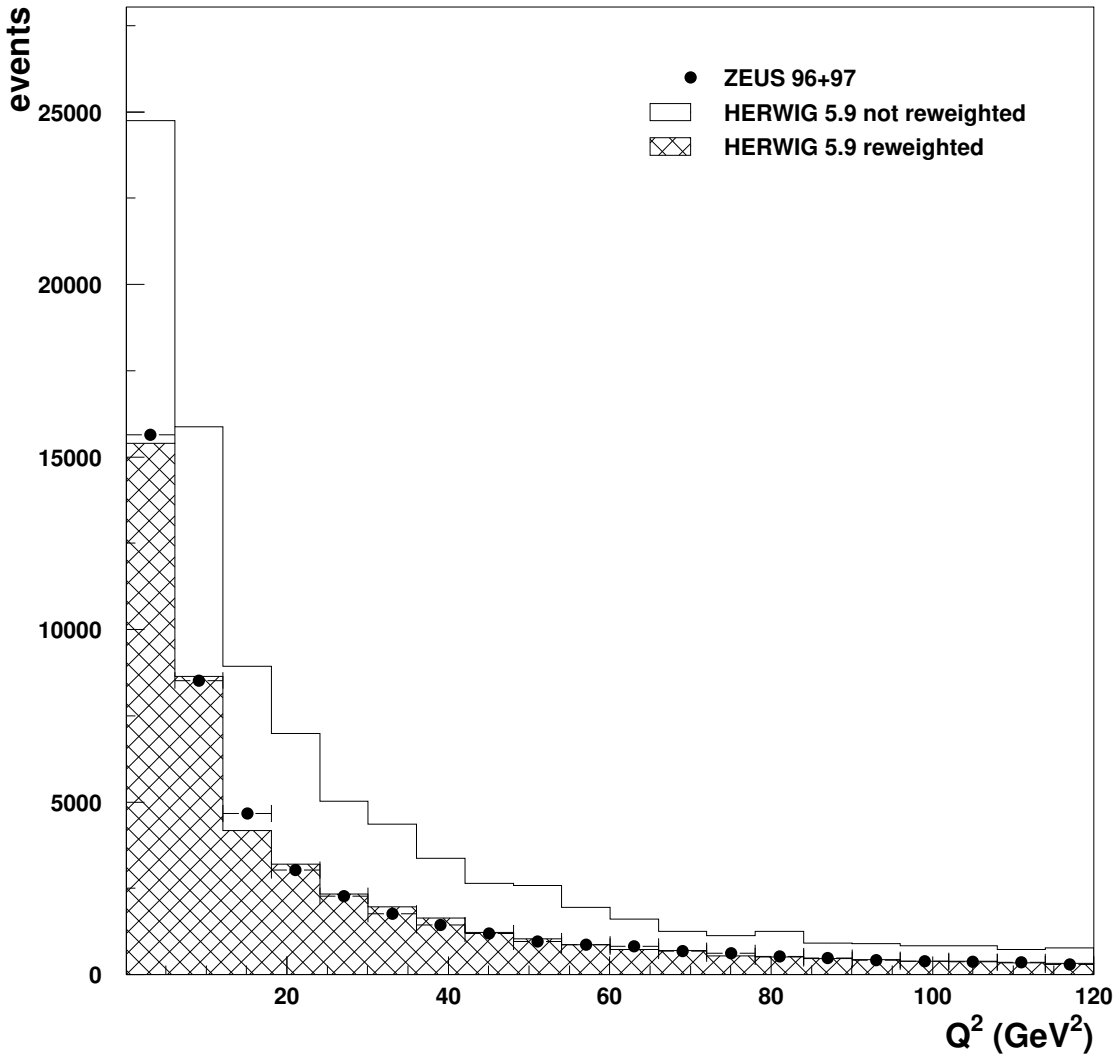

Figure 8.3: Same as for Fig. 8.2 but for the distribution of Q^2.

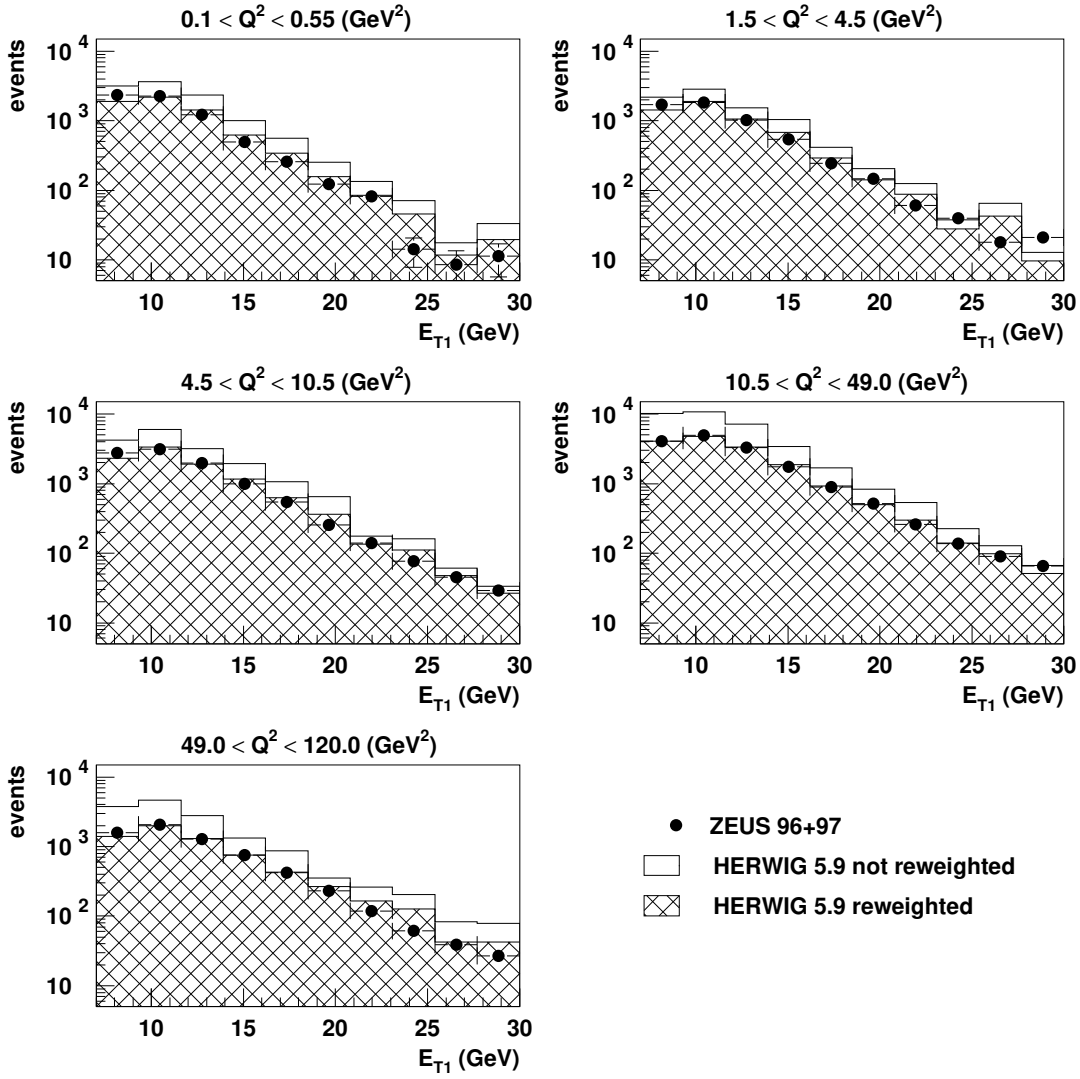

Figure 8.4: Same as for Fig. 8.2 but for the distribution of E_{T1}.

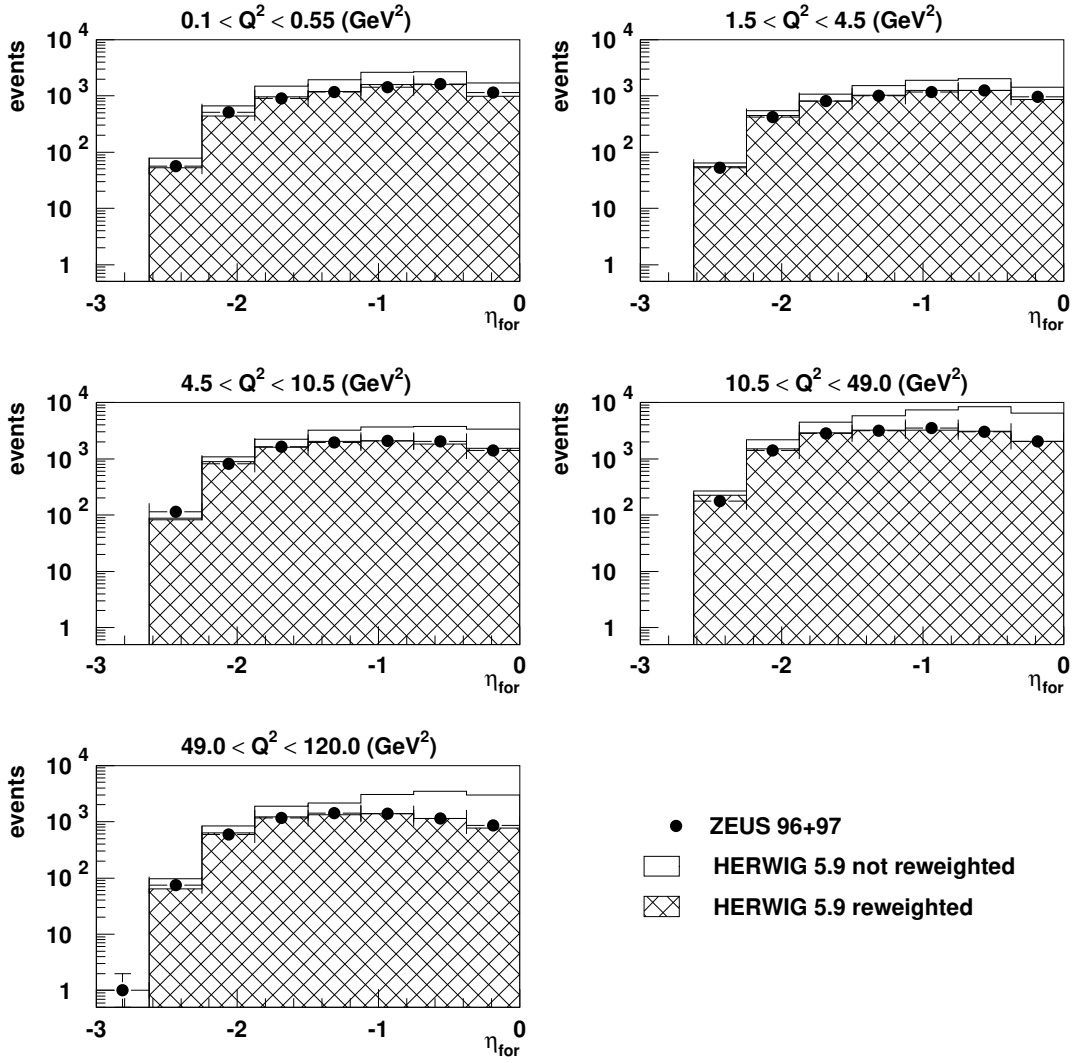

Figure 8.5: Same as for Fig. 8.2 but for the distribution of η_{for}.

8.4 Bin-by-Bin Correction Method

Having simulated events by the event generator (HAD-level) and passing them through the detector simulation (DET-level) one can correct the real data for detector effects. So let's consider the distribution of some physical quantity of the data, represented by a histogram. The corresponding distributions of the generated events on HAD and DET-level are filled, properly weighted of course, into histograms with the same number and width of bins. For the ith bin one gets the corrected content for the data distribution that is the data "corrected to HAD-level" by a simple relational ansatz:

$$\frac{N_{i,dat}^{corr}}{N_{i,dat}} = \frac{N_{i,HAD}}{N_{i,DET}}. \tag{8.15}$$

Here, $N_{i,dat}$ is number of events of the uncorrected data in bin i, $N_{i,dat}^{corr}$ the corresponding corrected number and $N_{i,HAD}$ and $N_{i,DET}$ are the bin contents of the histograms of the generated events on HAD and DET-level, respectively. So for the corrected data distribution one simply reads off:

$$N_{i,dat}^{corr} = \frac{N_{i,HAD}}{N_{i,DET}} \cdot N_{i,dat} \tag{8.16}$$

or

$$N_{i,dat}^{corr} = f_{i,corr} \cdot N_{i,dat} \tag{8.17}$$

with the correction factor defined by $f_{i,corr} = \frac{N_{i,HAD}}{N_{i,DET}}$. Because the correction is done for each bin independently this correction method is called "bin-by-bin" method. However, it remains one problem to solve. The errors of the resulting corrected data values must be computed. Usually this is done by means of the "law of error propagation" but this is only applicable when the involved quantities are not correlated. Unfortunately $N_{i,HAD}$ and $N_{i,DET}$ are correlated to 100% because $N_{i,DET}$ was computed from $N_{i,HAD}$ in the detector simulation process. One way to solve this problem would be to generate new event samples on HAD-level and to use them in connection with the DET-level events from the old HAD-level sample. However, to avoid the generation of new HAD-level events a different method was used in this analysis which additionally allows a straightforward evaluation of the purities and efficiencies[1] of the simulated distributions. Three numbers (N_1, N_2 and N_3) are introduced for each bin of a histogram which serve to decorrelate the HAD and DET-event samples. The definition of these numbers is as follows (the superscript i denotes the ith bin of a histogram):

[1] The meaning of these quantities is explained later in this section.

N_1^i: Number of events in bin i which belong to the same bin on HAD and on DET-level. That means the number of events which did not migrate in the detector simulation.

N_2^i: Number of events which belong to HAD-bin i but *not* to the corresponding bin on DET-level. So this is the number of events which migrated from HAD-bin i into different bins on DET-level in the detector simulation.

N_3^i: Number of events which belong to DET-bin i but *not* to the corresponding bin on HAD-level. This is the number of events in DET-bin i which migrated into it from different HAD-level bins in the detector simulation. In this way N_3^i is the complement of N_2^i.

This is also visualized in Fig. 8.6.

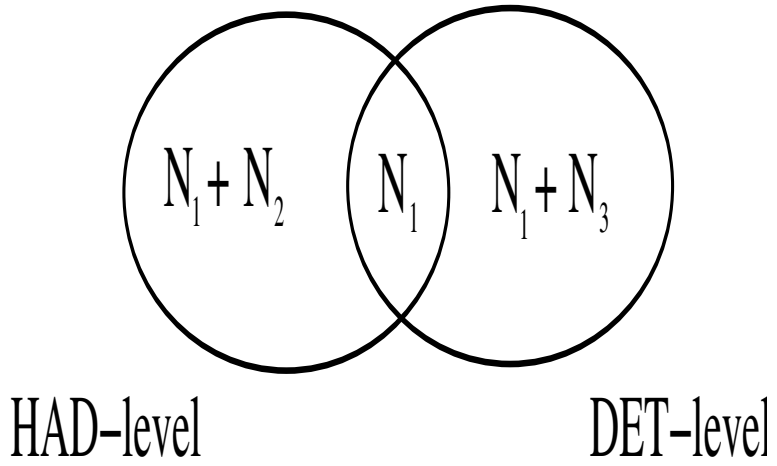

Figure 8.6: Visualization of the definition of the numbers N_1, N_2 and N_3 as given in the text.

Mathematically these definitions read:

$$N_1^i = \#\{\text{events} : \text{event} \in (\text{HAD-bin}^i) \wedge (\text{DET-bin}^i)\} \quad (8.18)$$

$$N_2^i = \#\{\text{events} : \text{event} \in (\text{HAD-bin}^i) \wedge \overline{(\text{DET-bin}^i)}\} \quad (8.19)$$

$$N_3^i = \#\{\text{events} : \text{event} \in \overline{(\text{HAD-bin}^i)} \wedge (\text{DET-bin}^i)\} \quad (8.20)$$

These numbers are constructed in a way that an event attributed to one of these numbers cannot contribute at the same time to one of the other numbers of the same bin. So these numbers are not correlated anymore. In praxis these numbers are also stored in histograms and the events are of

course filled into these histograms with the appropriate weight to ensure the correct mixing of direct and resolved events. In terms of these numbers the correction factor $f_{i,corr}$ reads:

$$f_{i,corr} = \frac{N_1^i + N_2^i}{N_1^i + N_3^i}. \tag{8.21}$$

For its error one finds by the law of error propagation:

$$\sigma_{f_{i,corr}} = \frac{1}{(N_1^i + N_3^i)^2}\sqrt{(N_3^i - N_2^i)^2 \cdot \sigma^2_{N_1^i} + (N_1^i + N_3^i)^2 \cdot \sigma^2_{N_2^i} + (N_1^i + N_2^i)^2 \cdot \sigma^2_{N_3^i}}. \tag{8.22}$$

The σ_{N^i} are the statistical error of the N's. The migrations of events from a given HAD-bin into a different DET-bin in the detector simulation are quantified by the "purity" defined by:

$$\mathrm{Pu}_i = \frac{N_1^i}{N_1^i + N_3^i} \tag{8.23}$$

and by the "efficiency" given by:

$$\mathrm{Eff}_i = \frac{N_1^i}{N_1^i + N_2^i}. \tag{8.24}$$

For the errors for these quantities one gets from the law of error propagation:

$$\sigma_{Pu_i} = \frac{1}{(N_1^i + N_3^i)^2}\sqrt{(N_3^i)^2 \cdot \sigma^2_{N_1^i} + (N_1^i)^2 \cdot \sigma^2_{N_2^i}} \tag{8.25}$$

$$\sigma_{Eff_i} = \frac{1}{(N_1^i + N_2^i)^2}\sqrt{(N_2^i)^2 \cdot \sigma^2_{N_1^i} + (N_1^i)^2 \cdot \sigma^2_{N_2^i}}. \tag{8.26}$$

The purity gives the fraction of events contained in a particular DET-bin which stems from the corresponding HAD-bin. So $1 - Pu_i$ gives the degree of contamination of DET-bin i by events from HAD-bins different from i. The efficiency on the other hand gives the fraction of events from a particular HAD-bin that do not migrate in the detector simulation. From this consideration it is clear that the bin width of an individual histogram should be chosen wide enough to give reliable purities and efficiencies for each bin, but at the same time it must also be small enough so that the histogram displays sufficient details of the data distribution. In any case the bin width has to be chosen in accordance with the resolution of the detector system. The resolution for a physical quantity X is obtained from the detector simulation and is given by the standard deviation of a Gaussian fitted to the distribution of the difference $\Delta X = X_{HAD} - X_{DET}$ for dimensionless quantities. For

quantities having a dimension the fit is done for $\Delta X/X_{HAD}$ to get a dimensionless distribution variable. The results of the fit are shown in Figs. 8.7 and 8.8. The detector resolutions are in the plots denoted as "Sigma" and are summarized in Tab. 8.1. The bin width of the histograms and the ranges

Physical Quantity	Detector Resolution (σ)
Q^2	0.07
E_{T1}	0.13
E_{T2}	0.14
η_1	0.08
η_{for}	0.09
y_{JB}	0.04
E_e (CAL)	0.05
E_e (BPC)	0.05
x_γ^{obs}	0.05

Table 8.1: Resolution of the ZEUS detector system for the quantities used in this analysis. The resolutions refer to dimensionless quantities as explained in the text.

in Q^2 in which the cross sections were measured (see last chapter) have been chosen as multiples of the detector resolution of the corresponding variables.

The purities of the distributions of Q^2, E_{T1}, η_{for} and x_γ^{obs} are shown in Figs. 8.9, 8.10, 8.11 and 8.12, respectively. Generally the purity is quite large in all distribution. They are a bit lower in the E_{T1}-distributions for low E_{T1}. For the Q^2-distribution (Fig. 8.9) they are between 0.65–0.7. In the E_{T1}-distributions (Fig. 8.10) the purity varies between 0.4 at low values of E_{T1} up to 0.5–0.8 at high values. The purity decreases with decreasing E_{T1}. The migration of events results from energy losses of the particles when they traverse inactive ("dead") material. So bins at lower E_{T1} at DET-level are enriched by events coming from HAD-bins at higher energy. The purities for the η_{for}-distributions (Fig. 8.11) are around 0.6 for all Q^2-ranges. For the x_γ^{obs}-distributions (Fig. 8.9) the purity is around 0.4 in all Q^2 ranges for $x_\gamma^{obs} < 0.75$ while for $x_\gamma^{obs} > 0.75$ it is around 0.7.

The efficiencies of these distributions are shown in Figs. 8.13, 8.14, 8.15 and 8.16.The efficiencies of the Q^2-distribution (Fig. 8.13) ranges from 0.55 to 0.65 in the higher Q^2-bins and from 0.13 to 0.2 in the two lowest Q^2-bins. The poor values in this low Q^2-range is again due to the small acceptance of the detector setup in this range. A similar behavior is apparent from the E_{T1}-distributions (Fig. 8.14). In the lowest Q^2-range the efficiency varies from 0.06 to 0.1 in the next higher Q^2-range it reaches a maximum of 0.3.

In the higher Q^2-ranges the efficiency varies from around 0.3 up to 0.6–0.7. All these distributions show a decrease of the efficiency with decreasing E_{T1}. The η_{for}-distributions (Fig. 8.15) show the same poor efficiency for the two lowest Q^2-ranges as the Q^2 and E_{T1}-distributions. In the lowest Q^2-range the efficiency varies around 0.1, in the next higher range around 0.17. The higher Q^2-ranges show efficiencies between 0.4 and 0.6. All the E_{T1}-distributions and the η_{for}-distributions in the higher Q^2-ranges show a decrease of the efficiency with decreasing E_{T1} and η_{for}, respectively. This is probably due to an acceptance effect as will be discussed in connection with the correction factor below. A similar picture is shown by the efficiency of the x_γ^{obs}-distributions (Fig. 8.16). In the lowest Q^2 range the efficiency rises from 0.07 for low x_γ^{obs} up to 1.05 for high x_γ^{obs}. In the next highest Q^2 range the efficiency is 0.08 in the lowest x_γ^{obs} range and varies between 0.15 and 0.19 in the higher x_γ^{obs} ranges. For the higher Q^2 ranges the efficiencies rise from 0.22 up to 0.6. As for the other quantities the efficiency for the x_γ^{obs}-distribution increases with increasing Q^2.

The correction factors for the distributions of Q^2, E_{T1}, η_{for} and x_γ^{obs} are shown in Figs. 8.17, 8.18, 8.19 and 8.20. The correction factor for Q^2 (Fig. 8.17) lies around 1 for the higher Q^2-ranges and is quite high (around 5.8 and 3.3, respectively) for the two lowest Q^2-ranges. The correction factors for E_{T1} (Fig. 8.18) and η_{for} (Fig. 8.19) show the same behavior. For the E_{T1}-distribution f_{corr} lies in between 4–7 for the lowest Q^2-range and between 2–4 in the next highest range in Q^2. In all other Q^2-ranges f_{corr} varies around 1. In the η_{for}-distribution f_{corr} lies in between 5.5–6 in the lowest and varies around 3.5 in the next higher Q^2-range. The same behavior is shown by f_{corr} for the x_γ^{obs}-distributions (Fig. 8.20). In the lowest Q^2 range f_{corr} varies between 5 and 7, and in the next highest Q^2 range between 2.7 and 3.9. For the higher Q^2 ranges f_{corr} is much smaller (between 0.7 and 1.4). The reason for this behavior is the low acceptance of the detector system for positron scattered under a small angle. The applied box cut removes many events and in particular in the lowest Q^2-range the scattered positron is measured by the BPC which has has a rather limited geometrical acceptance (see the discussion concerning the geometrical filter for the event generator at the beginning of this chapter).

To summerize from the above results: The reweighted event samples from HERWIG5.9 and the detector simulation describe the data quite well. The bin width of the histograms was chosen large enough to give reliable values of the correction factors, purities and efficiencies for all considered distributions. The quite high correction factors and low purities and efficiencies in the low Q^2 ranges are due to the low detector acceptance for scattered positrons in this Q^2 region and are therefore unavoidable.

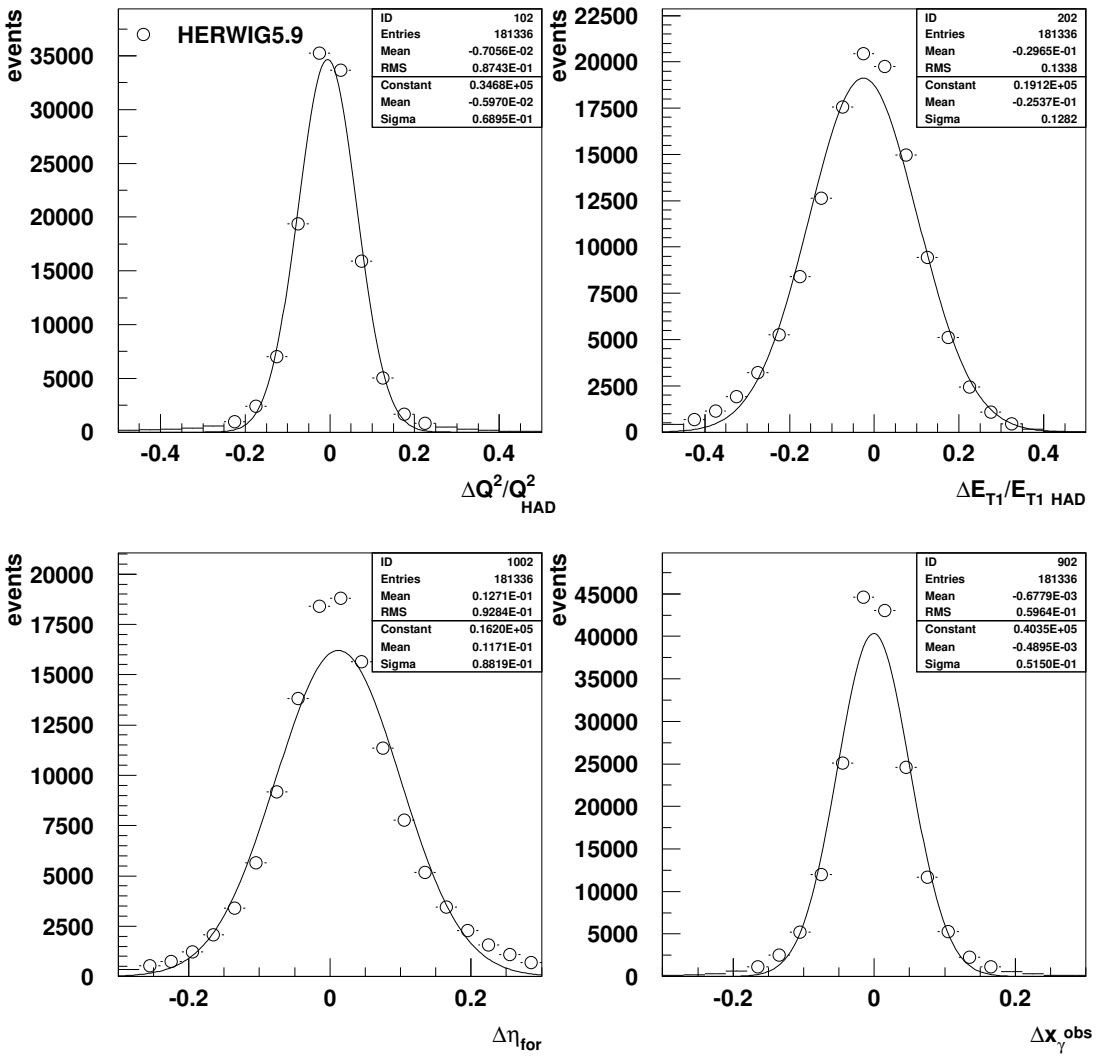

Figure 8.7: Gaussian fits (solid line) to the difference $\Delta X = X_{HAD} - X_{DET}$ or $\Delta X/X_{HAD}$ of the quantities Q^2, E_{T1}, η_{for} and x_γ^{obs} obtained from HERWIG5.9 using MRSA as parton density function of the proton and GRV-LO as parton density function of the photon. The resolution, "Sigma", of the detector system can be read off from the plots.

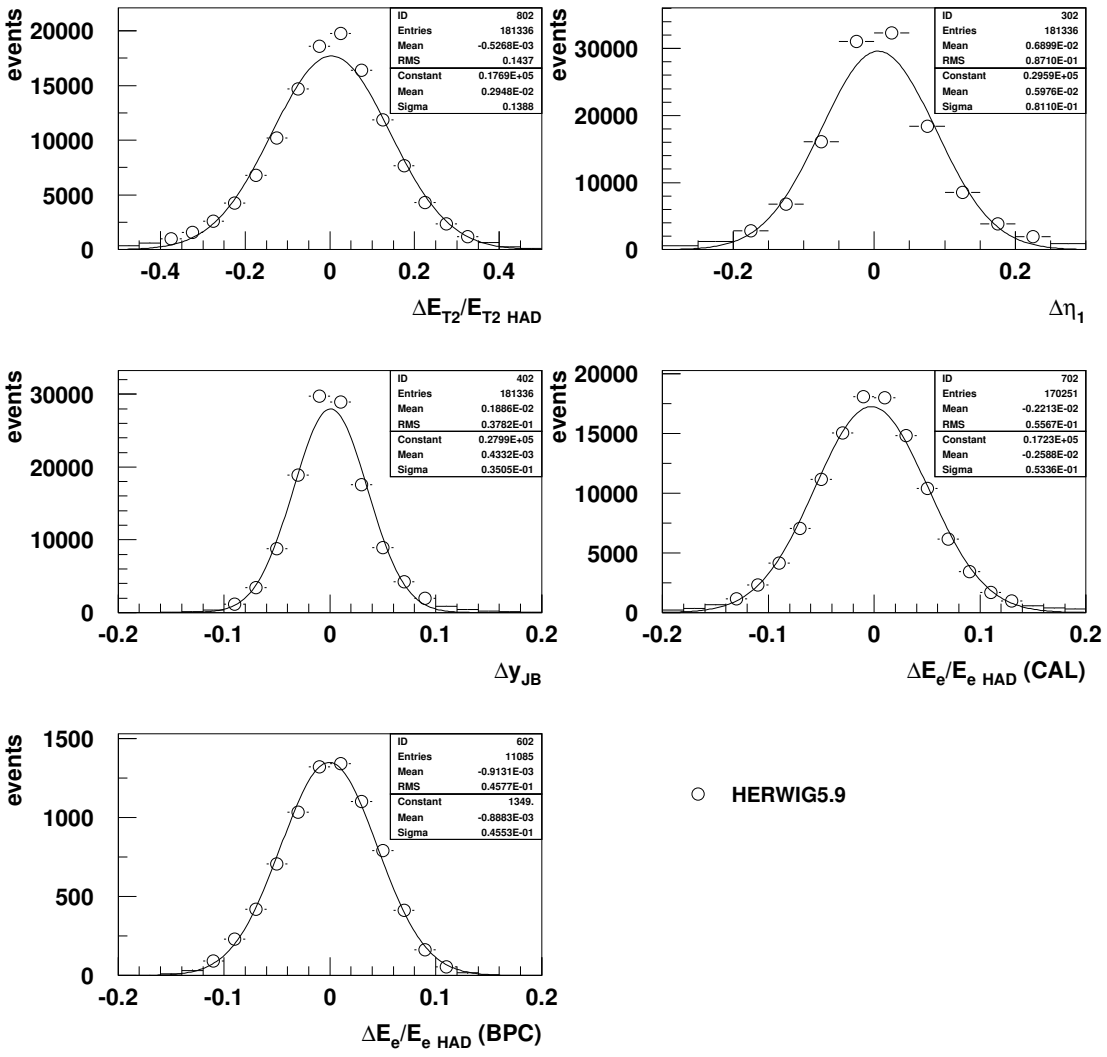

Figure 8.8: Same as in Fig. 8.7 but for the quantities E_{T2}, η_1, y_{JB} and the positron energy (E_e) as measured by the CAL and by the BPC, respectively.

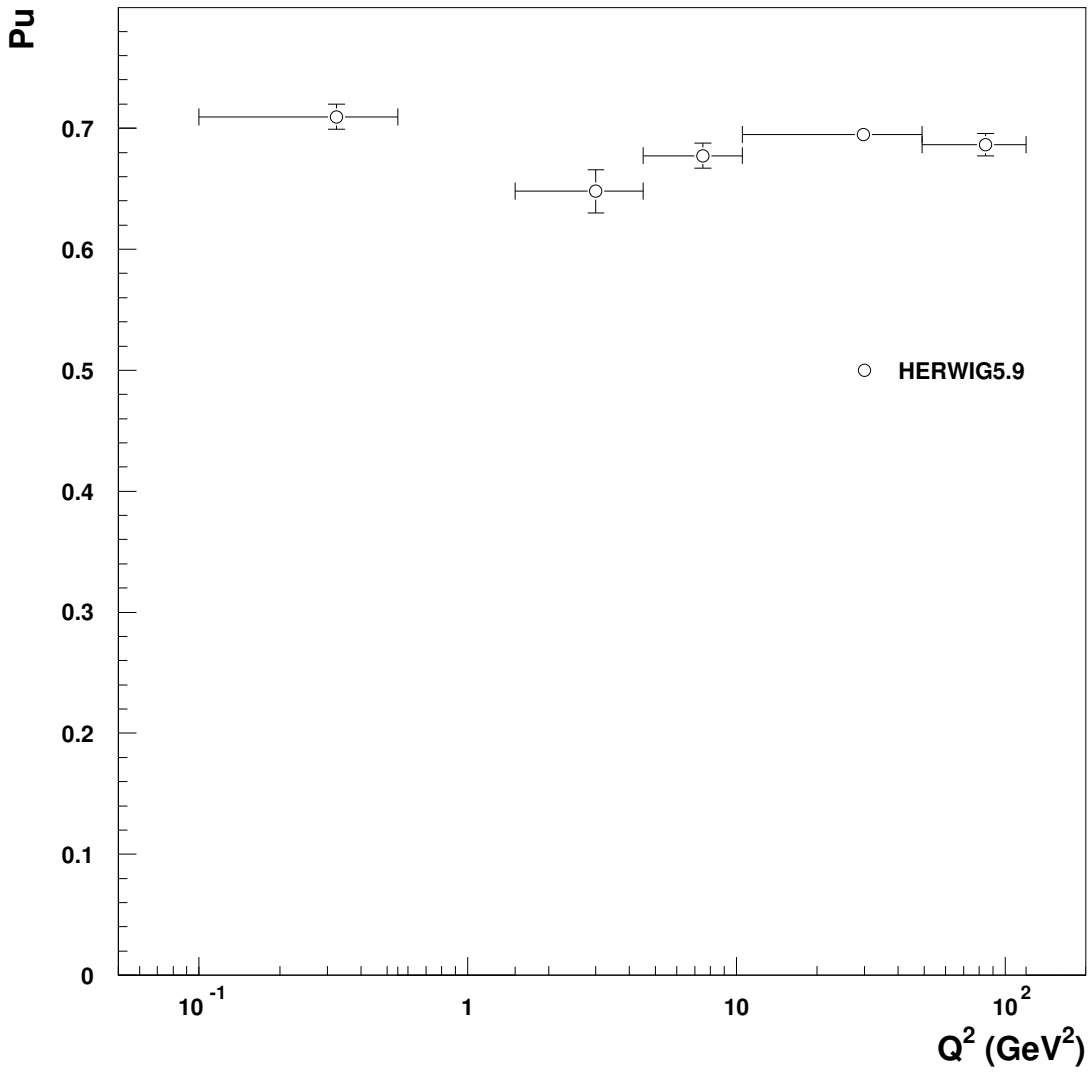

Figure 8.9: Purities for the distribution of Q^2 as obtained from events generated with HERWIG5.9 using MRSA as parton density function of the proton and GRV-LO as parton density function of the photon.

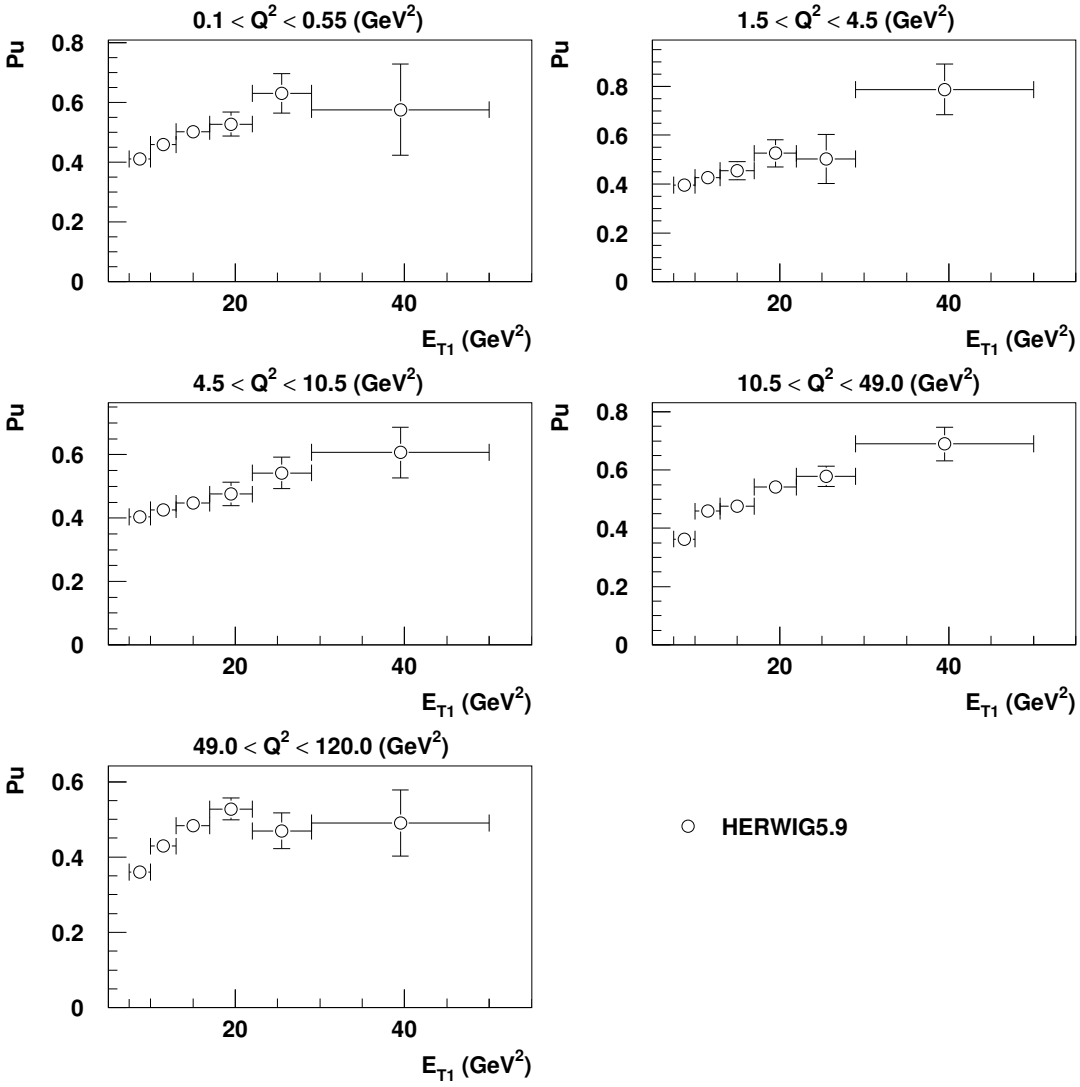

Figure 8.10: Same as in Fig. 8.9 but for the distribution of E_{T1}.

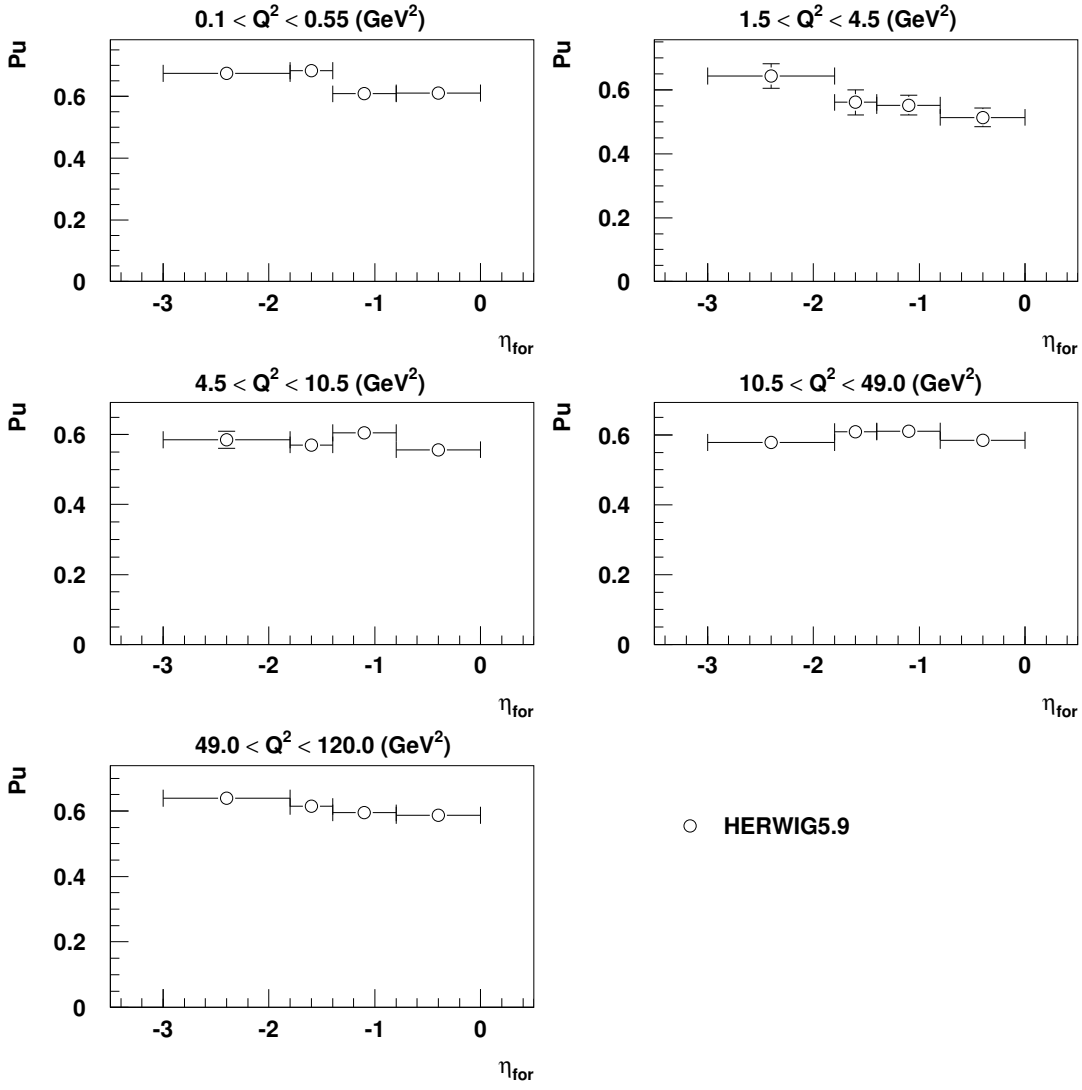

Figure 8.11: Same as in Fig. 8.9 but for the distribution of η_{for}.

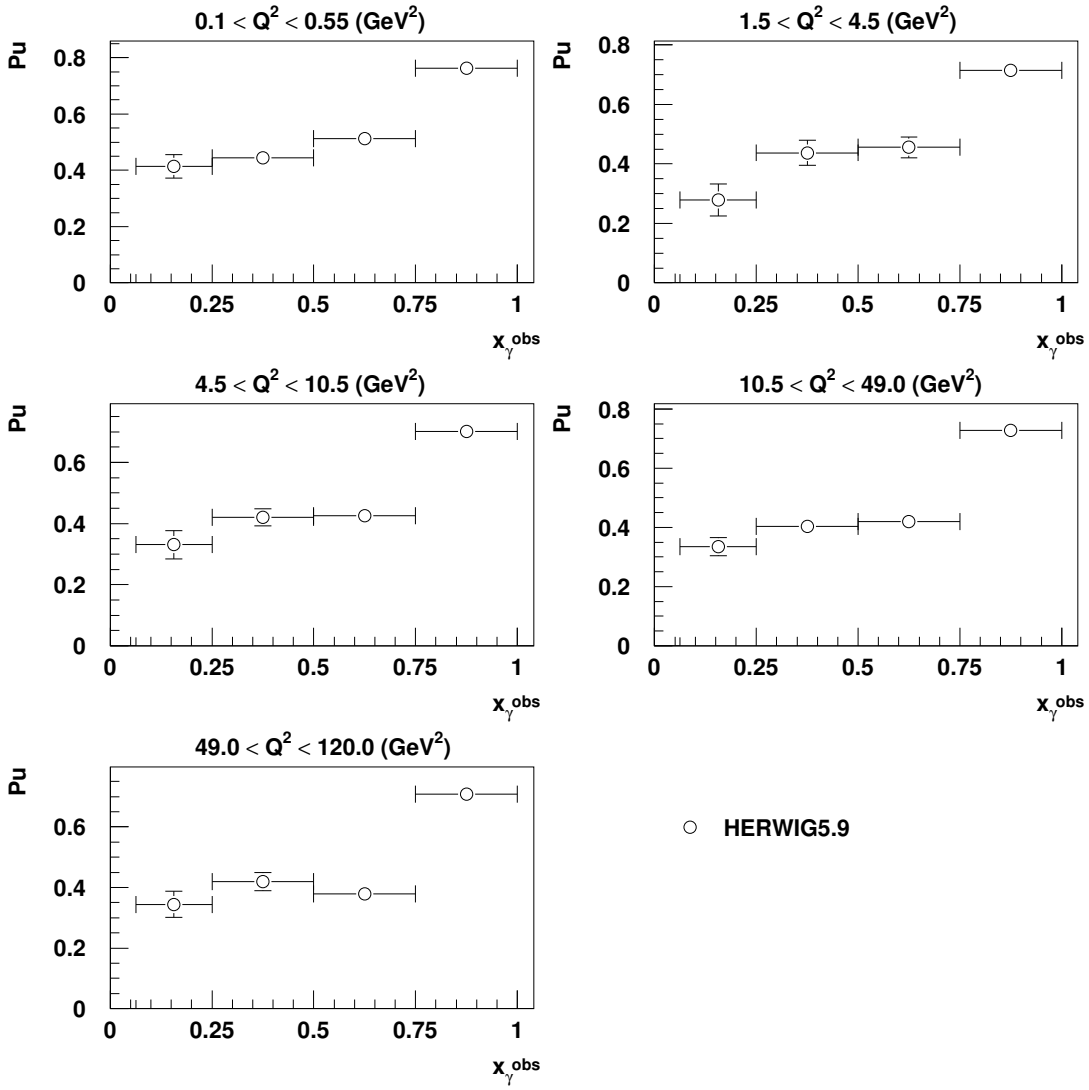

Figure 8.12: Same as in Fig. 8.9 but for the distribution of x_γ^{obs}.

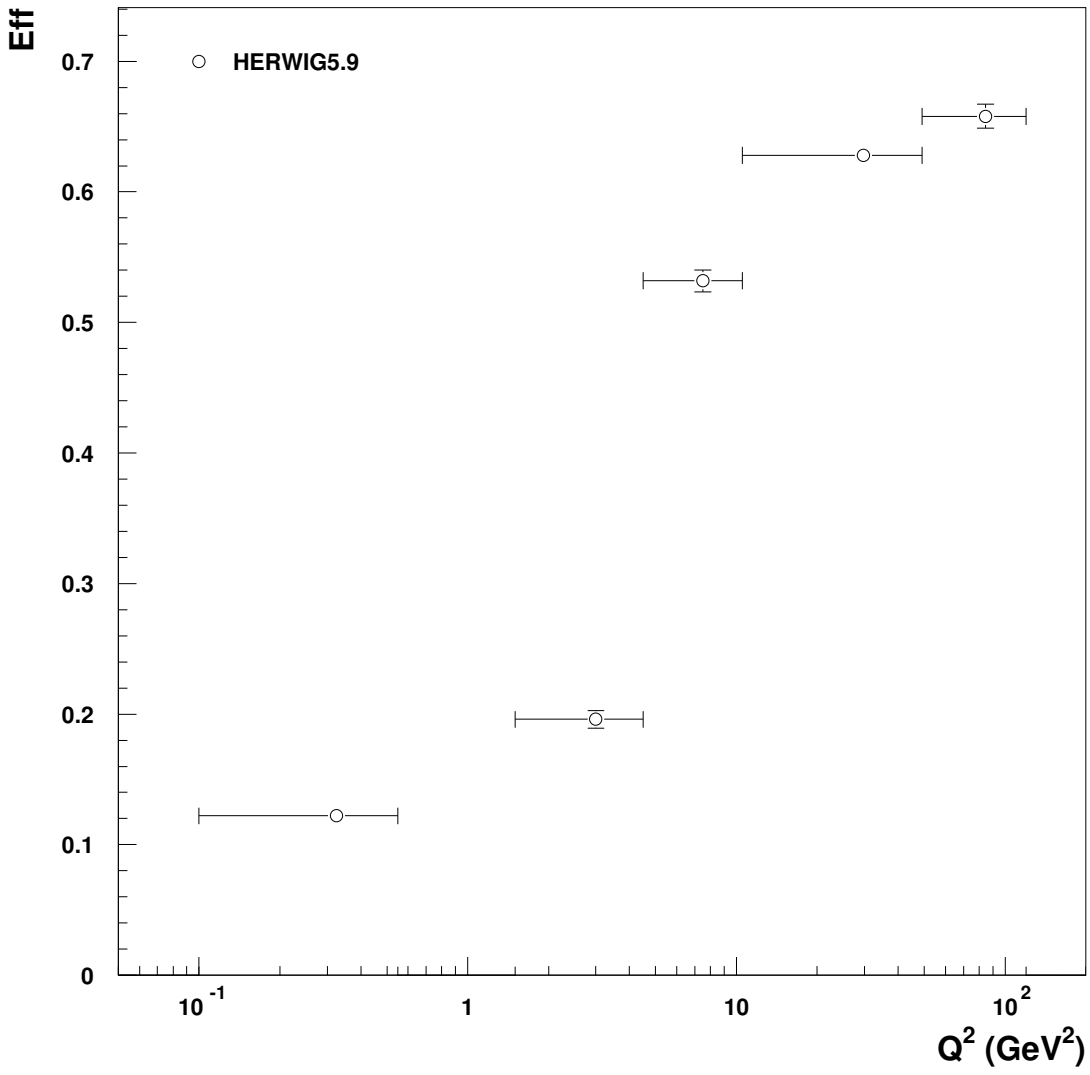

Figure 8.13: Efficiencies for the distribution of Q^2 as obtained from events generated with HERWIG5.9 using MRSA as parton density function of the proton and GRV-LO as parton density function of the photon.

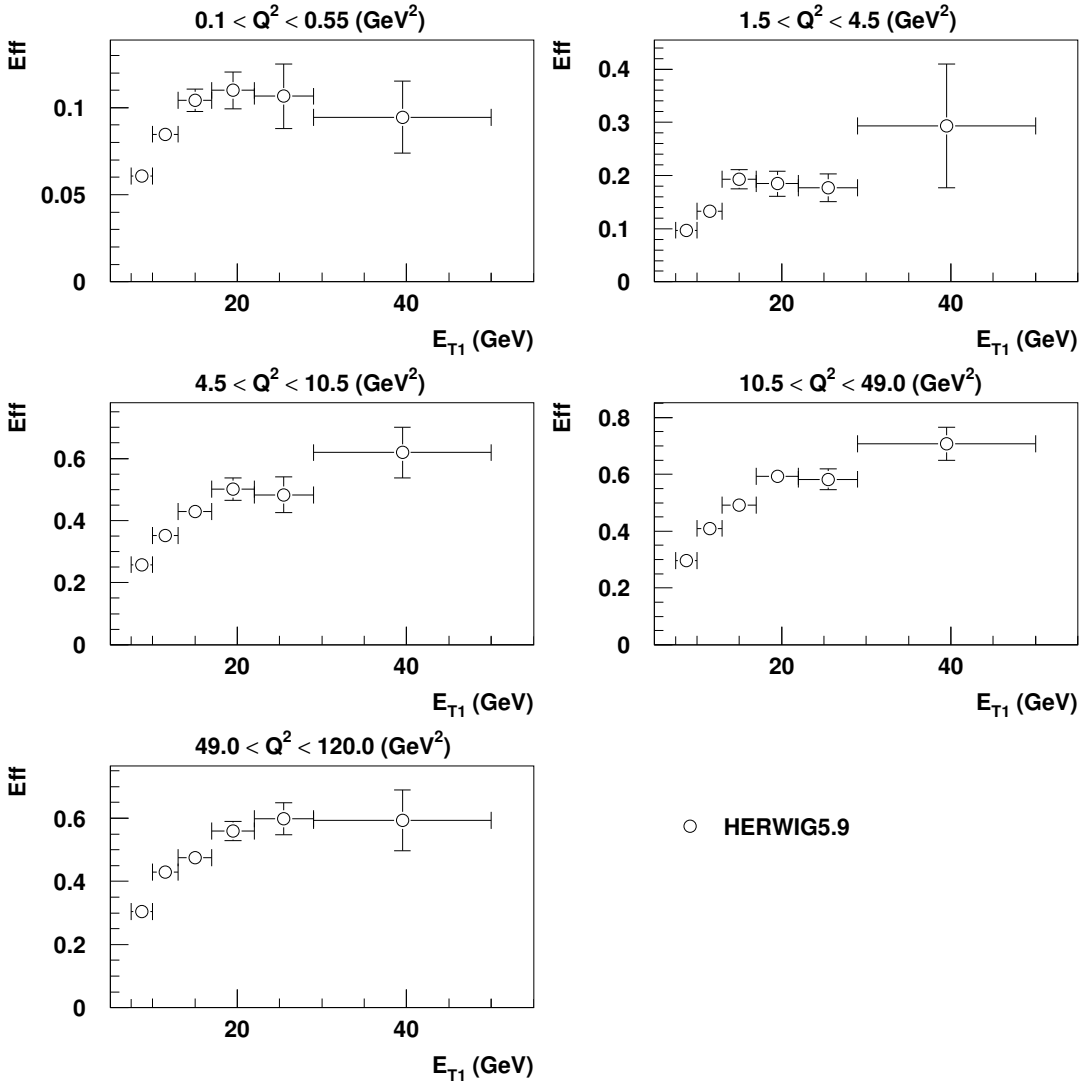

Figure 8.14: Same as in Fig. 8.13 but for the distribution of E_{T1}.

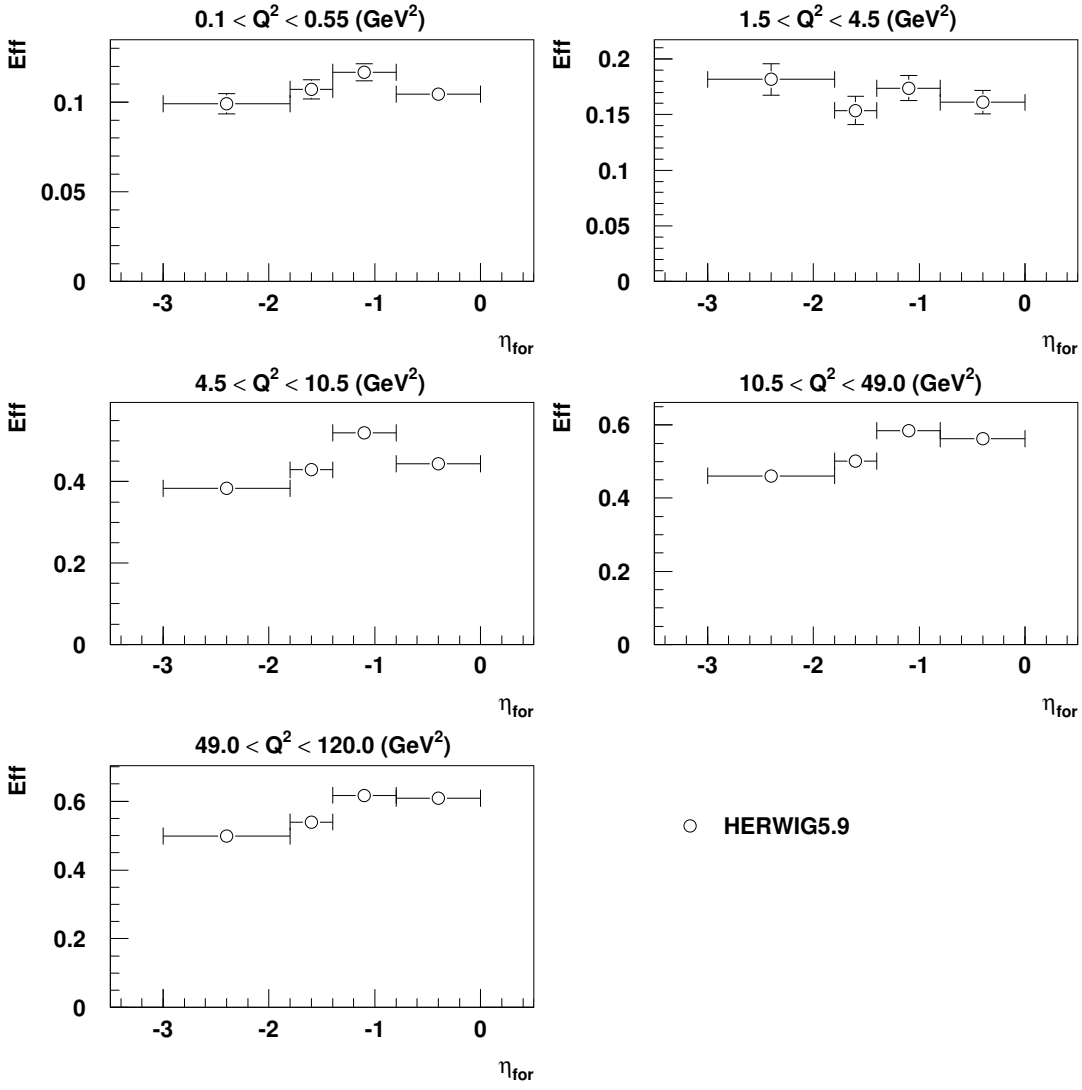

Figure 8.15: Same as in Fig. 8.13 but for the distribution of η_{for}.

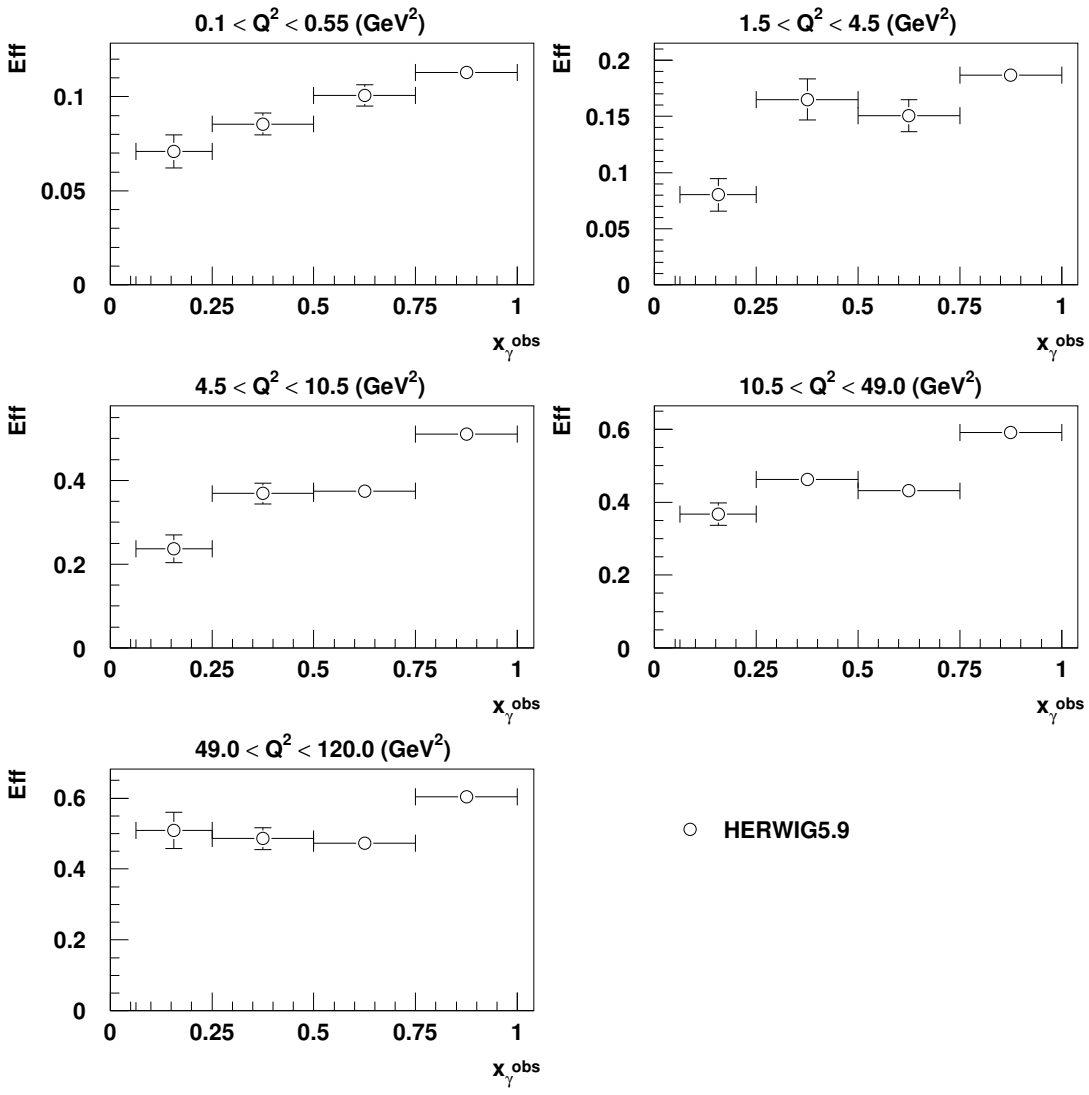

Figure 8.16: Same as in Fig. 8.13 but for the distribution of x_γ^{obs}.

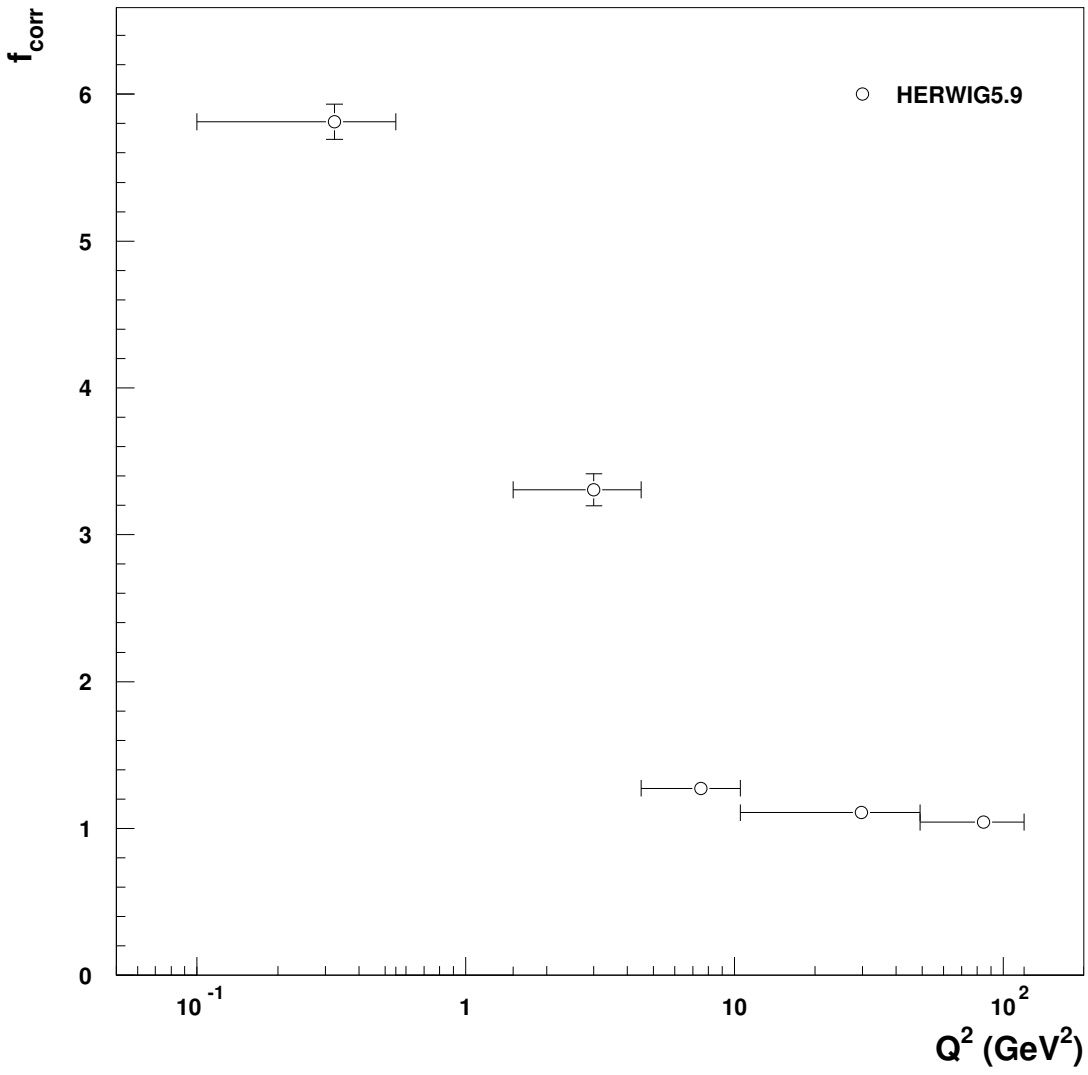

Figure 8.17: Correction factors for the distribution of Q^2 as obtained from events generated with HERWIG5.9 using MRSA as parton density function of the proton and GRV-LO as parton density function of the photon.

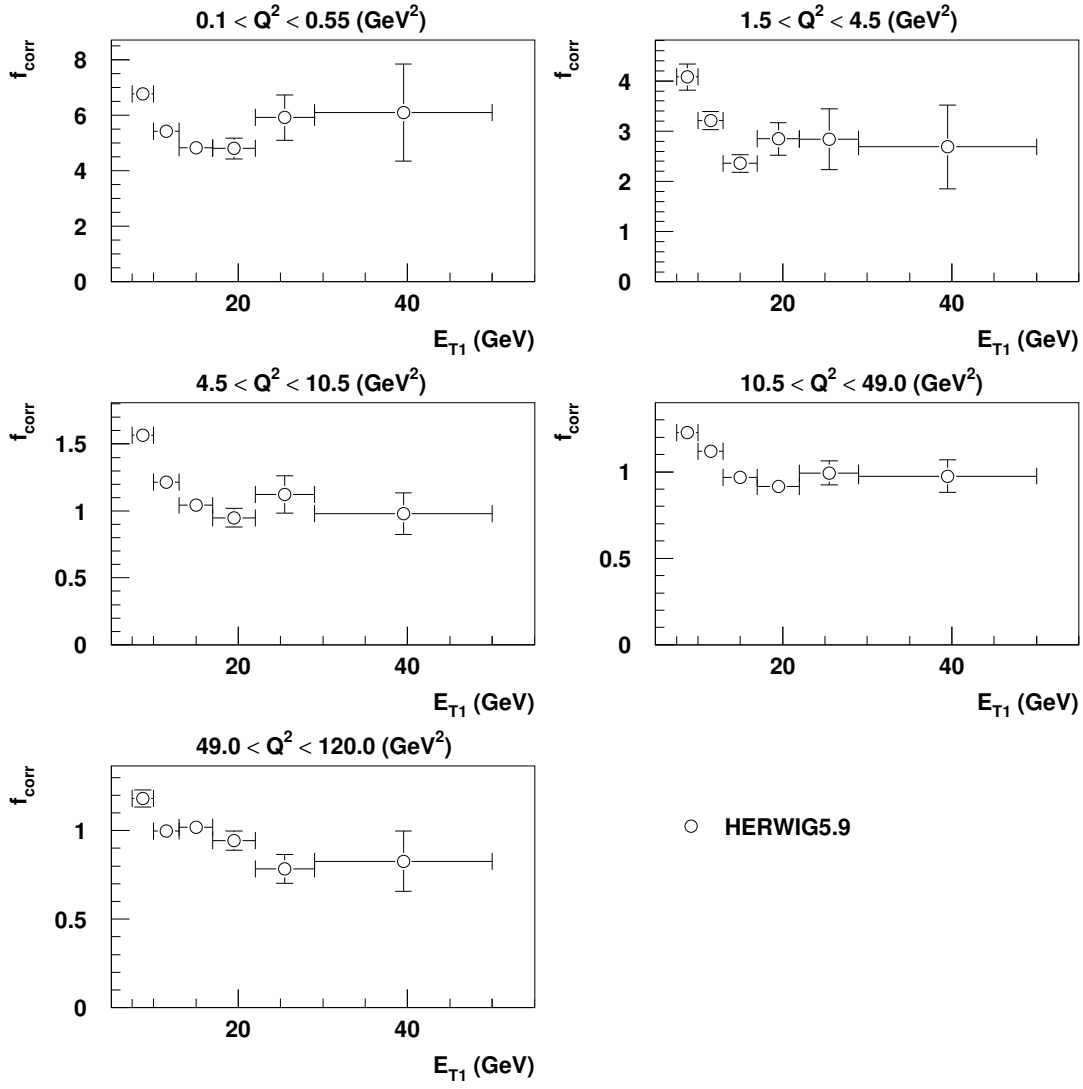

Figure 8.18: Same as in Fig. 8.17 but for the distribution of E_{T1}.

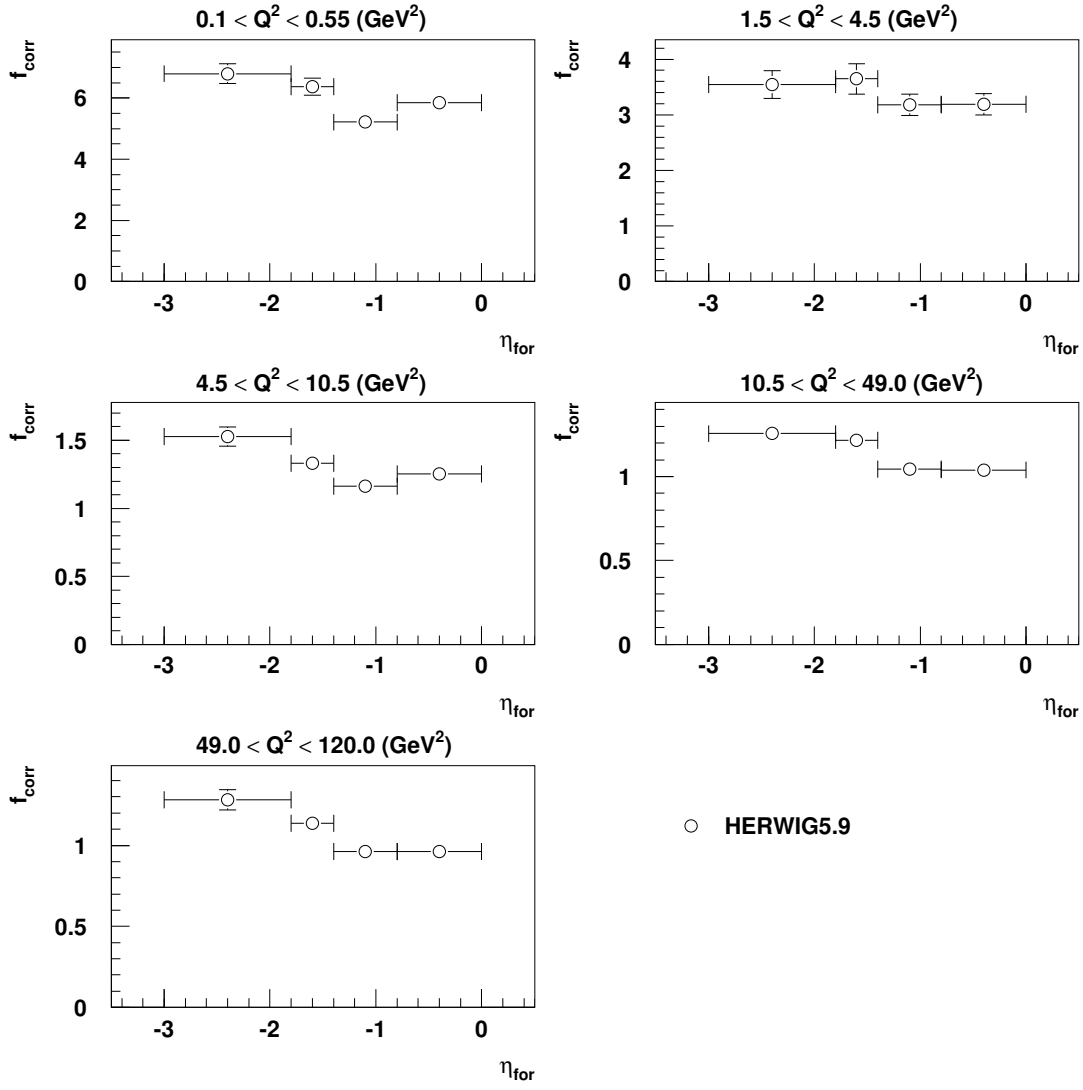

Figure 8.19: Same as in Fig. 8.17 but for the distribution of η_{for}.

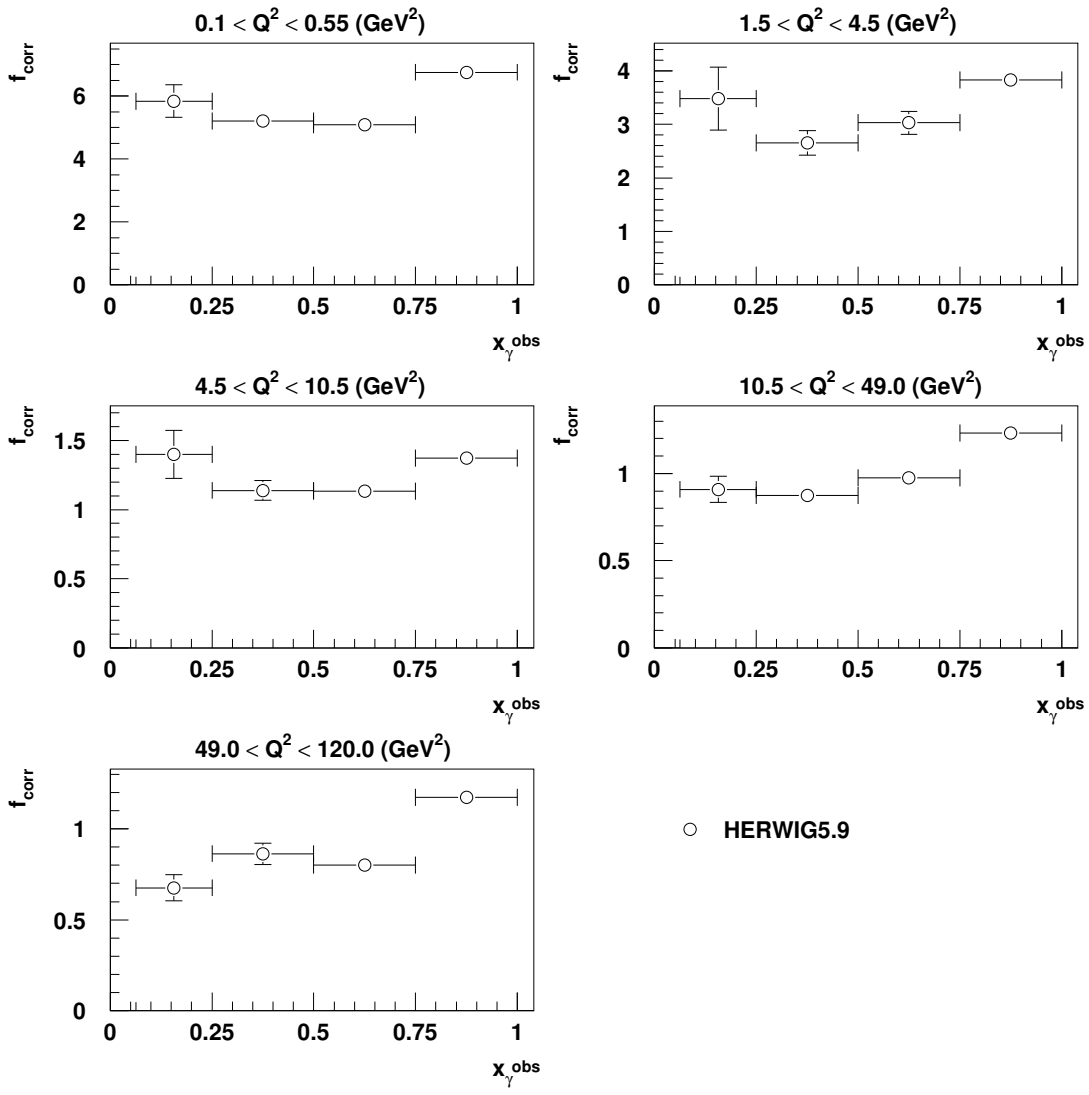

Figure 8.20: Same as in Fig. 8.17 but for the distribution of x_γ^{obs}.

8.5 Determination of the Uncertainties

8.5.1 Experimental Uncertainties

There are two types of uncertainties to be considered. One is of a pure statistical nature and originates from the fact that the data inside a bin of a histogram are Poisson distributed. Therefore this statistical error is simply given by $\sqrt{N_i}$ where N_i is the number of events in the ith bin. The other type of uncertainties stems from uncertainties related to the various measurements performed by the detector and are called "systematic uncertainties". They are due to an incomplete understanding of detector effects and imperfect detector simulation which directly affects the precision of the correction factors. Another source of systematic uncertainties is due to the modeling of the hadronization process leading to imperfections in the modeling of the hadronic final state e.g. of the energy flow in the detector. To estimate the size of the systematic uncertainty the analysis was repeated in a modified way as listed below. The cited "typical values" give the deviation of the altered to the standard settings in per cent which were observed in most of the bins of the variable distributions for which cross sections were determined. This gives an idea of the size of the corresponding systematic uncertainty. For the uncertainty calculation of the cross section of course every single value of each individual bin has been taken into account.

- The values of the cuts on the variables on DET-level were varied around their specified values up and down by one standard deviation of their respective resolutions. The cuts on HAD-level were kept constant because they define the phase space inside which the cross section was measured. In the following the details of this variation taking into account the different normalizations of the resolutions for dimensionless quantities and those with dimensions (see Tab. 8.1) are listed.

  * Cut on E_{T1}: $E_{T1} \pm E_{T1} \cdot \sigma_{E_{T1}}$, $(\sigma_{E_{T1}} = 0.13)$.
  * Cut on E_{T2}: $E_{T2} \pm E_{T2} \cdot \sigma_{E_{T2}}$, $(\sigma_{E_{T2}} = 0.14)$.
  * Cut on y_{JB}: $y_{JB} \pm \sigma_{y_{JB}}$, $(\sigma_{y_{JB}} = 0.04)$.
  * Cut on η : $\eta \pm \sigma_{\eta}$, $(\sigma_{\eta} = 0.08)$.
  * Cut on the positron energy measured by the CAL: $E_e \pm E_e \cdot \sigma_{E_{CAL}}$, $(\sigma_{E_{CAL}} = 0.05)$.
  * Cut on the positron energy measured by the BPC: $E_e \pm E_e \cdot \sigma_{E_{BPC}}$, $(\sigma_{E_{BPC}} = 0.05)$.

The values are changed independently that means while one cut was changed the others stayed unaltered. Also the box-cuts were changed. For DIS events the box edges were increased (decreased) by 0.5 cm while for photoproduction events the edges of the cross sectional area bounding the fiducial volume of the BPC where increased (decreased) by 1 mm. The total effect of all these changes except for the variation in E_T was observed to be less than 2%. The E_T cut variation by contrast amounts to 7–9%.

- To take the influence of different phenomenological event generator models into account the analysis was repeated using PYTHIA6.1. On average a deviation of 6% was found compared to HERWIG5.9.

- Using different parton density functions for event generation with HERWIG (GRS instead of GRV-LO for the photon and CTEQ5M1 instead of MRSA for the proton) gave a deviation of about 2%.

- Using only the electron method for reconstruction of the kinematical variables yielded a 0.6% deviation.

All these effects are uncorrelated with each other. The corresponding uncertainties were added to the statistical uncertainty in quadrature. This summation was done in a way that the error of those changes which lowered the cross section with respect to the original settings are added to the lower error bars while those changes which enhanced the cross section are added to the upper error bars.

There are other systematic uncertainties which affect the measurements of all quantities in the same way and are therefore totally correlated. These uncertainties are:

- The uncertainty in the determination of the luminosity for the data taking period 1996/97 is 1.5%. This affects each bin of the measured cross sections in the same way.

- The uncertainty in the absolute jet transverse energy scale of the calorimeter was estimated by comparing the balance of the transverse jet momenta by the transverse momentum of the scattered positron ($p_{T,\mathrm{positron}}$) in the laboratory frame in data and simulated high Q^2 neutral current events. This method is described in [Che01, Che02]. It was found that this scale uncertainty is $\pm 1\%$ for $E_T^{jet} > 7.5$ GeV and $\pm 3\%$ for $6.5 < E_T^{jet} < 7.5$ GeV, as shown in Fig. 8.21. The ratios $r = E_{T,\mathrm{eff}}/p_{T,\mathrm{positron}}$ were measured for data and for simulated events,

where $E_{T,\mathrm{eff}}$ is the sum of the projections of E_{T1} and E_{T2} on the transverse momentum of the positron. In the figure the ratio $r_{\mathrm{dat}}/r_{\mathrm{sim}}$ is plotted against $E_{T,\mathrm{eff}}$ of the jets. The thin vertical lines denote the 1% limit. To obtain the influence of this uncertainty on the cross section the transverse energies of the jets were changed by $\pm 1\%$ and $\pm 3\%$ in the respective E_T ranges. At very low Q^2 this led to a deviation in the cross section of approximately 9% which falls down to 6% at high Q^2.

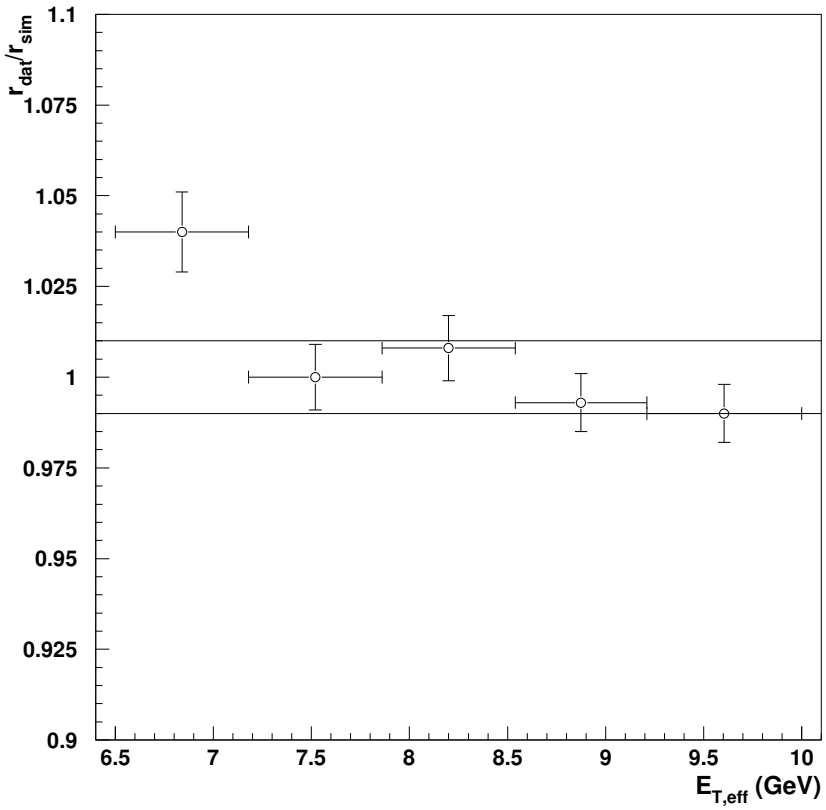

Figure 8.21: Ratio of the ratios $r = E_{T,\mathrm{eff}}/p_{T,\mathrm{positron}}$ of data (r_{dat}) and simulated events (r_{sim}) plotted against the $E_{T,\mathrm{eff}}$ (see text) of the jets to obtain the jet energy scale uncertainty. The vertical lines denote the 1% limit.

8.5.2 Theoretical Uncertainties

The theoretical uncertainties come from several sources. The theoretical calculations are performed to finite order, namely next-to-leading order, in

QCD. Therefore there will be some dependence of the calculated cross sections on the scale μ_R^2 and μ_F^2 introducing a systematic uncertainty into the calculations. Another uncertainty comes from the hadronization corrections. As was pointed out in chapter 2 the next-to-leading order calculations only yields parton quantities. For comparisons with the measured cross sections they have to be corrected to hadron level. This was done by the bin-by-bin correction method as explained above, except that here the method is applied to the differential cross sections instead of the reweighted event numbers. From (8.16) one gets:

$$d\sigma_{i,theory}^{corr} = \frac{N_{i,HAD}}{N_{i,PAR}} \cdot d\sigma_{i,theory} = C_{i,corr} \cdot d\sigma_{i,theory}. \tag{8.27}$$

The numbers $N_{i,PAR}$ and $N_{i,HAD}$ are the numbers of events in bin i on parton and hadron level, respectively. $d\sigma_{i,theory}$ is the bin content as calculated by the NLO QCD program. Other theoretical uncertainties are due to the parameterization of the used parton density function of the proton and the value of $\alpha_s(M_Z)$ used by the parton density function and the formula for the μ_R dependence of α_s, where M_Z refers to the mass of the Z° boson ($M_Z \approx 93$ GeV).

The size of these theoretical uncertainties are given below:

- The overall scale of JetViP ($\mu = \mu_F = \mu_R$) was varied by factors of 2 and 0.5. It was generally found that the cross sections vary by approximately 20% at very low Q^2 and 7% at high Q^2.

- For the hadronization corrections, events were generated using ARIADNE and LEPTO. Those events passing the experimental selection cuts were used to obtain the hadronization correction factors $C_{i,corr}$. The spread of the values of the hadronization correction factor between ARIADNE and LEPTO was found to lie in the range 2–3%. For the actual calculation of $C_{i,corr}$ the arithmetic mean of the values from both event generators were used.

- The uncertainty due to the value of $\alpha_s(M_Z)$ was estimated by repeating the NLO QCD calculations using the CTEQ4 series of parton density functions for the proton, corresponding to values of $\alpha_s(M_Z) = 0.110, 0.113, 0.116, 0.119$ and 0.122. The uncertainty was found to be 2–5%.

- The uncertainty due to the parameterization of the used parton density function of the proton was estimated by using MRST99 instead of CTEQ4M in the NLO QCD calculations. The uncertainty was found to lie in the range 2–4%.

The cited uncertainties were added in quadrature and are shown as a band in the cross section pictures of the theory shown in the next chapter.

Chapter 9

Results and Conclusions

Events, collected by the ZEUS experiment during 1996/97 were used for this analysis. The used data sample corresponds to an integrated luminosity of $\mathcal{L} = 38.6$ pb^{-1}. Of these events about 50000 passed the analysis cuts as specified in chapter 7 and are used for determining the cross sections. In the following sections the various measured dijet cross sections are compared to NLO QCD calculations performed with JetViP using CTEQ4M (SaS1M) as parton density function for the proton (photon). For the overall scale $\mu^2 = \mu_R^2 = \mu_F^2 = E_T^2$ was chosen. To these calculations the hadronic corrections were applied as discussed in the previous chapter.

9.1 The Differential Dijet Cross Section $d\sigma/dQ^2$

In Fig. 9.1 the differential dijet cross section $d\sigma/dQ^2$ as a function of Q^2 is shown and compared to NLO QCD calculations as performed with JetViP. The full circles represent the measured data. The histograms show the NLO QCD calculations. The solid line shows the JetViP calculations including a parton density function for the partonic photon structure. The dashed histogram shows the calculation without the photon parton density function, assuming that the interaction proceeds without the development of a hadronic photon structure. The shaded or hatched boxes around the lines represent the theoretical uncertainty as explained in the last chapter. The first bin is measured with the BPC while in the second bin corresponding to $0.55 < Q^2 < 1.5$ GeV^2 the scattered positron vanishes through the beam pipe and so no measurement can be performed here.

One clearly sees that the theoretical prediction is always lower than the data. At low Q^2 the NLO QCD calculations including an additional hadronic photon structure describe the data better than those without photon struc-

ture. In the higher Q^2 ranges except for the highest range, both calculations yield the same results at least inside the theoretical uncertainty. A more detailed picture is given by the lower plot. Here the relative deviations of the NLO QCD calculations from the data are plotted. The full (open) squares give this deviation with respect to the central value of the calculation including (not including) the photon structure. The shaded or hatched boxes indicate the theoretical uncertainties. The NLO QCD calculations including a hadronic photon structure is about $\sim$30% higher than the data and this deviation is almost constant over the whole Q^2-range, except for the last bin. Therefore one cannot conclude that even at low Q^2 where the NLO QCD calculations including a parton density function for the photon describe the measured data better than those without, such a parton density function is really necessary to describe the data. The calculations without photon structure deviate from the data by $\sim$60% in the lowest Q^2-bin and this deviation is decreasing with increasing Q^2. But even in the highest Q^2-range where no hadronic structure of the photon is expected the NLO QCD calculations approach the data not better than within $\sim$20%. This makes the interpretation again difficult. However, the differential cross sections studied in the subsequent sections will shed more light onto possible reasons for this discrepancy between the NLO QCD calculations and the measured data.

9.2 The Double Differential Dijet Cross Section $d^2\sigma/dQ^2dE_{T1}$

In Fig. 9.2 the double differential dijet cross section $d^2\sigma/dQ^2dE_{T1}$ is shown as a function of the E_T of the leading jet in bins of Q^2. The meaning of the symbols is as above. Generally one sees a tendency that in all Q^2-ranges the NLO QCD calculations including a parton density function for the photon describe the measured data better than those without. The deviation from the data for the NLO QCD calculation including a photonic parton density function varies between $\sim$10–80% and those without in between $\sim$10–90%. One clearly sees according to the NLO QCD calculations that the hadronic photon structure becomes less and less important with increasing Q^2. At high Q^2 both NLO QCD calculations (with and without a photonic parton density function) merge at least inside the theoretical uncertainties. From numerical studies [Dre89] it is known that with increasing E_T the hadronic photon structure becomes less important[1] so also inside the individual Q^2-

[1] It should be noted that this is also a phase space effect and not only due to a possible photon structure!

ranges both NLO QCD calculations should merge with increasing E_T. Inside the theoretical uncertainties this is indeed the case. However, in the last two high Q^2-ranges both NLO QCD calculations differ strongly in the low E_T bins. In addition the NLO QCD calculations without a parton density function for the photon gives here the better description of the experimental data contrary to the expected behavior in the resolved photon picture. This might indicate a problem in the calculation. Indeed there are approximations done in JetViP, e.g. the partons emerging from the photon are treated as on-shell even at high virtualities of the photon and it is not clear whether such a treatment is justified.

9.3 The Double Differential Dijet Cross Section $d^2\sigma/dQ^2d\eta_{for}$

The results for the double differential dijet cross section $d^2\sigma/dQ^2d\eta_{for}$ as a function of η_{for} in different Q^2 ranges are displayed in Fig. 9.3. For the two lowest Q^2-ranges the NLO QCD calculations including a parton density function for the photon describe the experimental data better (the deviation ranges from ∼10% to ∼50%) than those without, differing from the data in between ∼10–150%. For $4.5 < Q^2 < 49$ GeV^2 both NLO QCD calculations give almost the same results inside the theoretical uncertainties. In the highest Q^2 range the NLO QCD calculations without the photonic parton density function describes the experimental data better than the calculations including a parton density function for the photon. The deviation of the NLO QCD calculations from the measured data ranges in between ∼10–80% (∼10–60%) with (without) photonic parton density function. An exception is encountered in the backward region in the lowest η_{for} bin where the contribution of a photon structure should be low. Even here the NLO QCD calculations including an additional photon structure give a better agreement with the data than those without including one.

The forward region is in particular sensitive to parton dynamics at low x, see [Mue91]. So to study a possible influence of the small x dynamics, the most forward bin of the measurement shown in Fig. 9.3 is plotted as a function of Q^2 as shown in Fig. 9.4. The picture is similar to that of the measurement of $d\sigma/dQ^2$ in Fig. 9.1. The NLO QCD calculations including a parton density function for the photon describe the measured data better (the deviation between NLO QCD calculations and data is in between 20–60%) than those without including one (the deviation between NLO QCD calculations and the data is here in between 20–150%) except for the last Q^2

bin. For increasing Q^2 the NLO QCD calculations without a photonic parton density function merges at least inside the theoretical uncertainties with the calculations including one. However, because the deviation of the NLO QCD calculations with photonic parton density function from the measured data is almost flat as in the case of $d\sigma/dQ^2$ there is no clear evidence that for low Q^2 the photon structure becomes more important than for large Q^2. In fact, the discrepancy between NLO QCD calculations and the measured data in the forward region could well be due to a different physical effect. A possible candidate enhancing the energy flow in the forward region is e.g. a different parton dynamics at small x. This could also explain the excess of the NLO QCD calculations over the measured data found in the discussion of $d\sigma/dQ^2$ above.

For a more detailed study of such a hypothesis a NLO QCD calculation would be needed. However, as of today it is not available.

9.4 The Double Differential Dijet Cross Section $d^2\sigma/dQ^2dx_\gamma^{obs}$

The results for the double differential dijet cross section $d^2\sigma/dQ^2dx_\gamma^{obs}$ as a function of x_γ^{obs} in different Q^2 ranges are shown in Fig. 9.5. Only those points of the NLO QCD calculations are shown which deviate not more than 200% from the data to avoid that huge deviations hide the details of the comparison between NLO QCD calculations and the data. One clearly sees that in all Q^2 ranges the NLO QCD calculations including a parton density function for the photon describe the experimental data better than those without an additional photon structure. This is especially true for the region $x_\gamma^{obs} < 0.75$[2] where the influence of a partonic photon structure is expected. In the last x_γ^{obs}-bin where the photon is expected to act predominantly pointlike both calculations give the same result ($\sim$40% deviation from the data) inside the theoretical error. With increasing Q^2 the description of the data in the $x_\gamma^{obs} < 0.75$ region by the NLO QCD calculations without a photonic parton density function becomes better. The deviation of these calculations from the data (for $x_\gamma^{obs} < 0.75$) ranges from $> 200\%$ to 100% in the lowest Q^2 range down to 160–60% in the highest Q^2 range. In the same x_γ^{obs} region the NLO QCD calculations including a photonic parton density function deviate from the experimental data from $> 200\%$ to 5% in the lowest Q^2 range down to 40–5% in the highest Q^2 range. In conclusion, the shape of the x_γ^{obs} distribution is not well modeled by the NLO QCD calculations no matter

[2]The point $x_\gamma^{obs} = 0.75$ is marked by the left edge of the last bin.

whether they include a parton density function for the photon or not. It is therefore doubtful whether the picture of a photon with a partonic structure implemented in the NLO QCD calculations is supported by the data.

9.5 Influence of the Scale on the Dijet Cross Sections

The NLO QCD calculations presented in this analysis were performed with the choice $\mu^2 = \mu_R^2 = \mu_F^2 = E_T^2$. To study the influence of the scale the calculations were repeated using the $\mu^2 = Q^2$ and $\mu^2 = Q^2 + E_T^2$, respectively (not shown in this thesis). The scale $\mu^2 = Q^2 + E_T^2$ gave similar results as $\mu^2 = E_T^2$ what is not surprising because in the performed analysis, E_T^2 is always higher than Q^2. The scale $\mu^2 = Q^2$ on the other hand gave a huge scale uncertainty which was approximately 5–10 times larger than the scale uncertainty for $\mu^2 = E_T^2$ or $\mu^2 = Q^2 + E_T^2$ and was therefore not considered. Also the lowest Q^2 ($0.1 < Q^2 < 0.55$ GeV^2) was not available for this scale because to calculate $\alpha_S(\mu^2)$ a large scale is needed.

9.6 Summary and Conclusions

The measured differential dijet cross sections $d\sigma/dQ^2$, $d^2\sigma/dQ^2dE_{T1}$, $d^2\sigma/dQ^2d\eta_{for}$ and $d^2\sigma/dQ^2dx_\gamma^{obs}$ were shown and compared to next-to-leading order calculations in QCD as performed with JetViP. The program JetViP was chosen because it is the only one which can perform calculations including a parton density function for the virtual photon. However, this program contains approximations which make it unreliable at large Q^2.

Generally the comparison of the experimental data to the NLO QCD calculations showed that the calculations including a parton density function for the photon fits the data better than those without including such an additional photon structure. However, the data do not clearly support the need for such a partonic structure of the photon. Though there exists some indication, the uncertainties are too large. The bad description of the data at high E_T and high Q^2 where no partonic structure of the photon is expected does not support the hypothesis that the inclusion of such a photon structure alone improves the description of the data. Part of the bad description possibly arises from approximations done in JetViP. It is e.g. not clear whether an on-shell treatment of partons emerging from the virtual photon is reliable. However, the discussion of the double differential dijet cross section $d^2\sigma/dQ^2d\eta_{for}$ showed that most of the discrepancy between NLO QCD cal-

culations and measured data stems from the forward region. This might also account for the excess of the data over the NLO QCD calculations found in the discussion of the differential dijet cross section $d\sigma/dQ^2$, provided the calculations are correct. It is also known that the forward region is sensitive to parton dynamics at low x. So the predominance of the discrepancy between NLO QCD calculations and measured data in the forward region might indicate that other effects apart from photon structure have to be considered to get a more consistent picture. The parton density functions, e.g. are usually determined by means of the DGLAP evolution equations which do not hold at low x. Of course also the inclusion of higher orders in the perturbative series could yield an improvement.

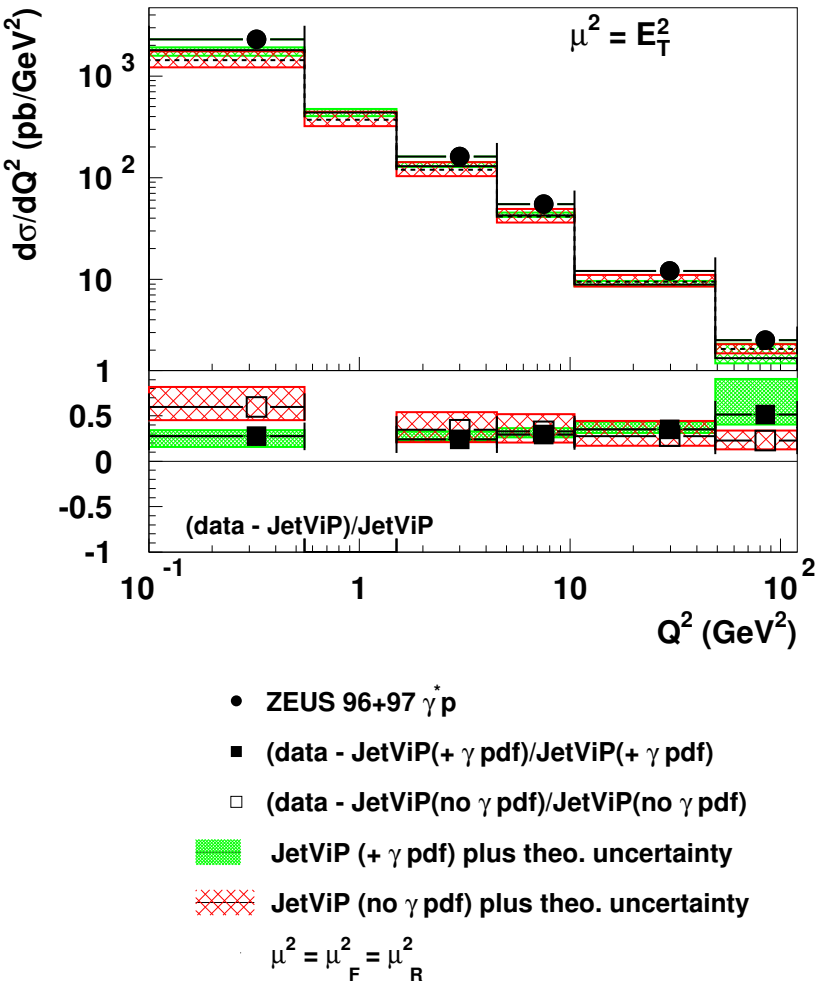

Figure 9.1: The differential dijet cross section $d\sigma/dQ^2$ compared with next-to-leading order calculations of JetViP including hadronization corrections (see text for details). The parton density function CTEQ4M was used for the proton and the parton density function SaS1M was used for the photon.

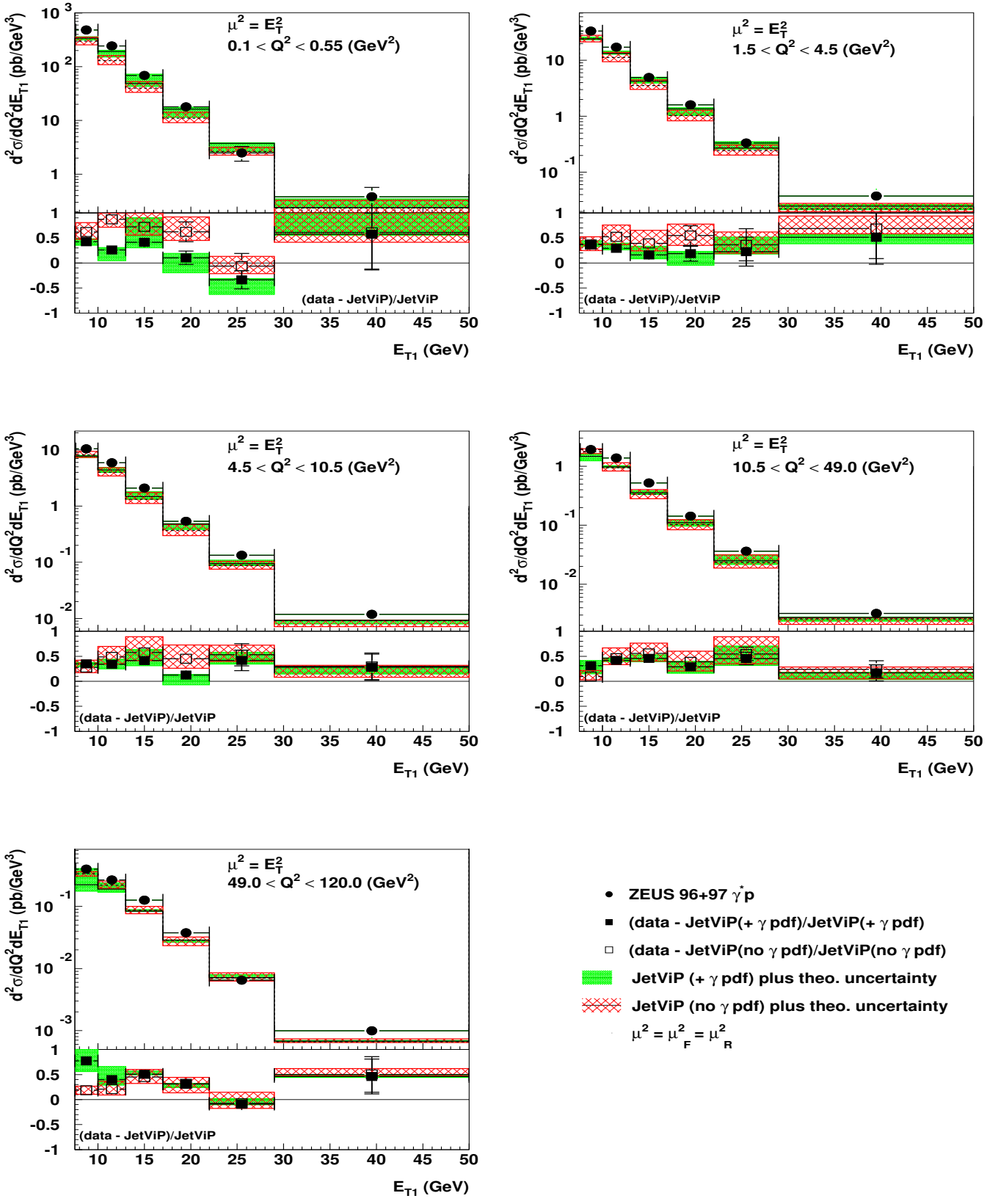

Figure 9.2: The double differential dijet cross section $d\sigma/dQ^2dE_{T1}$ compared with next-to-leading order calculations of JetViP including hadronization corrections (see text for details). The parton density function CTEQ4M was used for the proton and the parton density function SaS1M was used for the photon.

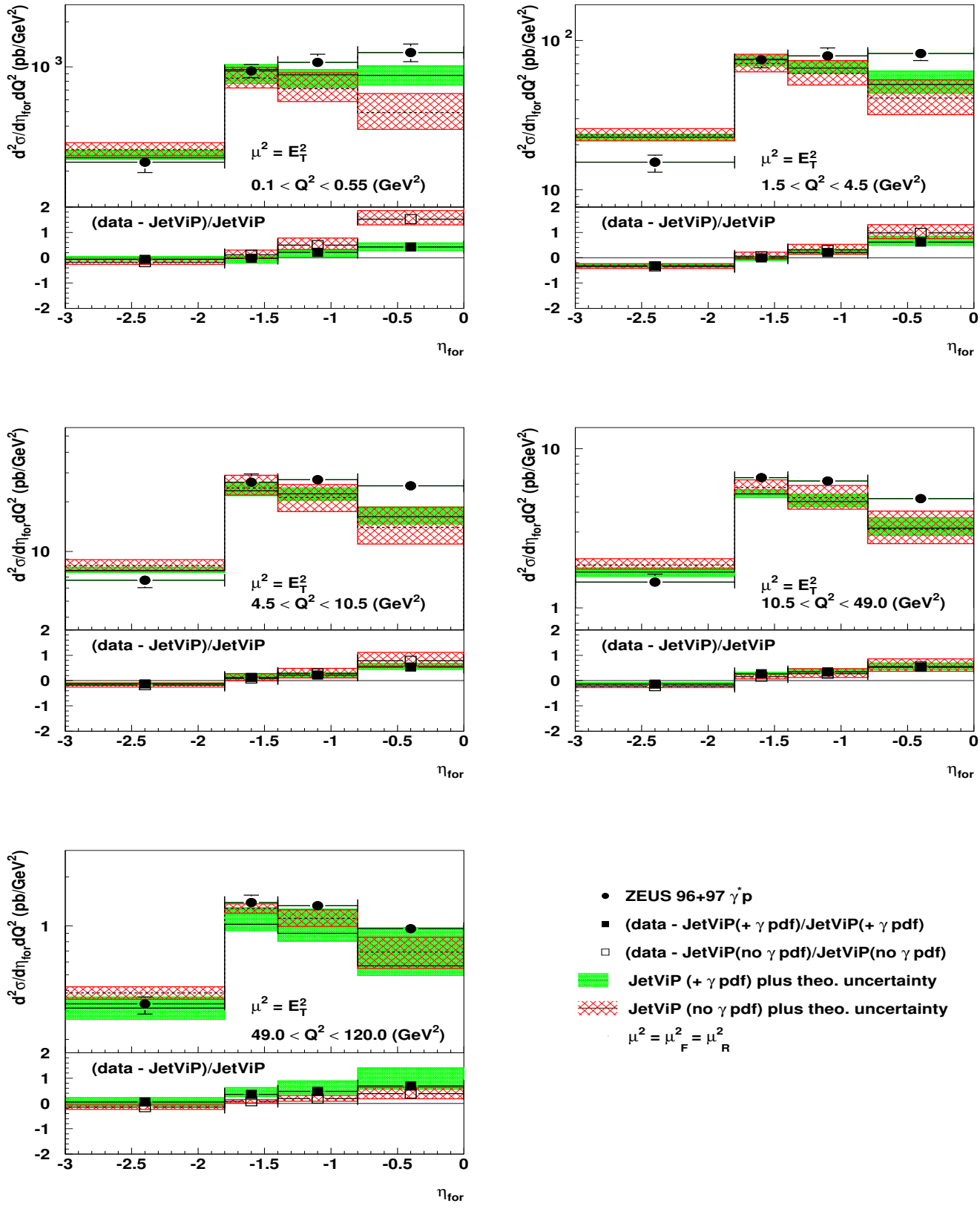

Figure 9.3: The double differential dijet cross section $d\sigma/dQ^2 d\eta_{for}$ compared with next-to-leading order calculations of JetViP including hadronization corrections (see text for details). The parton density function CTEQ4M was used for the proton and the parton density function SaS1M was used for the photon.

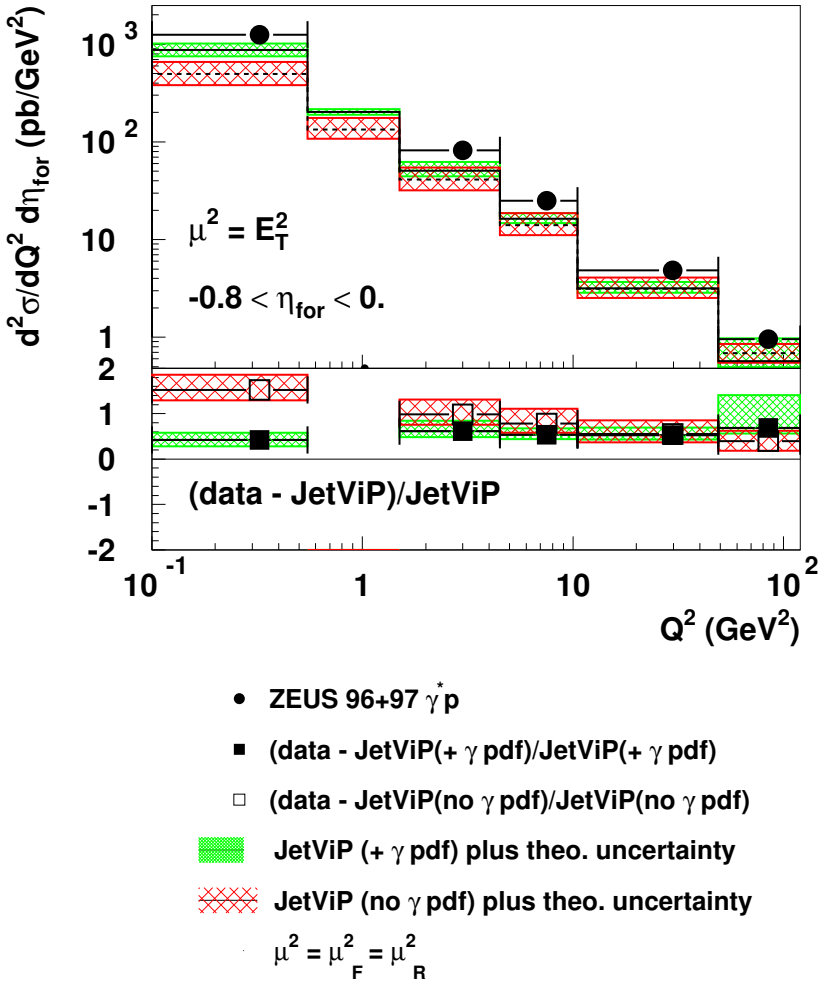

Figure 9.4: The forward bin $-0.8 < \eta_{for} < 0$ of the double differential dijet cross section $d\sigma/dQ^2 d\eta_{for}$ compared with next-to-leading order calculations of JetViP including hadronization corrections (see text for details). The parton density function CTEQ4M was used for the proton and the parton density function SaS1M was used for the photon.

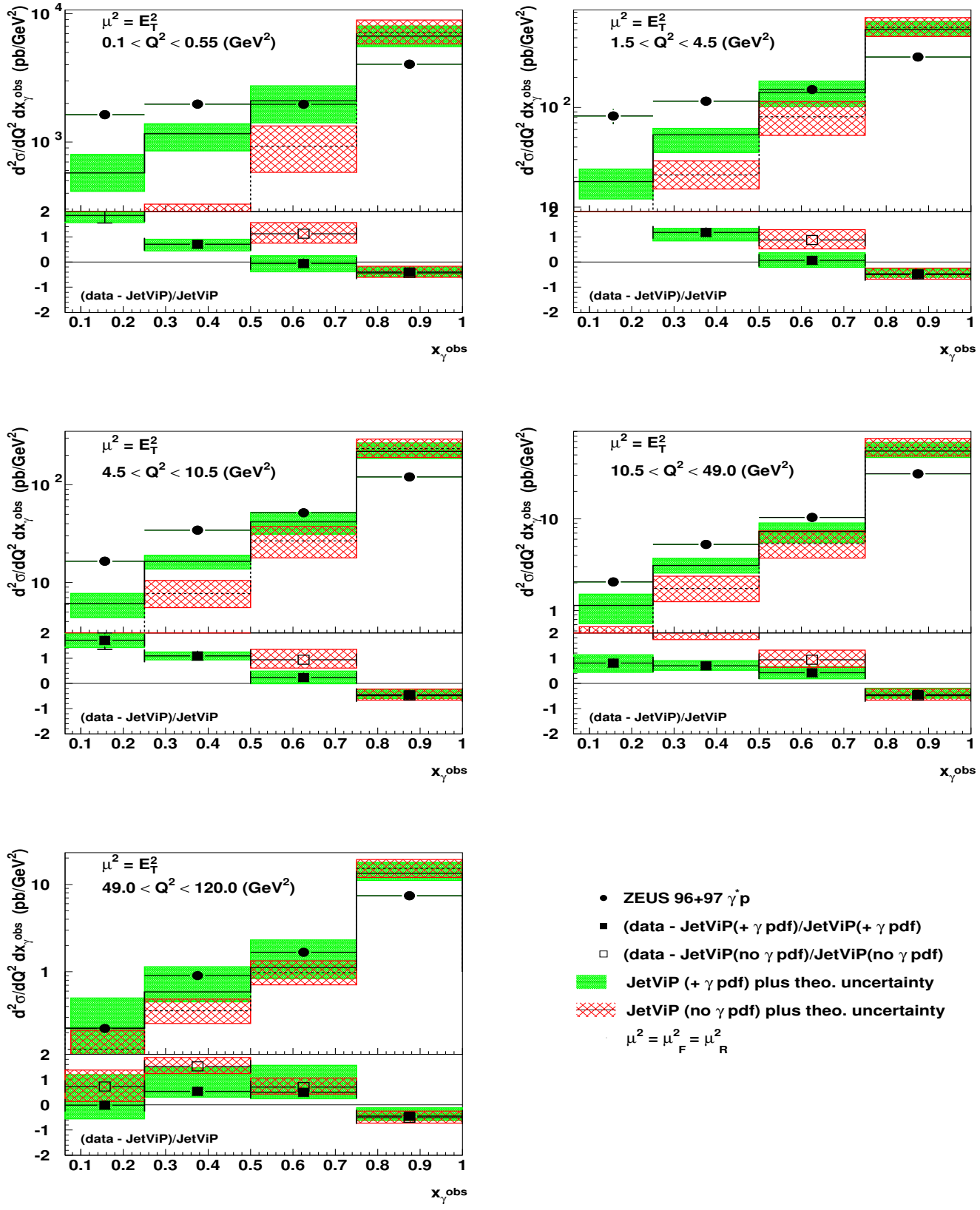

Figure 9.5: The double differential dijet cross section $d\sigma/dQ^2 dx_\gamma^{obs}$ compared with next-to-leading order calculations of JetViP including hadronization corrections (see text for details). The parton density function CTEQ4M was used for the proton and the parton density function SaS1M was used for the photon.

Bibliography

[Abb02] OPAL Collaboration, G. Abbiendi et al., *Eur. Phys. J.*, **C24**, 17 (2002).

[Abe92] F. Abe, *Phys. Rev.*, **D45**, 1448 (1992).

[Abr91] H. Abramowicz, K. Charchula and A. Levy, *Phys. Lett.*, **B269**, 458 (1991).

[Abr95] H. Abramowicz, A. Caldwell and R. Sinkus, *Neural Network Based Electron Identification in the ZEUS Calorimeter*, ZEUS–note (not published) (1995). R. Sinkus, *Nucl. Instr.*, **A361**, 290 (1995).

[Acc98] L3 Collaboration, M. Acciarri et al., *Phys. Lett.*, **B438**, 363 (1998).

[Adl00] H1 Collaboration, C. Adloff et al., *Eur. Phys. J.*, **C13**, 397 (2000).

[Aid95] H1 Collaboration, S. Aid et al., *Z. Phys.*, **C69**, 27 (1995).

[Alt79] G. Altarelli, R.K. Ellis and G. Martinelli, *Nucl. Phys.*, **B157**, 461 (1979).

[Ama79] D. Amati and G. Veneziano, *Phys. Lett.*, **B83**, 87 (1979).

[And86] B. Anderson, G. Gustafson and B. Söderberg, *Z. Phys.*, **C20**, 317 (1983), *Nucl. Phys.*, **B264**, 29 (1986). B. Anderson, G. Gustafson, G. Ingelman and T. Sjöstrand, *Phys. Rep.*, **97**, 33 (1983).

[And89] B. Anderson et al., *Z. Phys.*, **C43**, 625 (1989).

[And98] B. Anderson, *The Lund Model*, Cambridge University Press (1998).

[And33] C.D. Anderson, S.H. Neddermeyer, *Phys. Rev.*, **43**, 1034L (1930).

[And91] A. Andresen et al., *Nucl. Instr. and Meth.* **A 309** (1991) 101.

[And92] J. Andruskow et al., *DESY 92-066* (1992).

[Art74] X. Artru and G. Mennessier, *Nucl. Phys.*, **B70**, 93 (1974).

[Aur87] P. Aurenche et al., *Nucl. Phys.*, **B286**, 553 (1987).

[Aur94] P. Aurenche, J.-P. Guillet and M. Fontannaz, *Z. Phys.*, **C64**, 621 (1994).

[Bae89] H. Baer, J. Ohnemus, J.F. Owens, *Phys. Rev.*, **D40**, 2844 (1989).

[Bal78] Y.Y. Balitsky and L.N. Lipatov, *Sov. J. Nucl. Phys.*, **28**, 282 (1978).

[Bal88] A. Baldini et al., *Landoldt-Börnstein's New Series I/12b*, 345 (1988).

[Bam95] A. Bamberger et al., *ZEUS-Note 95-095* (1995).

[Bam96] A. Bamberger et al., *Nucl. Instr. and Meth.* **A 382** (1996) 419.

[Bam97] A. Bamberger et al., *Nucl. Instr. and Meth.* **A 401** (1997) 63.

[Bar78] W.A. Bardeen et al, *Phys. Rev.*, **D18**, 3998 (1978).

[Bas79] A. Bassetto, M. Ciafaloni and G. Marchesini, *Phys. Lett.*, **B83**, 207 (1979).

[Bau78] T.H. Bauer et al., *Rev. Mod. Phys.*, **50**, no. 2, 261 (1978).

[Baw89] A.C. Bawa, W.J. Sterling, *J. Phys*, **G15**, 1339 (1989).

[Ben91] S. Bentvelsen, J. Engelen and P. Kooijman, in *Proceedings of the Workshop on Physics at HERA*, ed. W. Buchmüller and G. Ingelman (1991).

[Ber83] PLUTO Collaboration, C. Berger in *International Symposiom of Lepton Photon Interactions at High Energies*, Ithaca, N.Y., ed. D.G. Cassel and D.L. Kreinick, Lab. Nucl. Studies 376 (1983).

[Ber87] C. Berger and W. Wagner, *Phys. Rep.*, **146**, 1 (1987).

[Ber93] B. Bernstein et al., *Nucl. Instr. and Meth.* **A 336** (1993) 23.

[Bet34] H. Bethe and W. Heitler, *Proc. Roy. Soc.* **A 146** (1934) 83.

[Bjo65] J.D. Bjorken, S.D. Drell, *Relativistic Quantum Fields*, Mc Graw-Hill Book Company (1965).

[Bjo67] J.D. Bjorken, *Phys. Rev.*, **179**, 1547 (1969).

[Bjo89] J.D. Bjorken, *Two Topics in Quantum Chromodynamics*, SLAC-PUB-5103 (not published) (1989).

[Blo69] E.D. Bloom et al., *Phys. Rev. Lett.*, **23**, 930 (1969a).

[Boe93] D. Bödeker, *Phys. Lett.*, **B292**, 164 (1992), *Z. Phys*, **C59**, 501 (1993).

[Boh55] N.Bohr and L. Rosenfeld, *K. Dansk. Vid. Selsk. Matt.-Fys. Medd.*, **12**, No.8 (1933).

[Bow81] M.G. Bowler, *Z. Phys.*, **C11**, 169 (1981).

[Bre69] M. J. Breidenbach et al., *Phys. Rev. Lett.*, **23**, 935 (1969).

[Bre97] ZEUS Collaboration, J. Breitweg et al., *Phys. Lett.*, **B407**, 432 (1997).

[Bre00] ZEUS Collaboration, J. Breitweg et al., *Phys. Lett.*, **B479**, 37 (2000).

[Bri98] G. Briskin, *Diffractive Dissociation in* ep *Deep Inelastic Scattering*, PhD Thesis University of Tel Aviv, DESY-THESIS-1998-036 (unpublished) (1998).

[Bru87] R. Brun et al., *GEANT3.13*, CERN DD/EE/84-1 (unpublished) (1987).

[Bud75] V.M. Budnev et. al., *Phys. Rept.*, **15**, 181 (1975).

[Cal98] A. Caldwell, W. Liu and B. Straub, *BCAL Electron Studies Part I: MC and Test Beam Energy Studies*, ZEUS–note (not published) (1998). A. Caldwell, W. Liu and B. Straub, *BCAL Electron Studies Part II: Energy Scale Calibration*, ZEUS–note (not published) (1998).

[Cat90] S. Catani, F. Fiorani and G. Marchesini,*Phys. Lett.*, **B234**, 339 (1990), *Nucl. Phys.*, **B336**, 18 (1990).

[Cat93] S. Catani, Y.L. Dokshitzer, M.H. Seymour, B.R. Webber, *Nucl. Phys.*, **B406**, 187 (1993).

[Cha30] C.Y. Chao, *Proc. Natl. Acad. Sci. U.S.*, **16**, 431 (1930).

[Cha01] D. Chapin, *A Measurement of Dijet Production in Neutral Current Deep Inelastic Sacttering with ZEUS at HERA*, Ph.D. thesis, Univ. of Wisconsin (2001).

[Che01] ZEUS Collaboration, S. Chekanov et al., *Phys. Lett.*, **B531**, 9 (2001).

[Che02] ZEUS Collaboration, S. Chekanov et al., *Eur. Phys. J.*, **C23**, 615 (2002).

[Chy00] J. Chyla and M. Tasevsky, *Phys. Rev.*, **D62**, 114025 (2000).

[Cia87] M. Ciafaloni, *Nucl. Phys.*, **B296**, 249 (1987).

[Col82] J.C. Collins and D.E. Soper, *Nucl. Phys.*, **B261**, 445 (1982).

[Col89] J.C. Collins, D.E. Soper and G. Sterman, in *Perturbative Quantum Chromodynamics*, ed. A.H. Mueller (World Scientific, Singapore), 1 (1989).

[Cur80] G. Curci, W. Furmanski and R. Petronzio, *Nucl. Phys.*, **B175**, 27 (1980).

[Der91] ZEUS Collaboration M. Derrick et al., *Nucl. Instr. and Meth.*, **A 309** (1991) 77.

[Der94] ZEUS Collaboration, M. Derrick et al., *Phys. Lett.*, **B322**, 287 (1994).

[De94a] ZEUS Collaboration, M. Derrick et al., *Z. Phys.*, **C63**, 391 (1994).

[DES94] DESY, *Annual report* (1994).

[Dir28] P.A.M. Dirac, *Proc. Roy. Sec (London)*, **A 118**, 351 (1928).

[Dir33] P.A.M. Dirac, *Physikalische Zeitschrift der Sowjetunion*, **3**, 64 (1933).

[Dok77] Y.L. Dokshitzer, *Sov. Phys. JETP*, **46**, 641 (1977); V.N. Gribov and L.N. Lipatov, *Sov. J. Nucl., Phys.*, **15**, 438 and 675 (1972); G. Altarelli and G. Parisi, *Nucl. Phys.*, **126**, 297 (1977).

[Don92] A. Donnachie and P.V. Landshoff, *Phys. Lett.*, **B296**, 227 (1992).

[Dre85] M. Drees and K. Grassie, *Z. Phys.*, **C28**, 451 (1985).

[Dre89] M. Drees and R.M. Godbole, *Phys. Rev.*, **D39**, 169 (1989).

[Dre94] M. Drees and R.M. Godbole, *Phys. Rev.*, **D50**, 3124 (1994).

[Dre58] S.D. Drell, in *Proceedings of the 1958 Annual International Conference on High Energy Physics at CERN*, edited by B. Ferretti (CERN, Geneva), p.27.

[Dys49] F.D. Dyson, *Phys. Rev.*, **75**, 486, 1736 (1949).

[Edi97] A. Edin, G. Ingelman and J. Rathsman, *Phys. Lett.*, **B366**, 371 (1996), *Z. Phys.*, **C75**, 57 (1997).

[Ell86] R.K. Ellis, J.C. Sexton, *Nucl. Phys.*, **B269**, 445 (1986).

[Ell81] R.K. Ellis, D.A. Ross, A.E. Terrano, *Nucl. Phys*, **B178**, 421 (1981).

[Ell92] S.D. Ellis, Z. Kunszt and D.E. Soper, *Phys. Rev. Lett.*, **23**, 1415 (1992).

[Ell93] S.D. Ellis and D.E. Soper, *Phys. Rev.*, **D48**, 3160 (1993).

[Fab82] K. Fabricius et al., *Z. Phys.*, **C11**, 315 (1982).

[Fie78] R.D. Field and R.P. Feynman, *Nucl. Phys.*, **B136**, 1 (1978).

[Fie83] R.D. Field and S. Wolfram, *Nucl. Phys.*, **B312**, 65 (1983).

[Fie89] R.D. Field, *Applications of Perturbative QCD*, PERSEUS BOOKS, Reading Massachusetts (1989).

[Fer24] E. Fermi, *Z. Phys.*, **29**, 315 (1924).

[Fey48] R.P. Feynman, *Rev. Mod. Phy.*, **20**, 367 (1948).

[Fey69] R.P. Feynman, *Phys. Rev. Lett.*, **23**, 1415 (1969).

[Fey72] R.P. Feynman, *Photon–Hadron Interactions*, Benjamin, New York (1972).

[Fos93] B.Foster et al., *Nucl. Instr. and Meth.* **A 338** (1993) 254.

[Fra59] W.R. Frazer and J.R. Fulco, *Phys.Rev. Lett.*, **2**, 365 (1959); *Phys. Rev.*, **117**, 1609 (1960).

[Fri99] U. Fricke, *Precision Measurement of the Proton Structure Function F_2 at low Q^2 and Very Low x at HERA*, DESY-THESIS-1999-043.

[Frx97] S. Frixione and G. Ridolfi, *Nucl. Phys.*, **B507**, 315 (1997).

[Gel64] M. Gell-Mann, *Phys. Lett.*, **8**, 214, (1964).

[Glu82] M. Glück, E. Hoffmann and E. Reya, *Z. Phys.*, **C13**, 119 (1982).

[Glu92] M. Glück, E. Reya and A. Vogt, *Phys. Rev.*, **D45**, 3986 , *Phys. Rev.*, **D46**, 1973 (1992).

[Glu95] M. Glück, E. Reya and M. Stratmann, *Phys. Rev.*, **D51**, 3220 (1995).

[Glu99] M. Glück, E. Reya and I. Schienbein, *Phys. Rev.*, **D60**, 54019 (1999).

[Gor26] W. Gordon, *Z. Physik*, **40**, 117 (1926).

[Gor92] L.E. Gordon and J.K. Storrow, *Z. Phys.*, **C56**, 307 (1992).

[Gor97] L.E. Gordon and J.K. Storrow, *Nucl. Phys.*, **B489**, 405 (1997).

[Gre89] M.G. Green, *RNBNC 89-01* (1989).

[Gro93] F. Gross, *Relativistic Quantum Mechanics and Field Theory*, John Wiley & Sons, Inc. (1993).

[Gro98] J. Grosse-Knetter, *Corrections for the Hadronic Final State*, ZEUS-98-031 (unpublished) (1998).

[Gus86] G. Gustafson, *Phys. Lett.*, **B175**, 453 (1986).

[Gus88] G. Gustafson and U. Petterson, *Nucl. Phys.*, **B306**, (1988).

[Hag95] K. Hagiwara, M. Tanaka and I. Watanabe, *Phys. Rev.*, **D51**, 3197 (1995).

[HER93] HERMES Collaboration, *Technical Design Report* (1993).

[HEB94] HERA-B Collaboration, *Technical Design Report*, DESY-PRC 95/01 (1995).

[HES91] Proposal for a hadron electron separator in the ZEUS forward and barrel calorimeter. *DESY–ZEUS-Note 91-044* (91/05,rec.June) 46.

[Hof56] R.W. McAllister and R. Hofstadter *Phys. Rev.*, **102**, 851 (1956); E.E. Chambers and R. Hofstadter *Phys. Rev.*, **103**, 1454 (1956).

[Hol93] ZEUS Collaboration, *The ZEUS Detector*, Status Report 1993, edited by U.Holm, (1993).

[Hoo72] G. t'Hooft and M. Veltman, *Nucl. Phys.*, **B44**, 189 (1972).

[Hug53] D.J. Hughes et al., *Phys. Rev.*, **90**, 497 (1953).

[Ing91] G. Ingelman in *Proc. Workshop on "Physics at HERA"*, eds. W. Buchmüller and G. Ingelman, Vol. 3 1366, Hamburg (1991).

[Ing97] G. Ingelman, A. Edin and J. Rathsman, *Comp. Phys. Comm.*, **101**, 108 (1997).

[Jac79] F. Jacquet and A. Blondel, in *Proceedings of The Study of an ep Facility for Europe*, ed. by U. Amaldi, (Hamburg, Germany, 1979).

[Kin62] T. Kinoshita, *J. Math. Phys.*, **3**, 650 (1962), T.D. Lee, M. Nauenberg, *Phys. Rev.*, **133B**, 1549 (1964).

[Kla95] M. Klasen, G. Kramer and S.G. Salesch, *Z. Phys.*, **C68**, 113 (1995).

[Kla96] M. Klasen and G. Kramer, *Z. Phys.*, **C72**, 107 (1996).

[Kla98] M. Klasen et al., *Eur. Phys. J. direct*, **C1**, 1 (1998).

[Kle27] O. Klein, *Z. Physik*, **41**, 407 (1927).

[Kra00] M. Krawczyk and Z. Zembrzuski, *Nucl. Phys. Proc. Suppl.*, **B82**, 167 (2000).

[Kur72] E.A. Kuarev, L.N. Lipatov and V.S. Fadin, *Sov. Phys. JETP*, **45**, 199 (1972).

[Lam51] W. E. Lamb,jr., *Repts. Progr. Phys.*, **14**, 19, (1951).

[Lam57] W. E. Lamb,jr., and R. C. Retherford, *Phys. Rev.*, **72**, 241, (1957).

[Lew26] G.N. Lewis, *Nature* **118** no. 2981, 874 (1926).

[Lon92] L. Lönnblad, *Comp. Phys. Comm.*, **71**, 15 (1992).

[Mar80] G. Marchesini, L. Trentadue and G. Veneziano, *Nucl. Phys.*, **B181**, 335 (1980).

[Mar92] G. Marchesini et al., *Phys. Comm*, **67**, 465 (1992).

[Mar02] A.D. Martin, R.G. Roberts, W.J. Sterling and R.S. Thorne, *Eur. Phys. J.*, **C23**, 73 (2002).

[McI56] J.A. McIntyre and R. Hofstadter, *Phys. Rev.*, **103**, 1464, (1956); *Phys. Rev.*, **98**, 158 (1955).

[Mel56] E. Melkonian et al., *Phys. Rev.*, **114**, 1571, (1956).

[Mue91] A. Mueller, *Nucl. Phys. B (Proc. Suppl.)*, **18C**, 125 (1990), *J. Phys.*, **G17**, 1443 (1991).

[Nam57] Y. Nambu, *Phys. Rev.*, **106**, 1366 (1957).

[Opp33] J.R. Oppenheimer, M.S. Plesset, *Phys. Rev.*, **44**, 53L (1933).

[Nis00] R. Nisius, *Phys. Rept.*, **332**, 165 (2000).

[Pio93] K. Piotrzkowski, *DESY F35D-93-06* (1993).

[Plo95] H. Plothow-Besch, *Int. J. Mod. Phys.*, **A10**, 2901 (1995).

[Pot99] B. Pötter, *Comp. Phys. Comm.*, **133**, 105 (1999).

[Pot00] B. Pötter, *Comp. Phys. Comm.*, **119**, 45 (2000). The program JetViP is available from `http://www.desy.de/~poetter/jetvip.html`.

[Pot01] B. Pötter, private communication.

[Pum02] J. Pumplin et al., *JHEP*, **0207**, 12 (2002).

[Rep96] J. Repond, *Jet Energy Corrections*, ZEUS–note (not published) (1996).

[Rey92] M. Glück, E. Reya and A. Vogt, *Z. Phys.*, **C53**, 651 (1992).

[Rey99] M. Glück, E. Reya and I. Schienbein, *Eur. Phys. J.*, **C10**, 131 (1999).

[Rob90] R.G. Roberts, *The Structure of the Proton*, Cambridge University Press (1990).

[Ryd96] L.H. Ryder, *Quantum Field Theory*, 2nd edition, Cambridge University Press, Cambridge (1996).

[Sak60] J.J. Sakurai, *Annals of Physics*, **11**, 1 (1960).

[Sas00] K. Sasaki and T. Uematsu, *Nucl. Phys. Proc. Suppl.*, **B89**, 162 (2000).

[Sav98] A. Savin, *Study of Calorimeter Noise in the 1996 Data*, ZEUS–note (not published) (1998).

[Sch26] E. Schrödinger, *Ann. Physik*, **81**, 109 (1926).

[Sch93] G.A. Schuler and T. Sjöstrand, *Phys. Lett.*, **B300**, 169, *Nucl. Phys.*, **B407**, 539 (1993).

[Sch95] G.A. Schuler and T. Sjöstrand, *Z. Phys.*, **C68**, 607 (1995).

[Sch96] G.A. Schuler and T. Sjöstrand, *Phys. Lett.*, **B376**, 193 (1996).

[Sey98] M. Seymour, *Nucl. Phys.*, **B513**, 269 (1998).

[Sjo94] T. Sjöstrand *Comp. Phys. Comm.*, **82**, 74 (1994).

[Sjo01] T. Sjöstrand et al., *Comp. Phys. Comm.*, **135**, 238 (2001).

[Sop96] D.E. Soper, in M. Golterman et al.eds. *Lattice '96 International Symposium on Lattice Field Theory*, St.Louis, June 1996 (Elsevier Science, Amsterdam).

[Ste77] G. Sterman and S. Weinberg, *Phys. Rev. Lett.*, **39**, 1426 (1977).

[Ste95] G. Sterman et al. *Rev. Mod. Phys.*, **67**, no. 1, 157 (1995).

[Sud56] V.V. Sudakov, *Sov. Phys. JETP*, **30**, 87 (1956).

[Tar32] G.T.P. Tarrant, *Proc. Roy. Soc. (London)*, **A128**, 345 (1930), **A135**, 223 (1932).

[Tun01] ZEUS-Collaboration, N. Tuning, *ZUFOs: Hadonic Final State Reconstruction with Calorimeter, Tracking and Backsplash Correction*, ZEUS–note ZEUS–01–021 (not published) (2001).

[Uij92] H. Uijterwaal, *The Global Second Level Trigger for ZEUS*, Ph.D. thesis, Univ. of Amsterdam (1992).

[Web84] B.R. Webber, *Nucl. Phys.*, **B238**, 492 (1984).

[Wei34] C.F. von Weizsäcker, *Z.Phys.*, **88**, 612 (1934).

[Wic50] G.C. Wick, *Phys. Rev.*, **80**, 268 (1950).

[Wil34] E.J. Williams, *Kgl. Danske Vidensk. Selskab. Mat.-Fiz. Medd.*, **N4**, 13, (1935).

[Yan54] C.N. Yang and R.L. Mills, *Phys. Rev.*, **96** 191 (1954).

[Zwe64] G. Zweig, *CERN-8182/TH 401* (1964); *CERN-8419/TH 402* (1964).

Acknowledgment

That's it! The hard work is over and what is left to do is to say "Thank you!" to all the people who supported me with my work in one or the other way, what is a big pleasure for me.

First of all I have to thank Prof. Dr. R. Klanner who gave an old bone like me the opportunity to make his PhD.

Many thanks also to A. Lupi and D. Kçira who taught me all the technical things I had to know to work with the ZEUS computing environment. The latter I have also to thank for providing me the ARIADNE and LEPTO runs.

My warmest thanks go to Dr. T. Carli who had the idea to this analysis and who supported me with his always useful and constructive comments. He even found the time next to his duties at CERN to carefully read the manuscript of this thesis and making many useful comments.

I would also like to thank the group "Nukleare Messtechnik" of the University of Hamburg who supported me strongly during my time as "Upilex man". I really enjoyed the time in this group! I would like to mention here in particular U. Pein who fulfilled every wish before it was spoken out and P. Buhmann for strongly helping me with my work and for all the fun we had.

Many thanks also to B. Koppitz with whom I shared the "Upilex hell" for all his support and friendship.

Last, but not least I have to thank all the ZEUS students for the nice working conditions and all the fun.